Dissertation

Submitted to the

Combined Faculties for the Natural Sciences and for Mathematics

Of the Ruperto-Carola University of Heidelberg, Germany

for the degree of

Doctor of Natural Sciences

presented by

Diplom-Molekularmedizinerin Maike Christine Nortmeyer

born in: Mannheim

Oral-examination: 04.06.2019

MYCN dependency of *MYCN* amplified neuroblastoma cell lines analyzed in relation to their interaction with BET proteins and in a novel orthotopic mouse model

Referees: Prof. Dr. Thomas Höfer

PD Dr. Frank Westermann

Summary

Neuroblastomas are the most common extracranial solid tumors in early childhood and account for 7% of all pediatric cancers. Amplification of the *MYCN* gene occurs in 20-30% of neuroblastoma cases and is associated with aggressive cancers and a poor outcome for the patients. Despite decades of research on *MYCN* and *c-MYC* and several known functions of these proteins, there are no therapeutic approaches targeting transcription factors of the MYC family.

BET inhibitors inhibit growth and induce apoptosis in several *MYC*-overexpressing cancer types. Based on these findings, BET inhibitors were tested as part of this thesis for *MYCN* amplified neuroblastoma *in vitro* and *in vivo*. A panel of 23 neuroblastoma cell lines was screened for sensitivity upon treatment with the BET inhibitor JQ1 by using viability assays, soft agar assays and FACS live/dead and cell cycle staining. Based on the viability screening, 55% of the *MYCN* amplified and 30% of the *MYCN* non-amplified cell lines were categorized as JQ1 sensitive. Reduced viability was mirrored by the absence of anchorage independent growth and an increase of G1 and sub-G1 fraction after JQ1 treatment. Protein expression data were estimated by western blot and Reverse Phase Protein Array, showing that MYCN protein levels were reduced in 70% of the *MYCN* amplified neuroblastoma cell lines and that further proteins related to the G1/S-transition of the cell cycle were lower expressed. A shRNA-mediated BRD4 knockdown in *MYCN* amplified IMR5/75 cells did not affect MYCN protein levels but reduced the expression of Cyclin D1. Global mRNA expression of four JQ1-treated cell lines was analyzed by RNA-sequencing, showing differential expression of genes related to cell cycle, damage response and chromatin methylation. *In vivo*, treatment with the BET inhibitor BAY1238097 prolonged the survival of mice harboring xenograft tumors deriving from the neuroblastoma cell line LS.

Common neuroblastoma mouse models either belong to the *MYCN* amplified or to the *MYCN* non-amplified group of neuroblastoma. No neuroblastoma mouse model is available harboring both a strong and a low *MYCN* gene expression, allowing the analysis of *MYCN* on and *MYCN* off conditions with the same genetic background. A *MYCN* high/low orthotopic neuroblastoma mouse model was established with a tumor growth rate of 80%. Tumor imaging was performed by Magnet-Resonance-Imaging and *in vivo* bioluminescence. The *MYCN* knockdown was analyzed and falcified by quantitative PCR and RNA-sequencing.

In conclusion, BET inhibitors are probably an efficient therapeutic option for a genetically preselected number of neuroblastoma cases, although amplified *MYCN* alone is not predisposing neuroblastoma tumors for a therapy with BET inhibitors. The *MYCN* high/low mouse model needs further research for the establishment of a stable *MYCN* knockdown.

Zusammenfassung

Das Neuroblastom ist mit 7 % aller pädiatrischen Krebserkrankungen der häufigste extrakraniale solide Tumor bei Neugeborenen und Kleinkindern. Eine Amplifikation des *MYCN* Gens liegt in 20-30 % der Fälle vor und ist mit aggressiven Verläufen assoziiert. Obwohl *MYCN* und *c-MYC* seit Jahrzehnten im Fokus der onkologischen Forschung stehen und eine Vielzahl an Funktionen bekannt sind, gibt es bislang noch keine auf *MYC* ausgerichtete Therapie.

Inhibitoren für BET Proteine reduzieren die Proliferation und induzieren Apoptose in einer Vielzahl von *MYC*-überexprimierenden Tumorentitäten. Basierend hierauf wurden BET Inhibitoren im Rahmen einer präklinischen Studie für *MYCN* amplifizierte Neuroblastome *in vitro* und *in vivo* getestet. Eine Gruppe von 23 Neuroblastomzelllinien wurde mit dem BET Inhibitor JQ1 behandelt und hinsichtlich ihrer Sensitivität untersucht. Hiervon wurden 55 % der *MYCN* amplifizierten und 30 % der Zelllinien ohne *MYCN* Amplifikation als sensitiv gegenüber JQ1 eingeordnet. Bei FACS-Analysen wurde ein Anstieg der G1 und sub-G1 Fraktionen beobachtet. Die Proteinexpression wurde mittels Westernblot und Proteinarrays (RPPA) analysiert, hierbei zeigte sich durch die Behandlung mit JQ1 eine Reduktion der MYCN-Proteinexpression in 70 % der *MYCN* amplifizierten Zelllinien. Des Weiteren konnten Effekte auf weitere zellzyklusrelevante Proteine, insbesondere für den G1/S-Übergang, nachgewiesen werden. Eine durch shRNA vermittelte Reduktion von BRD4 zeigte keine Auswirkungen auf die MYCN Proteinexpression von IMR5/75 Zellen, verringerte jedoch die Cyclin D1 Expression. Umfangreiche Genexpressionsanalysen von vier mit JQ1 behandelten Zelllinien zeigten Veränderungen in der Expression von Genen, die mit dem Zellzyklus, Methylierung des Chromatins oder Schäden an der DNA in Verbindung stehen. *In vivo* verlängerte eine Therapie mit dem BET Inhibitor BAY1238097 das Überleben von Mäusen mit Tumoren, die von der Neuroblastomzelllinie LS abstammten.

Standardmäßig genutzte Mausmodelle des Neuroblastoms gehören entweder zu den *MYCN* amplifizierten oder den nicht-amplifizierten Neuroblastomen. Es existieren keine Mausmodelle, die vor dem identischen genetischen Hintergrund alternativ eine starke oder schwache *MYCN* Expression zeigen. Im Rahmen der Arbeit wurde ein solches orthotopes Mausmodell etabliert. Als bildgebende Verfahren wurden Magnetresonanztomografie und *in vivo* Biolumineszenz eingesetzt. Eine Reduktion der *MYCN* Expression in den Tumoren konnte mittels quantitativer PCR und RNA-Sequenzierung nicht nachgewiesen werden.

Zusammenfassend sind BET Inhibitoren eine Option für die Therapie einer vorselektierten Gruppe von Neuroblastomen. Eine Auswahl potentiell geeigneter Patienten muss neben einer *MYCN*-Amplifikation auf weiteren Faktoren beruhen. Um im Mausmodell stabil eine erniedrigte *MYCN*-Expression zu erreichen sind weitere Versuche erforderlich.

Table of Content

1 Introduction

1.1 Neuroblastoma

1.1.1 Clinical characteristics of neuroblastoma

Neuroblastomas are the most common extracranial solid tumors in childhood. With about 130 cases per year in Germany they account for 7% of all pediatric cancers and 15% of the deaths caused by pediatric malignancies. Neuroblastomas occur early in childhood, the median age at diagnosis is 1 year 2 months. For boys the incidence is 30% higher than for girls [1, 2]. Familiar cases are responsible for 1% of neuroblastomas and go along with multicentric tumors and early tumor onset [3].

Origin of neuroblastoma tumors are neuronal precursor cells deriving from the neural crest cell lineage. The tumors show a wide field of clinical behavior: from neuroblastomas regressing without therapeutic intervention or tumors that mature to benign neuronal tissue or ganglioneuromas to progressive and aggressive metastatic disease with poor outcome [2].

The localization of neuroblastomas is strictly correlating with the tissues deriving from neural crest precursor cells. The majority of the tumors occur in the adrenal gland, followed by parasympathic ganglia. About 70% of the tumors are located in the abdomen and 20% in thorax or neck. The main metastatic sites are bone marrow and bone [4].

Symptoms of neuroblastoma tumors are unspecific; the majority of the tumors are detected because of lesion expansion. Tiredness or pain in the bones are described, in a small proportion of cases neurological signs or paraneoplastic disorders occur [2, 3].

Diagnosis is based on a histopathological analysis of tumor material, showing immature neuroblasts and a low content of swannian stroma cells [3]. The analysis is complemented by various imaging methods to determine the stage of the disease and by a genetic analysis of the tumor material for a small number of aberrations that are relevant for prognosis and choice of an adequate therapy.

Neuroblastoma spreading is categorized according to the INSS staging system (Table 1). It includes three different localized stages (1-3) with 50% of all neuroblastoma cases, the metastatic stage 4 with 40% of the tumors and stage 4S which is occurring in 10% of the cases [3]. Stage 4S describes a metastatic disease of infants younger than 18 months at diagnosis harboring small primary tumors and metastases exclusively in skin, liver and bone marrow. Tumors belonging to this category undergo spontaneous regression in nearly all cases without therapeutic intervention [5]. Additional to the tumor stage, the prognosis for the patients is based on the age of the patients with a more favorable outcome for younger children and on genetic factors as described in section 1.1.2.

Table 1: INSS staging system of neuroblastomas (Adapted from Maris, 2007 **[3]**).

INSS stage	primary tumor	lymph nodes	metastases
1	localized, complete resection	neg.	neg.
2A	localized, incomplete resection	neg.	neg.
2B	localized	ipsilateral	neg.
3	unresectable, midline infiltrating	pos. or neg.	neg.
	localized, unilateral	contralateral	neg.
	unresectable, midline, bilateral extension	pos. or neg.	neg.
4	any	distant	pos.
4S (<18 months)	localized		limited to skin, liver, bone marrow

Therapy of neuroblastomas includes surgery, chemotherapy and radiotherapy. Low risk tumors of INSS stage 1 or 2 are treated with surgery alone and chemotherapy is not necessary in most of these cases [6]. Patients with high risk neuroblastomas receive extensive high dose chemotherapy including myeloablative therapy with autologous stem cell transplantation, combined with surgery, radiotherapy and novel targeted drugs [7]. The overall survival of neuroblastoma patients ranges from more than 80-95% for intermediate and low risk cases to less than 40% for patients with high risk tumors [8, 9].

To date, no screening method is available for neuroblastomas. The attempt to examine the urine of infants for katecholamines increased the number of detected neuroblastoma tumors but could not reduce the mortality and was therefore abandoned [10, 11].

1.1.2 Biological characteristics of neuroblastoma

Over the past decades, neuroblastoma research revealed a number of genetic alterations occurring frequently in neuroblastomas. Most of them are associated with good or bad prognosis and can contribute to the risk stratification for individual patients (Table 2).

An amplification of the *MYCN* oncogene found in 20-30% of neuroblastoma cases is the genetic modification most important for risk stratification. It occurs mainly in INSS stage 4 neuroblastomas and is associated with a bad prognosis [12] (Figure 1). In *MYCN* amplified cases, the neuroblastoma cells contain 10-500 copies of the *MYCN* oncogene which can be structured as double minutes or homogeneously stained region [2]. In additional 8% of neuroblastomas the *MYCN* oncogene is not amplified in large extent but overexpressed by single copy gain or unbalanced translocations [13].

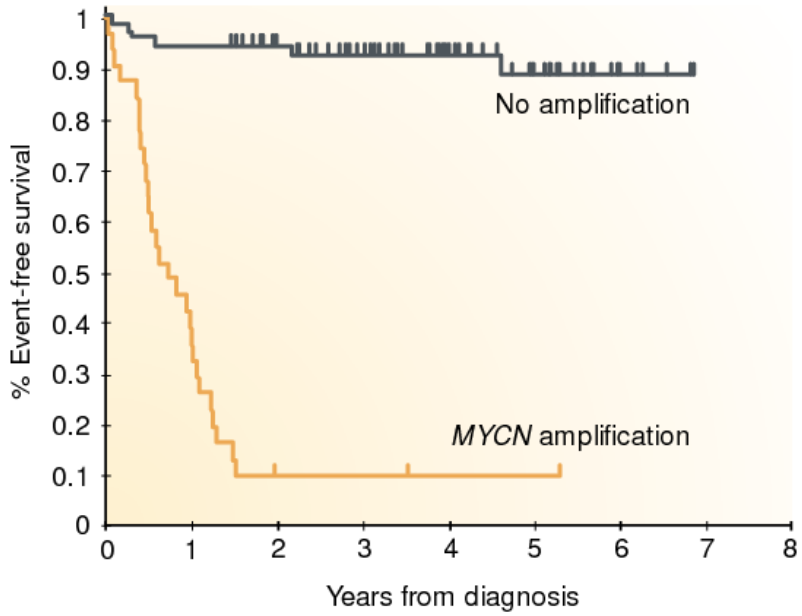

Figure 1: *MYCN* amplification as risk factor for poor outcome. Kaplan-Meier-plot of neuroblastomas comparing the overall survival of *MYCN* amplified and non-amplified cases (from Brodeur, G.M., 2003 [14]).

On chromosomal level, deletions of the chromosome arms 1p and 11q are associated with a poor outcome. These deletions occur frequently, a 1p deletion is found in 23% of neuroblastoma cases and deletions of 11q happen in 34% of neuroblastomas [15]. A number of genes have been identified in the deleted regions, for example loss of *CAMTA1* in 1p36 is linked to a poor outcome [16]. Another common structural aberration is a copy gain of region 17q which is found in about 60% of neuroblastomas and has no prognostic relevance [17]. Structural aberrations in other chromosomes are occurring less frequently, most of them go along with a bad prognosis [18]. Analysis of the ploidity of neuroblastomas revealed a good prognosis for triploid cases whereas diploid neuroblastomas have a poor prognosis [19].

Frequent genetic aberrations in neuroblastomas are overexpression or activating mutations of the *ALK* gene (anaplastic lymphoma kinase), found in 20-25% of neuroblastoma cases and associated with a poor outcome for the patients [20, 21]. An increased kinase activity of ALK results in higher proliferation and reduced apoptosis. ALK induces the expression of *MYCN*, leading to higher MYCN protein levels and plays a role in stabilizing the MYCN protein [22, 23]. A similar role is taken by *AURKA* (Aurora kinase A), this protein binds to MYCN and prevents it from proteasomal degradation and thus is a negative prognostic factor for neuroblastoma [24, 25]. *LIN28B* is another gene linked to *MYCN* expression in neuroblastoma. LIN28B upregulates the expression of *MYCN*, whereas MYCN induces *LIN28B* through micro-RNA regulation [22].

The neurotrophin receptors Trk A and Trk B are deregulated in a number of neuroblastoma cases. Whereas Trk A and its ligand NGF are leading to differentiation and regression of the

tumor and therefore go along with a good prognosis, overexpression of Trk B and its ligand BDNF occurs in unfavorable neuroblastomas and correlates with amplified *MYCN* [2].

In contrast to many adult cancer entities, well known oncogenes involved in tumorigenesis of these tumors such as *TP53*, *RAS* or *CDKN2A* are not mutated in new diagnosed neuroblastoma [3]. In the case of *TP53*, mutations occur solely in relapsed neuroblastomas at a low rate [26]. Additionally the *TP53* pathway may be inactivated in neuroblastoma through mutations of other components of the pathway despite *TP53* [27].

Mutations of *PHOX2B* are found in 2% of the neuroblastomas and show a coincidence with neurological diseases as hirschsprung disease [3, 28]. Together, *PHOX2B* and *ALK* mutations are responsible for most of the familiar neuroblastoma cases.

Recent findings link prolonged telomeres and telomerase activity with high risk neuroblastoma cases. TERT, a subunit of telomerase was found to be activated by rearrangements to chromosomal regions controlled by strong enhancers [29]. In other high risk cases the telomeres are prolonged by the ALT pathway, describing an alternative way for lengthening of telomeres independent from telomerase activation but involving an *ATRX* deletion in a high proportion of cases [30]. Including the information regarding telomere status, three independent groups of high-risk neuroblastomas can be defined that are not overlapping and are all related with a poor outcome: amplified *MYCN* is found in 37% of stage 3 and stage 4 neuroblastomas, *TERT* rearrangements in 23% and *ATRX* deletions in 11% of the stage 3 and 4 tumors [31].

Table 2: Favorable and unfavorable biologic characteristics of neuroblastomas.

	unfavorable	**favorable**	**no prognostic relevance**
MYCN	amplification, overexpression		
Structural aberrations	1p del., 11q del.		17q gain
Ploidity	near diploid	triploid	
Neurotrophin receptors	Trk B expression	Trk A expression	
ALK	activating mutation, amplification		
Telomeres	*TERT* rearrangement+activation, *ATRX* deletion		
others	*Aurora kinase, PHOX2B, LIN28-B*		

1.2 MYCN and c-MYC

1.2.1 MYC protein family

The family of MYC transcription factors comprises c-MYC MYCN and MYCL. *C-MYC* is globally expressed, whereas *MYCN* and *MYCL* are limited to certain tissues and phases during embryogenesis [32]. The *MYCN* gene is located on chromosome 2p24 and characterized by a high expression in early embryogenesis, becoming lower during cell differentiation. It is found especially in neuronal precursor cells and during brain and lung development [33]. The expression pattern of *MYCL* is even more limited [34]. MYC transcription factors are crucial during embryonic development, embryos negative for *MYCN* or *c-MYC* die between day 9 and 11 [35, 36]. As c-MYC, MYCN and MYCL resemble each other in structure and function, they are summarized as MYC in the sections 1.2.1 and 1.2.2.

MYC proteins harbor a basic region, a helix-loop-helix and a leucine zipper structure at the C-terminus, responsible for the formation of heterodimers and for recognition and binding of their DNA binding sites [32] (Figure 2). At the N-terminus four regions called mycboxes are located. Mycbox I includes phosphorylation sites and is responsible for turnover of the MYC protein through proteasomal degradation [37]. Mycbox III plays a role in MYC protein stability, transcriptional repression and apoptosis induction [38, 39]. The biologic functions of MYC, such as transcriptional activation and repression, as well as nuclear localization are involving protein binding to mycbox II [40].

For MYC mediated transcriptional activation, MYC forms heterodimers with MAX. The MYC-MAX heterodimers bind to E-box elements in promoter regions (CACGTG) and recruit p-TEFb, a complex of CDK9 and Cyclin T. P-TEFb phosphorylates the carboxyl-terminal domain of RNA polymerase II, which leads to the release of the RNA polymerase from the transcription initiation complex and to transcriptional elongation [41-43]. MYC mediated transcriptional repression works by dimerization of MAX with MAD or MNT. These heterodimers bind to E-box elements and impede MYC binding to the DNA [44, 45]. In a second, E-box independent way of transcriptional repression, MYC forms a complex with MIZ-1 and initiates DNA methylation resulting in transcriptional repression [46, 47].

MYC proteins are characterized by a short half life of 20-30 min and a high turnover rate [48]. The presence of MYC in the cells is regulated by transcription of the *MYC* gene on one hand and the degradation of MYC on the other hand. The transcription of *MYC* is regulated through a number of different signaling pathways involving for example Wnt/ β-Catenin or PI3K/AKT [32]. MYC degradation works via ubiquitination and proteasomal degradation. Phosphorylation of the serine 62 residue stabilizes MYC, whereas a sole threonine 58 phosphorylation marks the protein for ubiquitination through the SCF^{FBW7} ubiquitin ligase and degradation [49, 50].

MYC is involved in the regulation of a high proportion of genes, more than 25000 binding sites are known *in vivo*, with only a small fraction of them with E-boxes in the promoter region [51, 52]. It is supposed that MYC mediated transcription follows a general amplifier model with MYC activating the transcription on open promoters in the cell, resulting in individual gene expression patterns for different cell types [53]. Additional to the transcription of RNAs by RNA polymerase 2, MYC is also mediating transcription of tRNAs and rRNAs by the RNA polymerases 1 and 3 [54, 55].

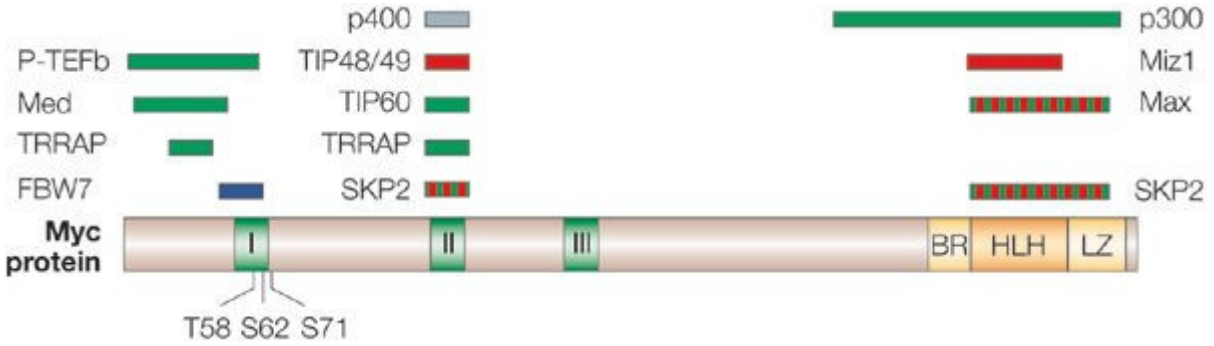

Figure 2: *MYC* domains and binding sites. C-terminus with basic region (BR), helix-loop helix (HLH) and leucine zipper (LZ) domains for dimerization of MYC with MAX or MIZ-1. N-terminus containing myc-boxes I-III, interacting with proteins responsible for MYC functions, MYC turnover, stability and with phosphorylation sites for regulation of proteasomal degradation (From Adhikary, S. and Eilers, M., 2005 [56]).

1.2.2 MYC and its cellular functions

A variety of different and contrary cellular processes are influenced by proteins of the MYC family. On one hand MYC is activating tumor promoting effects such as cell proliferation, inhibition of differentiation, cell growth, vascularization, genomic instability, reduced adhesion and metastasis. On the other hand, tumor suppressing processes, for instance apoptosis, cell differentiation or cell adhesion are positively influenced by MYC. MYC is also playing a role in metabolism [56].

Cell proliferation is mainly regulated at the transition from G1 to S phase of the cell cycle. MYC is involved in a number of control mechanisms at the G1/S transition whereof a deregulation of MYC proteins can lead to enhanced cell proliferation. One way of influencing cell cycle progression is through the MYC downstream targets CDK4 and D-type cyclins, with Cyclin D1 as the most prominent member of the family. The CDK4/Cyclin D1 complex phosphorylates Retinoblastoma protein (pRB), which leads to a conformational change of pRB. Thereby, the transcription factor E2F-1, bound to hypophosphosphorylated pRB, is released and initiates the synthesis of genes required for G1-S transition [57].

Whereas CDK4 protein expression is induced by MYC, it is not finally clarified how D-type cyclins, especially *CCND1*, are regulated by MYC proteins [58, 59]. In fibroblasts it was found that the *CCND1* expression is repressed by c-MYC [60]. In contrast, research on targets of the sonic hedgehog pathway indicates that Cyclin D1 is activated by MYCN, probably by an indirect pathway [61]. Cyclin D2 is a direct target of c-MYC [62].

Another way how MYC is influencing the G1-S transition involves TP53. When DNA damage occurs, TP53 is stabilized and induces the synthesis of the CDK inhibitor p21, which binds to CDK-Cyclin complexes and prohibits the phosphorylation of target genes [63]. Thereby, the replication start is impeded, and the cell is arrested in the G1 phase of the cell cycle. MYC directly represses the expression of p21, which results in enhanced proliferation irrespective of potential DNA damage [64, 65]. TP53 is also directly activated by MYCN and c-MYC, leading to the induction of a second, proapoptotic pathway involving TP53 [59, 66]. The activation of the expression of $p19^{ARF}$ by MYC promotes the apoptotic pathway by stabilization of TP53 through MDM2 inhibition [67].

MYC is also promoting apoptosis by repression of the antiapoptotic proteins BCL2 and BCL-x_L, as well as by the indirect induction of BIM, leading to the release of cytochrome c from the mitochondria [68, 69].

The oncogenic transformation by MYC is involving Ras, which stabilizes MYC by influencing the phosphorylation directly and indirectly through GSK3β [50]. In a second pathway promoting oncogenic transformation, the Ras downstream effector AKT phosphorylates MIZ-1 and thereby abrogates the MYC dependent transcriptional repression [70]. Additionally, AKT phosphorylates FOXO, which is a co-factor of MYC and inhibits MYC-dependent transcription of MYC target genes in its hypophosphorylated state [71].

1.2.3 MYCN as a target gene in neuroblastoma

A deregulated *MYCN* expression is found in a number of malignancies including neuroblastoma, medulloblastoma, rhabdomyosarcoma, Wilm's tumor, lymphatic leukemias, lung cancer, prostate cancer and basal cell carcinoma [72]. Therapeutic targeting of *MYCN* would be of significance for treatment of these diseases.

In vitro studies targeting *MYCN* by RNA interference in various neuroblastoma cell lines resulted in a growth arrest of the neuroblastoma cells in the G1 phase of the cell cycle, in cell death and differentiation of the tumor cells [73, 74]. Nevertheless achieving similar results *in vivo* is challenging. An attempt to target MYCN or other MYC transcription factors directly is not feasible as the structure of the MYC proteins does not provide structures on the surface where inhibitors could bind and prohibit MYC functions [75]. Therefore, indirect attempts were in the focus for targeting *MYCN* in neuroblastoma.

Inhibition of the MYCN-MAX dimerization through small molecule inhibitors resulted in cell death and differentiation of neuroblastoma cells under cell culture conditions [76]. Pharmacokinetic analysis of these inhibitors revealed a short half-life *in vivo*, which consequently makes them not suitable for clinical usage [77].

Stability and degradation of the MYCN protein are influenced by Aurora A kinase and the PI3K/AKT/mTOR signaling pathway. An Aurora A kinase inhibitor (alisertib) showed promising results in preclinical studies, however it was not effective for neuroblastoma patients in a phase I clinical trial, especially not for patients with *MYCN* amplified tumors [78, 79]. An activation of the PI3K/AKT/mTOR pathway decreases the expression of GSK3β, which results in a higher MYCN activity. Inhibition of this pathway using different small-molecule inhibitors, leads to growth arrest and cell death of neuroblastoma cells [80, 81].

Downstream of MYCN, the inhibition of ALK with Crizotinib results in a lower proliferation rate of neuroblastoma cells with mutations in the *ALK* gene [23]. *In vivo* ALK inhibitors show promising results, though treatment in combination with other chemotherapeutic drugs is advisable due to increasing resistance of the tumors [82]. The TP53 axis in neuroblastoma is often affected by MDM2 overexpression. Targeting MDM2 with nutlin-3 reestablishes the function of p53 and is therefore a potential therapeutic option, especially effective for MYCN overexpressing neuroblastoma cells [83].

Influencing the gene transcription activity of *MYCN* would be a promising therapeutic option for malignancies with deregulated *MYCN*. Usage of bromodomain inhibitors as an attempt to block transcription of the *MYCN* gene is a central topic of this work and deeply introduced in part 1.3.

1.3 BET proteins

1.3.1 BET family of transcription factors

The BET (bromodomain and extraterminal domain) protein family comprises of the transcription factors BRD2, BRD3, BRD4 and BRDT. At the N-terminus BET proteins have two bromodomains named BD1 and BD2. At the C-terminal they share an extra-terminal domain important for protein-protein interactions [84]. In general, BET proteins function as epigenetic readers.

Bromodomains recognize and bind acetylated lysine residues on histones and other cellular proteins [85]. They are composed of four α-helices connected by two loops. Together with the α-helices, these ZA and BC loops form a hydrophobic cavity binding aminoacetyl groups [86]. The binding affinity is increased with multiple acetylated sites compared to single acetylated lysines [87].

In the human genome, 61 bromodomains are encoded, belonging to 46 different bromodomain containing proteins. These proteins can be assigned to eight bromodomain containing protein families [87]. In general, the BD1 domains from different proteins are closer related than BD1 and BD2 on the same protein [86].

Among the BET protein family, BRD4 is the protein studied best. One mechanism of action is the participation with P-TEFb for transcriptional regulation (Figure 3). P-TEFb, comprising of CDK9 and Cyclin T, is recruited to the acetylated DNA by BRD4. Belonging to the transcription initiation complex, P-TEFb recruits RNA polymerase II to the DNA and phosphorylates the C-terminal domain (CTD) of RNA polymerase II to release the polymerase from the transcription initiation complex and to promote transcriptional elongation [88, 89].

Additionally, BRD4 itself harbors a kinase and acetyltransferase activity and can phosphorylate the CTD of RNA polymerase II and acetylate histones H3 and H4 directly [90, 91]. A third function of BRD4 is as histone chaperone. Thereby, BRD4 is facilitating the passage of RNA polymerase II along acetylated nucleosomes during transcriptional elongation [92].

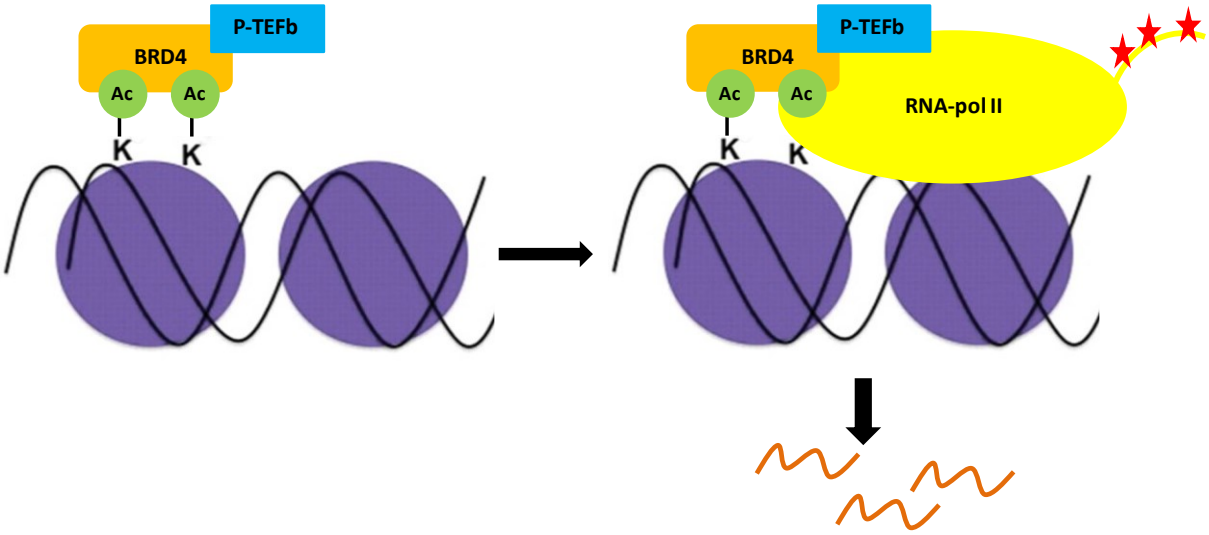

Figure 3: Transcriptional regulation by BRD4 and P-TEFb. BRD4 binds acetylates lysines on histones. P-TEFb phosphorylates the CTD of RNA polymerase II, leading to elongation of mRNA transcription. Purple=nucleosomes; green= aminoacetyl-groups; orange= BRD4; blue= p-TEFb; yellow=RNA polymerase II; red stars= phosphorylated sites (adapted from Popovic et.al., 2012 [93]).

BRD4 is part of the mediator complex incorporating RNA polymerase II with multiple transcription factors [94]. In this context, BRD4 stabilizes the binding of the transcription factors to the DNA, especially at enhancer and super enhancer regions [95, 96]. In contrast, a function as transcriptional repressor involving PPARγ was found for BRD2 [97].

BET proteins are involved in different pathological processes. For example, they play a role in inflammation and cardiac insufficiency [98, 99]. Viral gene expression of latent viruses such as HIV or HPV is also involving BET proteins [100, 101].

1.3.2 Role and function of BET proteins in cancer

BET proteins are involved in the biology of a variety of different haematologic and solid malignancies. An inhibition of BET proteins is leading to a lower phosphorylation of RNA polymerase II and to a severe reduction of global mRNA levels. This includes the suppression of proto-oncogenes, for example members of the *MYC* family or *Bcl2* [84].

BRD4 directly interacts with specific cancer promoting transcription factors, including p53, c-JUN or the MYC/MAX heterodimer [102]. By occupying the *MYC* promoter, BRD4 prevents the induction of the MYC-dependent apoptotic pathway resulting from DNA damage [103]. Aurora B, whose expression is depending on BRD4, is necessary for the chromosomal segregation during mitosis; thereby BRD4 is involved in cell proliferation [104]. BRD4 also promotes metastasis by direct interaction with the acetylated transcription factor Twist, which leads to the induction of epithelial-to-mesenchymal-transition [105].

Besides BRD4, BRD2 and BRD3 are also involved in cancer promoting pathways. BRD2 associates with the transcription factors E2F1 and E2F2 important for the synthesis of genes for the G1/S transition of the cell cycle [106]. BRD3 was found to downregulate the RB-E2F axis in nasopharyngeal cancer [107].

On the genome, BRD4 globally associates with active promoters and enhancers, the latter identified by acetylation of the histone H3K27 [95]. The enhancers bound by BRD4 are located near genes sensitive for BET inhibition [108, 109]. Especially high BRD4 occupancy and high levels of transcription factor and mediator binding were detected on large enhancers, called super-enhancers. In multiple myeloma these super-enhancers are associated with genes known to be involved in carcinogenesis such as *c-MYC*, *CCND2* or *Bcl-xL*. These super-enhancer regulated genes are highly dependent on BRD4 [95]. At the enhancers BRD4 is forming complexes with the Jmjd6 demethylase, facilitating the recruitment of P-TEFb to the location on the genome [110].

Cell cycle progression is influenced by BRD4 in different cell cycle phases. The G2/M transition is promoted by recruitment of P-TEFb for the transcription of postmitotic genes and thereby preparation of the next cell cycle [111]. In this context, BRD2 and BRD4 have the ability to bind to mitotic condensed chromatin [112]. The role of BRD4 at the G1/S transition is ambivalent: On one hand, BRD4 inhibition using shRNA leads to a G1 arrest and reduced expression of G1 genes [113]. On the other hand, ectopic BRD4 overexpression has the same effect. The repression of replication factor C mediated by BRD4 arrests the cells at the G1/S transition

[114]. Both studies rely on fibroblast cells (NIH 3T3) and were using serum starvation for synchronization.

1.3.3 BET protein inhibitors

As BET proteins, especially BRD4, are heavily involved in cancer progression and beyond that offer a strategy to target *MYC* indirectly, they have become a focus in cancer research during the past years.

First of all, *BRD4* was used as a target gene for NUT-midline carcinoma. This cancer harbors a *BRD4-NUT* translocation leading to high BRD4 protein expression [115]. Treatment with the BET inhibitor JQ1 results in abandoning of BRD4-NUT from the chromatin, in cancer cell differentiation and growth arrest [116].

JQ1, a thienotriazolodiazepine, targets the BD1 of BRD4 and other BET family proteins by competitive inhibition (Figure 4A). JQ1 has two enantiomeres, solely (+)-JQ1 has a high affinity for bromodomain binding [116, 117]. Similar characteristics concerning affinity and inhibition behavior account for the BET inhibitors I-BET762 and I-BET151 [98]. All three inhibitors are hydrophobic, which limits the bioavailability, shortens the half-life of the inhibitor *in vivo* and reduces the possibility for chemical modifications [118].

A

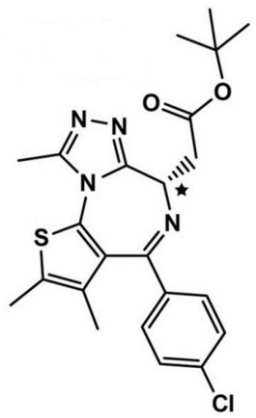

B

Preclinical	Clinical	
JQ1	ABBV-075	GS-5829
I-BET762	BAY1238097	GSK 525762
I-BET151	BI 894999	INCB054329
	BMS-986158	TEN-010
	CPI-0610	OTX015/MK-8628
	FT-1101	RO6870810

Figure 4: BET inhibitors. A) Chemical structure of JQ1 (from Filippakopouls et. al. [116]). B) List of currently available BET inhibitors for preclinical use and in clinical phase I and II studies (adapted from Gelato et. al. [119]).

A negative influence of BET inhibition on *MYC* gene expression was discovered in preclinical studies on multiple myeloma, acute myeloid leukemia, and lymphoma in 2011 [103, 108, 120]. Besides growth arrest and a reduction of tumorigenic characteristics, a direct downregulation of *MYC* mRNA and protein levels as well as *MYC* target genes was shown in all three cancer entities. For neuroblastoma, the first preclinical studies using BET inhibitors were published in 2013 [121, 122]. Both studies show growth inhibition, a cell cycle arrest in G1 and increased

fractions of cell death as well as reduced *MYCN* expression. A study with five different neuroblastoma cell lines using the BET inhibitor OTX015 suitable for clinical applications also reveals an influence on *MYCN* gene expression [123].

Up to date, 12 different BET inhibitors have been tested in clinical phase I and phase II trials (Figure 4B). These studies include NUT midline carcinoma, acute myeloid leukemia, myelodysplastic syndrome, lymphoma, multiple myeloma, breast-, prostate and colorectal cancer, pancreatic ductal adenocarcinoma and neuroblastoma [124]. Both single agent therapies and combination therapy with other drugs are tested.

1.4 Neuroblastoma mouse models

Modeling of neuroblastoma in animals is an important tool for neuroblastoma research, especially for analysis of tumorigenesis and for testing of promising therapeutic agents. Animal models deliver additional information concerning aspects of tumor diseases that cannot be modeled in cell culture. These include the formation of blood vessels with their contribution to tumor growth and therapeutic relevance, the role of the immune system in neuroblastoma tumorigenesis, invasive growth and metastasis of neuroblastomas, and the formation of complex tumors in the appropriate microenvironment.

For neuroblastoma a variety of mouse models have been established over the past decades [125, 126]. They can be assigned to the two main categories of transgenic neuroblastoma mouse models and xenograft neuroblastoma mouse models.

Transgenic neuroblastoma mouse models are generated by genetic modification and systematic breeding of mice. Once established, the tumors of these mice are developing on their own at early age and undergo a tumor evolution resembling the natural tumor evolution including early stages of disease. For neuroblastoma several different transgenic tumor models were established.

- The TH-*MYCN* mouse model is the transgenic mouse model mostly used for research. In this neuroblastoma mouse model *MYCN* is overexpressed in cells deriving from the neural crest [127]. The expression of *MYCN* in these mice is controlled by the rat tyrosine hydroxylase promoter, which is active in migrating cells from the neural crest cell lineage. The mice develop neuroblastoma-like tumors in thorax and abdomen. Analysis of TH-*MYCN* tumors revealed additional genetic and chromosomal changes in the tumors that resemble the genetics of human neuroblastomas.
- The LSL-*MYCN*;Dbh-iCre neuroblastoma mouse model is also based on *MYCN* overexpression [128]. In this double transgenic mouse model, *MYCN* is induced in neural crest cells expressing β-hydroxylase. The tumors of LSL-*MYCN*;Dbh-iCre mice resemble human neuroblastomas more than tumors of TH-*MYCN* mice with regard to

tumor location and genomic aberrations and show a higher incidence in a number of mouse strain backgrounds.

- Additionally to the models using *MYCN* overexpression, several other transgenic neuroblastoma mouse models exist, without being commonly used [125]. Many of those are involving viral constructs as SV40 T-antigen as driver for tumorigenesis. Compared to the *MYCN* involving models it is unsure if virus-based transgenic models are suitable for research on neuroblastoma tumorigenesis.

Neuroblastoma xenograft models are the second main category of neuroblastoma mouse models. In these models, human tumor material is introduced in immunocompromized mice; the human cancer cells settle and form tumors. Xenograft tumors allow the analysis of tumors close to the genetics and growth behavior of human neuroblastomas. Nevertheless the predictive value of these models concerning therapeutic attempts remains unclear. Among the xenograft tumor models, three different versions are in common use.

- In heterotopic xenograft tumor models the human tumor cells are injected at a location in the bodies of the mice that is not related to the tumorsite of origin. In most cases, the tumor cells are injected subcutaneously into the flank, which facilitates documentation of tumor size through the skin.
- Orthotopic xenografts are generated by implantation of human tumor cells at the original location of the tumor. This enables tumor growth in an adequate microenvironment with access to the blood vessels of the original tumor, which results in corresponding metastatic pathways. In orthotopic neuroblastoma mouse models the human tumor cells are injected into the adrenal gland or the surrounding fat pad of the mice [126].
- Patient derived xenografts (PDX) are the animal model closest to the original tumor of the patient and are performed by implantation of a human tumor piece in immunocompromized mice. Neuroblastoma PDX models were generated by implantation of the human tumor next to the adrenal gland, subcutaneously or in teratoma tissue [129-132]. PDX animal models are performed in circles, the tumors grown in mice are explanted, divided and reimplanted or established in cell culture until enough material for extensive experiments is available. The use of tumor tissue instead of established cell lines protects the structure of the original human tumor and allows a closer modeling of the patient's tumor as the stroma cells are of human origin- at least in the first generation of PDX.

All transgenic and xenograft neuroblastoma mouse models harbor advantages and limitations. The tumors of the transgenic mouse models develop influenced by an intact immune system, which is an important factor in cancer and lacks all xenograft models. As well, the xenograft

models do not undergo different stages of tumor evolution but are displaying the tumor stage and characteristics the human tumor material derives from. The transgenic models are not capable of representing the variety of genetics of different neuroblastoma tumors, in contrast to the xenograft models that are using tumor material originating from a large number of neuroblastoma cases. Additionally, the orthotopic and heterotopic xenograft models enable genetic modifications of the tumor cells prior to implantation. Due to cell culture artifacts collected by established neuroblastoma cell lines over time used for the heterotopic and orthotopic xenograft models, the PDX tumor model is the mouse model closest to human tumors.

Metastasis can occur in all neuroblastoma mouse models except the subcutaneously growing heterotopic xenograft model, though rate and location of metastasis are varying. The metastatic behavior closest to human neuroblastomas is observed in PDX models, whereas orthotopic neuroblastoma xenografts metastasize at a lower rate. Metastasis to the bone marrow is reduced in all neuroblastoma mouse models compared to human neuroblastomas [133].

With regard to practical aspects the subcutaneous xenograft model has advantages compared to the other models. The implantation of the human tumor cells is easy and time-saving and tumor growth can be measured through the skin. In contrast, orthotopic neuroblastoma mouse models (cell lines or PDX) need imaging methods to follow up tumor growth and for implantation of the human tumor material anesthesia and invasive methods are unavoidable. In the genetic models, tumor onset is non-invasive as the tumors are growing on their own, whereas for monitoring of tumor growth, imaging methods are used.

PDX neuroblastoma mouse models resemble the human tumors they are deriving from in many aspects. However, the material for first generation PDX mice is limited and tumor formation takes a long period of time. Differences between the first and following generations of one PDX lineage are a current focus of research [134].

Additional to mouse models, neuroblastoma tumorigenesis can also be modeled in zebrafish, which is a useful model for questions regarding neuroblastoma pathogenesis and high-throughput drug screenings [135]. Genetic manipulation of zebrafish is easier than for mice and the external evolution of the embryos facilitates insights into physiological and pathological behavior of neural crest cells. Available neuroblastoma tumor models in zebrafish are for example the *MYCN-ALK* model, the *PHOX2B* model or the *NF-1* deficient/*MYCN* model [136-138].

2 Aim of the project

Amplification of the proto-oncogene *MYCN* belongs to the most important risk factors within neuroblastoma disease. The resulting high *MYCN* expression levels are associated with poor response to therapy and a poor outcome for the patients. Despite *MYCN* was in the focus of neuroblastoma research since its importance was detected by Schwab et. al. in 1983, no therapeutic option is available yet targeting *MYCN* in neuroblastoma [12].

In 2011, Delmore *et al*., Mertz *et al.* and Zuber *et al.* have shown that inhibition of the BET protein BRD4 impairs the transcription of *c-MYC* and its target genes in *MYC*-dependent cancers [103, 108, 120]. Based on these findings, the effects of BRD4 inhibition in *MYCN* amplified and *MYCN* non-amplified neuroblastoma cell lines were analyzed in this thesis, focusing on the following tasks:

- Classifying the response to BET inhibition in different neuroblastoma cell lines and integrating the results regarding the genetic background and biologic characteristics of the cell lines.
- Characterization of the effects of BET inhibition on tumorigenic characteristics of the neuroblastoma cell lines, such as cell cycle or anchorage independent growth.
- Analysis of genes and pathways affected by BET inhibition besides and related to *MYCN* by high throughput analysis of the transcriptome and proteome.
- Performance of a treatment study with a BET inhibitor in a subcutaneous neuroblastoma mouse model.

Both, for fundamental and preclinical research it is essential that suitable animal models are available. For neuroblastoma, genetic models are based on MYCN overexpression. Alternatively, xenograft models are using neuroblastoma cell lines or tumor pieces deriving from either *MYCN* amplified or *MYCN* non-amplified human neuroblastomas. Nevertheless, no neuroblastoma mouse model is available harboring both *MYCN* high and *MYCN* low conditions. Aiming to have a *MYCN* high/low neuroblastoma mouse model available in the neuroblastoma genomics group at the DKFZ, such a model was established by working on the following topics:

- Generation of genetically modified neuroblastoma cells harboring both a luciferase gene and an inducible *MYCN* high/low system.
- Technical establishment of the orthotopic neuroblastoma mouse model aiming a tumor growth rate of 80%.
- Adaption of imaging methods and tumor sample handling for the orthotopic *MYCN* high/low mouse model.
- Quantification of the *MYCN* knockdown in the xenograft tumors.

3 Materials

3.1 Gadgets

Gadget	specification	company
bacteria centrifugation tubes	500 ml	Beckmann
bacteria shaker	Innova 4300	New Brunswick Scientific
bioanalyzer	2100 Bioanalyzer	Agilent genomics
bioluminescence imager	IVIS Spectrum	Perkin Elmer
	built in-house	DKFZ
blotting chamber	mini-PROTEAN	Bio-Rad
cell counter	LUNA automated cell counter	logos biosystems
cell culture hood	Cellgard	Integra bioscience
centrifuges	Allegra X-12	Beckmann Coulter
	Thermo 17	Heraeus
	J2-21M/G	Beckmann
chemiluminescence detection	Chemi-Capt 5000	Vilber
colony counter	gel doc	Bio-Rad
cryo container	Mr. Frosty	Nalgene
FACS	FACS Calibur	BD Biosciences
	MacsQuant	Milteny
falcon roller	Cat RM5	Neolab
freezer -20°C		Liebherr
freezer -80°C		Sanyo
fridge 4°C		Liebherr
gel holder/brace clip		Bio-Rad
gelelectrophoresis chamber	mini-PROTEAN	Bio-Rad
glass bottles	100, 500, 1000 ml	Schott Duran
glass plates/combs for mini gels		Bio-Rad
graduated cylinder	100, 250 ml	Vit Lab
heater/shaker (reaction tubes)	Thermomixer 5436	Eppendorf
heating pad		AccuLux
incubator cell culture	Hepa Class 100	Thermoelectron Corporation
isofluran vaporisator	vapor 19.3	Dräger
magnet resonance imager	Symphonie 1.5 tesla	Siemens
magnetic stirrer	MR 3001	Heidolph
microscopes	Axiovert 10	Zeiss
	CKX41	Olympus
microwave		Bosch
mouse magnetic coil	built in-house	DKFZ
multichannel pipettes	0.5-10, 30-300 µl	BioHIT
multistepper pipet	Multipipette M4	Eppendorf
Nano- Drop		Peq-Lab
narcotic box	built in-house	DKFZ
PCR cycler	Trio Thermoblock	Biometra

pH-meter	pH 540 GLP	WTW
photometer	GeneQuant 1300	GE Healthcare
pipetboy		Integra Bioscience
pipettes	0.5-10, 2-20, 10-100, 100-1000 µl	Eppendorf
plate reader	FLUOSTAR Optima	BMG Labtech
plate scanner	Perfection 2450 Photo	EPSON
power supply	PHERO-stab. 500	Biotec Fischer
pumping apparatus	built in-house	DKFZ
qPCR cycler	ABI Prism 7000	Life Technologies
Qubit 3.0 fluorometer		Life Technologies
scales	PE 3000, PM460	Mettler
shaker (plates)	KS250 basic	IKA Labortechnik
tissue homogenizer	dounce tisue grinder	Sigma-Aldrich
vortexer	Reax 2000	Heidolph
water bath	37°C	GFL

3.2 Consumables

material	**specification**	**company**
cell culture dishes	60, 100, 150 mm	TPP
cell culture flasks	25, 75, 150 cm²	TPP
cell scraper		TPP
cryo tubes		NUNC
cuvettes (single use)	half micro	Greiner bio-one
embedding molds	12 mm	polysciences
falcon tubes	15, 50 ml	Greiner bio-one
multistepper pipet tips	Combitips advanced	Eppendorf
needles	30 G, 27 G, 24 G	Braun
nitrocellulose membrane	Protran	Whatman Schleicher & Schuell
pasteur pipettes	150, 230 mm	WU Mainz
pH paper	7 mm width	Macherey-Nagel
pipet tips	10, 200, 1000 µl	Starlab
pipet tips, filter	10, 20, 100, 200, 1000 µl	Starlab
pipet tips, narrow	200 µl	Bioscience inc.
pipettes	5, 10, 25 ml	Costar
plates black	96 well	Greiner bio-one
plates transparent	6, 96 well	TPP
	12 well	NUNC
plates white	96 well	NUNC
qPCR plates	96 well	Biozym Scientific
qPCR top sheet	Micro Amp	Applied Biosystems
qubit tubes		Thermo scientific
reaction tubes, safe-lock	8x0.1, 0.5, 1.5, 2 ml	Eppendorf
reservoirs		Roth
scalpel, single use		fine science tools

sheet protector		Leitz
slides cell counter		logos biosystems
sponges (western blot)		Bio-Rad
staples		fine science tools
suture, absorbable	PGA, DSM 13	Resorba
syringes	1 ml	Dispomed
tissue paper		Satino
tube, flexible (mouse injections)	Portex polythese tubing, OD=0.61 mm	Smiths Medical International Ldt.
whatman-paper	3 MM Chr.	Whatman

3.3 Chemicals

chemical	**company**
acrylamide/ bis 40%	Serva
APS	Roth
bromophenol blue	Serva
BSA	Sigma-Aldrich
chloroform	Baker
citrate monohydrate	Riedel DeHaën
complete protease inhibitor	Roche
crystal violett	Serva
DAPI	AppliChem
DEPC	Roth
DMSO	Roth
doxorubicin hydrochloride	Sigma-Aldrich
DTT	AppliChem
EDTA	Roth
ethanol abs.	Sigma-Aldrich
formaldehyde 16%	Sigma-Aldrich
glycerol	Roth
glycine	Gerbu
goat normal serum	Dianova
H_2O dest	from millipore
HCl	Sigma-Aldrich
isopropanol	Sigma-Aldrich
KCl	Roth

chemical	**company**
KH_2PO_4	Merck
methanol	Sigma-Aldrich
$MgCl_2$	Roth
milk powder	Roth
Na_2HPO_4	Sigma-Aldrich
NaCl	Sigma-Aldrich
$NaHCO_3$	Merck
noble agar	US-Biological
phosStop phosphastase inhibitor	Roche
propidium iodide	Miltenyi
RPMI 1640 powder	PAN Biotech
SDS	Gerbu
sodium acetate	Roth
sucrose	Roth
TEMED	AppliChem
tris base	Sigma-Aldrich
tris HCl	AppliChem
Triton X-100	AppliChem
trypton	DIFCO-biotest
Tween 20	Gerbu
urea	Merck
yeast extrakt	Gerbu
β- mercaptoethanol	Roth

3.4 Mouse pharmaceuticals and applicants

material	**specification**	**company**
NaCl 0.9%, sterile	10 ml, ampulla	Fresenius Kabi
water, sterile	10 ml, ampulla	Fresenius Kabi
eye ointment	bepanthen eye and nose	Bayer

analgesic	metamizole, 500 mg/ml	WDT
Isofluran		Baxter
Matrigel	Matrix, high concentration	BD
Doxycycline		Sigma-Aldrich
D-luciferin		Synchem

3.5 Cell culture materials

3.5.1 Cell lines

All neuroblastoma cell lines used for this thesis were purchased from the laboratory-internal stock from the Neuroblastoma Genomics group at the DKFZ.

3.5.2 Media and supplemental

material	**specification**	**company**
RPMI-1640	L-Glutamin, 25 mM Hepes	Lonza
Opti-MEM		Gibco
Neurobasal A Medium		Gibco
PBS (sterile, for cell culture)		Gibco
fetal bovine serum (FCS)		Biochrom AG
Penicillin/Streptomycin	10000 U/m	Serva
B27 Supplement		Gibco
FGF-b human		PromoKine
EGF human		PromoKine
L-Glutamin	200 mM	Gibco
Heparin		Sigma Aldrich
Blasticidine	41,25 mg/ml	MP Biomedicals
Zeocin	100 mg/ml	Invitrogen
Hygromycin B	10 mg/ml	Roche
Tetracycline	10 mg/ml	Sigma
JQ1	(+)-enantiomere, item 11187	biomol
BAY1238097		Bayer Healthcare

3.5.3 Cell culture media (cell line specific)

basic cell culture medium, for all cell lines without stable transfections	
cell culture medium (500 ml)	RPMI-1640
FCS	10%
Penicillin/Streptomycin	100 u/ml

cell culture medium for suspension cells NB-S 124	
cell culture medium (500 ml)	Neurobasal A
B27 Supplement	2%
FGF-b human	20 ng/ml
EGF human	20 ng/ml
L-Glutamin	0.5 mM
Heparin	2 µg/ml
Penicillin/Streptomycin	100 u/ml

	IMR5/75 MYCN high/low	**IMR5/75 MYCN high/low / Luci**
cell culture medium (500 ml)	RPMI-1640	RPMI-1640
FCS	10%	10%
Penicillin/Streptomycin	100 u/ml	100 u/ml
Blasticidine	5 µg/ml	5 µg/ml
Zeocin	50 µg/ml	50 µg/ml
Hygromycin B	--	24 µg/ml

	IMR32 MYCN high/low	**IMR32 MYCN high/low / Luci**
cell culture medium (500 ml)	RPMI-1640	RPMI-1640
FCS	10%	10%
Penicillin/Streptomycin	100 u/ml	100 u/ml
Blasticidine	5 µg/ml	5 µg/ml
Zeocin	250 µg/ml	250 µg/ml
Hygromycin B	--	27 µg/ml

3.6 Surgical instruments/ mouse work

instrument	**specification**	**company**
sciccors	straight, curved	Fine science tools
forceps		Fine science tools
needle holder		Fine science tools
spatle	double, 6 mm	Laborhaus Scheller
ruler		Fine science tools
feeding needles	reuseable, 30 mm	Fine science tools
ear punch	3 mm	Fine science tools
clip applicator		Fine science tools
sterilisation container		Fine science tools

3.7 Enzymes, standards and special reagents

material	specification	company
alamar blue		Serotec
ampicillin		Sigma-Aldrich
benzonase		Merck Bioscience
bioanalyzer RNA kit	6000 Nano Assay Kit	Agilent genomics
bradford reagent		Bio-Rad
ECL detection reagent	BM Chemiluminescence Blotting substr.	Roche
glo lysis buffer		Promega
glycogen stock solution		Roche
protein standard 10-170 kDa	PageRuler Prestained Protein Ladder	Fermentas
Qiazol		Qiagen
Qubit RNA quantification	Qubit HS assay	Invitrogen
tissue tec		Sakura
transfection reagent (stable)	Effectene, EC buffer, enhancer	Qiagen
transfection reagent (transient)	Lipofectamine 2000	Invitrogen
Trizol		Ambion
trypan blue		Thermo fisher scietific

3.8 Kits

method	specification	company
maxiprep	Plasmid Maxi Kit	Qiagen
cDNA synthesis	First Strand cDNA Synthesis Kit	Fermentas
qPCR	Platinum SYBR Green qPCR SuperMix UDG	Invitrogen
luciferase expression	Steady glo luciferase assay	Promega
DNA digestion	DNase I set	Qiagen
RNA isolation/purification (tumor)	Nucleo Spin	Macherny-Nagel
RNA isolation/purification (cells)	RNeasy	Qiagen

3.9 Antibodies

3.9.1 Primary antibodies

Protein	Art	company	catalog no.
Actin	monoclonal	Sigma	A-5441
BRD2	monoclonal	Cell signaling technology	CST 5848
BRD3	polyclonal	Abcam	83478
BRD4	monoclonal	Abcam	ab128874
CDK4	monoclonal	Dianova	09583
c-MYC	monoclonal	Santa Cruz	sc-42

Cyclin D1	monoclonal	Dianova	08330
E2F-1	monoclonal	Santa Cruz Cell signaling technology	sc-251 CST 3742
GSK3-β	monoclonal	Cell signaling technology	CST 9315
phospho-GSK3-β	monoclonal	Cell signaling technology	CST 9323
MDM2	monoclonal	Santa Cruz	sc-965
phospho-MDM2	polyclonal	Cell signaling technology	CST 3521
MYCN	monoclonal	Santa Cruz	sc-53993
p53	monoclonal	Santa Cruz	sc-126
Rad17	monoclonal	Cell signaling technology	CST 8561

3.9.2 Secondary antibodies

Protein	**Art**	**company**	**catalog no.**
goat anti mouse POD	monoclonal	Dianova	115-035-003
goat anti rabbit POD	monoclonal	Dianova	111-035-003

3.10 Primers

gene		**sequence**	**company**
HPRT1	for	TGACACTGGCAAAACAATGCA	Sigma
	rev	GGTCCTTTTCACCAGCAAGCT	Sigma
SDHA	for	TGGGAACAAGAGGGCATCTG	Sigma
	rev	CCACCACTGCATCAAATTCATG	Sigma
MYCN	for	GGCCCTCAGTACCTCCGG	Sigma
	rev	AACGCCGCTTCTCCACAG	Sigma
c-MYC	for	QuantiTect Primer Assay	Qiagen
	rev		
CCND1	for	QuantiTect Primer Assay	Qiagen
	rev		
BRD4	for	CCCCTCGTGGTGGTGAAG	Sigma
	rev	GCTCGCTGCGGATGATG	Sigma
BRD3	for	QuantiTect Primer Assay	Qiagen
	rev		
BRD2	for	GTGGTCGGTACCATGGTGCAAAACGTGACTCCCCACA	Sigma
	rev	GGCTAGGAATTCAATCGTATTTTGTCCATG	Sigma

3.11 siRNAs/shRNAs

gene		sequence	company
MYCN shRNA	in pTer Plasmid	CTGGACAGTCACTGCCACT	
BRD4 siRNA 1	sense	AGAUUGAAAUCGACUUUGAtt	Ambion, silencer select
	antisense	UCAAAGUCGAUUUCAAUCUcg	
BRD4 siRNA 2	sense	CCUGAUUACUAUAAGAUCAtt	Ambion, silencer select
	antisense	UGAUCUUAUAGUAAUCAGGga	
BRD3 siRNA 1	sense	AGAGGAAGUUGAAUUAUUAtt	Ambion, silencer select
	antisense	UAAUAAUUCAACUUCCUCUtg	
BRD3 siRNA 2	sense	AGAUAGAAAUUGACUUUGAtt	Ambion, silencer select
	antisense	UCAAAGUCAAUUUCUAUCUcg	
BRD2 siRNA 1	sense	CUGGGAGUCUUGAGCCUAAtt	Ambion, silencer select
	antisense	UUAGGCUCAAGACUCCCAGga	
BRD2 siRNA 2	sense	GGUCUACCGGAUUAUCACAtt	Ambion, silencer select
	antisense	UGUGAUAAUCCGGUAGACCca	
Control siRNA		negative control siRNA #1	Ambion

3.12 buffers and prepared solutions

PBS and TBS have been prepared as a 10x concentrated stock solution. The table describes the final concentration used for experiments.

solution/buffer	chemicals	weight	storage
2x RPMI (500 ml)	RPMI powder $NaHCO_3$ (7,5% solution) H_2O dest. → pen/strep	15,87 g 26 ml 474 ml steril filtrated 10 ml	4°C
agar 1% (100 ml)	noble agar H_2O dest. →	1 g 100 ml boiled	55°C
agar 1,6% (100 ml)	noble agar H_2O dest. →	1,6 g 100 ml boiled	55°C
Amresco running buffer, SDS-PAGE (1 l)	0,025 M Tris (Base) 0,192 M glycine 0,1% SDS (20% solution) H_2O dest.	3,03 g 14,4 g 5 ml 995 ml	RT

BAY1238097 (15 ml)	BAY1238097 NaCl 0.9% sterile, ampulla →	30 mg 15 ml pH 4	4°C

complex blocking solution (1 l)	20% milk powder 20% FCS 3% BSA 1% goat normal serum 0,2% Tween 20 PBS	200 g 200 ml 30 g 10 ml 2 ml 788 ml	-20°C

crystal violet solution (50 ml)	0,1% crystal violet in ethanol PBS	2,5 ml 47,5 ml	RT

DEPC- water (500 ml)	0,1% DEPC H_2O dest. →	spatula tip 500 ml autoclaved	RT

glycine 1.25 M (200 ml)	glycine H_2O dest.	18,77 g 200 ml	4°C

Lämmli-buffer (50 ml)	0,5 M Tris HCl 4% SDS 20% glycerol β- Mercaptoethanol H_2O dest. bromophenole blue	4 g 10ml (20% solution) 10 ml 5 ml 25 ml spatula tip	RT

LB- Medium (1 l)	yeast extrakt trypton NaCl H_2O dest. →	5 g 10 g 10 g 1000 ml autoclaved	4°C

luciferin solution (10 ml)	D-luciferin potassium salt NaCl 0.9% sterile, ampulla	1 g 10 ml	-80°C

M-per buffer (10 ml)	phosphatase Inhibitor complete protease inhibitor EDTA 2mM H_2O dest.	1 tablet 1 tablet 40 µl 10 ml	4°C

PBS (1 l)	137 mM NaCl 2,68 mM KCl 10 mM Na_2HPO_4 1,76 mM KH_2PO_4 H_2O dest. →	8 g 0,2 g 1,42 g 0,24 g 1000 ml pH 7,4	RT
PBS-T (1 l)	+ Tween 20	1000 µl	RT
PBS-PI (50 ml)	+ complete protease inhibitor	1 tablet	4°C

PEG 80% (20 ml)	polyethyleneglycol H_2O sterile, ampulla	16 ml 4 ml	4°C

phospho- DAPI (100 ml)	$NaHPO_4$ DAPI- stock solution (1,26 mM) H_2O dest.	7,1 g 500 µl 100 ml	RT, dark

protein lysis buffer (50 ml)	Tris (Base) Triton X-100 Urea DTT $MgCl_2$ complete protease inhibitor H_2O dest.	1 ml (1M) 500 µl 21 g 5 ml (1M) 2 ml (1M) 2 tablets 42 ml	-20°C

running gel buffer, SDS-PAGE (500 ml)	1,5 M Tris (Base) 0,4% SDS (20% solution) H_2O dest. →	90,9 g 10 ml 500 ml pH 8,8	RT

stacking gel buffer, SDS-PAGE (100 ml)	1 M Tris (Base) 0,4% SDS (20% solution) bromophenol blue H_2O dest. →	12,1 g 2 ml spatula tip 100 ml pH 6,8	RT

TBS (1 l)	50 mM Tris 150 mM NaCl H_2O dest. →	6 g 8,8 g 1000 ml pH 7,6	RT
TBS-T	+ Tween 20	1000 µl	

Transfer buffer, western blot (1 l)	25 mN Tris (Base) 192 mM glycine 20% methanol H_2O dest.	3 g 14,4 g 200 ml 800 ml	4°C

Versene (100 ml)	PBS 10 mM EDTA →	100 ml 0,3 g pH 7,0	4°C

3.13 EDV

Hardware	PC (LG)
Software	Word, Excel, Powerpoint, Paint (Microsoft) Acrobat Reader, Photoshop (Adobe) EndNote X8 (Thomson Reuters) ABI Prism 7000 (Applied Biosystems) Chemi-Capt 5000 (Vilber) CW4000 FISH (Leica) FlowJo_V10 (Flexera Software) Imagescope (Aperio) Cell B Image (Olympus) ImageJ (Wayne Rasband) MITK (DKFZ)
Web-Tools	Venny 2.1.0 [139] Reactome [140] Uni-Prot [141] Molbiotools [142]

4 Methods

4.1 Mouse experiments

4.1.1 General animal keeping

For mouse experiments, seven week old male CD-1 nude and NMRI mice were purchased from Charles River Sulzfeld. NSG mice were breeded at the DKFZ animal core facility. The mice were kept in isolated ventilated Cages (IVC) in a room with 12h day and night illumination and at constant room temperature. Food and water were provided *ad libitum*. The animal basic service like feeding and cleaning of the cages was done by in-house animal keepers.

4.1.2 Anaesthesia and analgesia

Mice were anaesthetized using inhalation anesthesia. Oxygen flow rate was 0.5 l/min with 1.5-2 Vol% isofluran. Anaesthesia was initiated having the mice in a narcotic box. When the mice were narcotized, the eyes were protected using eye ointment and the mice were relocated to a heated ground to avoid cooling of the body.

Working with the orthotopic neuroblastoma mouse model, 200 mg/kg metamizol were applied subcutaneously before surgery. The analgetic therapy was continued for 48h, if necessary.

4.1.3 Subcutaneous neuroblastoma model

For the subcutaneous neuroblastoma mouse model, human neuroblastoma cells were injected in the right flank of immunocompromized mice. For this experiment, the cell lines IMR5/75, LS, NBL-S, SH-SY5Y and KELLY were used.

First of all, the cells were prepared for implantation. The cells were harvested, counted, washed twice and resuspended in PBS and matrigel, mixed in a 1:1 ratio. The concentration was adjusted so that for every mouse, $5x10^5$ cells in 100 µl PBS/matrigel were prepared in syringes. From cell line SH-SY5Y $1x10^6$ cells were diluted in 150 µl PBS/matrigel.

The mice were anaesthetized with isofluran. Then a 27 G needle was linked to the syringe with the cells prepared earlier and the cells were injected subcutaneous into the right flank of the mice.
After implantation the mice were monitored daily for weight and general health condition. The tumor size was measured with a caliper twice a week or daily, depending on the experimental conditions.

4.1.4 Orthotopic neuroblastoma model

Establishment of orthotopic neuroblastoma tumors was achieved by injecting tumor cells in the left adrenal gland of immunocompromized mice. The mice were anaesthetized and bedded on the right side. An incision of 1-1.5 cm was made through skin and peritoneum. The left adrenal gland was exposed by carefully dislocating the left kidney using a scoop.

For implantation of the tumor cells a special constructed pumping apparatus was used. A flexible tube was connected to a 30 G needle. Enough cells for 2 injections were gathered in the tube, then the needle was fixed with a needle holder and carefully inserted into the adrenal gland, taking care that the cutting of the needle was completely inside of the adrenal gland. Then $5x10^5$ cells were injected in a volume of 10 µl cell culture medium. Successful implantation could be visually determined by swelling of the adrenal gland or of the surrounding fat pad. After injection, the needle was kept in the adrenal gland for a few seconds and then was taken out slowly to prevent leakage of the tumor cell solution. The incision on the peritoneum was closed by surgical stitching, whereas for the skin staples were used.

During the first days after surgery wound healing was monitored daily. The staples were taken out 7-10 days after tumor cell implantation under short anesthesia using isofluran.

4.1.5 MYCN- repression

To induce repression of MYCN levels in orthotopic neuroblastomas, doxycycline was added to the drinking water of the mice. For each 250 ml bottle of drinking water, 0.5 mg doxycycline and 3.125 g sucrose were prepared, correlating with a final concentration of 2 g/l doxycycline and 12.5 g/l sucrose. Treatment with doxycycline-containing water started 14 days after tumor cell implantation and was continued until the end of the experiment.

4.1.6 Drug treatment

Drug treatment with BAY1238097 started when the tumor reached a size of 3 mm in diameter. BAY1238097 was administered by oral gavage to the mice. The drug was solved in 0.9% NaCl, pH adjusted to 4. All mice were treated once a day with 10 mg per kg bodyweight for maximum 30 days. The dose was adapted daily at the current weight of each animal. An appropriate volume was taken up with a syringe, a feeding needle was placed on the syringe and the remaining air was ejected. Then the mouse was fixed with one hand, the feeding needle was inserted down the throat until it reached the stomach and the drug was ejected.

Treatment with JQ1 was performed at the group of Johannes H. Schulte, Charité Berlin. JQ1 or the vehicle, 12.5% DMSO in PBS, were administered intraperitoneally. The mice were treated with 50 mg/kg body weight at the time points 0h, 12h, 24h and 36h.

4.1.7 Euthanasia and tumor tissue samples

The mice were euthanized at the end of the maximal duration of the experiment, when the maximal tolerable tumor size was reached, weight loss exceeded 20% or when they showed severe health problems. The mice were first anaesthetized with isofluran, and then euthanized by CO_2 intoxication.

The body of the dead mouse was opened on the ventral side (orthotopic tumors) or the flank (subcutaneous model) and pictures of the tumor in situ were taken. The tumor was taken out, weighed and photographed. The size was measured with a ruler, then the tumor was sliced into two parts. One piece was subsequently shock frozen in liquid nitrogen for RNA and protein analysis. The other part was embedded in tissue tec or formaline for histological analysis. From mice with huge orthotopic tumors, lung and liver were embedded in tissue tec to search for metastases. At the treatment study with BAY1238097, lung, colon, kidneys, liver, spleen and heart were conserved in formaline for toxicity evaluation.

4.2 In vivo imaging

4.2.1 Magnet resonance imaging

Magnet resonance imaging was done in cooperation with the DKFZ group “Molecular Imaging” headed by Dr. Dorde Komljenovic. A magnet resonance tomograph (MRT) for humans was modified with a mouse adapter with a small magnet coil for mice, which was installed 90° turned on the original MRT examination couch.

The mice were anaesthetized with isofluran, eye ointment was applied, and they were placed in the mouse coil. For every mouse, a positioner program was run first to calibrate the machine, then T2 measurements in coronar and sagital directions were performed. Width of slices was 1.0 mm, which was the smallest setting available. For analysis of the pictures and tumor volume calculation the software MITK was used.

4.2.2 In vivo bioluminescence imaging

For in vivo bioluminescence measurement two different imaging systems were tested. The first one was an imaging system built by the DKFZ group “Functional and Molecular Emission Computed Tomography” headed by Dr. Jörg Peter. The mice were anaesthetized with isofluran, eye ointment was applied and 150 µl luciferin solution were injected intraperitoneally. After two minutes, to ensure the luciferin reached the tumor cells, luminescence was subsequently measured. The measuring time varied between one and five minutes, images were taken from mice positioned on the back, on the side and on the venter. Additionally, incident light photographs were taken for positioning.

The second bioluminescence measurement was performed with an IVIS Spectrum. The procedure was similar to the first measurement. With this imager up to three mice could be scanned in parallel.

4.3 Basic cell culture methods

4.3.1 Culturing cells

Human derived neuroblastoma cell lines were cultured in RPMI 1640 medium containing 10% fetal bovine serum and 1% antibiotics (penicillin/streptomycin), hence called full medium. Adherent cells were cultured in cell culture flasks or cell culture dishes. Depending on the cell line, cell culture medium was changed up to three times per week.

NB-S 124 suspension cells were cultured in Neurobasal A medium with supplements, called suspension medium here. To change the medium of the suspension cells, cell culture flasks

were positioned on a side for a few minutes, until the cells had sedimented. Then the upper fraction of the cell culture medium was replaced.

The cells were kept in a cell culture incubator with 37°C temperature, 85% humidity and 5% CO_2.

4.3.2 Detaching cells

Adherent cells were detached from the cell culture plates using Versene. Versene is an EDTA-containing solution that detracts Ca^{2+}-ions from adherent junctions from the cells.

First, the medium was completely removed from the cell culture dish. Versene was added to the plate until the bottom was completely covered. The cells were incubated with Versene for 3-5 minutes at room temperature. When the cells rounded up, which was monitored under the microscope, they were rinsed by pipetting. Addition of cell culture medium stopped the reaction and the cells were capable to attach again to the surface of a cell culture dish.

Detaching of adherent cells was necessary for splitting of cultured cell lines, for counting and seeding for experiments and for harvesting of cells.

4.3.3 Pelleting cells

For some experiments, it was necessary to condense the cells to a pellet. This was achieved by centrifugation at 800 rpm for 5 minutes and room temperature.

4.3.4 Freezing cells

A freezing medium was prepared containing 45% RPMI 1640, 45% FCS and 10% DMSO. Cells were pelleted, and the supernatant was removed. Cells were resuspended in cold freezing medium; 1.5 ml cell suspension was transferred to each cryotube and the cells were put on ice quickly. Slow freezing of the cells was achieved by using a cryo container with isopropanol. This allows a continuous decrease of temperature by -1°C per minute. Cells were left at -70°C for about a week; afterwards they were brought to liquid nitrogen for long term storage.

4.3.5 Thawing cells

For thawing, a 15 ml falcon tube was prepared with 10 ml preheated full medium. 600 µl of the prepared medium were pipetted to the cryotube and transferred back to the falcon tube after a few seconds. This was repeated several times until the cells were completely thawed. The full medium with the cells was transferred to an appropriate cell culture flask. Medium was changed when the cells were attached, usually the next day.

4.3.6 Counting cells

For counting, 10 µl of cell suspension were mixed with 10 µl of 0.1% trypanblue and pipetted to a luna counting chamber. Cell number per mL and cell viability was calculated automatically using a luna automated cell counter.

4.3.7 Harvesting cells

At the end of an experiment, cells were harvested for further analysis. First, the cell culture medium was collected in an appropriate falcon tube. Then, the cells were detached using versene, added to the medium collected previously and pelleted by centrifugation. The supernatant was discarded. Further processing of the cell pellets was dependent on the experiments they were used for.

a) For RNA-Isolation followed by qPCR, 1 ml Trizol was used for resuspending.

b) Samples for RNA-sequencing were resuspended in 700 µl Qiazol. Samples were stored at -80°C.

c) Cells analyzed by FACS were resuspended in PBS for cell death or citric acid for cell cycle analysis and processed further directly for measurement.

4.4 Assays Cell Biology

4.4.1 Viability assay

For viability analysis of JQ1-treated cells, alamar blue viability assay was used.

The cells were harvested, counted and seeded in a 96 well plate, cell number ranging from 1.000 to 5.000 cells per well, depending on the doubling time of the tested cell line. To guarantee equal cell distribution of the cells to the wells, a multichannel pipette was used for seeding.

On the next day, cells were treated with different concentrations of JQ1. 100 µl medium containing different concentrations of JQ1 were added to each well. The final concentrations of JQ1 ranged from 0.05-5 µM JQ1. DMSO in the DMSO only control was equal to DMSO in the highest JQ1 concentration (Figure 5).

The treated cells were kept in the incubator for 72 hours. Then, 20 µl of alamar blue reagent were pipetted to the cells and the cells were put back to the incubator for another four hours. From each well, 100 µl were transferred to a black 96 well plate and the fluorescence was measured with the plate reader (extinction 540 nm, emission 580 nm).

Viability analysis with the BAY1238097 inhibitor was performed according to the same protocol.

	1	2	3	4	5	6	7	8	9	10	11	12
A												
B		Blank	DMSO	0.05 µM JQ1	0.1 µM JQ1	0.25 µM JQ1	0.5 µM JQ1	1 µM JQ1	2.5 µM JQ1	5 µM JQ1		
C		Blank	DMSO	0.05 µM JQ1	0.1 µM JQ1	0.25 µM JQ1	0.5 µM JQ1	1 µM JQ1	2.5 µM JQ1	5 µM JQ1		
D		Blank	DMSO	0.05 µM JQ1	0.1 µM JQ1	0.25 µM JQ1	0.5 µM JQ1	1 µM JQ1	2.5 µM JQ1	5 µM JQ1		
E		Cells	DMSO	0.05 µM JQ1	0.1 µM JQ1	0.25 µM JQ1	0.5 µM JQ1	1 µM JQ1	2.5 µM JQ1	5 µM JQ1		
F		Cells	DMSO	0.05 µM JQ1	0.1 µM JQ1	0.25 µM JQ1	0.5 µM JQ1	1 µM JQ1	2.5 µM JQ1	5 µM JQ1		
G		Cells	DMSO	0.05 µM JQ1	0.1 µM JQ1	0.25 µM JQ1	0.5 µM JQ1	1 µM JQ1	2.5 µM JQ1	5 µM JQ1		
H												

Figure 5: Layout of viability experiment. Blank= medium only, Cells=cells only control, DMSO=DMSO-treated control. For blank and cells three technical replicates were analysed. For each JQ1 concentration and DMSO control, six values were measured for each experiment.

4.4.2 Soft agar assay

Soft agar assays were performed in 6 well plates. A pipetting schedule, giving the amounts for a 6 well plate, is shown in table 3.

First, the base agar was prepared: 2x RPMI, FCS and JQ1 or DMSO were pipetted into a 15 ml falcon tube and prewarmed to 37°C in the waterbath. The 1.6% agar solution was added, the mixture was inverted and 1.5 ml were pipetted to each well. To get an even surface, the plate was slewed gently, then kept under the hood for hardening for 30 min and stored in the cell culture incubator overnight.

On the next day, the top agar, including the cells, was prepared. First, 2xRPMI, FCS and JQ1 or DMSO were mixed in a 15 ml falcon tube and prewarmed in the waterbath. The cells were harvested and counted, $5x10^4$ cells were pelleted and resuspended in 1 ml serum free RPMI medium. To the prewarmed solution, 1% agar was added and the solution was carefully mixed by inverting. The cells were added and the top agar was pipetted up and down a few times. To each well with base agar, 1 ml of top agar was added, the plate was slewed and kept under the hood for 30 min until the top agar was solid. In the meantime, full medium with 0.5 µM JQ1 or DMSO was prepared and after the 30 min hardening time, 3 mL were pipetted carefully to each well and the plates were placed in the cell culture incubator.

The soft agar assay was monitored for 2-4 weeks, every week 2 ml of medium were replaced by fresh medium containing JQ1 or DMSO. When colonies were visible, the plates were

stained using crystal violet. Therefore, medium was removed completely, 500 µl crystal violet solution were applied to each well and the plates were incubated at 37°C for 1h. After incubation, crystal violet was removed and the plates were scanned. Counting was performed automatically with the gel doc program.

Table 3: Reagents for soft agar assays. Amount is named for one plate with 6 wells each.

	base agar	top agar	medium
RPMI full medium			20 ml
2x RPMI	6 ml	4 ml	
FCS	1.5 ml	1 ml	
JQ1/DMSO	0.68 µl	0.5 µl	1.00 µl
cells/ RPMI		$5x10^4$ in 1 ml	
Agar 1.6%	6 ml		
Agar 1.0%		4 ml	

per well	1.5 ml	1 ml	3 ml

4.4.3 Sensitivity testing

To determine the amount of selection markers needed for selection of stably-transfected cells, a sensitivity testing was performed separately for each cell line used for stable transfections. The cells were harvested, counted and $1x10^5$ cells were seeded with 2 ml medium in each well of a 12 well plate. On the next day, different concentrations of hygromycin were added in the range 0-100 µg/ml, always three wells containing the same concentration. The metabolic activity of the remaining living cells was tested after seven days. Therefore, 1.000 µl of medium per well were discarded and 100 µl alamar blue were added to each well. After 3 hours incubation in the cell culture incubator 2x 100µl from each well were transferred to a black 96 well plate and the fluorescence was measured with a plate reader (extinction 540 nm, emission 580 nm).

4.4.4 Stable transfection/establishment of monoclonal cell lines

For stable transfection with the luciferase containing plasmid pGL4.50, the transfection reagent effectene was used. First, $3x10^5$ cells were seeded in a 25 cm² flask. On the next day, 150 µl EC buffer, 8 µl enhancer and 1 µg plasmide DNA were mixed in a reaction tube. After 5 min of incubation, 25 µl effectene were added, the solution was mixed carefully and kept under the hood for 10 min to form lipid complexes. Meanwhile the medium of the cells was replaced by 5 ml fresh cell culture medium. After incubation, the transfection complexes were transferred to the cells dropwise and the cells were kept in the incubator overnight.

One day after transfection, the medium was changed to selection medium containing hygromycin, the concentration was depending on the transfected cell line. The medium was changed every 2-3 days, until the surviving cells started growing again despite presence of the selection marker. Then the cells were expanded and polyclonal cells were frozen as backup.

To generate monoclonal cell lines, cells were seeded in 96 well plates with the goal to have only one single cell per well. This was achieved by a special pipetting schedule, which diluted the cells down to single cells per well (Figure 6). After 3-4 weeks single cell clones were picked and expanded. The luciferase expression of the different clones was checked by luciferase assay.

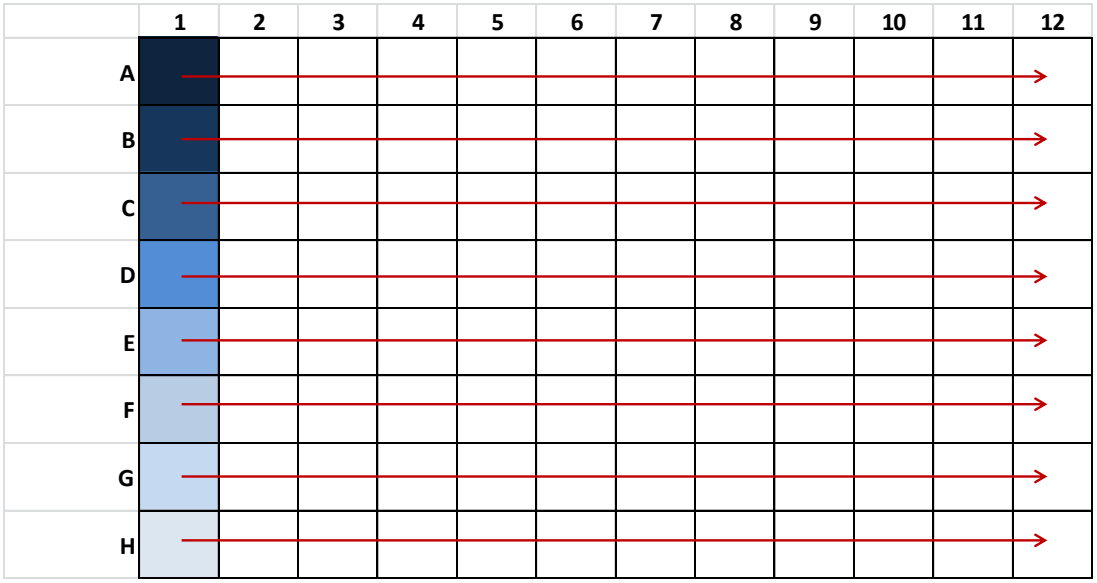

Figure 6: Pipetting schedule to generate monoclonal cell lines. Per well 100 µl, in column 1 200 µl medium were pipette to each well. In well A1 100 µl medium containing 1x10^5 cells were added, mixed and 100 µl were transferred to well B1. This was continued along the whole column. Next, the cells were horizontally diluted the same way, resulting in continuous thinning out of the cells from the upper left to the lower right corner of the plate. (Adapted from Ryan, J.A., 2008 [143])

4.4.5 Luciferase assay

From each clone, 1x10^6 cells were seeded in a 100 mm cell culture dish. The cells were harvested at 80% confluence, which took approximately three days. The cell pellet was lysed with 100 µl glo lysis buffer. To estimate the protein concentration of the sample, a Bradford assay was performed as described in section 4.6.4.

For luciferase measurement, 300 µg protein lysate from each sample were transferred to a white 96 well plate and the volume was complemented with glo lysis buffer to a total volume of 80 µl. As substrate, 80 µl of steady glo luciferase assay were added per well. The 96 well plate was mixed on the shaker for 3 min, then the luminescence signal was measured at the

plate reader. The luminescence signal was recorded for 30 seconds per well and the average was used for further calculation.

For each clone, technical duplicates were analyzed. The luciferase expression was compared to a positive and a negative control. As a positive control, stable luciferase expressing Hela cells were used. As negative control, untransfected cells from the same cell line were taken.

4.4.6 siRNA transfection

siRNA transfection was performed with lipofectamine 2000. For RNA, $3.75x10^5$ cells were seeded in 60 mm dishes, for protein analysis 100 mm plates were prepared with $1x10^6$ cells per dish (Table 4). For each condition, two dishes for RNA and two dishes for protein were seeded. Cells were transfected on the next day, at a confluency of about 30%. For each transfection, two falcons were prepared with 2 ml Opti-MEM medium. To one of the falcons, 40 µl lipofectamine 2000 were added, to the other one 16 µl of siRNA (50 µM). The two falcons were pooled and lipofectamine and siRNA were incubated for 20 min. In the meantime, medium of the prepared cells was changed. To 60 mm dishes, 5 ml of cell culture medium were added, protein plates received 15 ml medium. After incubation, the Opti-MEM medium containing the transfection complexes was divided between RNA and protein dishes: To the RNA dish, 1 ml of the transfection medium was added dropwise, 3 ml were pipetted to the 100 mm dish.

All transfections were stored at the incubator for 48 h, and then harvested according to the harvesting protocol for RNA and protein.

Table 4: siRNA transfection. Amount is named per cell culture dish.

	RNA	protein
cells	$3.75x10^5$ in 60 mm dish	$1x10^6$ in 100 mm dish
siRNA	200 pmol in 500 µl Opti-MEM	600 pmol in 1500 µl Opti-MEM
Lipofectamine 2000	10 µl in 500 µl Opti-MEM	30 µl in 1500 µl Opti-MEM
cell culture medium	5 ml	15 ml

4.5 Molecular biology methods

4.5.1 Plasmid preparation

For plasmid preparation, first 500 ml lysogeny broth (LB) medium were inoculated with E. coli carrying the plasmid of interest and kept at the shaker overnight at 37°C. On the next day, the LB medium with the bacteria was transferred to centrifugation tubes and the bacteria were pelleted by centrifugation with 6.000 g for 15 min at 4°C. The supernatant was discarded.

For isolation of plasmid DNA, the Qiagen maxi kit was used. The bacteria pellet was resuspended in 10 ml buffer P1, 10 mL of buffer P2 were added and the suspension was mixed by inverting 5-6 times. After incubation for 5 min at room temperature, 10 ml of ice-cold buffer P3 were added. Again, the suspension was mixed by inverting and incubated on ice for 20 min followed by centrifugation with 20.000 g at 4°C for 30 min. The supernatant, containing the soluble cell components, was transferred to a new tube. To eliminate the cell debris completely, a second centrifugation step was performed with 20.000 g at 4°C for 15 min.

Meanwhile, a DNA binding column was equilibrated with 10 ml QBT buffer. The supernatant was applied on the column and let run through. The column was washed two times by applying 30 ml QC buffer per washing step on the column and let it flow through. For elution the column was placed over a new 50 ml falcon and 15 ml of buffer QF were applied on the column and collected together with the plasmid DNA in the falcon. DNA was precipitated by adding 10.5 ml isopropanol to the DNA and pelleted by centrifugation with 15.000 g at 4°C for 30 min. The supernatant was discarded and the DNA pellet was washed with 5 ml 70% ethanol. After centrifugation with 15.000 g for 10 min, the supernatant was discarded and the pellet was air-dried by turning the falcon upside down for 5-10 min. The plasmid DNA was resolved with 500 µL H_2O and transferred to a 1.5 ml reaction tube. DNA concentration was measured using a nanodrop and the DNA was stored at -20°C.

4.5.2 RNA isolation and purification for qPCR (cell culture)

Cells were harvested as described and the cell pellet was resuspended in 1 ml Trizol reagent. The samples were frozen at -80°C.

For isolation and purification of total RNA, samples were thawed at room temperature and 200 µl chloroform were added to every sample. The samples were shaken vigorously for approximately 15 seconds and then incubated 3 min at room temperature. By centrifugation with 11.500 rpm at 4°C for 15 min, the RNA accumulated in the upper aqueous phase and was separated from DNA and proteins. The upper phase was transferred to a new reaction tube. For RNA visualization and precipitation 1 µl Glycogen and 500 µl isopropanol were added and the samples were incubated for 10 min at room temperature. After centrifugation with 11.500

rpm at 4°C for 10 min, the RNA was pelleted at the bottom of the reaction tube. The supernatant was discarded and the pellet was washed with 1 ml 75% ethanol, followed by centrifugation with 7.500 rpm at 4°C for 5 min. The supernatant was completely discarded and the pellet was air-dried for 5 min. The RNA was resolved by adding 70 µl H_2O and 10 min incubation at 56°C. Total RNA concentration was measured using a nanodrop. The RNA was stored at -80°C.

4.5.3 RNA isolation for RNA-sequencing (cell culture)

The samples resuspended in qiazol were thawed at room temperature. To each sample, 140 µl chloroform were added, the samples were shaked vigorously for 15 sec and incubated at room temperature for 2-3 minutes. Centrifugation for 15 min with 12.000 g at 4°C separated the samples into two phases. The aqueous phase was transferred to a new reaction tube, 700 µl of 70% ethanol were added and the samples were mixed by vortexing. The samples were applied on RNeasy Mini spin columns and centrifuged with 10.000 rpm for 15 sec at room temperature. The flow-through was transferred to a new reaction tube and stored at -80°C for potential isolation of miRNAs later on. On the column binding the mRNAs, 350 µl RWT buffer were applied, the columns were centrifuged with 10.000 rpm for 15 sec at room temperature and the flow-through was discarded. For DNA digestion, a master mix was prepared. Per sample, 10 µl DNase I stock solution and 70 µl buffer RDD were mixed. On each column, 80 µl of the DNase master mix were pipetted and the columns were incubated for 15 min at room temperature. After the incubation, 350 µl buffer RWT were added, the columns were centrifuged with 10.000 rpm for 15 sec at room temperature and the flow-through was discarded. Next, the samples were washed two times with 500 µl buffer RPE each, the flow-through was discarded both times. The columns were placed on new collection tubes and the mRNA was eluted from the column with 40 µl RNase free water. For this step, the water was applied on the column; the columns were incubated for 2 min at room temperature and then centrifuged for 1 min with 10.000 rpm at room temperature.

RNA concentration was measured using a Nanodrop. RNA quality was checked by running the samples on a bioanalyzer. For RNA-seq, 2.200 ng of RNA were diluted with H_2O dest. to a total volume of 50 µl and submitted to the DKFZ core facility for further sample preparation and sequencing. Remaining RNA was stored at -80°C.

4.5.4 RNA isolation (tumor tissue)

For RNA-Isolation from mouse tumor tissue the NucleoSpin kit from Macherey-Nagel was used. Between 10 and 100 mg tumor tissue were weighted and disrupted into small pieces using a scalpel. For lysis, 350 µl buffer RA1 were added and mixed with the sample by pipetting up and down for several times. The lysate was transferred to a reaction tube. With an additional 350 µl RA1 the remaining tissue fragments were collected, lysed and transferred to the same reaction tube. Disruption and lysis were performed on dry ice to avoid thawing of the tumor tissue. To the lysate, 7 µl of β-Mercaptoethanol were added, and the lysate was incubated on a shaker at room temperature for 10 min.

The lysate was pipetted on a NucleoSpin filter column and the column was centrifuged for 1 min with 11.000 g at room temperature. After centrifugation, the column was discarded and the flow-through was transferred to a new reaction tube. 700 µl ethanol 70% were added to the lysate and mixed by vortexing. Half of the lysate was loaded on a NucleoSpin RNA column and centrifuged for 1 min with 11.000 g at room temperature. The flow-through was discarded and loading was repeated with the rest of the lysate using the same column. Next, 350 µl MDB buffer were applied on the column, followed by centrifugation for 1 min with 11.000 g. For DNA digestion, a mastermix was prepared with 90 µl reaction buffer and 10 µl rDNase per sample. From the DNase mastermix 95 µl were pipetted on each column and incubated for 15 min at room temperature. The reaction was stopped by adding 200 µl buffer RAW2, then the column was centrifuged for 30 sec with 11.000 g at room temperature and flow-through and collection tube were both discarded. The column was washed two times with buffer RA3, first time with 600 µl followed by 30 sec centrifugation, second time with 250 µl RA3 followed by 2 min centrifugation with 11.000 g at room temperature. After the second washing step, the collection tube was discarded and the column was placed in a new reaction tube. To elute the RNA, 60 µl RNase free water were pipetted on the column and incubated for 5 min at room temperature. Then the column was centrifuged for 1 min with 11.000 g.

The RNA concentration was measured using a Nanodrop, quality was checked by running a bioanalyzer chip. For RNA-seq, 2.200 ng of RNA were diluted with H_2O dest. to a total volume of 50 µl and submitted to the DKFZ core facility for further sample preparation and sequencing. For RNA analysis in qPCRs, the cDNA and qPCR protocols were followed. Remaining RNA was stored at -80°C.

4.5.5 cDNA synthesis

For the synthesis of cDNA the First strand cDNA synthesis kit was used, all enzymes and other reagents were provided with the kit. From each sample, 1 µg of RNA was transferred to a 0.5 ml reaction tube and H_2O was added up to a total volume of 10 µl. To each sample, 1 µl random hexamer primer was added and RNA and primer were incubated for 5 min at 70°C. In the meantime, a mastermix containing the remaining reagents was prepared:

4 µl/ sample 5x reaction buffer
2 µl/ sample dNTP mix
2 µl/ sample MuLV reverse transcriptase
1 µl/ sample ribolock

The heated samples were spinned down for a few seconds and then 9 µl of mastermix were added to each sample. Using a cycler, the samples were incubated according to the following protocol:

25°C for 10 min
37°C for 60 min
70°C for 10 min

When synthesis was finished, the samples were spinned down and the cDNA was stored at -20°C.

4.5.6 Quantitative real time PCR

The quantification of mRNA was based on an internal standard curve and the comparison with two different housekeeping genes. To prepare the different mRNA standards, a small amount of each cDNA sample was separated, pooled and diluted with H_2O dest. to a total volume of 80 µl (160 µl for more than 10 samples) (Table 5). This first standard was diluted four times in a ratio of 1:4 to have a standard curve with five dilutions. The remaining cDNA samples were diluted with H_2O dest. to a total volume of 60 µl. Genomic DNA and H_2O dest. were included as controls. All samples, standards and controls were measured in triplicates.

Primer dilutions were prepared for each plate directly before pipetting according to table 6. SDHA and HPRT1 were included as housekeeping genes and used to calculate the relative changes in gene expression for the genes of interest. Samples, standards and controls were measured for every primer pair, which allows a direct comparison calculation of mRNA expression based on the standard curve for every single gene.

Table 5: Pipetting schedule for qPCR standard curve. Volumes depending on the number of samples.

No. of samples		**8**	**9**	**10**	**11**	**12**
For standard curve	per sample	4 µl	3 µl	3 µl	5 µl	5 µl
	samples sum	32 µl	27 µl	30 µl	55 µl	60 µl
	add H_2O	48 µl	53 µl	50 µl	105 µl	100 µl
	total volume	80 µl	80 µl	80 µl	160 µl	160 µl
Remaining sample		16 µl	17 µl	17 µl	15 µl	15 µl
	add H_2O	44 µl	43 µl	43 µl	45 µl	45 µl
	total volume	60 µl	60 µl	60 µl	60 µl	60 µl

Table 6: Primer dilutions for qPCR.

mRNA	**Primer for (100 pmol/µL)**	**Primer rev (100 pmol/µL)**	**H_2O dest**
MYCN	4 µl	4 µl	192 µl
c-MYC	primer assay used, no dilution necessary		
CCND1	primer assay used, no dilution necessary		
BRD4	6 µl	6 µl	188 µl
BRD3	primer assay used, no dilution necessary		
BRD2	6 µl	6 µl	188 µl
HPRT1	6 µl	6 µl	188 µl
SDHA	6 µl	6 µl	188 µl

A master mix was prepared with 13 µl SYBR-mix, 2.5 µl primer dilution and 7 µl H_2O dest. per sample. From the master mix, 22.5 µl were pipetted into each well, 2.5 µl of sample, standard or control were added and the plate was sealed with a transparent foil. After a short centrifugation step to spin down the samples completely, the plates were put in the qPCR machine to start and measure amplification of the cDNA using the following protocol.

50°C	2:00 min	
95°C	2:00 min	
95°C	0:15 min	40 cycles
60°C	0:30 min	
60°C→ 95°C (melting curve)		

4.6 Biochemical methods

4.6.1 Cell lysis for SDS-PAGE (cell culture)

Cells were harvested as described. The cells were disrupted by resuspending the cell pellet in 30-100 µl protein lysis buffer, depending on the size of the cell pellet. After this step, lysates could be stored at -80°C.

To digest DNA and RNA, 1 µl of benzonase was added to each sample and the samples were incubated at 37°C for 15 min. The cell debris was pelleted by centrifugation at 10.000 rpm for 3 min and the supernatant containing the proteins was transferred to a clean reaction tube and stored at -80°C.

4.6.2 Cell lysis for SDS-PAGE (tumor tissue)

For protein lysates, a piece of 50-100 mg was cut from every tumor sample. The tumor piece was placed on a cell culture plate on dry ice and was shredded into small pieces using a scalpel. In the next step, 150-200 µl protein lysis buffer were added to the tissue pieces and the tumor tissue was minced together with the buffer. The sample was transferred to a 1.5 ml reaction tube and the cell culture plate was washed out with additional 100 µl of protein lysis buffer to have no tissue left on the plate. The lysate was grinded by pipetting up and down until all visible pieces of tumor tissue had disappeared. In a last step, the lysate was transferred to a tissue homogenizer to finalize lysis.

To the completely homogenized tissue lysates, 1 µl of benzonase was added to digest DNA and RNA. The lysates were incubated at 37°C for 15 min and the debris was pelleted by centrifugation at 10.000 rpm for 3 min. The supernatant was transferred to a clean reaction tube and stored at -80°C.

4.6.3 Cell lysis for RPPA (cell culture)

Cells were harvested as usual. Cells pelleted by centrifugation were resuspended and lysed in 25 µl M-PER buffer. Lysates were stored at -80°C. After determining the protein concentration using Bradford-assay, the samples were handed over to the core facility for further analysis.

4.6.4 Bradford assay

Protein concentration was determined using the Bradford assay. A cuvette with 200 µl Bradford reagent and 800 µl water was prepared for every protein sample. 1 µl protein lysate was added and the sample was mixed by vortexing.

The photometer was calibrated at 595 nm wavelength using a blank sample without protein. The absorbance of all samples was measured with the photometer. Additionally, eight different protein standards with defined protein concentrations in the range 0-20 µg/µl were measured to generate a standard curve for calculation of the protein concentrations of the samples.

4.6.5 Polyacrylamide gels

For preparation of polyacrylamide gels the BioRad system for mini gels was used. The glass plates were cleaned with water and 70% ethanol, braced with a plate clip and fixed in the gel holder. The running gel was prepared as described in table 7. APS and TEMED were added directly before use. The running gel solution was filled in the gap between the glass plates up to 1 cm below the upper border and was overlayed with 500 µl isopropanol to get an even surface on the running gel. Polymerization of the running gel took approximately 30 min. After polymerization the isopropanol layer was removed completely. The stacking gel was prepared, filled in the remaining space between the glass plates up to the upper border and a comb was inserted immediately to create pockets for the samples. The polymerization of the stacking gel took about 15 min. Then the gels were taken out of the gel holder and used directly or wrapped in wet paper and stored for up to two weeks at 4°C.

Table 7: Preparation of polyacrylamide gels. Each column gives the reagents for two gels.

	running gel 15%	running gel 12,5%	stacking gel
running gel buffer	3,75 ml	3,75 ml	--
stacking gel buffer	--	--	1,2 ml
H_2O dest.	5,4 ml	6,4 ml	2,75 ml
20% SDS	75 µl	75 µl	25 µl
Acrylamid/bis-acrylamide 40%	5,7 ml	4,7 ml	0,375 ml
10% APS	150 µl	150 µl	150 µl
TEMED	6 µl	6 µl	6 µl

4.6.6 SDS-PAGE

From each sample for SDS-PAGE 50 µg of protein were taken and lämmli buffer was added to a total volume of 15 µl. The samples were heated to 95°C for 5 min and spinned down for a few seconds in a centrifuge. Two of the gels were braced in a running chamber and amresco electrophoresis buffer was filled in the chamber and between the gels. After taking out the combs, the pockets were cleared by rinsing amrecso buffer. The samples were loaded on the gel. To estimate molecular weight of the bands, 6 µl PAGE ruler were loaded in an additional pocket. The voltage was set to 80 V until the samples had passed the stacking gel and were collected to the same level. When entering the running gel, the voltage was raised to 120 V.

Gel electrophoresis was stopped when the lowest PAGE ruler band had passed the gel completely. The gels were taken out of the electrophoresis chamber and were either wrapped in wet paper and kept at 4°C overnight or were directly used for western blot.

4.6.7 Western blot

The proteins were transferred from the polyacrylamide gel to a nitrocellulose membrane by wet blot technique. The glass plates enclosing the gel were opened, the stacking gel was discarded and the running gel was taken out and equilibrated in transfer buffer. Then the blot was stacked, starting from the anodic side: Sponge, 3x whatman paper, nitrocellulose membrane, polyacrylamide gel, 3x whatman, sponge. All components were soaked with transfer buffer before use. Air bubbles were eliminated by rolling the blot. The blot was put in a transfer chamber and covered completely with transfer buffer. To keep the temperature low, ice falcons were placed inside the chamber and the blotting chamber was kept on ice. The transfer was running for 2h at 440 mA.

The blot was disassembled, the membrane was taken out, shortly washed with PBS-T and the positions of the bands of the protein standard were marked on the membrane. To reduce unspecific binding of antibodies, the membrane was incubated with blocking solution for 1h at room temperature. Afterwards, the membrane was washed 3x for 5 min at room temperature. The first antibody against the protein of interest was diluted in 5% milk or BSA (see table 8 below) and incubated on the membrane overnight at 4°C. On the next day, the first antibody was taken off and the membrane was washed again 3x for 5 min. The second antibody, conjugated with a peroxidase, was incubated on the membrane for 2h at 4°C. Then, the membrane was washed again 3x for 5 min.

Table 8: Dilution of antibodies for western blot.

protein	origin	buffer and dilution	molecular weight
β- Actin	mouse	5% milk in PBST, 1:5.000	42 kDa
BRD2	rabbit	5% milk in PBST, 1:1.000	110 kDa
BRD3	rabbit	5% milk in PBST, 1:1.000	85 kDa
BRD4	rabbit	5% milk in PBST, 1:1.000	132 kDa
CDK4	mouse	5% milk in PBST, 1:1.000	34 kDa
c-myc	mouse	5% milk in PBST, 1:1.000	67 kDa
Cyclin D1	mouse	5% milk in PBST, 1:1.000	36 kDa
E2F-1	mouse	5% milk in PBST, 1:1.000	60 kDa
MYCN	mouse	5% milk in PBST, 1:1.000	65 kDa
p53	mouse	5% milk in PBST, 1:1.000	53 kDa

For detection, 3 ml solution A and 30 µl solution B from the ECL-kit from Roche were pipetted on the membrane and incubated for about 1 min on room temperature. The membrane was placed in the chemicapt and a photograph was taken from the chemiluminescent bands. After detection, the membrane was washed again 3x for 5 min and either another first antibody was incubated over night or the membrane was dried and stored at -20°C.

4.7 Flow Cytometry

4.7.1 Live/dead measurement

For live/dead analysis by FACS the cells were harvested and resuspended in 500 µl PBS as described in 4.3.7. For each time point and condition triplicates were analysed. The measurement of cell death was done with a MACSQuant FACS machine. The complete 500 µl samples were transferred to FACS tubes. Immediately before measurement, 5 µl propidium iodide were added and the sample was mixed by flipping the tube. From each sample, 200 µl were analysed using FACS. The software Flow-Jo was used for data evaluation.

4.7.2 Cell cycle measurement

As described in 4.3.7, cells harvested for cell cycle analysis were resuspended in 500 µl citric acid, which destroyed the cell membrane and only left the nuclei for FACS analysis. Technical triplicates were harvested and analyzed per condition and time point. The samples were kept at 4°C for up to one week, then stained with phospho-DAPI solution and measured by Dr. Volker Ehemann, a collaboration partner from the pathological institute at the University Hospital Heidelberg.

4.8 Histological analyses

Histological analyses were performed by the pathological institute. The cryo-conserved material was sectioned and stained with haematoxylin eosin staining. Material conserved by formaline was embedded in paraffin, sectioned and stained with haematoxylin eosin. A professional evaluation of the tumor material was done by Dr. med. vet. Tanja Poth. The tumor samples were characterized in regard to tumor entity, and necrosis and stroma parts were described.

5 Results

5.1 Characterization of a MYCN high/low cell culture model

An amplification of the *MYCN* gene is an important risk factor for bad outcome of neuroblastoma disease. Different *MYCN* amplified and *MYCN* non-amplified neuroblastoma cell lines have limited value for analyzing the role of *MYCN* in neuroblastoma because of manifold genetic aberrations differing between the cell lines. Therefore a *MYCN* knockdown model inducible by tetracycline was established for *MYCN* amplified neuroblastoma cell lines in the DKFZ group of Neuroblastoma Genomics. This *MYCN* high/low model has the advantage that high and low levels of *MYCN* gene expression can be compared in the same genetic background. The effects observed can be assigned directly to low or high *MYCN* and are not distorted by other genetic factors of the cell lines.

So far, for the two neuroblastoma cell lines IMR5/75 and IMR32 the *MYCN* high/low model was already established. As these cell lines were used for several experiments of this thesis, the working principle and a short characterization of the IMR5/75 *MYCN* high/low cell line are described at the beginning of the results part.

5.1.1 Concept of the *MYCN* knockdown in *MYCN* amplified neuroblastoma cells

The *MYCN* knockdown is based on two plasmids: The first plasmid is coding for the tetracycline repressor (TetR), a protein that binds tetracycline molecules and thereby changes its conformation. The second plasmid contains a *MYCN* shRNA. In the promoter region of the shRNA binding sites for the tetracycline repressor ($TetO_2$-element) are included, regulating the expression of the *MYCN* shRNA (Figure 7).

Without the presence of tetracycline the TetR binds to the $TetO_2$-elements and blocks the transcription of the *MYCN* shRNA. In absence of *MYCN* shRNA the *MYCN* expression is not affected and the cells are in the *MYCN* high condition.

When tetracycline is present, it binds to the TetR. The TetR changes its conformation towards its inactive form and dissociates from the $TetO_2$-elements of the DNA. The *MYCN* shRNA is transcribed and the *MYCN* mRNA is degraded, leading to decreasing levels of MYCN in the *MYCN* low condition.

The *MYCN* high/low cell models deriving from IMR5/75 and IMR32 were established as monoclonal cell lines. The tetracycline derived knockdown model is also sensitive to treatment with doxycycline instead of tetracycline.

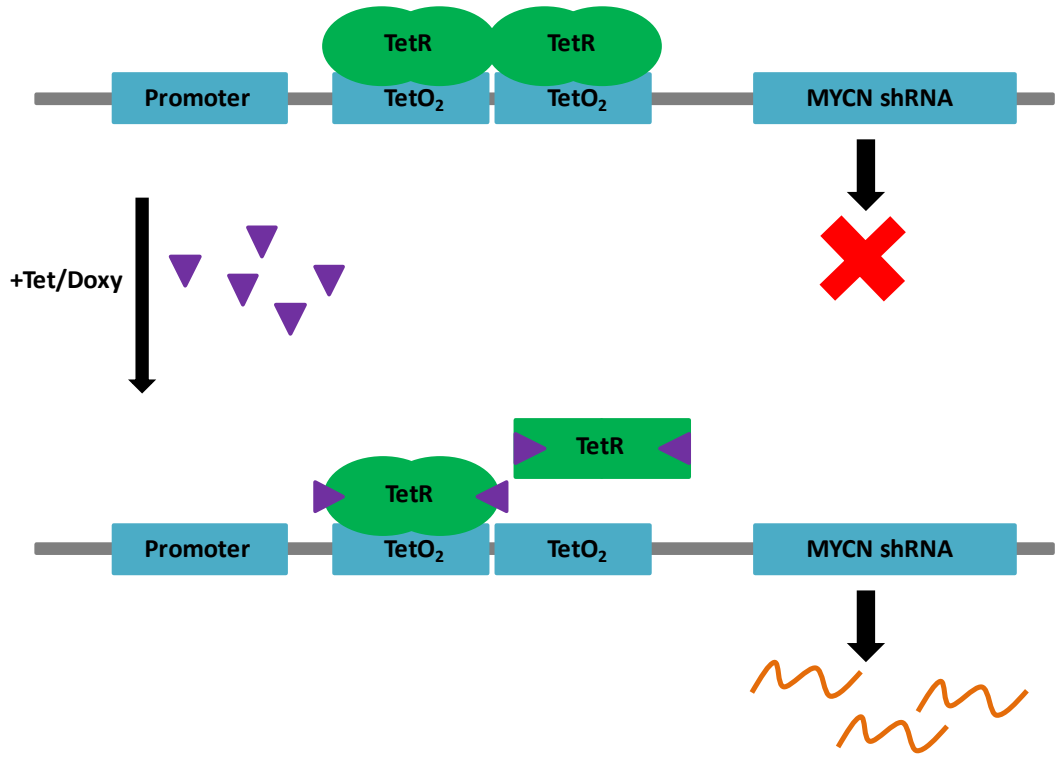

Figure 7: Schematic presentation of the *MYCN* knockdown. Upper line: genetic construct in absence of tetracycline. The TetR is bound to the $TetO_2$-elements and blocks the transcription of the *MYCN* shRNA. Lower line: situation in presence of tetracycline. Tetracycline inactivates the tetracycline repressor and the *MYCN* shRNA is transcribed. $TetO_2$= tetracycline operator sequence, TetR= tetracycline repressor, purple triangle= tetracycline/doxycycline molecule (adapted from Invitrogen, T-REx System User Manual [144]).

5.1.2 Quantification of the *MYCN* knockdown in IMR5/75 neuroblastoma cells

To estimate the magnitude of the *MYCN* knockdown, IMR5/75 *MYCN* high/low cells were treated with tetracycline for 48h and the MYCN protein expression was analyzed by western blot (Figure 8). Both western blots showed a decrease of the MYCN protein expression under the tetracycline treated MYCN low condition (Figure 8A and 8B). Quantification and normalization against the loading control β-actin revealed a marginal significant decrease in MYCN protein expression (Figure 8C). The mean of the remaining MYCN protein expression was 25.6%, which was low enough to clearly observe MYCN dependent effects.

Experiments from colleagues using the *MYCN* high/low cells revealed, that the extent of the MYCN knockdown varies during the first few hours after induction of the expression of the *MYCN* shRNA in a periodic manner (data not shown). To analyze cells with a stable knockdown, tetracycline pretreatment for 48h was performed for all experiments with the *MYCN* high/low cell lines.

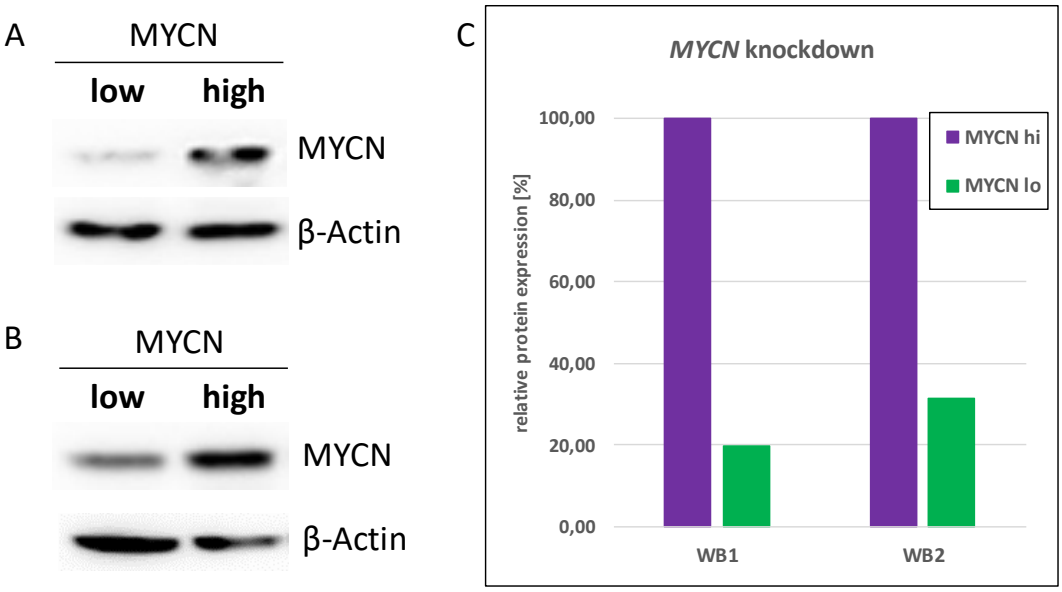

Figure 8: MYCN protein expression in IMR5/75. IMR5/75 *MYCN* high/low cells were treated with 1 µM tetracycline or appropriate amount 70% ethanol for 48h. The MYCN protein knockdown was quantified by western blot with β-actin as loading control. A)+B) Western blot analysis of two biological replicates. C) Quantification of MYCN protein expression, normalized to the β-actin bands of the western blots (WB= western blot). P-value was <0.05 (student t-test).

5.1.3 *MYCN* knockdown prolongs the cell cycle of IMR5/75 neuroblastoma cells

After proving the effectiveness of the *MYCN* knockdown achieved in the IMR5/75 *MYCN* high/low cells, the cells were characterized regarding their *MYCN* high and *MYCN* low conditions. As cell division is essential for tumorigenesis and *MYCN* target genes are involved in cell cycle regulation [56], the cell cycle distribution was analyzed by flow cytometry.

Upon *MYCN* knockdown, an increase of the G1 fraction from 48% to 61% of total cells was observed (Figure 9A). The S-phase fraction decreased from 34% to 26%, the G2- fraction was slightly smaller in *MYCN* low IMR5/75 cells. The results suppose that IMR5/75 with low *MYCN* expression remain longer in the G1 phase, resulting in a slow down of the cell cycle.

A more precise analysis of the cell cycle effects on IMR5/75 *MYCN* high and *MYCN* low cells has been achieved by synchronization of the cells (Figure 9B). This experiment was concepted and performed by Dr. Emma Bell [145]. The IMR5/75 cells were synchronized by a thymidine block. In both *MYCN* high and *MYCN* low conditions the G1-fraction increased during the first 10 hours after release from the thymidine block. After 15h the *MYCN* high cells showed an increase of the S-phase fraction and a decrease of the G1 arrested fraction. In contrast, the *MYCN* low cells stayed arrested in the G1 phase for more than 24h.

These results show that the *MYCN* amplified IMR5/75 cells are highly dependent on the expression of *MYCN* for passaging through the cell cycle and cell division.

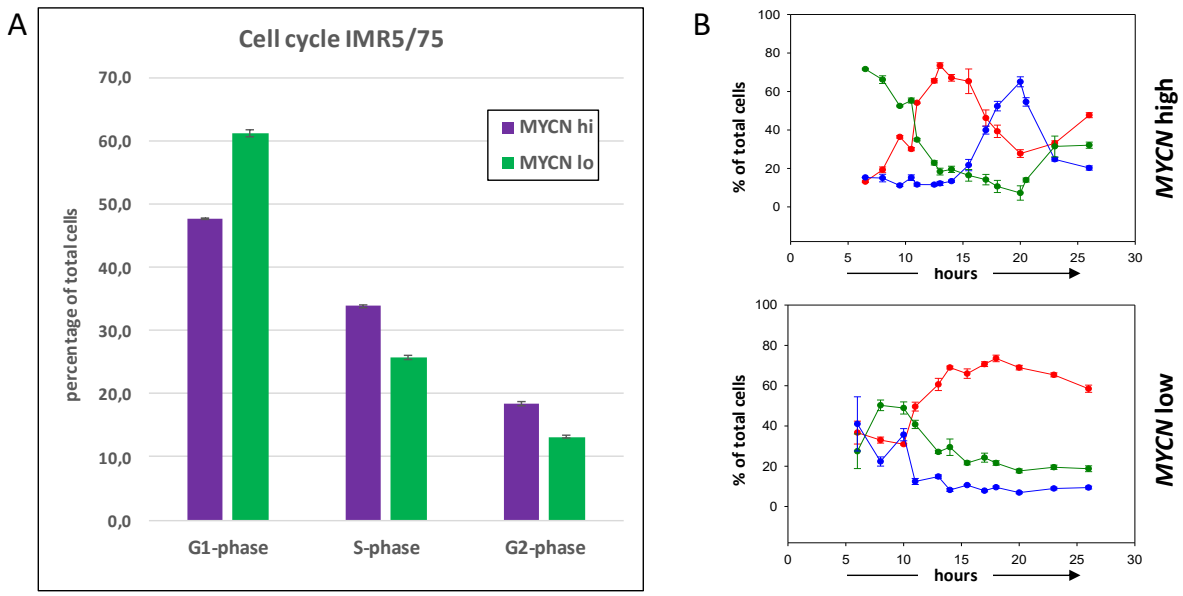

Figure 9: Cell cycle analysis of IMR5/75 *MYCN* high/low cells. A) Cell cycle distribution of IMR5/75 *MYCN* high/low cells. The cells were treated with 1 µM tetracycline or appropriate amount of 70% ethanol for 48h and analyzed by flow cytometry. One biological replicate with three technical replicates was analyzed. Due to the low number of replicates, no significance test was performed. B) Cell cycle analysis of IMR5/75 *MYCN* high/low cells synchronized by thymidine block. The cells were analyzed by flow cytometry. Red= G1-phase, blue= S-phase, green=G2-phase (Figure 9B gently provided by Dr. Emma Bell, [145]).

5.1.4 *MYCN* knockdown increases cell death in IMR5/75 neuroblastoma cells

As *MYCN* target genes are also involved in cell death signaling [56], cell death was measured in the *MYCN* high/low IMR5/75 cell line using flow cytometry to estimate if the induction of spontaneous cell death is dependent on *MYCN* expression in *MYCN* amplified neuroblastoma cells.

Cell death increased upon *MYCN* knockdown in IMR5/75 cells from 20% in *MYCN* high cells to 33% in *MYCN* low cells (Figure 10). The total levels of cell death in both the *MYCN* high as well as in the *MYCN* low samples were relatively high, probably due to rupture of cells during sample preparation.

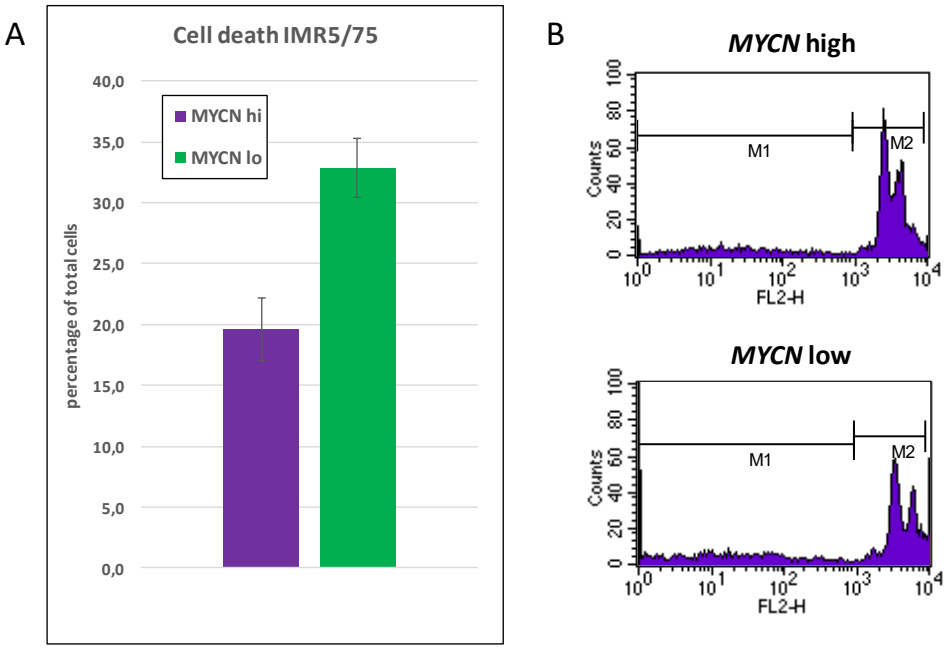

Figure 10: Cell death in IMR5/75 *MYCN* high/low cells. A) Cell death analysis of IMR5/75 *MYCN* high/low cells. The cells were treated with 1 µM tetracycline or equal amount of 70% ethanol for 48h and analyzed by flow cytometry. One biological replicate with three technical replicates was analyzed. Due to the low number of replicates, no significance test was performed. B) Flow cytometry analysis of IMR5/75 MYCN high/low cells. M1= sub-G1 fraction of dead cells. M2=fraction of viable cells.

Taken together, the *MYCN* high/low system effectively reduces the MYCN expression of IMR5/75 cells after 48h of tetracycline treatment. Thereby, the system is a valuable tool for the analysis of the role of MYCN in *MYCN* amplified neuroblastoma cells. Nevertheless, when working with this system it is important to keep in mind that biological characteristics of the neuroblastoma cells are influenced by the knockdown. The increase of cell death and the influence on the cell cycle resulting in a decrease of the doubling time have to be considered when interpreting the data collected with this system.

The experiments presented here were focusing on the IMR5/75 neuroblastoma cell line. The same *MYCN* high/low system is available for the *MYCN* amplified neuroblastoma cell line IMR32.

5.2 Treatment of neuroblastoma cell lines with BRD4 inhibitors

It has been shown that the BRD4-mediated transcriptional regulation is essential for many cancer entities with overexpressed or amplified genes of the MYC protein family, which includes neuroblastoma having a deregulated *MYCN* gene in a high proportion of high-risk cases [103, 108, 120]. The effectiveness of BRD4 inhibitors, such as JQ1, on neuroblastoma has been tested in a number of studies [121-123]. Yet, most of them include only few cell lines in their analysis.

The present BRD4 treatment study included a large panel of 23 neuroblastoma cell lines with different genetic backgrounds. The treatment of neuroblastoma cell lines with varying genetics aimed to identify factors that help to estimate if a patient's tumor with similar biological characteristics would be sensitive for treatment with BRD4 inhibitors.

For the experiments with BRD4 inhibition this work was supported by Dr. Emma Bell. Bioinformatic data were analyzed by Dr. Chunxuan Shao, Umut Toprak and Dr. Carl Herrmann.

5.2.1 JQ1 treatment reduces viability of selected neuroblastoma cell lines

First of all, the effectivity of BRD4 inhibition on neuroblastoma cells was estimated by a viability screen on a panel of 23 different neuroblastoma cell lines with different genetic backgrounds. The cells were treated with different concentrations of JQ1 or DMSO only control and the viability was measured using the alamar blue assay. The algorithm for calculation of the IC50 and EC50 values was gently provided by Xiaoqi Jiang (DKFZ department Biostatistics).

The panel of cell lines used for the viability screening is composed of 12 *MYCN* amplified cell lines and 11 *MYCN* non-amplified cell lines, including also one *MYCN* non-amplified cell line which expresses moderate levels of *MYCN* because of a translocation. Additional genetic changes are for example a *p53* mutation in 7 out of the 23 cell lines, *ALK* mutations in five of the cell lines, a *TERT* activation in four of the tested cell lines or *MDM2/CDK4/CCND1* amplifications in three cell lines (Table 9).

The IC50 values were not used for evaluation of the sensitivity. The varying dose response curves or low effects of JQ1 treatment on several of the neuroblastoma cell lines did not allow a calculation of IC50 values for 11 of the tested 23 cell lines.

To rate the results of the viability screen, three different categories were defined, based on the EC50 values. Cell lines with an EC50 lower than 0.1 µM were categorized as JQ1 sensitive, cell lines with an EC50 value over 0.5 µM were defined as JQ1 resistant. All cell lines with an EC50 between these two borders were classified as JQ1 intermediate responders.

Table 9: Genetic aberrations of neuroblastoma cell lines. Cell lines listed in alphabetical order. Amp= amplified; non amp= non-amplified; tl= translocated; act= activated; mut= mutated; wt= wild type; dp= duplicated; del= deleted; bal= balanced; meth= methylated; het= heterozygous.

Cell line	MYCN	c-MYC	TERT	ALT	TP53	MDM2	CDK4	CCND1	p16/p14	ALK	1p	doubling time
CHLA-90	non amp			mut	mut				wt		tl	59h
GIMEN	non amp		act		wt				meth	wt	del	24h
HD-N-33	non amp								del			
IMR32	amp				wt			wt	wt	amp/wt	del	20h
IMR5/75	amp							wt	wt		tl, bal	20h
KELLY	amp		act		mut			wt		mut		30-40h
LAN-1	amp				mut				wt	mut	tl, bal	100h
LAN-5	amp				wt			wt	wt	mut	del	100h
LAN-6	non amp			mut	wt			dp	del		del	150-170h
LS	amp				wt	amp	amp	amp				45h
NB69	non amp	tl			wt				wt		del	
NBL-S	tl				wt				wt			36h
NGP	amp		act		wt	amp	amp	wt	wt	wt	tl, bal	50-70h
NMB	amp				mut					wt	del, bal	40-50h
SH-EP	non amp	tl			wt			wt	del	mut		
SH-SY5Y	non amp	tl			wt			wt	wt	mut		48h
SJNB1	non amp									wt		
SK-N-AS	non amp	tl	act		mut				del, het	wt	del	39h
SK-N-BE(2)	amp				mut						del	30h
SK-N-BE(2)c	amp				mut			wt	wt	wt		18h
SK-N-FI	non amp			mut	mut				wt			
SMSKCNR	amp				wt					mut	del	72h
TR14	amp				wt	amp	amp	wt	wt		del, bal	72h

In the group of the 12 *MYCN* amplified cell lines (Figure 11A), there are six cell lines counting to the group of JQ1-sensitive cell lines (IMR32, TR14, IMR5/75, NMB, SK-N-BE(2)c, LS) and four cell lines defined as JQ1-resistant (KELLY, LAN-5, SMS-KCNR, NGP). Only one cell line shows an intermediate response to JQ1 treatment (SK-N-BE(2)).

For LAN-1 the used algorithm failed to calculate EC50 and IC50 values, probably due to high variability of the replicates.

Among the *MYCN* non-amplified cell lines (Figure 11B), three cell lines were categorized as JQ1 sensitive (SH-EP, SK-N-AS, HD-N-33) and three cell lines as JQ1 resistant (GIMEN, SJNB1, SK-N-FI). Four cell lines belonged to the JQ1 intermediate response group (CHLA-90, NB69, SH-SY5Y), including the *MYCN* expressing NBL-S cell line. For LAN-6 the used algorithm failed to calculate the values due to variation in the data. SJNB1 and SK-N-FI were categorized as very resistant cell lines with no effect on viability measured at all. Due to the absence of viability reduction no EC50 values could be calculated for these cell lines.

Neither for *MYCN* amplified nor for *MYCN* non-amplified cell lines the genetic background could help to identify additional criteria how the neuroblastoma cell lines would react on JQ1 treatment. A separate analysis for *TP53* mutant and *TP53* wild type did not reveal differences in viability of both groups (data not shown). Additionally, JQ1 sensitivity was compared to the doubling time of the cell lines to exclude a low doubling time as a rescue factor for the resistant

cell lines. Although the cell lines with very fast doubling times of 24h and less showed high sensitivity in the viability screen, the doubling time does not strictly correlate with JQ1 sensitivity.

Comparing the results for *MYCN* amplified and *MYCN* non-amplified cell lines, it was noticeable that the *MYCN* amplified cell lines belonged either to the JQ1 resistant or the JQ1 sensitive group, nearly no *MYCN* amplified cell lines were categorized as intermediate responding. The *MYCN* non-amplified cell lines on the contrary were quite equally distributed over all three categories of JQ1 sensitivity.

Based on the results of the viability screen, it was decided to work with 0.5 µM JQ1 as standard working concentration for further experiments.

A

Cell line	EC50 [µM]	*MYCN* status
IMR32	0,03	amp
TR14	0,05	amp
IMR5/75	0,06	amp
NMB	0,06	amp
LS	0,07	amp
SK-N-BE(2)c	0,08	amp
SK-N-BE(2)	0,38	amp
KELLY	0,54	amp
LAN-5	0,66	amp
SMSKCNR	0,80	amp
NGP	1,18	amp
LAN-1	#NV	amp

B

Cell line	EC50 [µM]	*MYCN* status
SH-EP	0,07	non amp.
SK-N-AS	0,07	non amp.
HD-N-33	0,09	non amp.
CHLA-90	0,11	non amp.
NB69	0,13	non amp.
SH-SY5Y	0,20	non amp.
NBL-S	0,29	translocated
GIMEN	0,57	non amp.
SJNB1	res.	non amp.
SK-N-FI	res.	non amp.
LAN-6	#NV	non amp.

Figure 11: EC50 values of JQ1-treated neuroblastoma cell lines. The cells were treated with seven different JQ1 concentrations from 0.05-5 µM plus DMSO only control for 72h. Viability was measured using alamar blue reagent. Cells are categorized based on the EC50 values as JQ1 sensitive (EC50<0.1 µM), JQ1 intermediate response (EC50=0.1-0.5 µM) or JQ1 resistant (EC50>0.5 µM). A) EC50 values of *MYCN* amplified cell lines. B) EC50 values of *MYCN* non-amplified cell lines. NBL-S is non-amplified but expressing *MYCN* because of a translocation. Res= cells resistant, no effects detectable. #NV= algorithm not able to calculate EC50 values.

As a comparison, a second viability screen was performed with a second BRD4 inhibitor named BAY1238097. For this experiment, 10 neuroblastoma cell lines were chosen from the cell line panel tested with JQ1. Among the chosen neuroblastoma cell lines were *MYCN* amplified and non-amplified as well as JQ1 sensitive and JQ1 resistant cell lines.

The BRD4 inhibitor BAY1238097 had similar effects on the neuroblastoma cell lines as JQ1. Cell lines categorized as JQ1 sensitive also showed high sensitivity when treated with BAY1238097 and JQ1 resistant cell lines were also resistant to BAY1238097 (Figure 12A). For all tested cell lines, the EC50 values for BAY1238097 were higher than the EC50 values

achieved with JQ1. The dose response curves of JQ1 and BAY1238097 clearly show this difference in an exemplarily chosen cell line sensitive to BRD4 inhibition (Figure 12B). In the resistant SK-N-FI cell line, no reduction in viability was detectable, neither with JQ1 nor with BAY1238097 (Figure 12C). Altogether, neuroblastoma cell lines are more sensitive to JQ1 than to BAY1238097 treatment.

A

Cell line	EC50 JQ1 [µM]	EC50 BAY [µM]	*MYCN* status
IMR32	0,03	0,22	amp
IMR5/75	0,06	0,22	amp
SH-EP	0,07	0,20	non amp.
LS	0,07	0,47	amp
SH-SY5Y	0,20	0,46	non amp.
NBL-S	0,29	1,18	translocated
KELLY	0,54	2,41	amp
GIMEN	0,57	1,02	non amp.
NGP	1,18	3,83	amp
SK-N-FI	res.	res.	non amp.

B

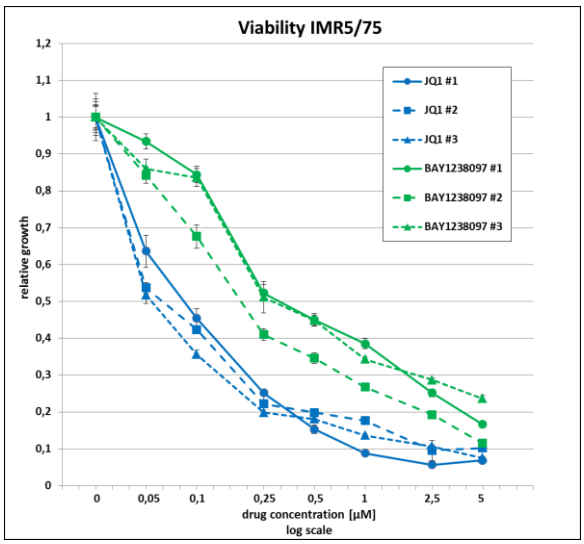

C

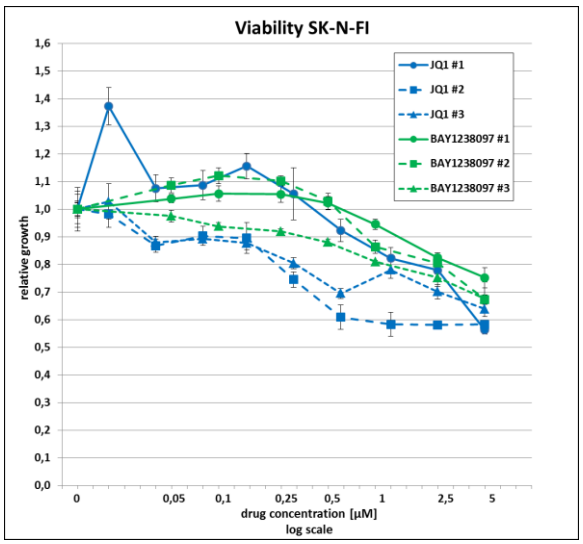

Figure 12: Comparison of BAY1238097 and JQ1-treated neuroblastoma cell lines. The cells were treated with 7 different concentrations of JQ1 or BAY1238097 ranging from 0.05-5 µM plus DMSO only control for 72h. A) Overview of EC50 values of all cell lines tested with both components. B) Dose response curves of IMR5/75 cells sensitive to BRD4 inhibition. JQ1 treatment shown in blue, BAY1238097 treatment shown in green. C) Dose response curves of SK-N-FI cells resistant to BRD4 inhibition.

Neuroblastoma cells treated with the working concentration of 0.5 µM JQ1 were also examined morphologically. First changes in morphology could be detected after 24h of JQ1 treatment with effects being most clearly at time point 48h.

The different neuroblastoma cell lines showed a broad panel of morphological changes when treated with JQ1. Four examples are shown in Figure 13. The JQ1 sensitive IMR5/75 cells rounded up and completely detached from the cell culture plate. In contrast, JQ1-sensitive LS

cells showed only marginal morphological changes and a slight increase of floating cells. The JQ1 resistant NGP cells detached and formed large, floating clusters. *MYCN* non-amplified and JQ1 sensitive SH-EP cells stayed adherent but changed their morphology becoming longer and thinner. The morphologic effects on neuroblastoma cells treated with BAY1238097 were similar to effects on JQ1-treated cells from the same cell line.

In summary, the morphological changes upon JQ1 treatment occured within 24h and were most prominent after 48h. No correlation was found between pattern of morphological changes and sensitivity to JQ1.

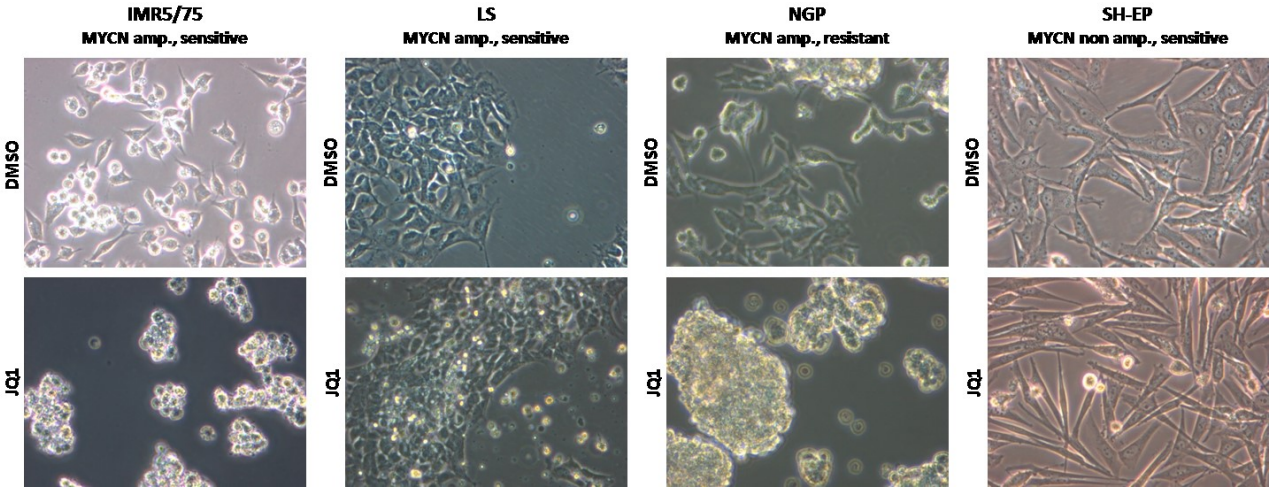

Figure 13: Morphology of JQ1-treated cells. Pictures were taken after 48h treatment with JQ1 or DMSO using an objective lens with 20x magnification.

5.2.2 JQ1 treatment induces changes in cell cycle distribution

The cell cycle distribution of different neuroblastoma cells was analyzed by flow cytometry for up to 72h of JQ1 treatment to identify and characterize a potential growth arrest.

The panel of cell lines used for cell cycle analysis consisted of ten different neuroblastoma cell lines. It contained JQ1 sensitive, intermediate responding and resistant cell lines as well as both *MYCN* amplified and *MYCN* non-amplified neuroblastoma cell lines. The effects on cell cycle distribution were most prominent at the 24h time point and are shown exemplarily in Figure 14A.

Upon JQ1 treatment, a prominent G1 arrest with a statistically significant increase of the G1 fraction was observed for all seven sensitive and intermediate responding cell lines, both in the *MYCN* amplified and *MYCN* non-amplified ones ($p<0.001$). The S-phase fraction was decreased in all JQ1 sensitive and intermediate responding cell lines. For example, the G1 fraction in JQ1 sensitive IMR5/75 cells increased from 35.98% in DMSO control-treated to 63.27% in JQ1-treated cells, whereas the S-phase fraction decreased from 46.35% to 28.26%.

For the G2 fraction, there was no consistent pattern detectable in JQ1 sensitive and intermediate responding cell lines. A decrease was detected in 3 out of 7 JQ1 sensitive and intermediate responding cell lines upon JQ1 treatment. In three cell lines there was no difference of G2 between JQ1-treated and DMSO control cells and in one JQ1 sensitive cell line the G2 fraction increased significantly.

In the three tested JQ1 resistant neuroblastoma cell lines, only marginal changes in cell cycle distribution were measureable, irrespective of their *MYCN* status.

For 12h and 48h JQ1 treatment, the cell cycle distribution measured for the individual cell lines was similar to the effects detected for 24h upon JQ1 (Figure 14B, IMR5/75 cell line exemplarily shown). At the 12h time point, the effects in cell cycle distribution were not yet established to full extent. The differences between JQ1 and DMSO control-treated cells were only statistically significant for the JQ1 most sensitive cell lines IMR5/75, IMR32 and SH-EP, although the tendency was seen in all tested cell lines as for 24h treatment. After 48h JQ1 treatment the results also resembled the cell cycle distribution measured after 24h JQ1, but with a significantly higher sub-G1 fraction of dead cells (sub-G1 data not shown). After 72h treatment with JQ1, the fraction of sub-G1 cells further increased and the differences between JQ1 and DMSO control-treated cells were less clearly, especially in the G1-fraction. Possibly, the cells arrested in the G1-phase after 24h JQ1 treatment partially underwent cell death after 48 or 72h.

In summary, analysis of cell cycle distribution revealed a significant increase of the G1 fraction and a decreased S-phase fraction in JQ1 sensitive and intermediate responding cell lines. In JQ1 resistant cell lines, no difference in cell cycle distribution was detected. This is true both for *MYCN* amplified and *MYCN* non-amplified neuroblastoma cell lines.

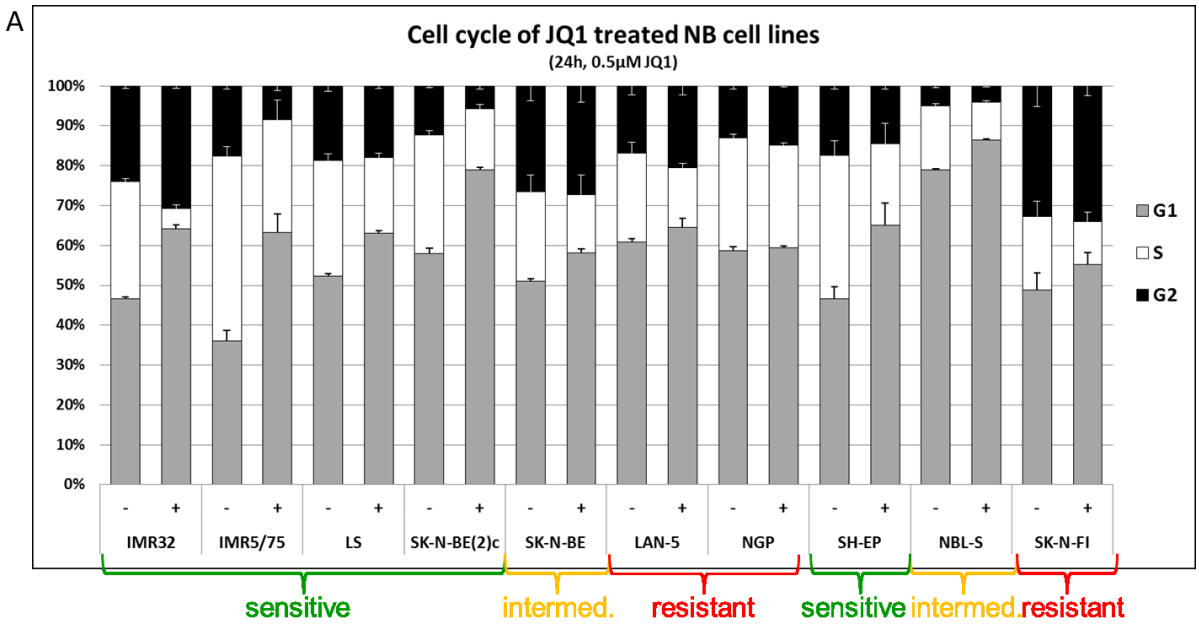

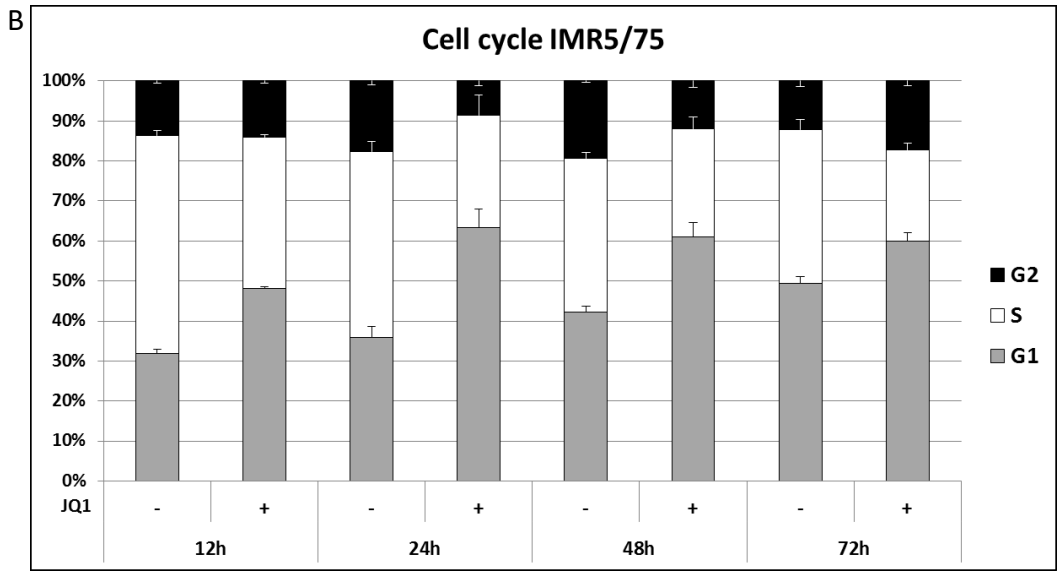

Figure 14: Cell cycle analysis of JQ1-treated cells. Neuroblastoma cells were treated with 0.5 µM JQ1 for 12, 24, 48 or 72h. Harvested cells were fixed with citric acid, stained with phospho-DAPI and analyzed by flow cytometry. Biological and technical triplicates were analyzed. Significance was tested with student t-test. A) Cell cycle analysis after 24h JQ1 treatment. Green=JQ1 sensitive cell lines. Yellow= JQ1 intermediate responding cell lines. Red= JQ1 resistant cell lines. Left panel= *MYCN* amplified NB cell lines. Right panel= *MYCN* non-amplified NB cell lines. B) Cell cycle analysis of IMR5/75 cells over a period of 72h.

5.2.3 Cell death is increased in selected JQ1-treated neuroblastoma cell lines

To determine if the neuroblastoma cells treated with JQ1 are growth arrested or undergo cell death, cell death was analyzed by flow cytometry. For cell death analysis ten different neuroblastoma cell lines were tested, seven of them were *MYCN* amplified and three belonged to the *MYCN* non-amplified group. The cell line panel consisted of JQ1 sensitive, intermediate responding and resistant cell lines.

At the time points 12h and 24h nearly no differences in cell death rates were detectable comparing JQ1 and DMSO control-treated samples (Figure 15A). After 48h treatment, an increase of cell death was measureable in both JQ1 sensitive and *MYCN* amplified neuroblastoma cell lines IMR5/75, IMR32 and SK-N-BE(2)c. Cell death further increased upon 72h JQ1 treatment in IMR5/75 from factor 2.43 after 48h to factor 3.84 after 72h and in IMR32 from factor 1.75 (48h) to 2.43 (72h). The elevated levels of cell death were statistically significant for these two cell lines ($p<0.001$). In contrast, the sub-G1 fraction decreased in SK-N-BE(2)c after 72h. The *MYCN* amplified, intermediate responding cell line SK-N-BE showed a slight increase in cell death. Among the JQ1 resistant *MYCN* amplified cell lines, marginally elevated levels of cell death were observed in NGP cells, whereas no induction of cell death was seen in LAN-5 cells over 72h JQ1 treatment.

In contrast to the *MYCN* amplified JQ1 sensitive cell lines IMR5/75 and IMR32, the *MYCN* non-amplified and JQ1 sensitive SH-EP cells did not show an increase in cell death over a period of 72h JQ1 treatment (Figure 15A). In the other two *MYCN* non-amplified cell lines, belonging to the JQ1 intermediate responding and resistant groups, no increase of cell death was detected as well.

In Figure 15B, cell death measured in the JQ1 sensitive cell lines IMR5/75 and LS, as well as in the JQ1 resistant cell line NGP is shown for JQ1 and DMSO control treatment. The Figure reveals that the total levels of cell death in the DMSO-treated controls were varying between the cell lines. In LS, the total levels of cell death were low both in the DMSO and in the JQ1-treated samples, with a sub-G1 fraction of less than 10%. In contrast, cell death in control-treated IMR5/75 cells was ranging from 11% to 20%. In JQ1 resistant NGP cells no effect of JQ1 treatment on the sub-G1 fraction was detectable before 48h.

Altogether, in *MYCN* amplified cell lines an increase of cell death can be detected in 4 out of 7 neuroblastoma cell lines. The JQ1 sensitivity of the cell lines does not correlate with the proportion of cell death. The elevated levels of cell death upcoming at later time points are consistent with the results from cell cycle analysis, where larger sub-G1 fractions were detected after 48h and 72h JQ1 treatment. In *MYCN* non-amplified neuroblastoma cell lines, elevated levels of cell death were not observed.

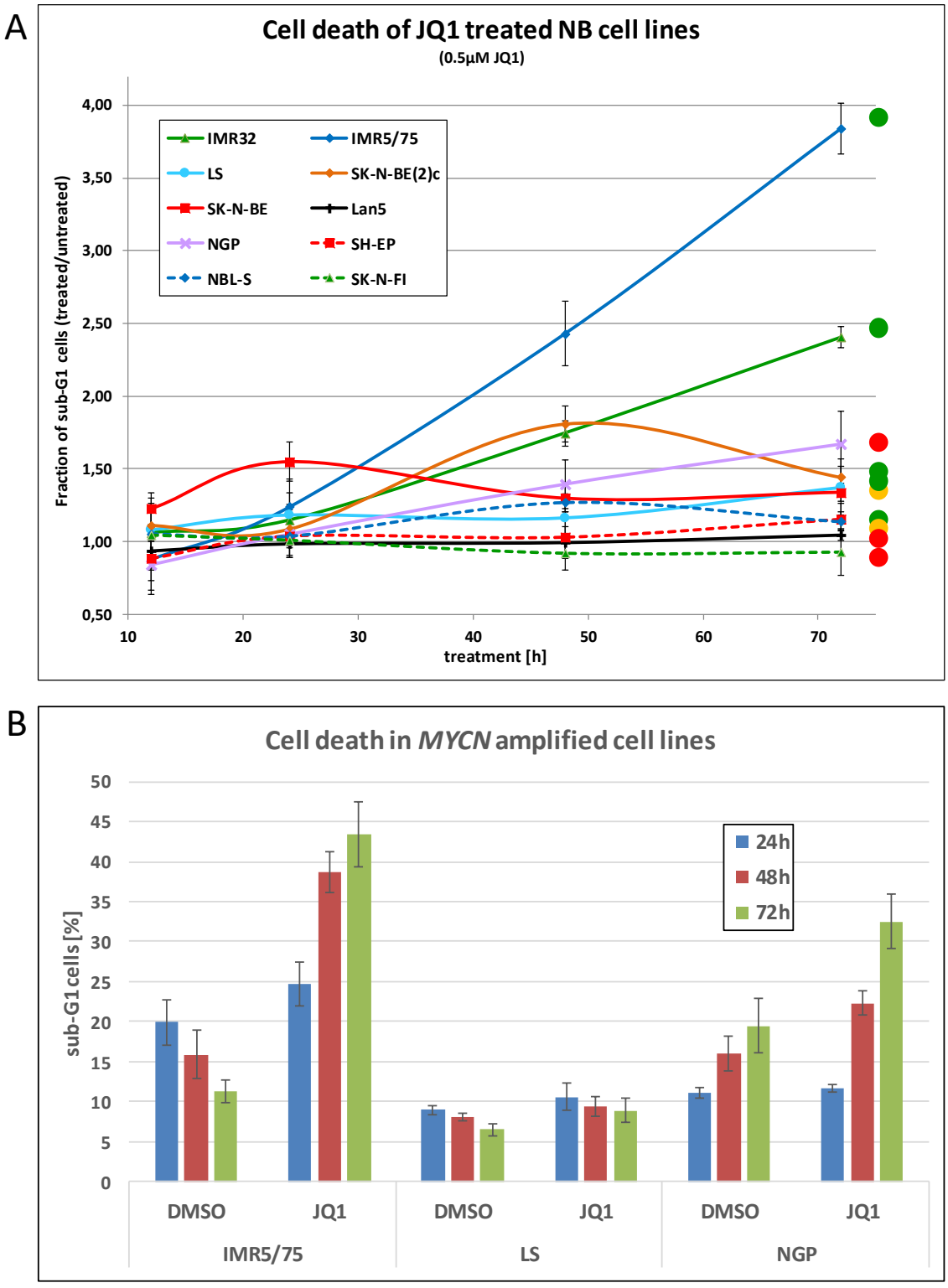

Figure 15: Cell death analysis of JQ1-treated cells. Neuroblastoma cells were treated with 0.5 µM JQ1 or DMSO only control for 12, 24, 48 or 72h. The cells were resuspended in PBS, stained with propidium-iodide and analyzed by flow cytometry. Biological and technical triplicates were analyzed. Significance was tested with student t-test. A) Relative fraction of dead cells, calculated JQ1/DMSO-treated. Green dots = JQ1 sensitive cell lines. Yellow dots = JQ1 intermediate responding cell lines. Red dots = JQ1 resistant cell lines. Interrupted lines = *MYCN* non-amplified cell lines. B) Cell death analysis of 3 MYCN amplified cell lines.

5.2.4 Neuroblastoma cells show regrowth after JQ1 washout

Taken together the results from viability, cell cycle analysis and cell death measurement, it remained unclear which proportion of neuroblastoma cells undergoes permanent damage resulting in cell death and if JQ1-treated cells are able to regrow after removing the inhibitor. As IMR5/75 cells belonged to the most sensitive cell lines in the viability screen and showed the highest proportion of cell death upon JQ1 treatment, this cell line was analyzed in the regrowth experiment. Additionally, to examine the influence of *MYCN* expression on the ability of JQ1-treated cells to regrow after treatment, the *MYCN* high/low system of this cell line was included as an additional parameter (described in section 5.1). *MYCN* low cells were treated with tetracycline throughout the whole experiment to achieve a knockdown of *MYCN*. The experimental outline of the experiment is shown in Figure 16.

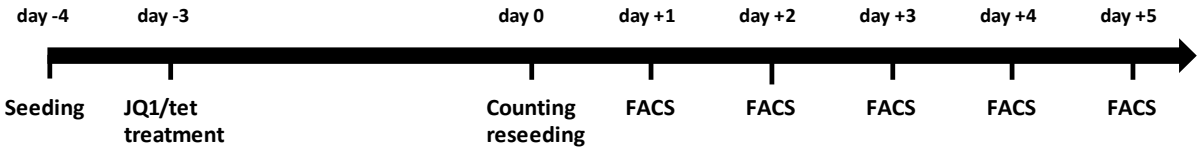

Figure 16: Experimental outline of regrowth experiment. Cells were seeded at day -4 and treated with 0.5 µM JQ1 or DMSO and tetracycline or 70% ethanol at day -3. At day 0, cells were counted and $5x10^4$ cells were reseeded. Daily measurement of live and dead cell fraction using PI staining followed for five days. Per time point and condition technical triplicates were performed.

Up to 48h after washout of JQ1 or DMSO, nearly no difference in growth was observed comparing JQ1- or DMSO-treated and *MYCN* high and *MYCN* low conditions (Figure 17). The *MYCN* high cells treated with DMSO started to regrow at day three after washout, nearly achieving 100% confluence after five days. In the MYCN high, JQ1-treated cells regrowth started approximately 24h later than in the DMSO-treated control cells. Additionally to the belayed regrowth, the cell proliferation rate was lower in the JQ1-treated *MYCN* high cells compared to DMSO control.

In contrast, the *MYCN* low cells pretreated with JQ1 or DMSO were both regrowing very slowly. A small increase in the number of viable cells was not seen before day four after washout in both JQ1 and DMSO-treated cells.

The results of the JQ1 regrowth experiment resemble observations with doxorubicin-treated neuroblastoma cells. Ryl et al. found that *MYCN* low cells undergo permanent senescence after treatment, whereas *MYCN* high cells treated shortly after cell division are capable of clonal regrowth [145]. Supposedly, like the doxorubicin-treated cells, JQ1-treated *MYCN* high cells do not undergo a permanent cell cycle arrest or differentiation and JQ1 is not capable to inhibit neuroblastoma tumor cell growth far beyond the treatment time. As the effects of JQ1

treatment are not permanent in *MYCN* high cells, *MYCN* promotes cell proliferation shorly after removing the inhibitor.

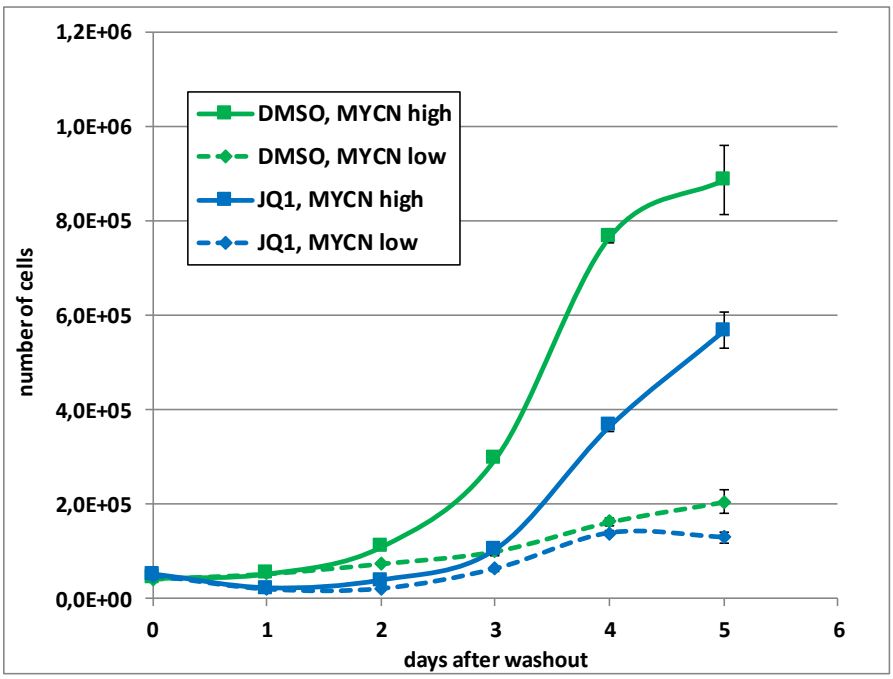

Figure 17: Regrowth of JQ1 pretreated cells. Total number of cells measured one to five days after JQ1 washout. IMR5/75 cells were used. *MYCN*-knockdown was achieved by induction of an *MYCN*-shRNA by adding tetracycline. Cells were stained with propidium-iodide and analyzed by flow cytometry. P-value was <0.01 at day 4 in *MYCN* high cells (student t-test).

5.2.5 Anchorage independent growth is absent in JQ1-treated cells

Anchorage independent growth is a malignant characteristic of many neuroblastoma tumor cells. To test if treatment with JQ1 can prevent neuroblastoma cells from forming anchorage independent colonies, neuroblastoma cells from eight different cell lines were seeded in soft agar accompanied by JQ1 treatment.

Colony formation was effectively inhibited by JQ1 treatment in all eight tested neuroblastoma cell lines (Figure 18A). In IMR32, IMR5/75, SK-N-BE(2)C, NGP and NBL-S, no colonies could be detected upon JQ1 treament compared to extensive colony growth in the DMSO control. In Figure 18B, soft agar assays with the JQ1 sensitive IMR5/75 and JQ1 resistant NGP cells are shown exemplarily. In the panel of cell lines used for soft agar assay, there is no difference detectable according to JQ1 sensitivity or *MYCN* amplification status. In LS, SK-N-BE(2) and NB69 sporadic colonies were assessed upon JQ1 treatment. Compared to the untreated control, the reduction of anchorage independent growth was highly significant ($p<0.001$).

Taken together, anchorage independent growth is highly significantly inhibited in all tested neuroblastoma cell lines, independent from JQ1 sensitivity or *MYCN* status.

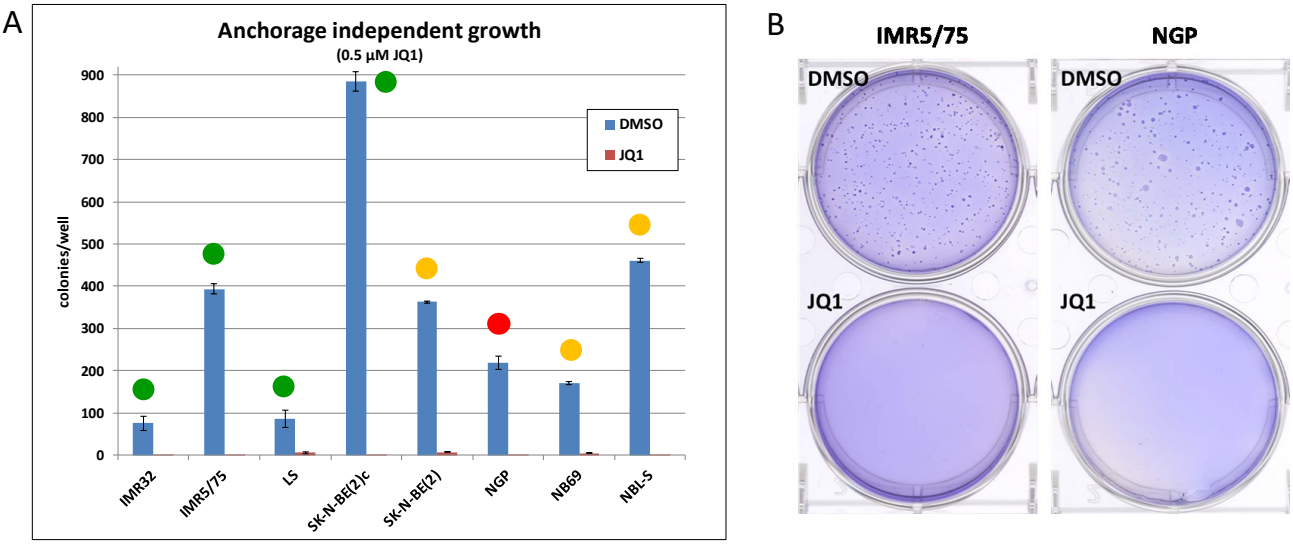

Figure 18: Anchorage independent growth of JQ1-treated cells. Cells were seeded in soft agar and treated with 0.5 µM JQ1 or DMSO in base agar, soft agar and cell culture medium. Cell culture medium was replaced weekly. Cells were cultured for 3-4 weeks. Colonies grown in soft agar were stained with crystal violet and counted automatically. Per cell line and condition, 6 wells were analyzed. Significance was tested with student t-test. A) Number of colonies counted for different NB cell lines treated with JQ1 or DMSO only control. Green dots = JQ1 sensitive cell lines. Yellow dots = JQ1 intermediate responding cell lines. Red dots = JQ1 resistant cell lines. Spotted dots = *MYCN* non-amplified cell lines. B) Exemplary pictures of soft agar from IMR5/75, JQ1 sensitive and NGP, JQ1 resistant cells.

5.2.6 Changes in MYCN expression are induced by JQ1 treatment in *MYCN* amplified neuroblastoma cell lines

In the previous sections it has been shown that different *MYCN* amplified and *MYCN* non-amplified neuroblastoma cell lines respond individually and irrespective of a comparable genetic background to JQ1 treatment. Aiming to illuminate the molecular reactions of the cells on JQ1 treatment and to verify that the *MYCN* expression is influenced by JQ1 treatment [121-123], MYCN protein levels were analyzed by western blot and RPPA in *MYCN* expressing neuroblastoma cell lines.

Protein quantification by western blot included the *MYCN* amplified cell lines IMR32, IMR5/75, LS, SK-N-BE(2)c, SK-N-BE(2) and NGP as well as the *MYCN* translocated cell line NBL-S (Figure 19). A strong MYCN downregulation was detected in the JQ1 sensitive neuroblastoma cell lines IMR32 and SK-N-BE(2)c ($p<0.05$ for SK-N-BE(2)c and $p<0.005$ for IMR32). In the JQ1 sensitive IMR5/75 cells the MYCN protein levels were slightly reduced as well as in LS and SK-N-BE(2) cells at the 24h time point. For LS, the quantification of the MYCN protein expression at the 48h time point showed a strong upregulation. Though, the MYCN detection

of the western blot from LS was weak and the bands were blurred, which in total hampered MYCN quantification for this cell line. In the JQ1 resistant cell line NGP the MYCN protein levels were upregulated at both time points. In the MYCN translocated cell line NBL-S the MYCN protein expression was not affected.

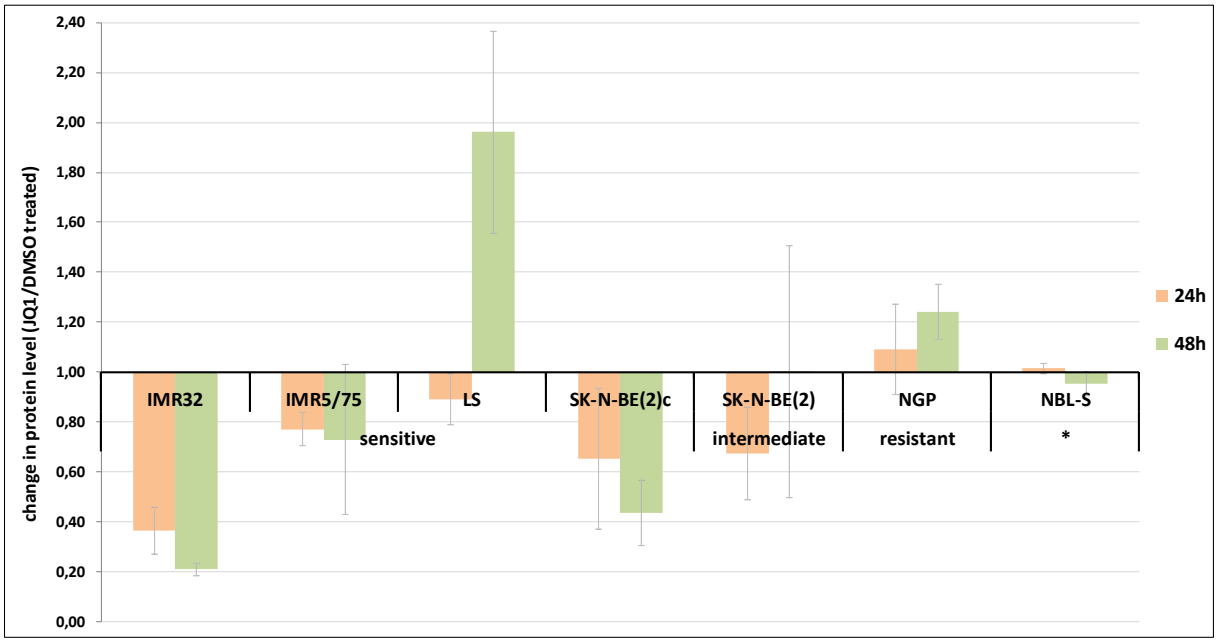

Figure 19: MYCN protein concentration analyzed by western blot. Neuroblastoma cells from six *MYCN* amplified and one *MYCN* translocated (*) cell lines were treated with 0.5 µM JQ1 or DMSO control for 24h or 48h. Three biological replicates were analyzed. The MYCN protein expression was detected by western blot. β-actin was used as loading control. The protein levels were quantified using ImageJ. Protein expression change was calculated JQ1-treated/DMSO-treated condition. The JQ1 sensitivity estimated by viability assays is noted. Significance was tested with student t-test.

By Reverse Phase Protein Array (RPPA) the protein expression of nine *MYCN* amplified and six *MYCN* non-amplified neuroblastoma cell lines were analyzed in a high throughput manner including the quantification of 50 different proteins.

Figure 20A shows the MYCN protein expression for the time points 12-48h, normalized to β-Actin protein levels. A reduction of MYCN protein levels was detected in 7 out of 9 *MYCN* amplified neuroblastoma cell lines. The most effective MYCN downregulation was measured in the JQ1 sensitive cell lines IMR32 and SK-N-BE(2)c as well as in the JQ1 resistant cell line LAN-5. For IMR5/75 no effect on the MYCN protein expression was detected by RPPA. LS cells showed a slight decrease of MYCN protein levels, which is contrary to the observations of the western blot. In KELLY, belonging to the JQ1 resistant cell lines, the MYCN protein expression was reduced at all three time points, whereas solely in the resistant NGP cells the MYCN protein levels were elevated.

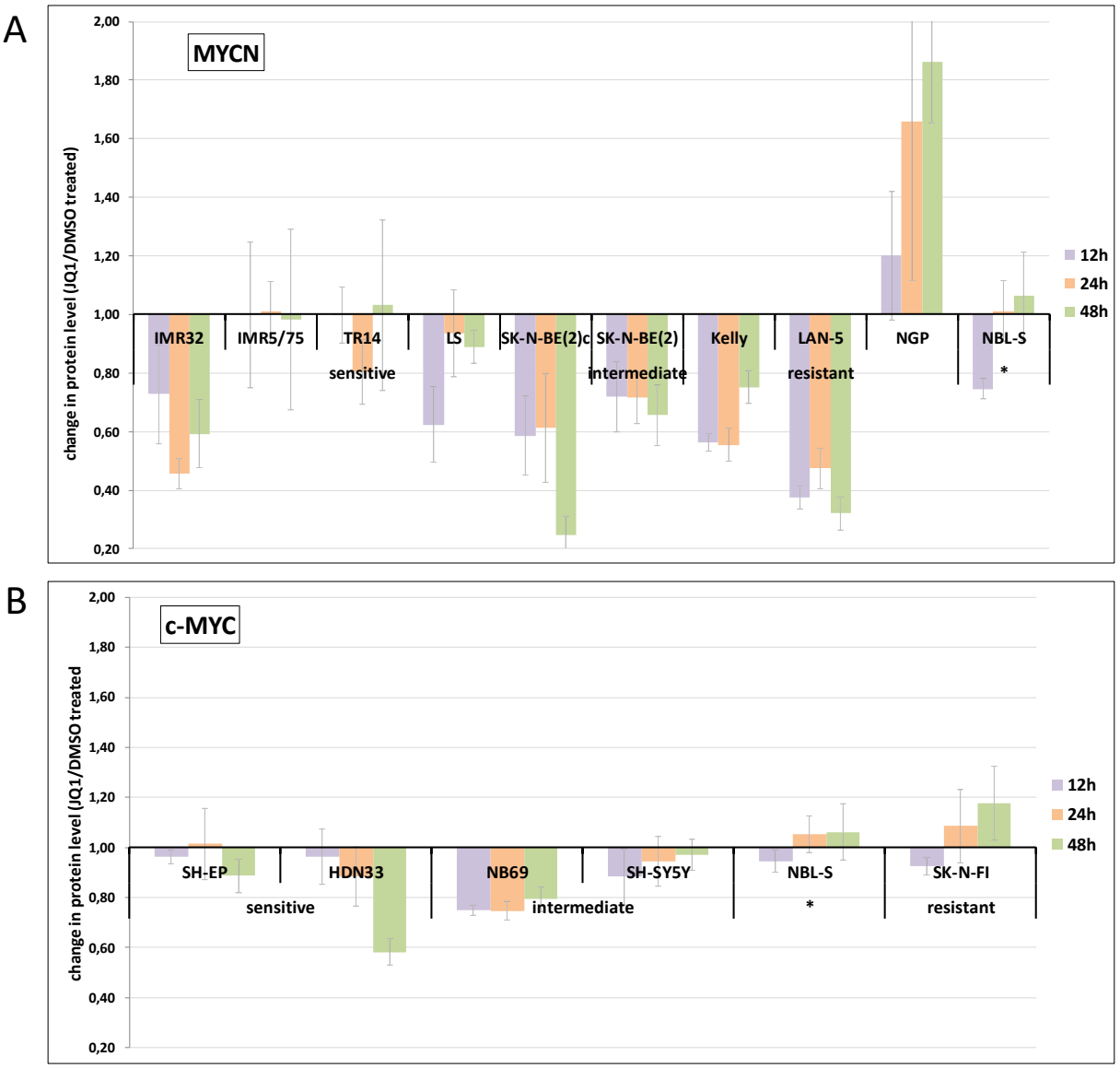

Figure 20: MYCN and c-MYC protein concentration analyzed by RPPA. Neuroblastoma cells were treated with 0.5 µM JQ1 or DMSO for 12h, 24h or 48h. The protein expression was analyzed by RPPA and normalized against β-actin. Changes in protein expression were calculated JQ1-treated/DMSO-treated condition. Per time point, 3 biological replicates were analyzed. The categories observed in the viability assays are given. The *MYCN* translocated cell line NBL-S is marked (*). P-value was >0.05 for the majority of cell lines and time points (student t-test). A) Mean MYCN protein concentration of 9 *MYCN* amplified neuroblastoma cell lines and *MYCN* overexpressing NBL-S cell line. B) Mean c-MYC protein concentration of 6 *MYCN* non-amplified neuroblastoma cell lines.

Altogether, western blot and RPPA delivered comparable results regarding MYCN protein expression after JQ1 treatment. With both methods, the strongest MYCN downregulation was observed in the JQ1 sensitive IMR32 and SK-N-BE(2)c cell lines, whereas in resistant NGP both methods revealed a strong upregulation of MYCN protein expression. Differences were mainly detected for IMR5/75, where no effects on MYCN protein expression have been

detected in RPPA in contrast to a slight reduction of MYCN protein levels observed with western blot. These relatively small differences can be explained by cell culture effects.

The analysis of MYCN protein levels revealed that the reduction of MYCN is not correlating with the sensitivity of the cell lines towards JQ1 treatment. Among the group of JQ1 sensitive cell lines, IMR5/75 and TR14 showed no or slight differences in MYCN protein expression. In contrast, the JQ1 resistant neuroblastoma cell lines KELLY and LAN-5 responded with a strong MYCN downregulation on protein level upon JQ1 treatment. Hence, the third JQ1 resistant *MYCN* amplified cell line NGP showed a strong MYCN upregulation.

In the *MYCN* non-amplified neuroblastoma cells included in the panel of cell lines for RPPA analysis, c-MYC protein expression was analyzed instead of MYCN (Figure 20B). A reduction of c-MYC protein levels was observed in NB69 and at the 48h time point of HD-N-33. In SH-EP cells highly sensitive towards JQ1 treatment the c-MYC protein expression was not affected. As expected, the effects on c-MYC protein expression were marginal compared to the effects on MYCN protein levels in the *MYCN* amplified cell lines. Summarizing the results from western blot and RPPA, about 70% of the *MYCN* amplified neuroblastoma cell lines showed a reduction of MYCN protein expression upon JQ1 treatment. This does not correlate with the sensitivity of the individual cell lines determined by viability assays. The c-MYC protein expression was marginally affected by JQ1 treatment.

5.2.7 Cell cycle related proteins are affected by JQ1 treatment

The analysis of MYCN protein expression in neuroblastoma cells revealed that MYCN protein levels are repressed in most, but not all *MYCN* amplified cell lines and that downregulation of MYCN does not strictly correlate with JQ1 sensitivity. To identify other possible targets of BET proteins affected by JQ1 treatment, further proteins were analyzed by RPPA and western blot.

Out of 54 proteins analyzed by RPPA, using more than 70 different antibodies, 21 proteins (39%) were up- or downregulated in the *MYCN* amplified cell lines and 16 proteins (30%) showed changes in protein expression in *MYCN* non-amplified neuroblastoma cell lines. The analysis of the RPPA results focused on the late time points (12-48h) as the strongest effects were detected after at least 12h JQ1 treatment, whereas 3-6h treatment with JQ1 did not result in deviant protein expression. The proteins that were found to have the most interesting expression patterns upon JQ1 treatment will be described in the following section.

a) Cyclin D1 and CDK4

The analysis of cell cycle distribution of JQ1-treated neuroblastoma cells showed an assembly in the G1 phase of the cell cycle, at least regarding the cell lines belonging to the sensitive and intermediate responding groups. This suggests that the G1/S transition of the cell cycle is influenced by JQ1. CDK4 and its corresponding binding partner Cyclin D1 are important for cell cycle progression into the S-phase. Especially Cyclin D1 is likely to be regulated by BRD4 because its expression is regulated by a large Super-Enhancer region known to involve BRD4 binding [146].

Antibodies for both CDK4 and Cyclin D1 were included in the RPPA antibody panel. The data for the *MYCN* amplified cell lines are presented in Figure 21. The CDK4 and Cyclin D1 levels of the *MYCN* non-amplified cell lines are not shown.

In the RPPA analysis the Cyclin D1 protein expression was downregulated in all *MYCN* amplified samples at the 12h time point (Figure 21A). After 24h and 48h of JQ1 treatment, a decrease in Cyclin D1 protein levels was observed in most of the cell lines, at least for one of the two time points. In the JQ1 sensitive cell lines, Cyclin D1 downregulation was more prominent. The strongest decrease was detected in SK-N-BE(2)c cells. Among the *MYCN* non-amplified cell lines analyzed by RPPA, Cyclin D1 upregulation was detected in one of the JQ1 sensitive cell lines, whereas the other five *MYCN* non-amplified cell lines were not affected (data not shown).

Downregulation of Cyclin D1 protein levels was validated by western blot, showing lower Cyclin D1 protein expression in 5 out of 6 *MYCN* amplified neuroblastoma cell lines and at the 24h time point of the *MYCN* translocated cell line NBL-S (Figure 22). In contrast to the results from the RPPA analysis, JQ1-treated LS cells analyzed by western blot did not show a downregulation, but instead presented with a slight increase of Cyclin D1 protein levels. Though, this increase is not significant and not consistent in all three biological replicates of the western blot.

CDK4 is less dependent on periodic expression than Cyclin D1 [147]. A lower CDK4 protein expression was observed by RPPA in most JQ1 sensitive *MYCN* amplified and *MYCN* non-amplified neuroblastoma cell lines (Figure 21B). The JQ1 resistant cell lines either showed equal levels of CDK4 or an upregulation. These results were comparable with the findings in western blots.

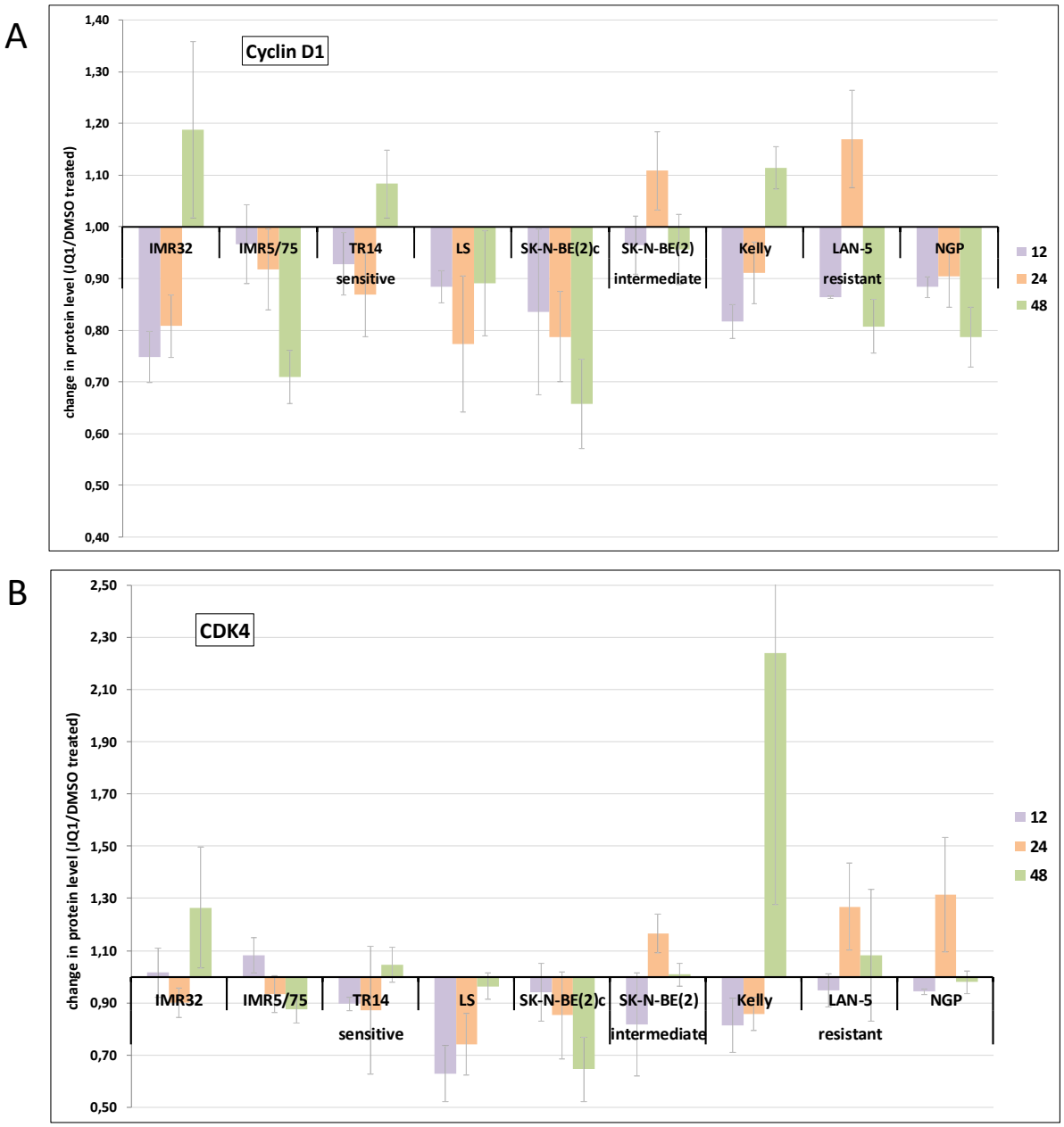

Figure 21: Protein concentration of Cyclin D1 and CDK4 analyzed by RPPA. *MYCN* amplified neuroblastoma cells were treated with 0.5 µM JQ1 or DMSO for 12h, 24h or 48h. The protein expression was analyzed by RPPA and normalized with β-actin protein levels. Changes in protein expression were calculated JQ1-treated/DMSO-treated condition. The categories observed in the viability assays are given. A) Cyclin D1 protein concentration of nine *MYCN* amplified neuroblastoma cell lines. P-value was >0.05 for the majority of cell lines and time points (student t-test). B) CDK4 protein concentration of nine *MYCN* amplified neuroblastoma cell lines. P-value was >0.05 (student t-test).

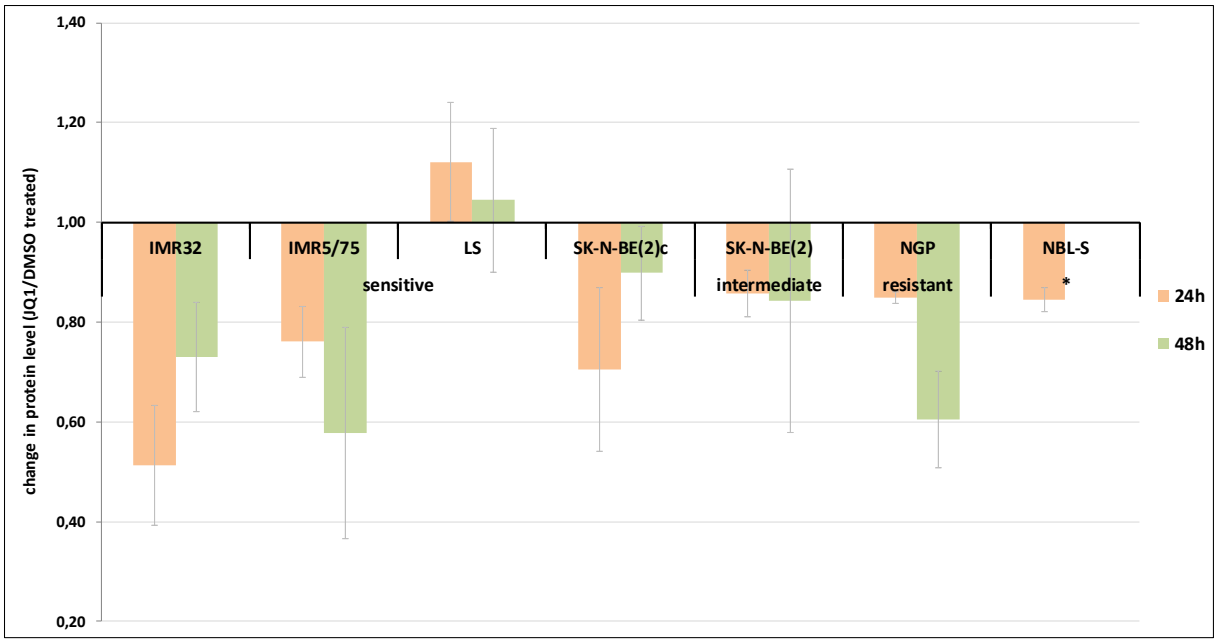

Figure 22: Cyclin D1 protein concentration analyzed by western blot. Neuroblastoma cells from six *MYCN* amplified and one *MYCN* translocated (*) cell lines were treated with 0.5 µM JQ1 or DMSO control for 24 or 48h. MYCN protein expression was detected by western blot. β-actin was used as loading control. The protein levels were quantified using ImageJ. The change in protein expression was calculated JQ1-treated/DMSO-treated condition. P-value was <0.05 for IMR32 (student t-test). The categories observed in the viability assay are noted. For NBL-S 48h no quantification is available.

b) E2F-1

E2F-1 belongs to the main cell cycle promoting genes inducing the transcription of a number of genes required for the S-phase of the cell cycle. Therefore E2F-1 was in the focus of the protein analysis of JQ1-treated neuroblastoma cells. Due to an insufficient E2F-1 antibody quality in the RPPA application, results for the E2F-1 protein expression are only available from western blot for six *MYCN* amplified neuroblastoma cell lines (data not shown). Lower E2F-1 protein levels were detected for the JQ1 sensitive cell lines IMR32, LS and SK-N-BE(2)c as well as for the JQ1 resistant cell line NGP. No differences were detected for IMR5/75 and SK-N-BE. The downregulation of the E2F-1 protein expression fits with the cell cycle arrest in JQ1 sensitive cell lines and a lower Cyclin D1/CDK4 activity estimated by RPPA.

c) p53 and MDM2

Another central protein at the G1/S transition is p53, responsible for cell cycle arrest or the induction of proapoptotic pathways. The RPPA analysis showed a downregulation of p53 protein levels in all JQ1 sensitive *MYCN* amplified cell lines (Figure 23). The cell lines from the intermediate responding and resistant categories showed varying responses of p53 protein expression. Among the panel of *MYCN* amplified cell lines analyzed by RPPA, three cell lines harbored known inactivating mutations in the *TP53* gene. These are SK-N-BE(2)c, SK-N-BE(2)

and KELLY. The informative value of the p53 protein expression is limited for these cell lines. The decrease of p53 protein expression in JQ1 sensitive cell lines was confirmed by western blot analysis, although interpretation of the results was impeded by technical difficulty, especially for IMR5/75 and LS (data not shown).

The protein levels of the ubiquitin ligase and p53 regulator MDM2 were estimated by RPPA using antibodies both for MDM2 in its phosphorylated and unphosphorylated form. MDM2 regulates the activity of p53 in a negative feedback loop [148], limiting growth arrest and impeding cell death in undamaged cells. In RPPA, MDM2 reflected the behavior of the p53 protein upon JQ1 treatment. The MDM2 protein expression was not validated by western blot.

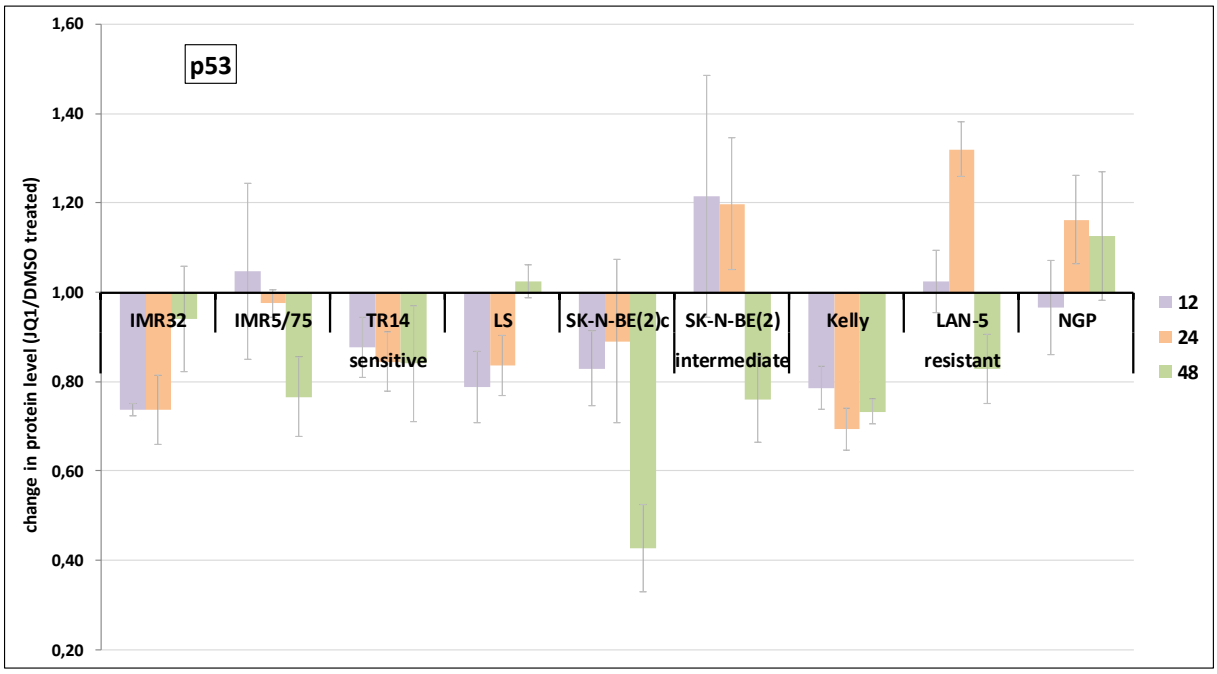

Figure 23: p53 protein concentration analyzed by RPPA. Cells from nine *MYCN* amplified neuroblastoma cell lines were treated with 0.5 µM JQ1 or DMSO for 12h, 24h or 48h. The p53 protein expression was analyzed by RPPA and normalized with β-actin protein levels. Changes in protein expression were calculated JQ1-treated/ DMSO-treated condition. P-value was >0.05 for the majority of cell lines and time points (student t-test). The categories observed in the viability assays are given.

d) GSK3-β

The glycogen synthase kinase 3 β (GSK3-β) regulates the synthesis of glycogen by phosphorylation of the glycogensynthase and is part of a number of signaling pathways, for example Wnt, Shh or PI3K/AKT [149, 150]. Besides, GSK3-β plays an important role in the turnover of Myc proteins [151]. GSK3-β and phospho-GSK3-β have been included in the antibody panel for RPPA.

Among the *MYCN* amplified neuroblastoma cell lines, elevated protein levels of GSK3-β were detected in 7 out of 9 cell lines after 24h and in 8 out of 9 cell lines after 48h JQ1 treatment

(Figure 24). Upregulation of GSK3-β was not correlated with sensitivity to JQ1. In the group of *MYCN* non-amplified cell lines, 4 out of 5 neuroblastoma cell lines showed increased GSK3-β protein levels. For the *MYCN* translocated cell line NBL-S similar GSK3-β protein expression levels were detected in JQ1-treated and control cells.

Phosphorylation of GSK3-β at Serine 9 leads to inactivation of GSK3-β [152]. Phospho-GSK3-β was not affected by JQ1 treatment of *MYCN* expressing cells. Among the *MYCN* non-amplified cell lines, lower levels of phospho-GSK3-β were detected after 48h treatment with JQ1. The effects on GSK3-β protein expression may be related to its role in MYC protein turnover [50], further discussed in section 6.2.

Taken together, the analysis of more than 50 different proteins by RPPA revealed an influence of JQ1 treatment on 39% of the tested proteins in *MYCN* amplified and on 30% in *MYCN* non-amplified cell lines. The proteins affected by JQ1 treatment included regulatory proteins of the cell cycle, such as Cyclin D1, p53 and E2F-1 or GSK3-β, the last being involved in MYC turnover. The results from RPPA were confimed by western blot.

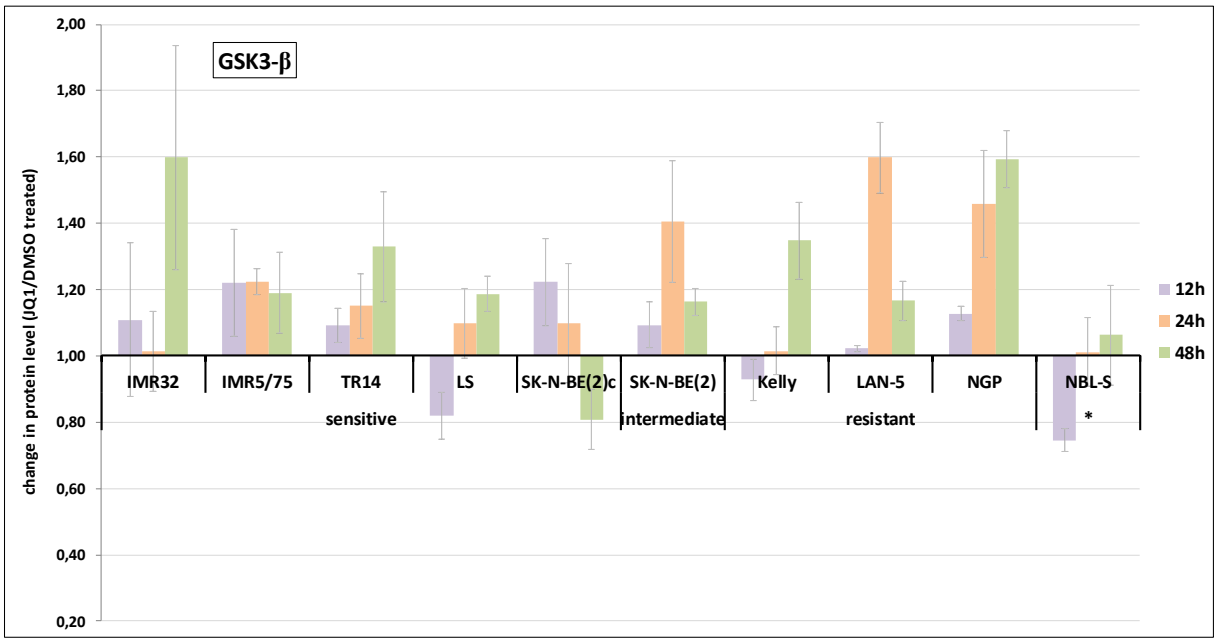

Figure 24: GSK3-β protein concentration analyzed by RPPA. Cells from nine *MYCN* amplified neuroblastoma cell lines were treated with 0.5 µM JQ1 or DMSO for 12h, 24h or 48h. The GSK3-β protein expression was analyzed by RPPA and normalized with β-actin protein levels. Changes in protein expression were calculated JQ1-treated/ DMSO-treated condition. P-value was <0.05 in NGP cells at 12h and 48h time points (student t-test). The categories observed in the viability assays are given.

5.2.8 *MYCN* is not a target of BRD4 in neuroblastoma

The analysis of the MYCN protein concentration revealed that MYCN is downregulated in most but not all *MYCN* amplified neuroblastoma cell lines treated with JQ1. Especially in the JQ1 sensitive cell lines IMR5/75 and TR14 as well as in the JQ1 resistant cell line NGP the effects of JQ1 treatment on the MYCN protein expression were marginal. To investigate if *MYCN* is directly regulated by BRD4 in neuroblastoma, IMR5/75 cells were transfected with siRNA against the BET proteins BRD2, BRD3 or BRD4 in separate experiments (Table 10).

Table 10: Overview of experiments with BET siRNA in IMR5/75 cells.

<table>
<tr><th></th><th>not transf.</th><th>neg. Ctrl. siRNA</th><th>siRNA 1 BET</th><th>siRNA 2 BET</th><th>shRNA MYCN</th><th>JQ1</th></tr>
<tr><td>Exp. 1: BRD4 knockdown</td><td rowspan="3">untreated cells</td><td rowspan="3">transfected with unspecific siRNA</td><td>siRNA BRD4/1</td><td>siRNA BRD4/2</td><td rowspan="3">1µM Tetracycline → shRNA mediated MYCN knockdown</td><td rowspan="3">0,5µM JQ1</td></tr>
<tr><td>Exp. 2: BRD2 knockdown</td><td>siRNA BRD2/1</td><td>siRNA BRD2/2</td></tr>
<tr><td>Exp. 3: BRD3 knockdown</td><td>siRNA BRD3/1</td><td>siRNA BRD3/2</td></tr>
</table>

The knockdown of BRD4 was effective, with both siRNAs reducing the BRD4 protein expression to 21% of the BRD4 protein concentration in untreated IMR5/75 cells (Figure 25A, $p<0.05$). Despite the strong BRD4 knockdown, the MYCN protein expression was not decreased in the samples transfected with *BRD4* siRNA. Knockdown of *MYCN* induced by treatment with tetracycline reduced the MYCN protein expression significantly to 51%, whereas the JQ1-treated cells had MYCN protein levels of 69% compared to control (both $p<0.05$). The Cyclin D1 protein expression was significantly lower in all treated samples, especially in the JQ1-treated cells (15% remaining, $p<0.005$) and in those transfected with siRNA BRD4/1 (16% remaining, $p<0.005$). Transfection with siRNA BRD4/2 reduced the Cyclin D1 protein level to 48% whereas the MYCN shRNA cells expressed 63% of Cyclin D1 compared to control ($p<0.05$). The results from the western blot regarding BRD4, MYCN and Cyclin D1 were verified by qPCR (data not shown).

Transfection with siRNAs targeting the other two globally expressed BET-family members *BRD2* and *BRD3* led to an effective knockdown of the target proteins (20-35% remaining) compared to control. A change in MYCN or Cyclin D1 protein expression was observed neither with siRNAs targeting *BRD3* nor with *BRD2* siRNAs (data not shown).

As a comparison, transfection with *BRD4* siRNAs was repeated in SK-N-BE(2)c cells, a cell line with a strong response regarding MYCN downregulation upon JQ1 treatment (Figure 25B). Nevertheless, neither the MYCN nor the Cyclin D1 protein expression were affected by

transfection with BRD4 siRNAs in this cell line, although the knockdown of BRD4 was highly effective.

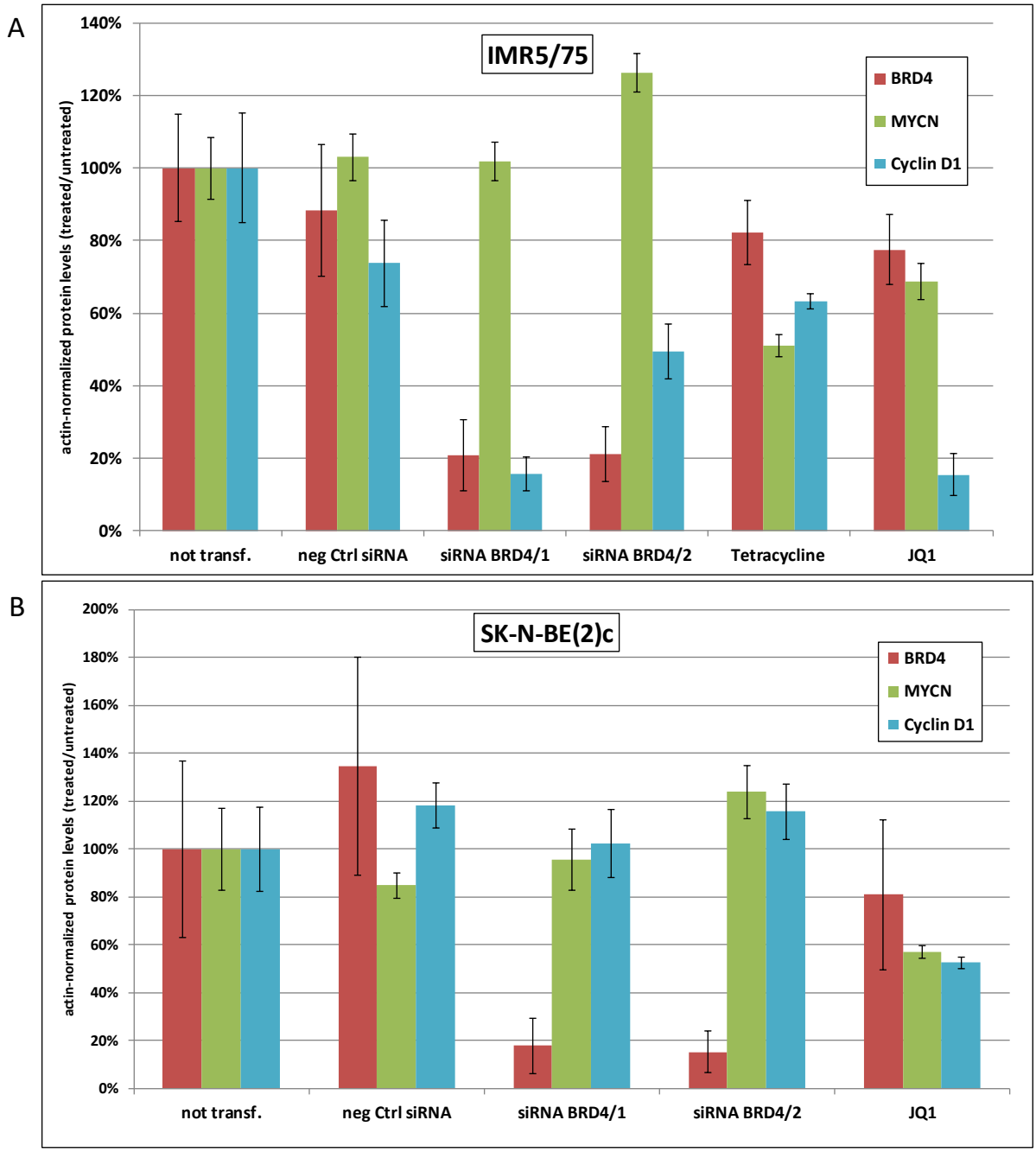

Figure 25: Comparison of BRD4- and MYCN knockdown and JQ1 treatment. Cells were transfected with two *BRD4* siRNAs, treated with 0.5 µM JQ1 or treated with 1 µM tetracycline to induce a *MYCN* shRNA (Figure 25A only, introduced in results part 5.1). Untreated cells and cells transfected with a negative control siRNA were used as control. Three biological replicates, each with two technical replicates were analyzed. Cells were harvested after 48h. Protein expression was analyzed by western blot and quantified with ImageJ. β-Actin was used for normalization. Untransfected cells were set to 100%. Significance was tested with student t-test. A) Protein expression of IMR5/75 cells. Data partly published in Nortmeyer, M., diploma thesis [153]. B) Protein expression of SK-N-BE(2)c cells.

For further comparison of the impact of BRD4 knockdown and JQ1 treatment on MYCN and Cyclin D1 protein levels, those were analyzed in a time dependent manner, using IMR5/75 *MYCN* high/low cells.

A reduction of the MYCN protein expression upon shRNA-mediated *MYCN* knockdown was observed for all time points (Figure 26). Upon JQ1 treatment the strongest downregulation of MYCN was observed at the 12h time point. After 6h of JQ1 treatment slightly lower MYCN protein levels were detected. Cyclin D1 protein expression was affected after 12h JQ1 treatment and a strong decrease was detected at the 48h time point. At the 48h time point the total protein of all samples was lower observed in the detection of MYCN and Cyclin D1 as well as for the β-actin loading control.

Altogether the comparison of the genetic knockdown of BRD4 by siRNA and the pharmacological inhibition by JQ1 treatment reveals distinct deviance between both methods to abrogate BRD4 functions. This leads to the conclusion that *MYCN* is not a direct target of BRD4-mediated gene transcription.

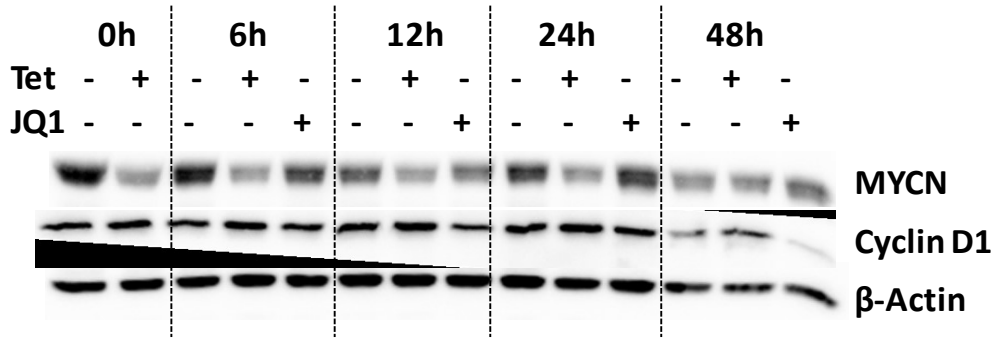

Figure 26: Time dependent comparison of *MYCN* knockdown and JQ1 treatment. IMR5/75 cells were pretreated with 1 µM Tetracycline for induction of a MYCN shRNA (introduced in results part 5.1) or treated with 0.5 µM JQ1 for 6h, 12h, 24h or 48h. MYCN and Cyclin D1 protein levels were estimated by western blot. β-Actin was used as loading control. Data partly published in Nortmeyer, M., diploma thesis [153].

5.2.9 High troughput analysis of JQ1-treated neuroblastoma cells and tumor models reveals large changes in gene expression

So far, the analysis of the effect of JQ1 treatment on neuroblastoma cells was focusing on the protein expression. Aiming to get further insight into the genes and cellular functions affected by JQ1 on the transcriptional level, RNA-sequencing was performed. An overview of the experimental plan is shown in Figure 27.

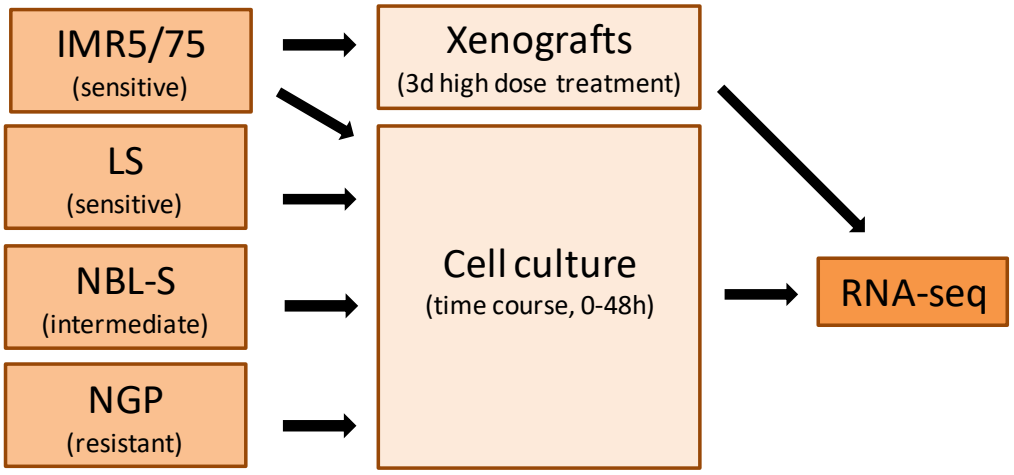

Figure 27: Overview on RNA-sequencing. A time course was performed with the neuroblastoma cell lines IMR5/75, LS, NBL-S and NGP treated with 0.5 µM JQ1 or DMSO only control. Samples were collected after 6h, 12h, 24h and 48h and analyzed by RNA-sequencing. With cell line IMR5/75, orthotopic xenografts were generated and treated peritoneally four times in three days with 50 mg/kg JQ1 (xenograft experiment performed by the group of Johannes H. Schulte, Charité Berlin).

For the *in vitro* part, four different neuroblastoma cell lines were analyzed, including the two JQ1 sensitive cell lines IMR5/75 and LS, the intermediate responding cell line NBL-S and the resistant cell line NGP (Figure 28). Both, the sensitive and resistant cell lines included in this analysis are *MYCN* amplified, the intermediate responding cell line NBL-S harbors a *MYCN* translocation and is expressing *MYCN*, albeit in lower extent.

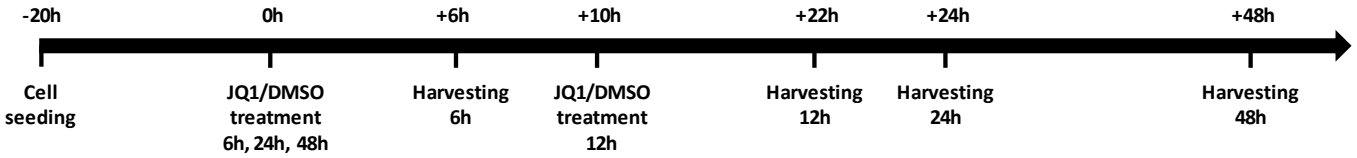

Figure 28: Timeline for RNA-sequencing in cell culture. $2x10^5$ cells for early time points and $1.5x10^5$ cells for late time points were seeded 20h before treatment start. The cells were treated with 0.5 µM JQ1 or DMSO only control. For the 12h time point the treatment was time-shifted. Isolated RNA was sent to the DKFZ core facility for sample preparation and sequencing.

In a second part, the RNA sequencing profile from JQ1-treated IMR5/75 cell cultures was compared with xenograft tumors deriving from the same cell line. Mice harboring the xenograft tumors were treated with 50 mg/kg JQ1 for 4 times in 36h, then the mice were sacrificed and the tumor material was prepared for RNA sequencing (Figure 29).

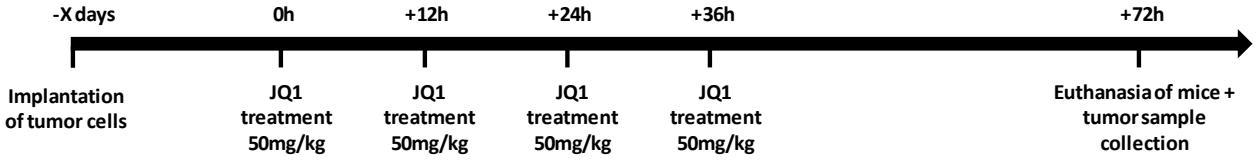

Figure 29: Timeline for RNA-sequencing in xenografts. IMR5/75 cells were implanted in the adrenal gland of immunodeficient mice. When tumors were established, the mice were treated with 50 mg/kg JQ1 for four times in 36h. Mice were euthanized 72h after the first treatment and the tumor material was collected for RNA-sequencing.

a) RNA-sequencing: IMR5/75 in cell culture

The RNA-sequencing analysis of IMR5/75 was performed as described in Figure 28.

First, a principal component analysis was performed with the data, showing that the mRNA expression profile at time point 48h differed from the time points 0-24h and that both biological replicates harvested after 48h JQ1 treatment diverged. Knowing from cell cycle and cell death analyses (section 5.2.2 and 5.2.3) that the fraction of dead cells significantly increased in IMR5/75 after 48h treatment with JQ1, a difference between the early and the late time points is allegeable. Due to the different gene expression patterns, the analysis of the IMR5/75 gene expression profile was focused on the time points 0-24h.

The global gene expression patterns of the most significantly differentially expressed genes sorted by hierarchical clusters are presented in a heatmap (Figure 30A). A small group of strong upregulated genes are indicated in dark orange. The majority of those genes plays an important role in inducing cell cycle arrest at the G1/S cell cycle checkpoint or is involved in the recognition of DNA damage and pathways activated upon oxidative stress. Among the group of strong upregulated genes were *CDKN1C* and *CDKN2D*, coding for two inhibitors specific for the CDK-Cyclin complexes CDK4/6-Cyclin D and CDK2- Cyclin A/E that are active in G1 and at the G1/S transition. A larger group of genes downregulated upon JQ1 treatment is indicated in blue in the heatmap. Genes related to DNA damage response and repair or to the cytoskeleton and thereby involved in mitosis and cytokinesis were overrepresented among the downregulated genes. There were also several genes required for the G1/S transition or controlling cell cycle progression. One example for the JQ1 downregulated genes was *CDK6*, a CDK binding D-type cyclin in its active form and functionally involved in the cell cycle progression from G1 to S-phase. Other downregulated genes were *URGCP*, regulating *CCND1* expression and *E2F2*, a transcriptional activator for genes required for the early S-phase. Taken together, the upregulation of cell cycle inhibiting genes and downregulation of genes required for cell cycle progression at the G1-S transition should result in cell cycle arrest, as observed for JQ1-treated IMR5/75 cells.

Figures 30B and 30C present the gene expression profile of *MYCN* and *CCND1* as exemplary genes throughout the time course for both biological replicates. The *MYCN* mRNA levels of the first replicate were reduced upon JQ1 treatment compared to the *MYCN* expression in DMSO-treated IMR5/75 cells (Figure 30B). In the second replicate the JQ1-treated cells showed a constant high *MYCN* gene expression. These ambiguous results concerning the *MYCN* expression upon JQ1 treatment in IMR5/75 cells are comparable with the results from the analysis of MYCN protein levels by western blot and RPPA. The *CCND1* mRNA expression was considerably reduced in JQ1-treated IMR5/75 cells in both biological replicates (Figure 30C).

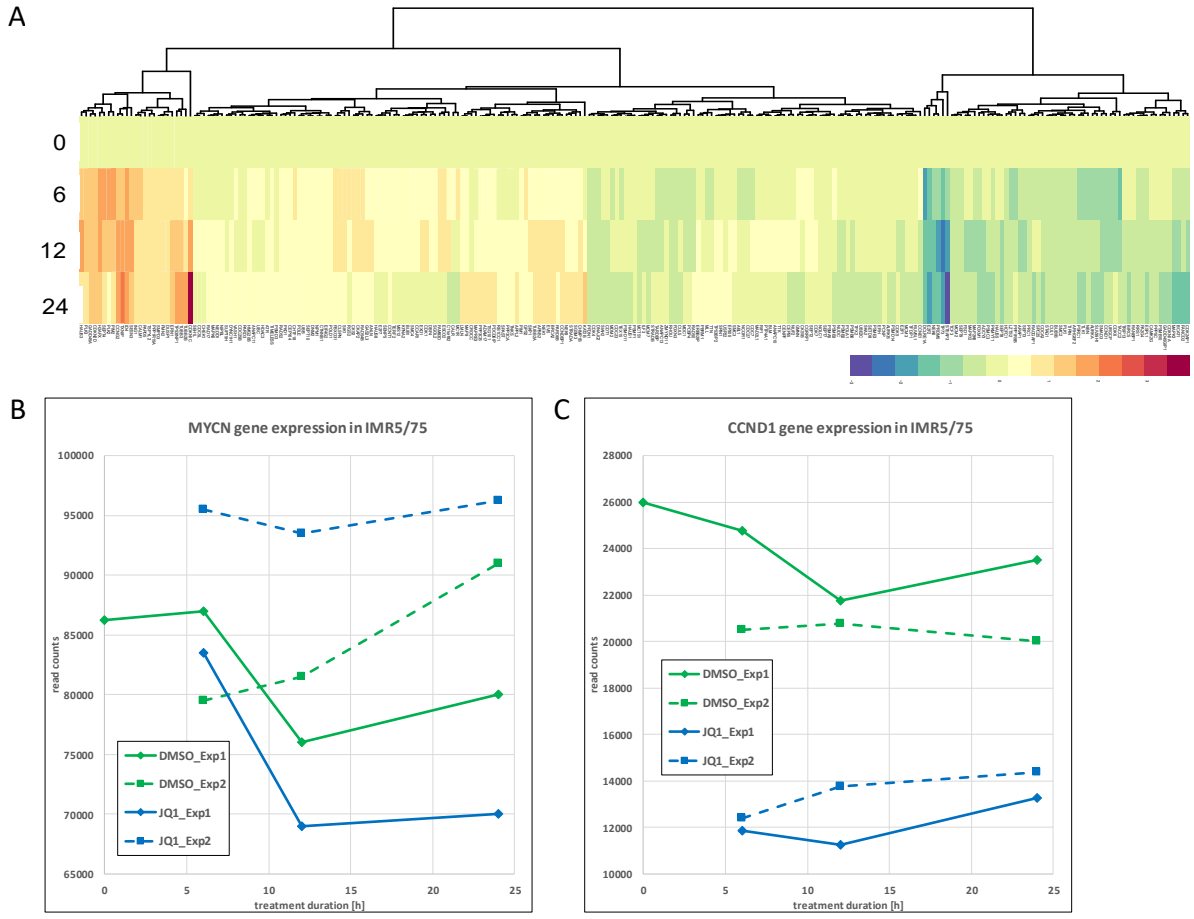

Figure 30: RNA-sequencing of JQ1-treated IMR5/75 cells. IMR5/75 cells treated with 0.5 µM JQ1 or DMSO as control were analyzed by RNA-sequencing. A) Clustering heatmap visualizing genes induced or repressed by JQ1 treatment. Red = high expression, blue = low expression. B) *MYCN* mRNA expression throughout the time course. C) *CCND1* mRNA expression throughout the time course.

A Reactome analysis [140] of the cellular signaling pathways affected by JQ1 treatment in IMR5/75 neuroblastoma cells showed a focus of the differentially expressed genes on several cell cycle related pathways. Genes related to all cell cycle phases were found both among the upregulated and the downregulated genes (Table 11). Nevertheless, the downregulated genes

were best represented by G1/S transition related pathways, whereas the upregulated genes were found in G2/M gene expression profiles. Functional signatures for mitosis and cell cycle checkpoints were equally overrepresented in both JQ1 up- and downregulated gene expression data. Pathways belonging to DNA damage repair were overrepresented in the JQ1 upregulated gene expression profile only, whereas the JQ1 downregulated genes were associated with p53 related DNA damage response and checkpoints. General transcriptional regulation induced by *TP53* was associated with both JQ1 up- and downregulated gene expression profiles.

Table 11: Pathway analysis of IMR5/75 RNA-sequencing data.

Category	JQ1 up- and downregulated	JQ1 downregulated	JQ1 upregulated
DNA damage response and repair		- p53-dependent G1/S DNA damage checkpoint - p53-dependent G1 DNA damage response - G1/S DNA damage checkpoints	- HDR through Homologous Recombination (hrr) or Single Strand annealing (SSA) - DNA double-strand break repair - Homology directed repair
p53 related pathways	Transcriptional regulation by *TP53*		*TP53* regulates transcription of cell cycle genes
Cell cycle, unspecific	- Cell cycle - Regulation of mitotic cell cycle - Cell cycle, mitotic		
DNA-replication/ S-Phase	- S-phase - DNA replication - DNA replication pre-initiation	- Assembly of the pre-replicative complex - Synthesis of DNA	
Cell cycle checkpoints	- Cell cycle checkpoints - G1/S transition - M/G1 transition phase - Mitotic G1-G1/S-phase	- Cyclin E associated events during G1/S transition - Cyclin A:Cdk2-associated events at S phase entry	- G2/M transition - G2/M checkpoints
Mitosis	- Mitotic anaphase - Mitotic metaphase and anaphase - M-phase - Separation of sister chromatids	Switching of origins to a postreplicative state	- Mitotic G2-G2/M phases - Mitotic prometaphase

b) RNA-seq: IMR5/75 *in vivo*

In vivo RNA-sequencing profiles were performed in Nude mice with xenograft tumors deriving from human IMR5/75 neuroblastoma cells. The xenografts were injected with JQ1 or control intraperitoneally as described (Figure 29).

The IMR5/75 RNA-sequencing profiles generated *in vivo* were compared with the *in vitro* IMR5/75 RNA-sequencing data. The gene expression data of both models were plotted in a diagram for the genes with the highest differential expression in JQ1-treated normalized to DMSO-treated conditions (Figure 31). Both IMR5/75 RNA-sequencing profiles are highly correlating with most genes either upregulated or downregulated both *in vivo* and *in vitro*.

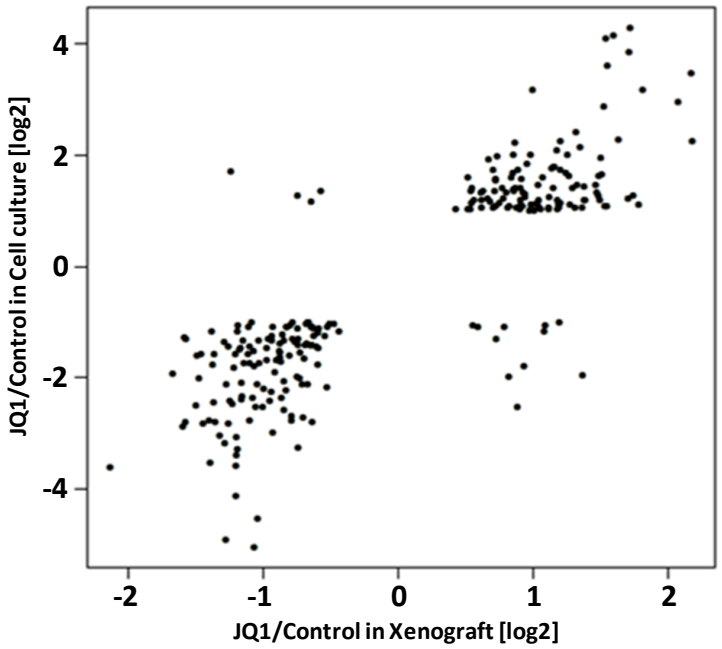

Figure 31: Correlation of RNA expression profiles *in vivo* and *in vitro*. Xenografts and cells were treated with JQ1 or vehicle as control. The gene expression changes of the xenograft tumors and the *in vitro* cell cultures were plotted for correlation analysis. The cutoff for DEG was set to a FDR of 0.01.

The similarity of the *in vivo* and *in vitro* RNA-sequencing signatures was confirmed by analyzing the differentially expressed genes in Venn diagrams. The genes upregulated upon JQ1 treatment are shown in Figure 32A. From the upregulated genes, 111 genes (88%) were upregulated upon JQ1 treatment both *in vitro* and *in vivo*. Among the most differentially expressed genes, four genes were upregulated *in vitro* but not *in vivo* and 11 genes were upregulated *in vivo* only. The top hits among the upregulated genes identified by comparison of the 20 genes with the highest fold change in both the *in vivo* and *in vitro* RNA-sequencing profiles included several histone genes and members of growth promoting pathways, such as *Jun* or *EGR1*.

The genes downregulated upon JQ1 treatment were analyzed by similar procedures (Figure 32B). In both *in vivo* and *in vitro*, 126 genes (89%) were downregulated upon JQ1 treatment. A total number of 11 genes were identified as downregulated *in vitro* only, whereas four genes were downregulated *in vivo* but not *in vitro*. The list of the top hits comprised genes belonging to different functional and molecular terms, for example the gene *TAL1* related to the NFκB-

pathway, genes with metabolic functions, such as *HS3ST4* or *ARSJ*, and genes involved in alternative splicing (*SYT2*, *CALN1*).

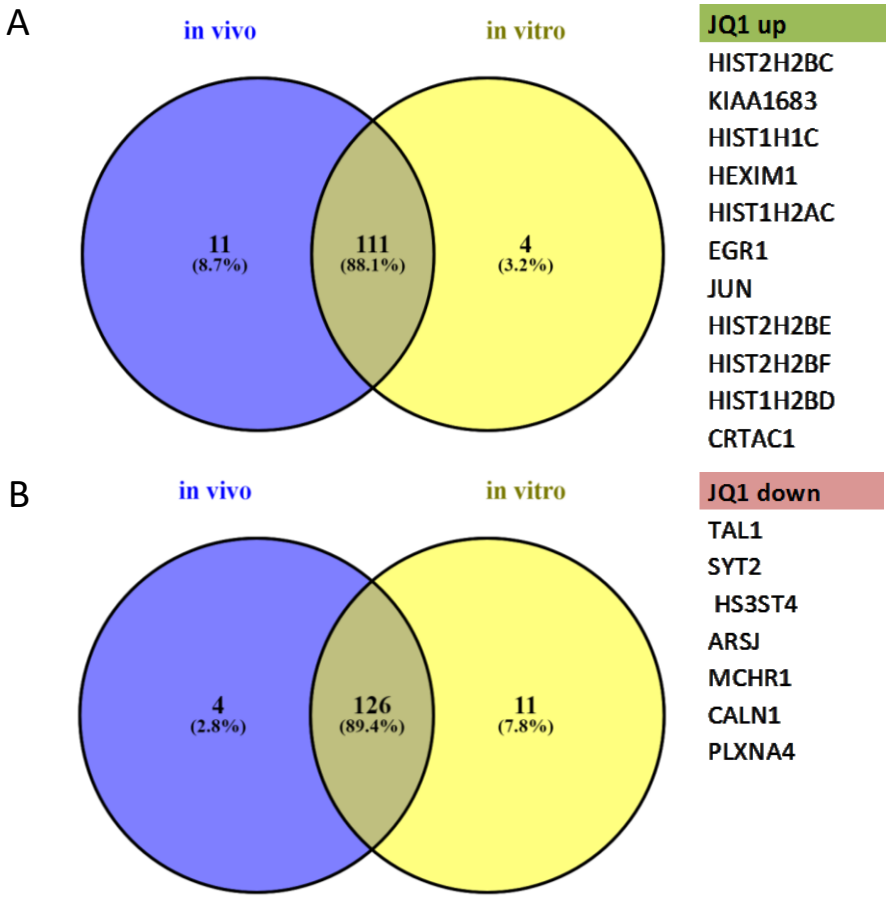

Figure 32: Combined signatures of JQ1-treated IMR5/75 cell cultures and xenograft tumors. Comparison of the gene expression profiles generated *in vivo* and *in vitro*. A venn plot of the up- and downregulated genes is given, as well as the top candidates for both categories. Venn plots were generated by Venny 2.1.0 [139]. The cutoff for DEG was set to a FDR of 0.01. A) Genes upregulated upon JQ1 treatment. B) Genes downregulated upon JQ1 treatment.

c) RNA-seq: LS, NBL-S and NGP cell cultures

With the aim to generate a broad insight into the gene expression patterns of JQ1-treated neuroblastoma cell lines, RNA-sequencing profiles from three additional neuroblastoma cell lines were generated. For the analysis, one cell line from each viability category was chosen: JQ1 sensitive LS and JQ1 resistant NGP, both *MYCN* amplified, and NBL-S cells, intermediate responding to JQ1 and *MYCN* translocated. The experiments were performed as described for IMR5/75 RNA-sequencing and as shown in Figure 28.

The first analysis performed with the RNA-sequencing data from LS, NBL-S and NGP was a Principal Component Analysis (PCA), with the purpose to control the variance of the data especially regarding the similarity of the two biological replicates (Figure 33). For NGP and

NBL-S all samples from the same cell line closely clustered together and could clearly be separated from the samples of the other cell lines. The samples from cell line LS in general showed a similar clear clustering. However, two of the LS samples from the control group clustered together with the group of NBL-S samples instead of LS. It is assumed that a sample swap occurred in this case. To avoid a bias in the results, these two samples were excluded from further analysis.

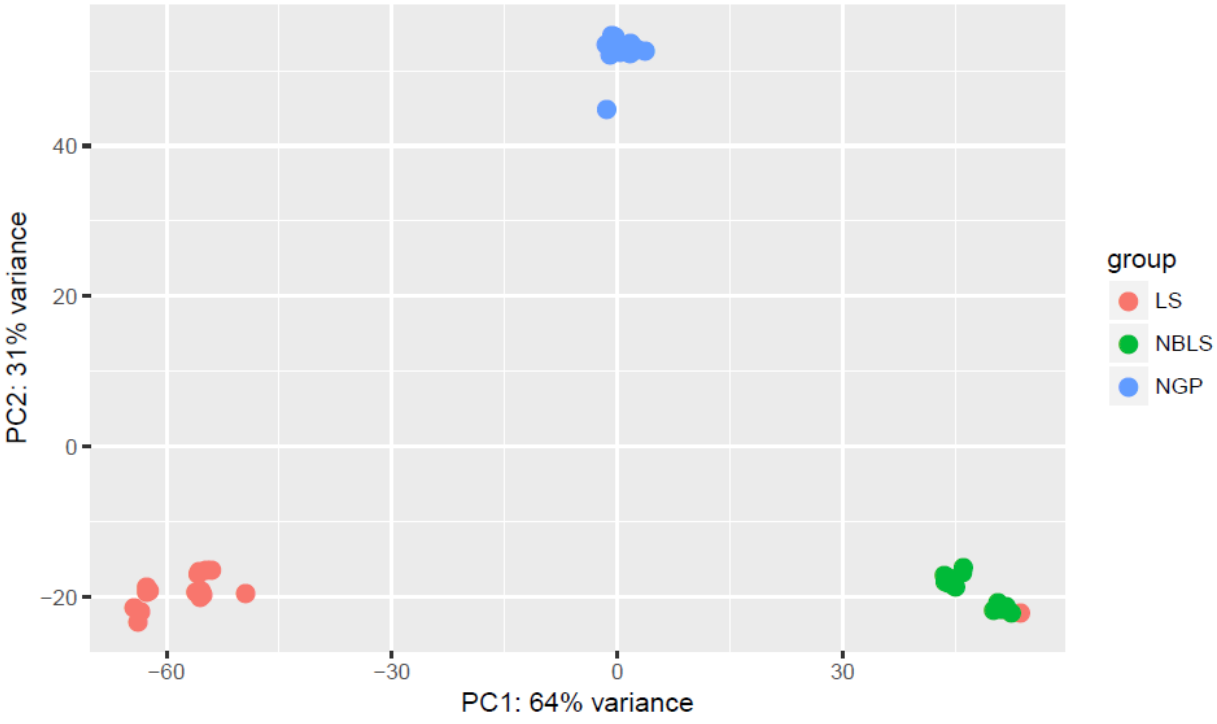

Figure 33: PCA Analysis of JQ1-treated cells. Principal component analysis of the RNA-sequencing profiles of LS, NBL-S and NGP. Red= LS samples, green=NBL-S samples, blue=NGP samples.

The cell line LS was categorized as JQ1 sensitive in the viability screening. With an EC50 of 0.07 µM LS ranked slightly behind IMR5/75. Genetically, LS cells harbor amplification statuses of *MYCN, CCND1*, *CDK4* and *MDM2*.

Differentially expressed genes, defined by a FDR of 0.01 or lower, were not identified for all time points of JQ1-treated LS cells. Upregulated genes were identified for the time points 24h and 48h, but not for 6h and 12h JQ1. The total number of upregulated genes was about 2.5 times higher at the 24h time point compared to 48h JQ1 treatment (Figure 34A). A Venn diagram illustrates the overlap of 360 genes between both time points, which equates to 22.5% of the total upregulated differentially expressed genes. The top hits of the upregulated genes were identified by comparing the 50 genes with the lowest FDR of 24h and 48h JQ1-treated LS cells. The list includes *EGR1*, a transcription factor and tumor suppressor as well as *NAB2*, a transcriptional repressor for *EGR1* and *EGR2*. Another top upregulated gene was *DHRS2*, which is known to stabilize p53 via the MDM2 axis and thereby induces a cell cycle arrest. In

contrast, *SERTAD1* codes for a protein involved in cell proliferation by activation of the CDK4/Cyclin D1 complex. Further top upregulated genes are involved in metabolism or synaptic signal transmission and synaptic plasticity. Like the differentially expressed genes identified for IMR5/75, the list of upregulated genes of JQ1-treated LS cells included several genes for histone subunits. Those were excluded from the list of upregulated genes and are discussed separately.

On the Reactome platform, a pathway analysis of all differentially expressed genes upon JQ1 treatment in LS cells was performed (data not shown). For each time point, the 25 pathways with the lowest FDR were appraised. The pathway “RNA-Polymerase I promoter opening” was the only pathway upregulated at both the 24h and 48h time point. Additionally, for both time points upregulated pathways were identified related to the field of cellular senescence, telomeres and stress response. Besides this, upregulated genes at the 24h time point belonged to pathways of cellular transport and translation/protein synthesis. Upon 48h of JQ1 treatment, pathways related to cell cycle, especially G1/S transition, to DNA repair, to *TP53* and to DNA methylation were upregulated.

Downregulated differentially expressed genes in JQ1-treated LS cells were identified at the 6h, 24h and 48h time point, whereas the number of differentially expressed genes at the 6h time point accounted for less than 5% of all downregulated genes identified by RNA-sequencing in LS cells (Figure 34B). The late time points 24h and 48h shared 997 genes identified as differentially expressed in both data sets, which equates to 43% of all downregulated genes. In contrast, the overlay between the downregulated genes at the 6h time point and the later time points was very low. The highest number of downregulated genes in LS cells was identified upon 24h of JQ1 treatment. A list of top hits among the downregulated genes was compiled as described for the JQ1 upregulated genes, complemented by the three differentially expressed genes downregulated at all three time points. Those shared genes were *ANK1*, *DBH* and *SGIP1*. Further interesting genes were *RARG*, coding for a retinoic acid receptor, *TNFRSF10C* belonging to the TNF receptor superfamily and *SORBS3* involved in EGF signaling.

Like the procedure for the JQ1 upregulated genes, a reactome pathway analysis was performed for the genes downregulated upon JQ1 treatment in LS cells. For each time point, the 25 pathways with the lowest FDR were viewed. The pathway analysis for the 6h time point came up with “neuronal system” as the sole pathway affected. At both late time points 24h and 48h of JQ1 treatment, the downregulated genes were associated with pathways related to elastic fibres and extracellular matrix, to VEGF signaling and to *TP53* related cell death. At the 24h time point only, pathways associated with cell cycle and mitosis were downregulated, whereas Notch signaling and TRKA activation were downregulated at the 48h time point only.

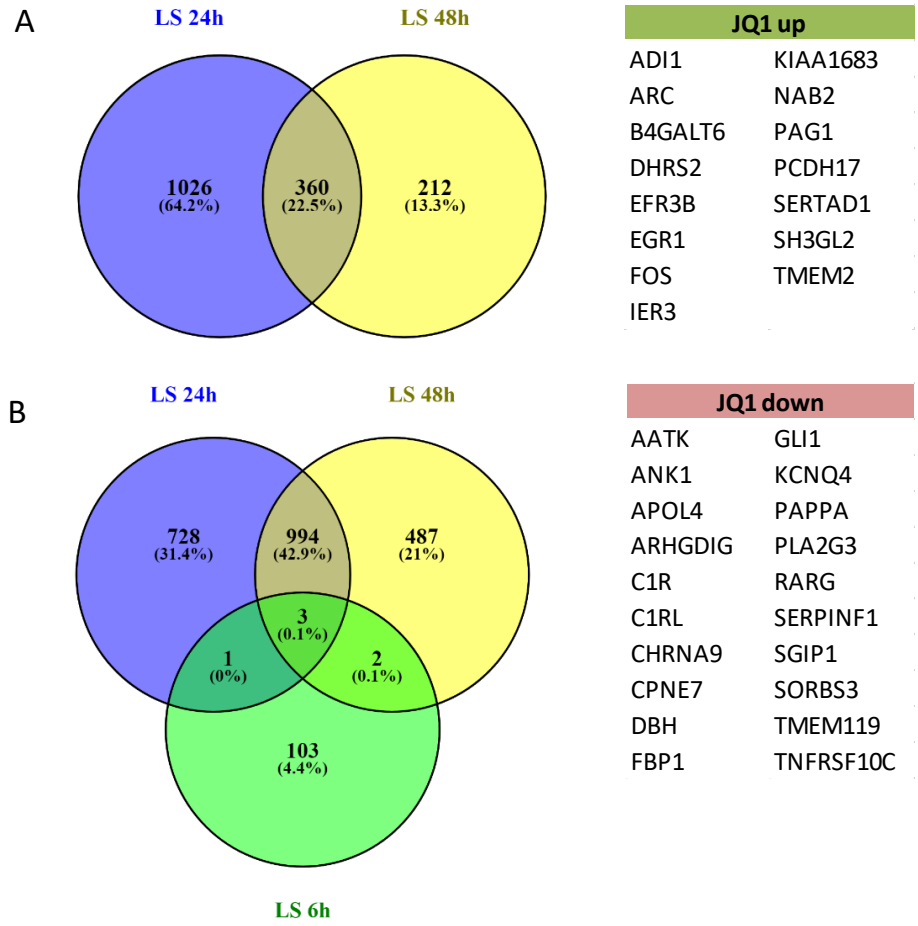

Figure 34: RNA-sequencing of JQ1-treated LS cells. Analysis of the gene expression profiles of LS cells treated with 0.5 µM JQ1. Venn plots illustrate the overlap of DEG at different time points. The top target genes were identified by comparison of the 50 strongest DEG at 24h and 48h and all 6h down genes. The cutoff for DEG was set to a FDR of 0.01. A) Genes upregulated upon JQ1 treatment. For the time points 6h and 12h no upregulated DEG were identified. B) Genes downregulated upon JQ1 treatment. For time point 12h no downregulated DEG were identified.

With an EC50 of 0.29 µM, the neuroblastoma cell line NBL-S was intermediate responding to JQ1 treatment in the viability screening. NBL-S cells are *MYCN* translocated and therefore express elevated levels of MYCN.

In JQ1-treated NBL-S cells, the effects on the transcriptional level were broadly distributed. Differentially expressed genes, both up- and downregulated, were identified for all time points (Figure 35). At each of the early time points (6h and 12h) more than 2.000 genes were upregulated and downregulated, which is about 10-fold higher than the total number of upregulated genes after 24h of JQ1 treatment and 20-fold higher than the upregulated genes at the 48h time point.

By comparison of the upregulated genes, 54 genes were identified that were upregulated at all time points, which are 1.9% of all genes upregulated in NBL-S upon JQ1 treatment (Figure 35A). As visualized by the Venn diagram, a large proportion of genes was shared between the

early time points. The top hits among the 54 genes upregulated at all time points were selected by comparing the 200 differentially expressed genes with the lowest FDR. Those included *HEXIM1*, which is known to interact with Cyclin T1, *TP53INP1* being involved in oxidative stress response and having proapoptotic functions or the transcription factors *ZCCHC24* and *CSRNP2*. A pathway analysis using Reactome revealed 14 pathways upregulated at all time points (Table 12). The main fields the upregulated pathways belonged to were chromatin methylation and acetylation, transcription of rRNAs, and cellular senescence and telomeres.

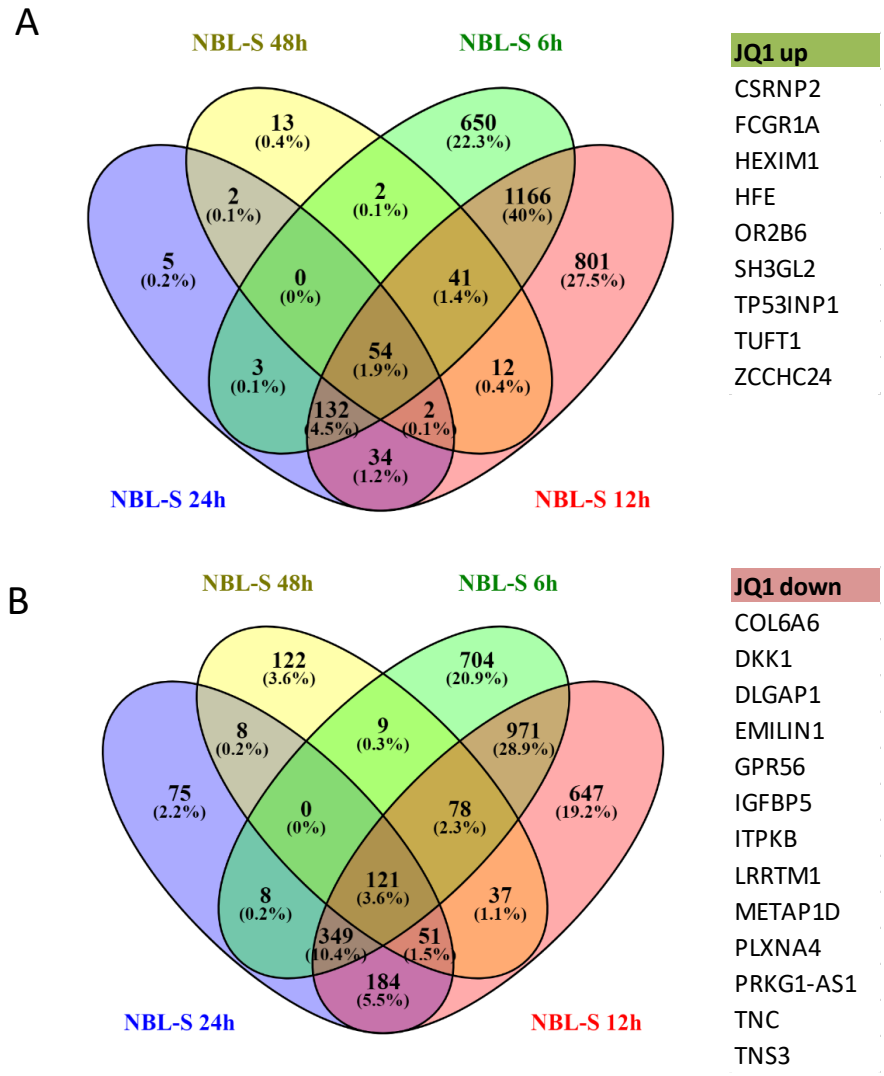

Figure 35: RNA-sequencing of JQ1-treated NBL-S cells. Analysis of the gene expression profiles of NBL-S cells treated with 0.5 µM JQ1. Venn plots illustrate the overlap of DEG at different time points. The top target genes were identified by comparison of the 200 strongest DEG of all time points. The cutoff for DEG was set to a FDR of 0.01. A) Genes upregulated upon JQ1 treatment. B) Genes downregulated upon JQ1 treatment.

Table 12: Pathway analysis of NBL-S RNA-sequencing data. Preselected pathways up-/downregulated at least at two time points are presented.

Category	JQ1 downregulated	JQ1 upregulated
Histone methylation+ acetylation		- DNA methylation (6-48h) - PRC2 methylates histones and DNA (6-48h) - HATs acetylate histones (6-48h) - HDACs deacetylate histones (6-48h)
Extracellular matrix	- Elastic fibre formation (12-48h) - molecules associated with elastic fibres (24+48h) - extracellular matrix organization (24+48h) - Collagen formation (24+48h) - Collagen chain trimerization (24+48h) - Collagen biosynthesis and modifying enzymes (24+48h)	
Senescence + Telomeres		- Packaging of telomere ends (6-48h) - Senescence-Associated Secretory Phenotype (SASP) (6-24h) - DNA Damage/Telomere stress induced senescence (6+12h)
rRNA expression		- RNA Polymerase I promoter opening (6-48h) - RNA polymerase I chain elongation (6, 24, 48h) - RNA Polymerase I promoter clearance (24+48h) - B-WICH complex positively regulates rRNA expression (6-48h) - ERCC6 (CSB) and EHMT2 (G9a) positively regulate rRNA expression (6-48h) - positive epigenetic regulation of rRNA expression (12-48h) - SIRT1 negatively regulates rRNA expression (6-48h) - NoRC negatively regulates rRNA expression (24+48h)
TCF/WNT, RUNX1/ RUNX3	-RUNX3 regulates immune response and cell migration (6-24h) - RUNX1 regulates transcription of genes involved in BCR signaling (12+24h)	- RUNX1 regulates genes involved in megakaryocyte differentiation and platelet function (12-48h) - Formation of the beta-catenin:TCF transactivating complex (6-48h)
TRKA	- Activation of TRKA receptors (6+24h) - NGF-independent TRKA activation (6+24h)	
others	- NCAM1 interactions (6, 12, 48h)	- Amyloid fibre formation (6-48h) - Meiotic recombination (6-48h) - Condensation of Prophase Chromosomes (6-48h) - Activated PKN1 stimulates transcription of androgen receptor regulated genes KLK2 and KLK3 (6-48h)

In NBL-S in total more genes were down- than upregulated at all time points. Main effects were detectable at the early time points, with a large overlap of genes downregulated both at the 6h and at the 12h time point (Figure 35B). A comparison of the differentially expressed genes revealed that 121 genes were downregulated at all time points, which equates to 3.6% of all downregulated genes. Among the top hits of downregulated genes were several genes associated with the extracellular matrix (*COL6A6*, *EMILIN1*, *GPR56*, *TNC*). *TNC* is also functionally related to retinoic acid response and FGF signaling. Further growth factor related genes among the top hits were *IGFBP5* involved in IGF signaling and *TNS3* associated to

EGF. The gene *DKK1* codes for the Dickkopf protein and has an antagonizing function in WNT-signaling and anti-apoptotic properties. The results of the pathway analysis of the downregulated genes in NBL-S were less consistent than for the upregulated genes comparing the different time points (Table 12). No pathway was downregulated at all time points comparing the 25 pathways with the lowest FDR for each time point. A large number of downregulated pathways was related to the extracellular matrix, especially at the late time points 24h and 48h, which is consistent with the analysis of the top downregulated genes. Further pathways downregulated at more than one time point were related to TRKA, RUNX1 and RUNX3 or cell adhesion. On the other hand, several pathways were specifically downregulated at one time point: For example, two pathways related to SERBP were lower expressed after 12h JQ1 treatment, whereas two pathways involving NOTCH3 were downregulated at the 6h time point only.

The cell line NGP was categorized as JQ1 resistant in the viability screening. This finding was confirmed by the RNA-sequencing data. After 6h of JQ1 treatment, 853 upregulated and 1046 downregulated genes were listed. The upregulated genes included histone genes and several genes belonging to the top hits found in RNA-sequencing profiles of the JQ1 sensitive cell lines, for example *HEXIM1*, *CDKN2D* or *EGR1*. Among the downregulated genes, amongst others *E2F2* and *CDK6* were detected. In contrast, at the time points 12h, 24h and 48h no differentially expressed genes were identified. This shows that JQ1 treatment leads to short-term effects only in the resistant NGP cell line, whereas no changes in gene expression were assessed from 12h treatment onwards.

d) Comparison of cell lines

In the previous sections, the RNA sequencing results of IMR5/75, LS, NBL-S and NGP were described independently from each other. In the following part, the RNA expression profiles of the different cell lines will be compared regarding to general similarity, total numbers of differentially expressed genes and gene expression at single time points. Due to methodic differences in the analysis of IMR5/75 compared to the other cell lines, IMR5/75 RNA-sequencing data cannot be included in all analyses of the present section.

For assessment of the similarity of the gene expression profiles from all samples, a heatmap was generated, showing a hierarchical clustering of the top 100 differentially expressed genes of LS, NBL-S and NGP (Figure 36). DMSO and JQ1-treated samples, as well as both biological replicates of each sample were analyzed independently.

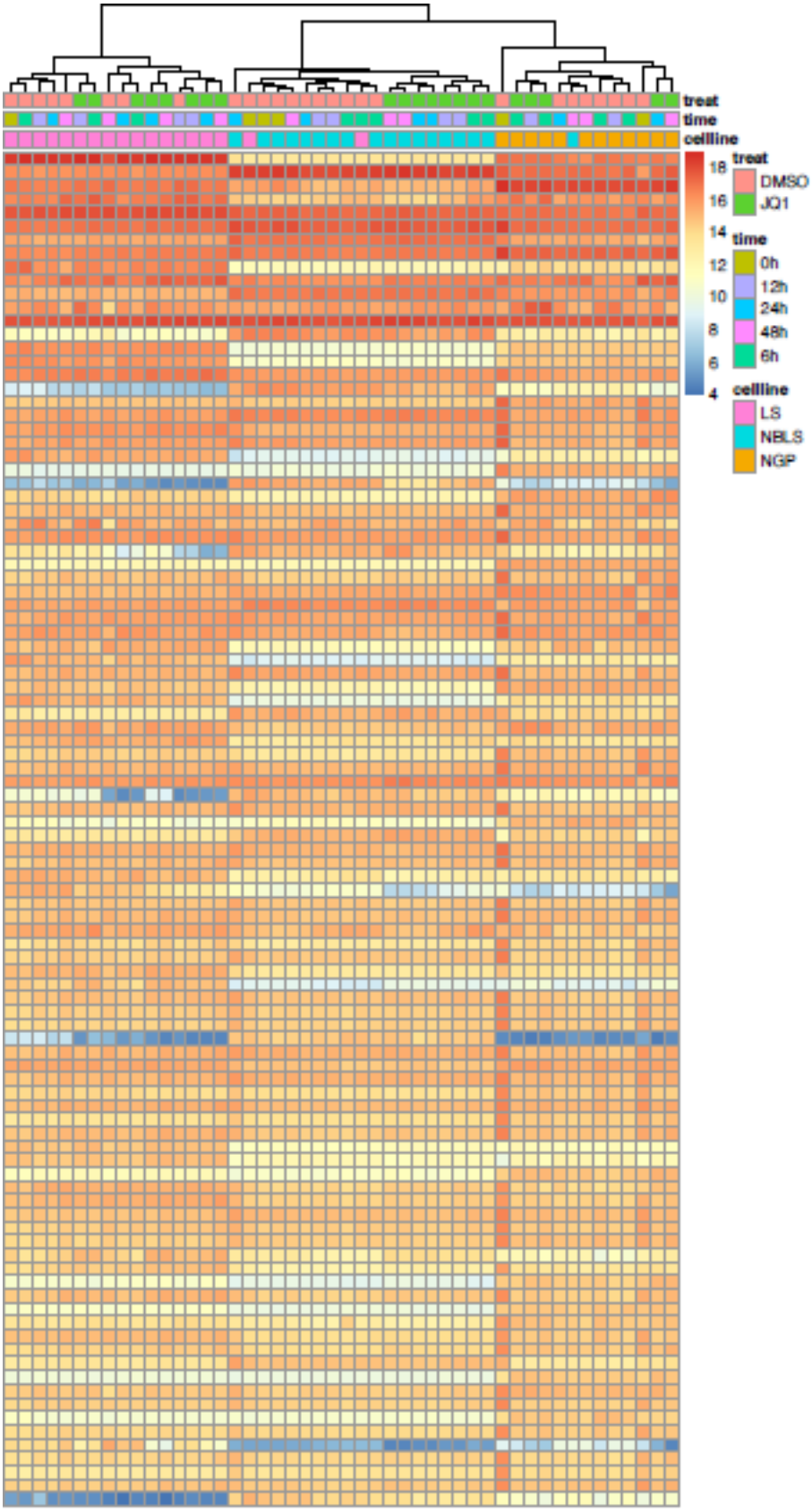

Figure 36: Heatmap of RNA-sequencing data upon JQ1 treatment. Hierarchical clustering of all samples based on the 100 top DEG. Neuroblastoma cell lines LS, NBL-S and NGP were treated with 0.5 µM JQ1 or DMSO only control in two biological replicates. JQ1-treated samples are displayed in green, DMSO control samples are indicated in pink.

The hierarchical clustering effectively sorted the cells by cell lines, for all three cell lines all samples from the same cell line, JQ1 and DMSO-treated, clustered closely together, with the exeption of two LS samples already identified as sample swap as shown in Figure 33. For NBL-S, the group of JQ1-treated samples and the DMSO control samples clustered apart from each other within the block of NBL-S cells. Thereby the JQ1-treated samples were strictly sorted by time points, with 48h upon JQ1 treatment closest to the DMSO control samples.

In NGP, the samples treated with JQ1 formed two blocks, separated by the total number of control samples. One block comprised of the JQ1-treated samples of the early time points 6h and 12h, the other block comprised of the late JQ1-treated time points 24h and 48h. In contrast to the other cell lines analyzed, the 12h, 24h and 48h time points were represented by a single row instead of two biological replicates. This was due to the absence of differentially expressed genes at those time points.

As described, the samples of the cell line LS clustered together. In contrast to NBL-S and NGP, no clear pattern was observed in LS samples differing between JQ1-treated and DMSO-treated cells.

An analysis of the total numbers of differentially expressed genes revealed large differences between the cell lines and time points. Figure 37A visualizes the total numbers of downregulated genes, Figure 37B the upregulated genes.

In general, the total numbers of downregulated genes were higher than the number of upregulated genes. In LS cells, high numbers of differentially expressed genes were identified at the later time points 24h and 48h of JQ1 treatment. At the early time points 6h and 12h of JQ1 treatment, minimal effects were detected regarding the gene expression level. At the 12h time point no genes were differentially expressed, at the 6h time point no genes were upregulated and a small number of 109 genes had lower expression levels.

For NBL-S cells, the distribution of the differential expressed genes to the time points was invers. The highest numbers of differentially expressed genes were detected at the early time points 6h and 12h with more than 2.000 genes up- and downregulated at each time point. On the late time points 24 and 48h the number of differentially expressed genes was constantly decreasing to 126 up- and 426 downregulated genes after 48h treatment with JQ1.

The analysis of the JQ1 resistant NGP cells revealed no more than short time effects at time point 6h. At all other time points no differentially expressed genes have been identified.

Based on the lists of the differentially expressed genes, certain potential key genes and genes of the pathways affected by JQ1 treatment in general were analyzed. A comparison of the upregulated and downregulated genes in this context revealed more similarities between the cell lines among the upregulated genes. A few genes have been upregulated in nearly all

samples harboring differentially expressed genes, for example *HEXIM1*, *EGR1*, *GSK3-β* or *HAUS3*. Additionally, many different histone genes were upregulated upon JQ1 treatment in all four cell lines, ranging from 14 different histone genes upregulated in LS to 42 genes in NBL-S cells.

In contrast, the downregulation of genes was more individual with less similarities across cell lines and time points. This variance was true both for different time points in the same cell line, and for the same time point in different cell lines. By the absence of differentially expressed genes in several samples the analysis of genes globally downregulated upon JQ1 treatment became more complicated.

Similar findings were true for the analysis of pathways across all 3 JQ1 sensitive and intermediate responding cell lines. Based on the lists of upregulated genes, pathways related to methylation, rRNA expression, Rho, cellular senescence and telomeres, and DNA repair were identified as upregulated in several cell lines and time points. Using the lists of downregulated genes, the variance of pathways affected was higher. Nevertheless, pathways related to extracellular matrix, *TP53*, Cell cycle and mitosis and Notch have been correlating with the downregulated genes of samples from more than one cell line.

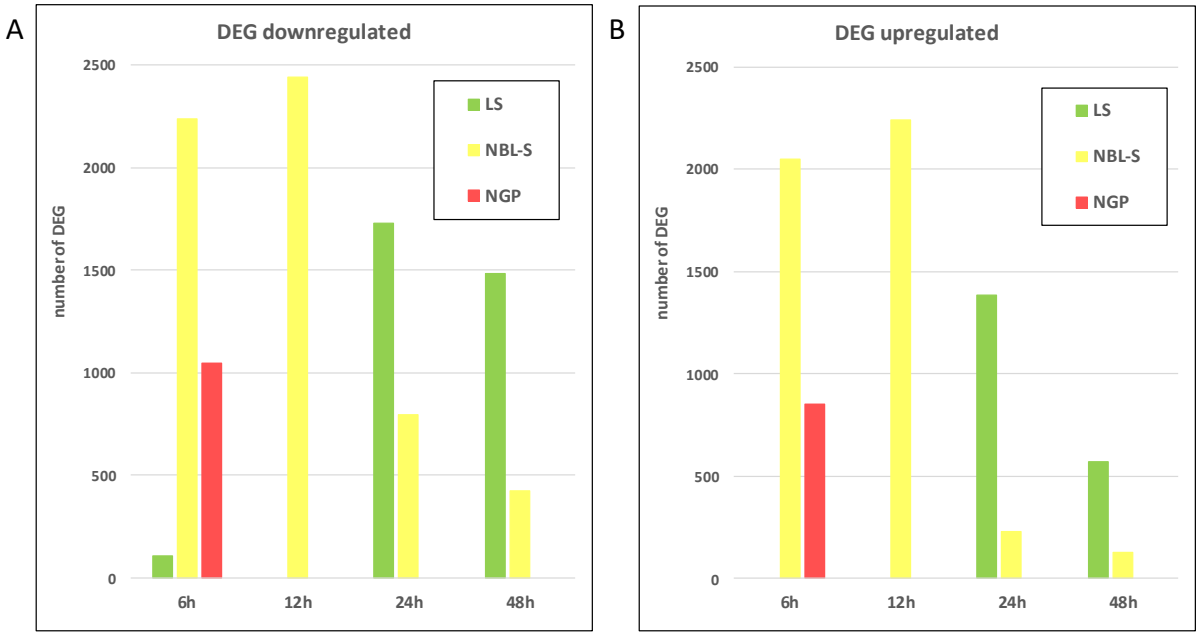

Figure 37: Differentially expressed genes upon JQ1 treatment. Total numbers of DEG comparing JQ1 and DMSO-treated cells. The FDR was set to 0.01 to define DEG. A) Numbers of downregulated DEG upon JQ1 treatment. B) Numbers of upregulated DEG upon JQ1 treatment.

To get insight in patterns of differential gene expression at early and late time points, the gene expression profiles of the three neuroblastoma cell lines LS, NBL-S and NGP were analyzed in a time-resolved manner. The Venn diagrams presented in Figure 38 show the overlap among the most differential expressed genes for each time point separately. IMR5/75 gene

expression data could not be included in this analysis, as the gene expression of this cell line has not been analyzed separated by time points. At the 12h time point, differentially expressed genes have been identified for NBL-S only, therefore no data are presented for this time point.

With 6h upon JQ1 treatment, a high similarity was detected between the gene expression profiles of NBL-S and NGP, sharing 25.1% of the downregulated and 30.1% of the upregulated genes (Figure 38A). In LS cells, few genes were downregulated and no genes were upregulated at the 6h time point. Therefore, no more than 18 genes (0.7%) have been downregulated in all three cell lines.

At the 24h and 48h time points no genes were differentially expressed in JQ1-treated NGP cells, so NBL-S and LS were the only cell lines compared at these time points (Figure 38B+C). For both time points an overlap of 10.1 respective 15.4% of all downregulated genes and of 6.6% or 9.9% of all upregulated genes has been detected. These relatively small proportions must be put in relation to the discrepancy regarding the total number of differentially expressed genes for both cell lines. As shown in Figure 37, the total number of differentially expressed genes was in average 4 times higher for LS at the late time points compared to NBL-S. Normalization of the shared genes on the total number of differentially expressed genes in NBL-S resulted in about 40% analogy for the downregulated genes. For the upregulated genes, 63% analogy were detected after 24h and 34% after 48h of JQ1 treatment when normalizing as described.

Taken together, JQ1 treatment induced broad changes in the gene expression profiles of the sensitive and intermediate responding cell lines included in this analysis. Affected genes can be assigned to central signaling pathways of G1/S transition, DNA damage response or senescence. Nevertheless, differences between the cell lines have been observed regarding effects occurring at early or late time points.

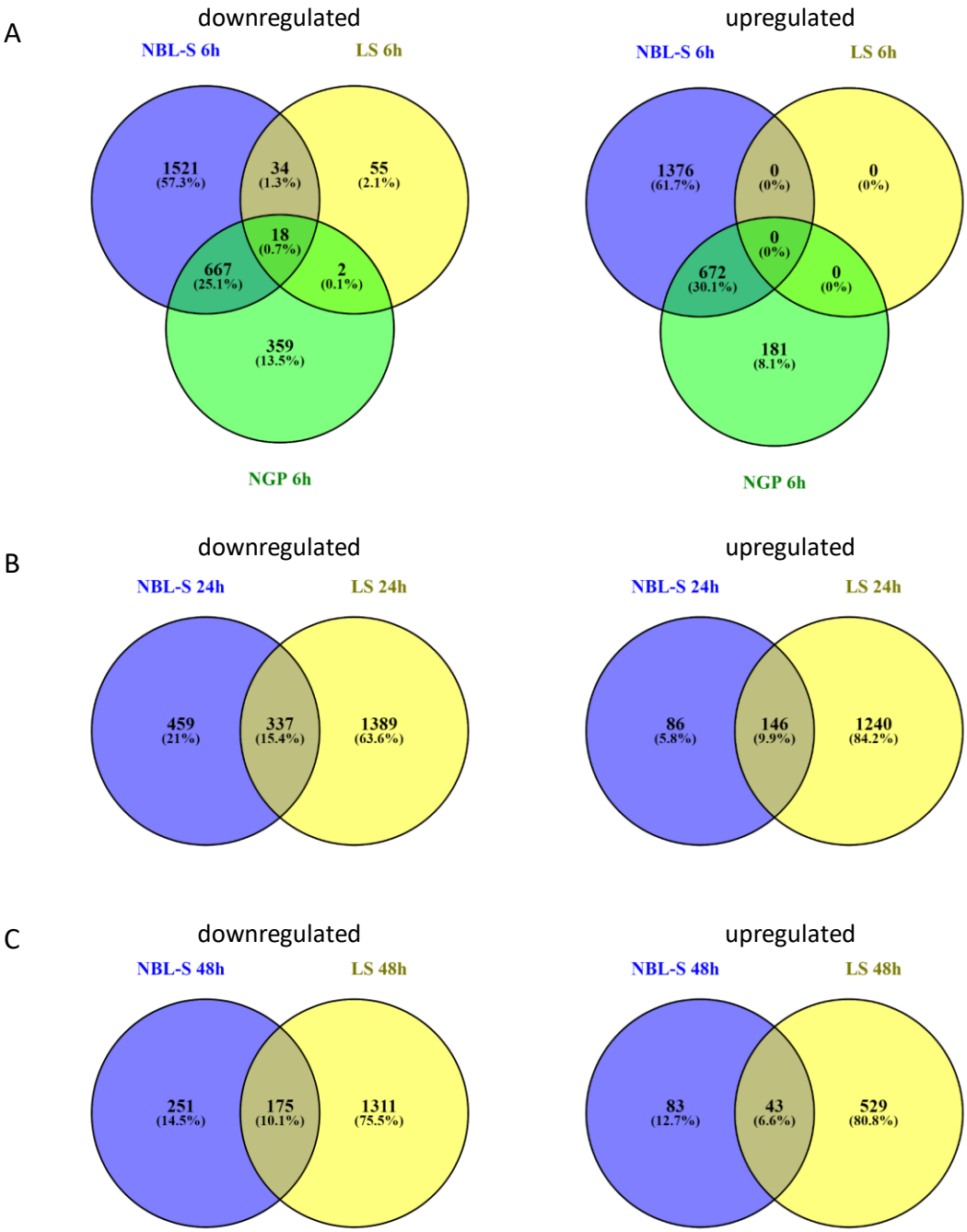

Figure 38: Time-resolved gene expression profiles upon JQ1 treatment. Venn diagrams of genes upregulated and downregulated comparing LS, NBL-S and NGP neuroblastoma cells treated with 0.5 µM JQ1 or DMSO only control and analyzed by RNA-sequencing. The data were sorted by treatment duration. A) DEG at the 6h time point. B) DEG at the 24h time point. C) DEG at the 48h time point.

5.2.10 Combined treatment of neuroblastoma cells with JQ1 and doxorubicin is more effective than single treatment

In the majority of cases, chemotherapeutics are applied in combinatory therapies of two or more substances to avoid resistance development of cancer cells and thereby to increase the success of the therapy. As the RNA-seq results especially of the IMR5/75 neuroblastoma cell line revealed differential expression of DNA damage response genes, it is likely that JQ1 influences those signaling pathways, but this is not resulting in massive cell death or permanent growth arrest. Combining JQ1 with a DNA intercalating drug could possibly increase the DNA damage to a level that cannot be compensated and consequently may then lead to cell death. Additionally, a successful combination of JQ1 and the intercalating chemotherapeutic drug doxorubicin is already described for leukemia cells [154].

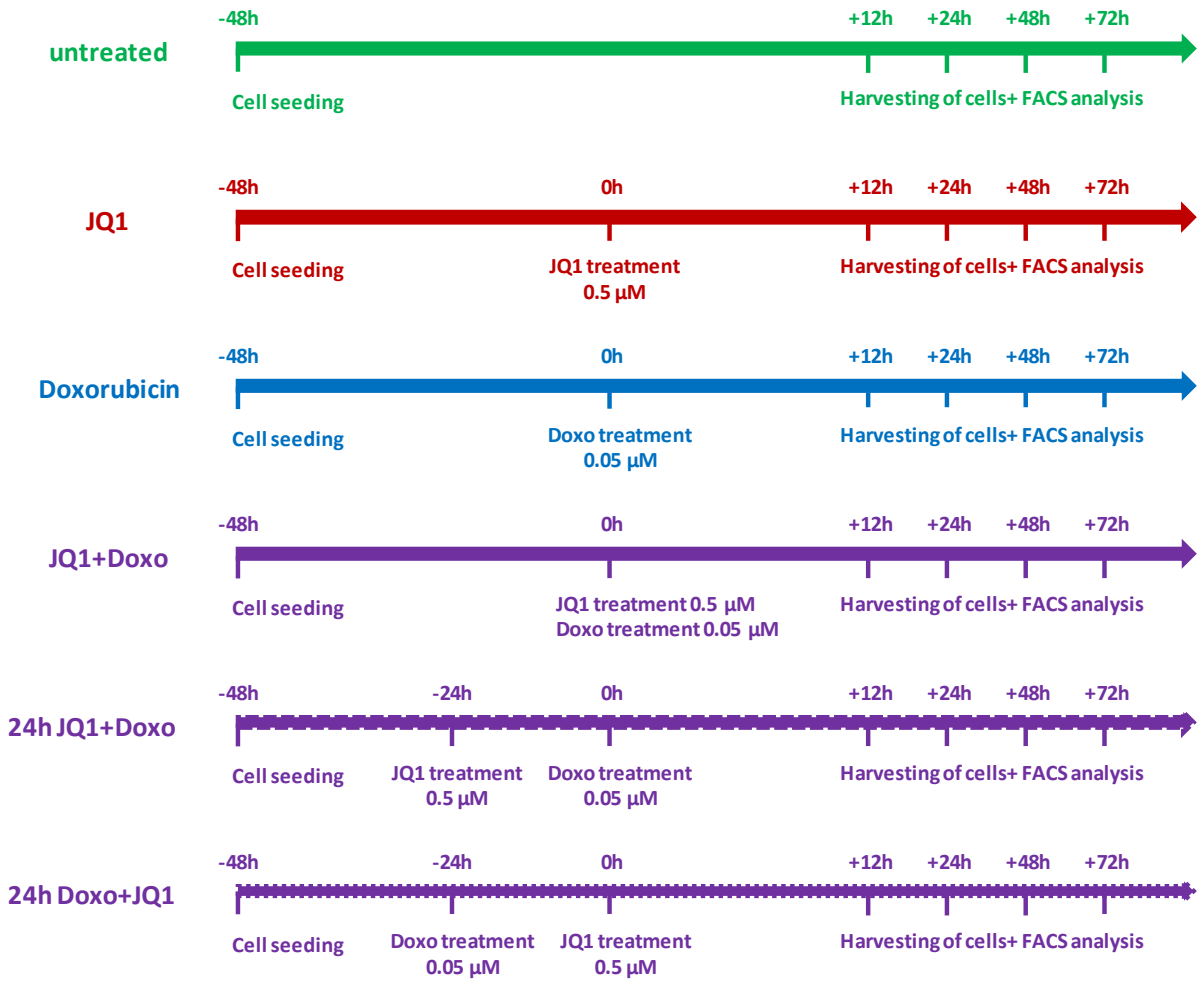

Figure 39: Timeline for combination treatment of JQ1 and doxorubicin. IMR5/75 cells were seeded 24h-48h before treatment depending on the different treatment protocols. The cells were treated with 0.5 µM JQ1 or 0.05 µM doxorubicin or both. Treatment with both drugs was done in parallel or time-shifted. The cells were harvested and analyzed by flow cytometry.

IMR5/75 cells were treated with JQ1 or doxorubicin alone as well as with a combination of both drugs (Figure 39). The two drugs were either applied simultaneously or time-shifted. In the time-shifted experiments, the IMR5/75 cells were pretreated with the first drug, adding the second substance 24h later (= time point 0h).

The analysis of IMR5/75 cells upon treatment with JQ1 and doxorubicin revealed clear differences between the treatments (Figure 40). After 12h of treatment the fraction of dead cells was similar for all treatment protocols. Differences were observed after 48h of treatment, which was the same time point when an increase of cell death was observed not only for JQ1-treated IMR5/75 cells but also for other *MYCN* amplified neuroblastoma cell lines (section 5.2.3). At the 48h time point, simultaneous application of both drugs was most effective, increasing the fraction of dead cells to 23%, compared to less than 10% in the untreated control and 14% with JQ1 single treatment. The time-shifted variants of the combination therapy both showed 17% cell death.

At the 72h time point a statistically significant increase of cell death was measured for all samples compared to control ($p<0.01$). The highest rates of cell death were observed in the samples simultaneously treated with JQ1 and doxorubicin and in the samples pretreated with doxycycline before adding JQ1. In both cases the fraction of dead cells amounted 35%. Treatment with JQ1 alone resulted in 22% cell death and was thereby less effective than the single doxorubicin treatment.

Summarizing, JQ1 was more effective when it was applied in combination therapy, either given simultaneously or with a doxorubicin pretreatment. It would have been expected that the JQ1 pretreatment is more effective than doxorubicin pretreatment, with JQ1 downregulating DNA damage repair pathways prior to massive DNA damage induced by doxorubicin. On the other hand, it can be supposed that the DNA damage induced by doxorubicin treatment cannot be repaired effectively by the cells upon JQ1 treatment due to downregulation of DNA damage response pathways.

The differential expression of DNA damage repair genes in JQ1-treated IMR/75 cells might be related to the function of BRD4 as histone chaperone. The combination of DNA intercalation by doxorubicin and inhibited histone chaperone function by JQ1 might result in high grade DNA damage leading to cell death.

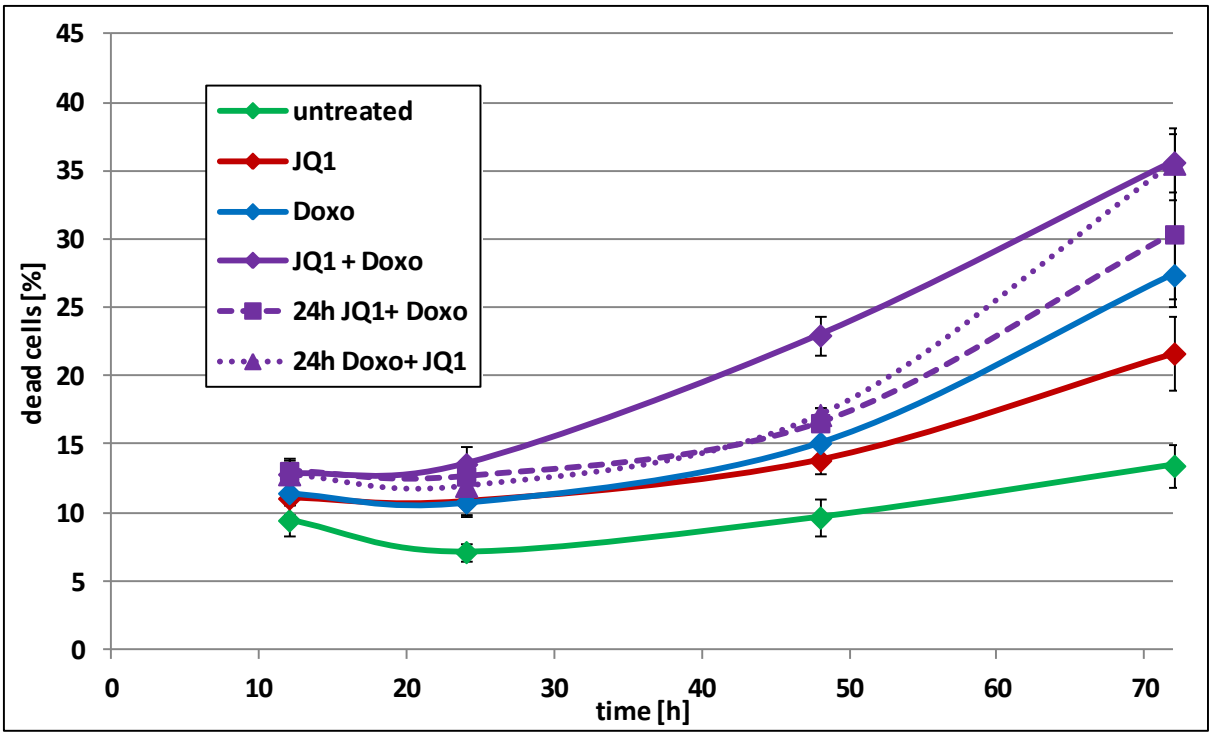

Figure 40: Cell death of IMR5/75 treated with JQ1 drug combinations. IMR5/75 cells were treated with 0.5 µM JQ1 and 0.05 µM doxorubicin in different combinations (Fig. 39). Samples were harvested after 12h, 24h, 48h and 72h. The cells were stained with propidium-iodide and analyzed by flow cytometry. Biological and technical triplicates were analyzed. Significance was tested with student t-test.

In summary, treatment with the BET-Inhibitor JQ1 was highly effective in reducing the viability of 55% of the *MYCN* amplified and 30% of the *MYCN* non-amplified neuroblastoma cell lines. Among the 23 cell lines treated with the inhibitor, no further genetic factors besides *MYCN* were found priming the cells unambiguous as JQ1 sensitive or resistant. FACS analyses revealed an accumulation of JQ1 sensitive and intermediate responding cells in the G1-phase as well as an increase of cell death for *MYCN* amplified cell lines. Nevertheless, IMR5/75 cells showed a fast regrowth when removing the inhibitor. MYCN protein levels were reduced upon JQ1 treatment in most of the *MYCN* amplified neuroblastoma cell lines, though treatment of IMR5/75 cells with siRNA against different BET-proteins revealed that the *MYCN* knockdown was not directly induced by BET inhibition. Differential gene and protein expression were detected for a number of cell cycle related genes. Especially among the gene expression data, differences regarding time points and pathways affected in JQ1-treated cells were described. A combination therapy of JQ1 and doxorubicin was shown to be more effective than single treatment with the drugs.

5.3 Therapy with BET inhibitor BAY1238097 using a subcutaneous neuroblastoma mouse model

In cell culture experiments, the two bromodomain inhibitors JQ1 and BAY1238097 showed high affectivity on 43% of the neuroblastoma cell lines in the panel used for viability screening, whereas 33% of the neuroblastoma cell lines were not affected by BRD4 inhibition. Especially anchorage independent growth was potently inhibited in all tested cell lines. Due to these promising results, therapeutic studies with the bromodomain inhibitor BAY1238097 were performed in mice. For these studies a subcutaneous neuroblastoma mouse model was chosen, because in this model, the xenograft tumor is palpable and measureable through the skin, which facilitates constant follow up of tumor growth.

The experiments with the subcutaneous neuroblastoma mouse model were supported by Dr. Sina Gogolin and the Core Facility Tumor Models at the DKFZ and financed by Bayer AG.

5.3.1 Method establishment of subcutaneous neuroblastoma xenograft models

First, subcutaneous neuroblastoma mouse models were established for different neuroblastoma cell lines, including the *MYCN* amplified cell lines IMR5/75, LS and KELLY, the *MYCN* non-amplified cell line SH-SY5Y and the *MYCN* non-amplified, but translocated cell line NBL-S. Despite of the *MYCN* status, the cell lines were chosen to represent further mutations characteristic for certain subgroups of neuroblastoma tumors (Table 9, chapter 5.2.1).

Two CD-1 nude mice per cell line were subcutaneously injected with neuroblastoma cells mixed with matrigel 1:1 in the right flank or with tumor cells only. The tumor growth was controlled and measured twice a week.

A first control of tumor growth was performed seven days after implantation. At this time point one tumor deriving from IMR5/75 cells was detectable, whereas all other mice did not show tumors until day 12 or 18 of the experiment (Figure 41). Implantations of tumor cells without matrigel did not result in tumor growth (data not shown).

The tumors arising from the cell lines LS, NBL-S and SH-SY5Y showed moderate tumor growth, reaching the maximum tolerable tumor size between day 30 and 49 after implantation. The growth behaviour of the two IMR5/75 tumors noticeably differed from each other. One of the mice harbored a very fast growing tumor that reached the maximum tumor size at day 18 after implantation. In contrast, the tumor of the second IMR5/75 mouse was not palpable until day 18 after implantation and presented a moderate tumor growth reaching the maximum tumor size at day 38 after implantation. The neuroblastoma cell line KELLY formed very small

tumors that were detectable at day 18 and did not show a relevant further tumor growth over the following 30 days until the end of the experiment.

Due to the fact that the tumors of KELLY neuroblastoma cells were not growing at all, it was decided to renounce this cell line for further experiments. It also became obvious from these experiments, that the usage of matrigel is essential for the growth of subcutaneous neuroblastoma xenograft tumors.

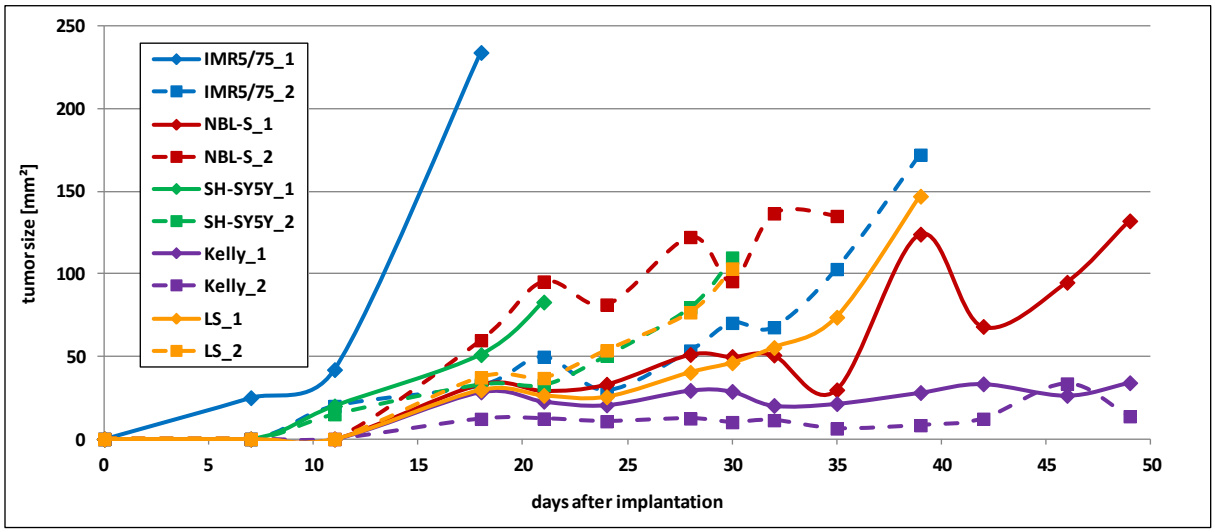

Figure 41: Growth of subcutaneous neuroblastoma xenograft tumors. Tumor growth after implantation of cells together with matrigel from five different neuroblastoma cell lines. Two CD-1 nude mice per cell line were implanted with the tumor cells.

5.3.2 Treatment of CD-1 nude mice harboring IMR5/75 xenograft tumors with BAY1238097

As tumor growth was successfully estimated in 4 out of 5 neuroblastoma cell lines in the preliminary experiment, a preclinical study with a BAY1238097-treated and a control group was approached.

7-8 weeks old CD-1 nude mice were subcutaneously injected with IMR5/75 neuroblastoma cells and matrigel in the right flank. The mice were examined daily, which comprehended measurement of tumor size, weighting and registration of general health condition. Mice with tumors were randomized into a control and a BAY1238097 treatment group. Treatment of the mice started, when the tumor reached an area of 25 mm² and was continued for up to 30 days. The dosage was 10 mg/kg BAY1238097 in NaCl 0.9% with pH=4, administered once daily per oral gavage. Because the control group was also used for comparison with two other inhibitors tested in parallel to BAY1238097, 80% PEG was given once per day as control vehicle.

The control group comprised 22 mice, from these seven animals were excluded from the analysis due to intraperitoneal tumor localization or a shortened treatment frame of less than

five days (Table 13). From the remaining 15 animals nine mice were treated for 30 days until the endpoint of the experiment, whereas the other six mice had to be euthanized at an earlier timepoint when reaching the maximum tolerable tumor size, which was 14 mm diameter in any direction. The group treated with BAY1238097 (BETi) counted 16 animals. From those, four mice were excluded before randomization, resulting in 12 mice that were finally used for BETi treatment. In the end, two mice were treated for 30 days and seven animals had to be euthanized earlier because of the tumor burden. From the remaining three mice, one mouse was excluded from the study because of weight loss and 2 mice were injured- one during oral gavage and one by biting.

Five mice of the control group were reinjected with IMR5/75 neuroblastoma cells in the left flank four weeks after the first implantation, because no tumor growth was detected in these animals up to this time point. The data from these mice are indicated in the following analyses.

Table 13: Overview of the CD-1 nude IMR5/75 xenografts. Reasons for excluding animals from the analysis were treatment less than five days or intraperitoneal tumor localization. Mice euthanized due to weight loss or injuries are categorized as "others".

Control	BETi
total animals: 22 (excluded: 7)	total animals: 16 (excluded: 4)
remaining animals: 15 → endpoint: 9 (60%) → tumor size: 6 (40%) → others: 0	remaining animals: 12 → endpoint: 2 (17%) → tumor size: 7 (58%) → others: 3 (25%)

a) Tumor growth of BAY1238097-treated and control CD-1 nude mice

Tumor growth of the IMR5/75 subcutaneous tumors was heterogeneous among both groups. In the control as well as in the BAY1238097-treated group were some tumors that were not or nearly not growing over the whole experimental period, whereas other tumors showed fast growth and reached the maximum tumor size in a short time frame. The growth curves of all tumors in this experiment are shown in Figure 42, starting from the first day of treatment until death of the mouse.

Among the control group eight tumors nearly showed no tumor growth over the 30 days treatment period (Figure 42A). In contrast, a faster tumor growth was observed for seven of the 15 animals. The growth curves of these mice separated from the mice with no further tumor growth after about 15-20 days treatment. The growth behavior of the mice reinjected with tumor cells, because no tumor was growing in the first attempt (indicated in light blue in the Figure), did not differ from the other mice and included fast growing as well as not growing tumors.

In the group treated with BAY1238097 most mice showed a fast and continuous tumor growth (Figure 42B). The growth curves of these fast growing tumors separated from those with no growth after 10-15 days of treatment, and thereby five days earlier than the control tumors. Among the BAY1238097 group was one tumor growing very fast (BETi_3), one tumor showed no growth at all (BETi_10) and one started fast tumor growth late during the treatment period (BETi_5). The mice for whose the experiment ended earlier for irregular reasons, such as injuries or weight loss, are indicated in light green in the Figure.

Altogether the BAY1238097-treated group of tumors behaved more uniform than the control group. Health problems occurred for one mouse from the BAY1238097-treated group that lost 15 % of its body weight. Beside this, the inhibitor and the control substance were well tolerated by the mice.

Additional to the growth curves of the single tumors, the average tumor size on each treatment day was calculated for the control and BAY1238097-treated animals. These mean values are presented in Figure 43. Until treatment day 13 the mean tumor growth of the control and BAY1238097-treated animals proceeded quite parallel. From day 14 on, the BAY1238097-treated tumors grew faster than the control tumors. This effect was detectable until treatment day 23. Then the mean tumor size of the BAY1238097-treated animals remained static, because four of the animals with large tumors were euthanized within two days. The control group showed slow but continuous tumor growth throughout the experiment.

In total, the BAY1238097-treated group presented a faster and more homogeneous tumor growth than the control group. This is contrary to the expected results, based on the finding that BAY1238097 acted as a potent inhibitor in cell culture and effectively reduced viability in IMR5/75 cells. The high variability and the significant number of not growing tumors among the control group hindered a detection of potential inhibitory effects of the tested agent.

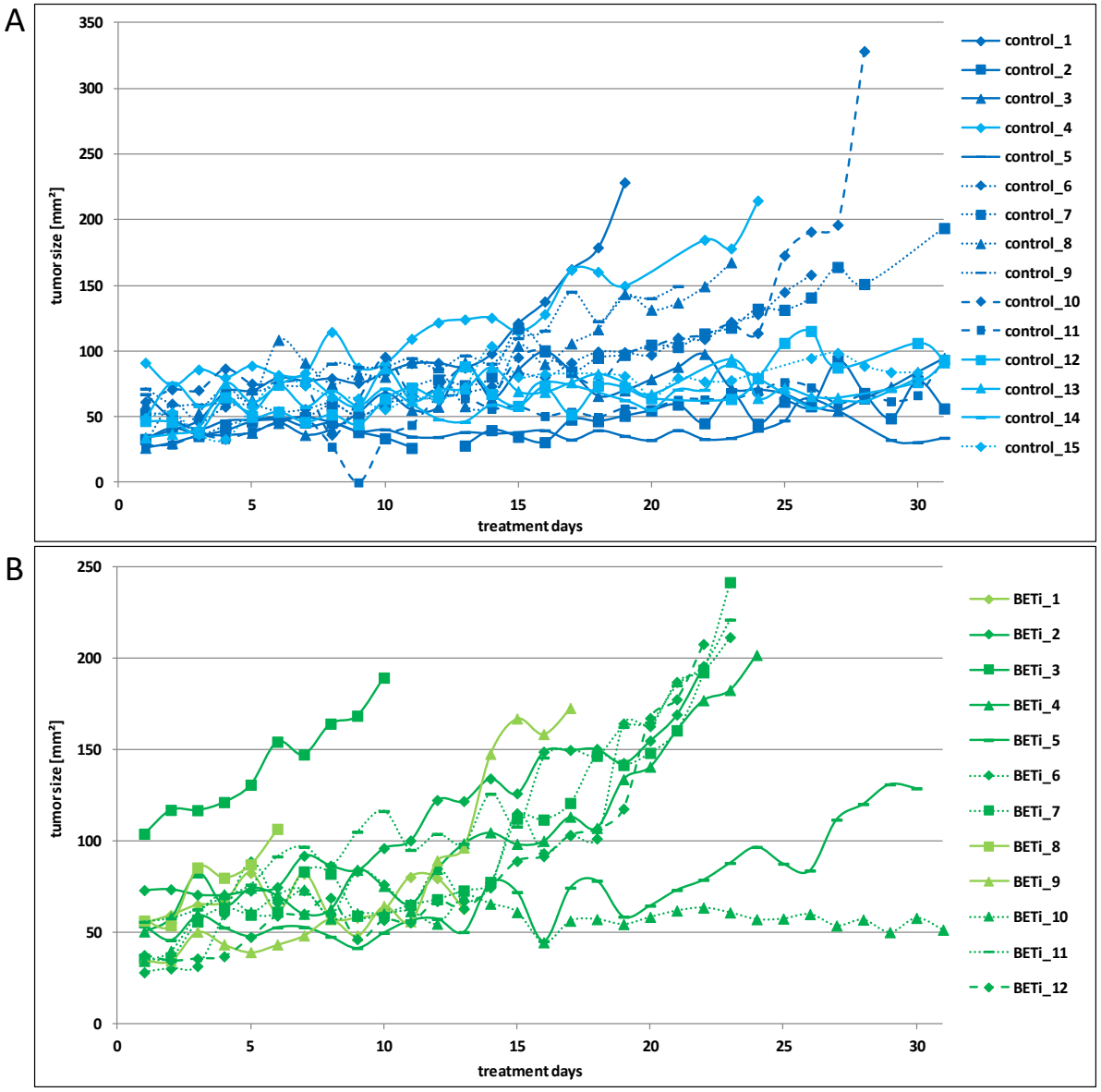

Figure 42: Tumor growth of each animal during treatment. Tumor growth curves of all animals starting from first day of treatment. Tumor size was measured through the skin with a caliper. A) Tumor growth of control animals. Dark blue graphs show animals with regular tumor growth. Light blue graphs show animals that were injected with tumor cells a second time on the opposite side. B) Tumor growth of BAY1238097-treated animals. Dark green graphs show animals with regular tumor growth. Light green graphs show animals that dropped out of the experiment due to irregular reasons (injury, weight loss).

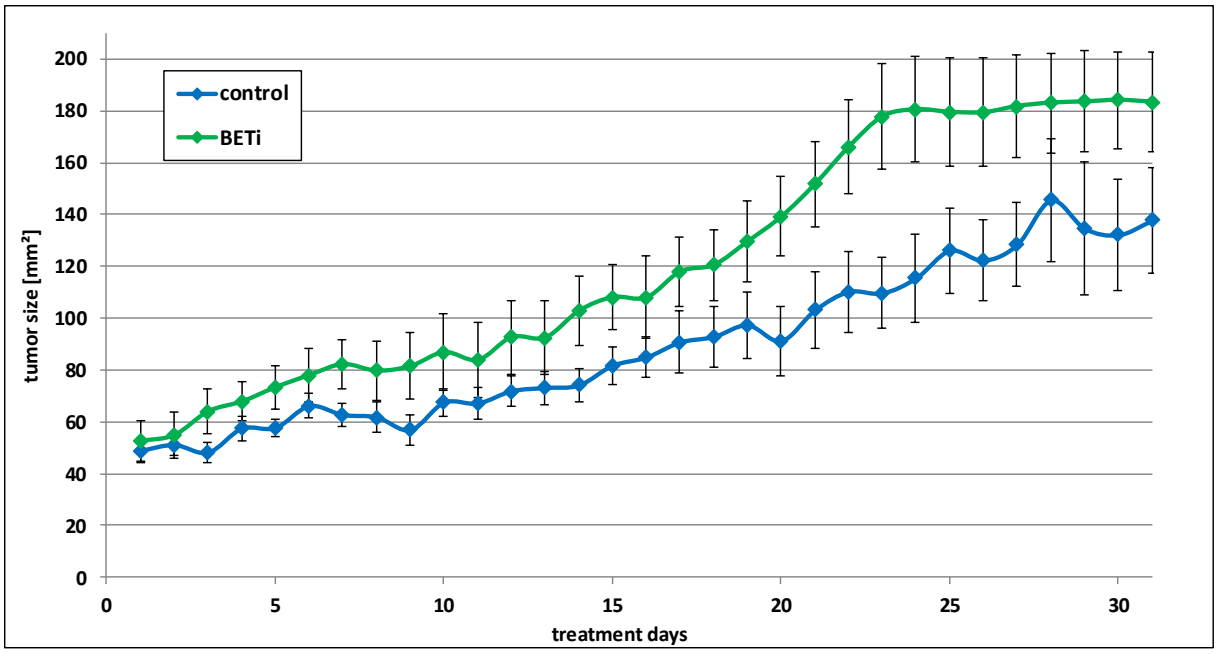

Figure 43: Comparison of tumor growth of BAY1238097-treated and control mice. The diagram shows the mean values of the tumor size from all animals for each treatment day. The LOCF method was used, calculating with the last value observed for animals excluded before end of the observation time. Animals that dropped out of the study for irregular reasons were not considered in the analysis. Tumor size was measured through the skin using a caliper. Significance was tested with student t-test ($p>0.05$).

b) Effect of BAY1238097 treatment stated on treatment duration and tumor size

Tumor growth curves are not the only way to assess the effectivity of the tested inhibitor BAY1238097 *in vivo*. Total treatment time and maximum tumor size provide additional information to state the effect of BAY1238097 treatment on IMR5/75 based xenograft tumors.

Figure 44A demonstrates how many days the mice were treated during the experiment. The mice were treated with BAY1238097 or control vehicle for maximum 30 days and were euthanized the next day after measurement of tumor size *in situ*, which resulted in a total experimental duration of up to 31 days. Shorter periods occurred because of tumor burden or health reasons. For a successful therapy it would have been expected that treatment with BAY1238097 slows down tumor growth and thereby increases the time the mice remain in the study.

Among the control group, several animals were in the experiment for the maximum duration of 31 days, consequently the mean treatment duration was high with 27.9 days (median 30 days). In the BAY1238097-treated group (BETi), the mean and median treatment duration was clearly lower with 23.1 and 23.0 days, respectively. Altogether, the mice in the BAY1238097 group stayed in average one week shorter in the experiment, which was unexpected.

The tumor size *in situ* of control and BAY1238097-treated mice is shown in Figure 44B. In the control group the tumors were smaller than in the BAY1238097-treated group: The mean size

of the control tumors was 138 mm², compared to 183 mm² in the BAY1238097 animals, measured *in situ* in living mice. After dissection of the euthanized animals the tumor size was measured again. The difference in size of the tumors *ex situ* was even higher with a mean size of 76 mm² for the control group and 144 mm² for the BAY1238097-treated animals. The variability of the control tumors was larger than for the BAY1238097-treated group, spanning from 34 to 328 mm². This variability was to be expected according to the inconsistent growth curves of the control animals.

The finding that the tumors in the control group were smaller than the tumors of the BAY1238097-treated animals is contrary to the expected results. Together with the results from the treatment duration and the tumor growth, no inhibitory effect of BAY1238097 could be seen on IMR5/75 xenografts in CD-1 nude mice. In contrast, the tumors treated with BAY1238097 grew even better than those from the control mice.

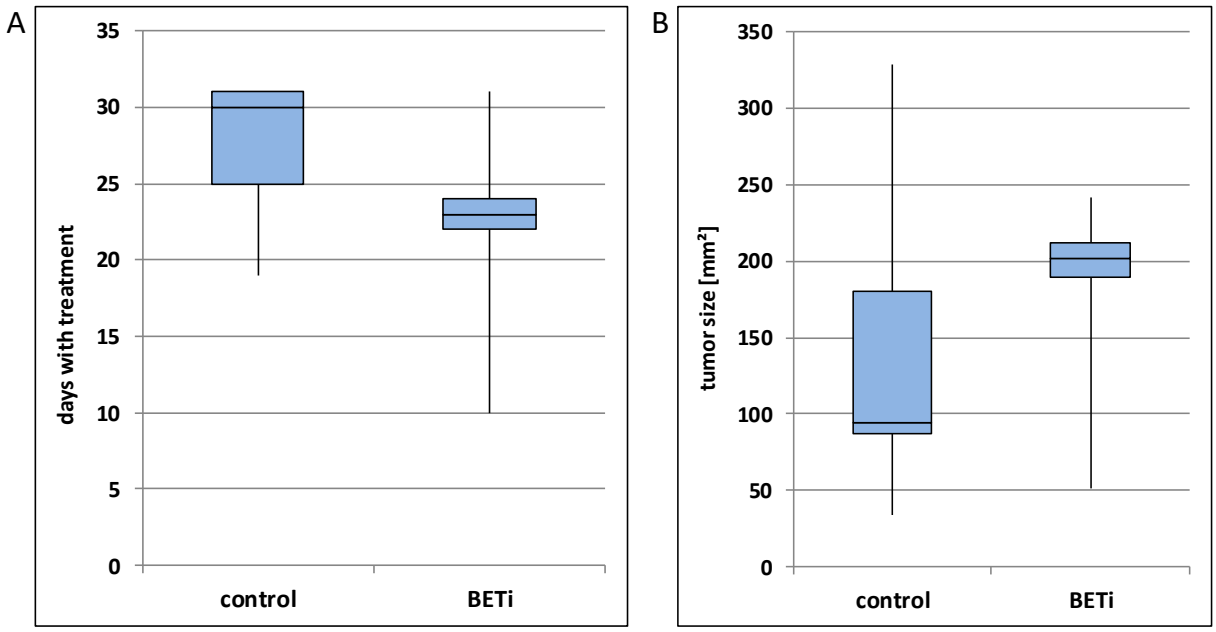

Figure 44: Effect of BAY1238097 treatment on treatment duration and tumor size. Animals that dropped out of the study for irregular reasons were not considered in the analysis. Significance was tested with student t-test ($p>0.05$). A) Treatment duration with BAY1238097 compared to the control group. The numbers of days the mice were followed up after treatment start in the BETi and the control group is presented. B) Tumor size at the end of the experiment. The tumor was measured in situ the day after the last treatment of the mice, using a caliper.

c) Heterogeneity of tumor growth onset

IMR5/75 xenograft tumors in CD-1 nude mice show high variability in tumor growth and tumor size. This is especially true for the control animals. Some differences are also seen in terms of the start of tumor growth, concretely the time from implantation of the tumor cells until the tumors reached a size of 25 mm², which was the cutoff size for the treatment start. The tumor onset of the control and BAY1238097-treated animals is shown in Figure 45A.

The tumor onset of the control group is divided into three subgroups. The largest group with 11 out of 15 animals has an early tumor onset with a period of 5-10 days between implantation and treatment start. One mouse took an intermediate time for tumor onset with 16 days, whereas tumor growth started late in three animals with more than 20 days incubation. The tumors from the mice reinjected with tumor cells all belonged to the early onset group, indicated in light blue in the Figure. The mice in the BAY1238097-treated group had either early or late tumor onset. Both groups consisted of six animals. The incubation time till tumor onset was equal to the time for the control group, with 6-9 days for early onset and 19-28 days for late tumors.

To find out if an early or late tumor onset correlates with the tumor growth behavior, the treatment start and the treatment duration for each animal were plotted in a separate diagram (Figure 45B). No correlation was observed between tumor onset and treatment time. Both, the tumors with early and late tumor onset included slowly growing tumors from mice that were in the experiment until the 30 day treatment was finished as well as faster growing tumors that reached the maximum tumor size before the experiment ended.

In summary, the differences in tumor onset are not the reason for the high variability of the tumor growth, as the control and BAY1238097-treated mice are similar distributed into early and late onset animals and as no correlation was found between tumor onset and growth behavior.

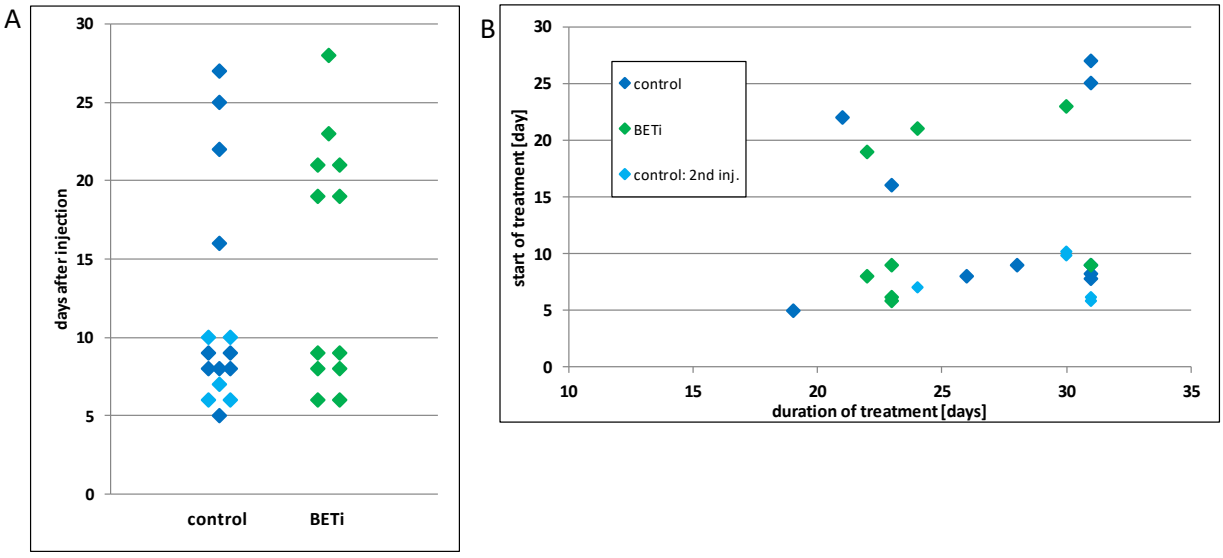

Figure 45: Growth characteristics of IMR5/75 xenografts in CD-1 nude mice. A) The period of time between neuroblastoma cell implantation and tumor onset is demonstrated. Reinjected control mice are indicated in light blue. Significance was tested with student t-test ($p>0.05$). B) Correlation of treatment start and duration of treatment. Animals that dropped out of the study for irregular reasons were not considered in the analysis.

d) Macroscopic and histological differences

At the end of the experiment the mice were euthanized. Photos were taken from the tumors *in situ* and after they were dissected, tumor size and weight were documented. Differences between the tumors were visible on the first glance regarding color and structure of the tumors. Some tumors were dark red, some light red with a marbled surface and some not colored at all, looking pale (Figure 46). Concerning the structure there were few tumors with a nodose structure, whereas most of the tumors had a smooth surface. A number of animals harbored two or three tumors close by but separated from each other. Those multiple tumors either belonged to the same or to different categories regarding tumor color.

For histological appraisal, cryoslices were prepared and stained with hematoxylin/eosin. The appraisal was done by Dr. Tanja Poth from the pathology department. All tumors were identified as neuroblastoma. Further analysis regarding differentiation status of the tumor samples was not possible because the quality of the tumor material was not satisfactory.

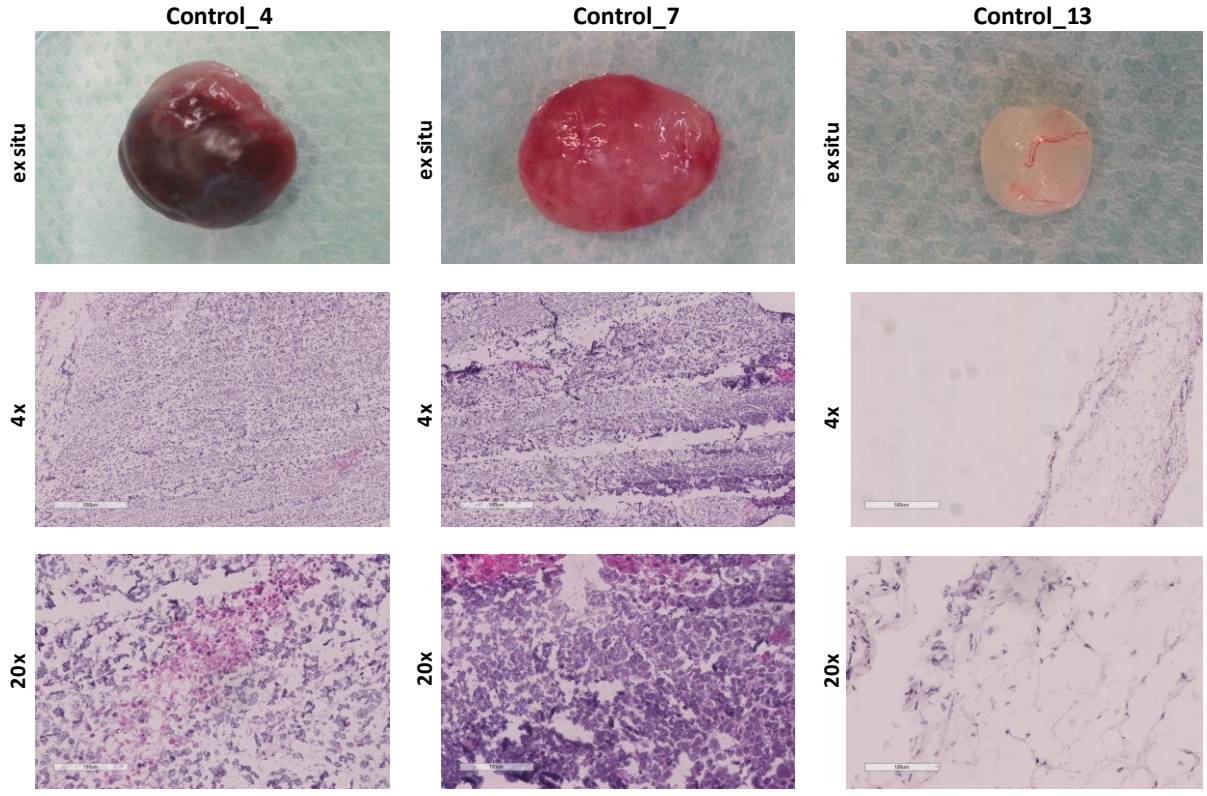

Figure 46: Macroscopic and histological appearance of IMR5/75 xenografts. Exemplary pictures from a dark red (Control_4), a light red (Control_7) and a pale (Control_13) subcutaneous xenograft tumor with the corresponding histological presentation are shown.

The results for each mouse concerning tumor growth, onset and size as well as macroscopy and histology are summarized in table 14 for control and table 15 for BAY1238097-treated animals.

Table 14: Overview of IMR5/75 xenograft control mice.

mouse	tumor in situ			tumor ex situ			histology		
	growth	onset	size [mm²]	size [mm²]	weight [mg]	macroscopy	diagnosis	tumor content	necrosis
control_1	++	early	228	143	450	light red	NB	80%	No
control_2	-	early	56	39	40	pale	NB	90%	No
control_3	-	early	95	69	60	pale	NB	80%	No
control_4	++	early	215	162	510	dark red	NB	90%	No
control_5	-	late	34	28	20	pale	NB	10%	No
control_6	+	early	158	122	170	light red	NB	90%	No
control_7	+	late	194	130	320	light red	NB	100%	No
control_8	++	intermediate	168	115	190	dark red/pale	NB	90%	No
control_9	++	late	149	150	300	light red	NB	90%	Yes
control_10	+	early	328	132	280	dark red/light red	NB	90%	No
control_11	-	early	93	56	80	dark red	NB	90%	No
control_12	-	early	93	38	50	pale	NB	100%	No
control_13	-	early	91	30	30	pale	NB	10%	No
control_14	-	early	79	25	30	pale	NB	50%	No
control_15	-	early	84	22	20	pale	NB	20%	No

Table 15: Overview of IMR5/75 xenograft BAY1238097-treated mice. For BETi_1 and BETi_8 the growth behavior could not be categorized because the mice dropped out due to irregular reasons after 13 and 6 days.

mouse	tumor in situ			tumor ex situ			histology		
	growth	onset	size [mm²]	size [mm²]	weight [mg]	macroscopy	diagnosis	tumor content	necrosis
BETi_1	?	late	63	67	77	light red	NB	80%	Yes
BETi_2	++	late	196	156	426	dark red	NB	90%	Yes
BETi_3	+++	late	190	126	233	dark red/pale	NB	100%	Yes
BETi_4	++	late	202	123	251	dark red	NB	100%	No
BETi_5	+	late	129	94	118	light red	NB	60%	No
BETi_6	++	early	212	188	464	pale	NB	80%	No
BETi_7	++	early	242	160	490	dark red/pale	NB	95%	No
BETi_8	?	late	107	74	133	light red	NB	90%	No
BETi_9	++	early	173	155	359	light red	NB	70%	No
BETi_10	-	early	52	54	15	pale	NB	70%	No
BETi_11	++	early	221	181	447	pale	NB	80%	No
BETi_12	++	early	208	210	421	dark red/pale	NB	80%	No

The majority of pale tumors were not or slowly growing, whereas the tumors colored light or dark red grew constantly in most cases. In the control group 4 out of 7 pale tumors had a low tumor content of 50% or less in the histological analysis. In contrast, all colored tumors had a tumor cell content >80%. From the five reinjected animals, in four mice the tumor was not

growing. These mice have in common that the tumors were pale and small and 3 out of 4 had a low tumor content of 50% and below in the histological analysis.

When comparing the size of the tumors that was measured *in situ* through the skin with the real size measured after taking out the tumors, it was seen that in nearly all cases the real tumor size was smaller than measured in situ throughout the experiment. Especially in the control group were big differences between the size measured *in situ* and *ex situ*.

Summarizing the results from the IMR5/75 xenograft tumors treated with BAY1238097 in CD-1 nude mice, the expected effects were not seen. Treatment with the bromodomain inhibitor BAY1238097 did not result in growth inhibition, neither in smaller tumor size nor prolonged survival. In contrast, the tumors were more likely growing better when treated with the inhibitor compared to the control group. The high variability in the control group with many tumors that were not or slowly growing has distorted the results and caused the observed putative growth promoting effect of BAY1238097.

Among the control group 8 out of 15 mice harbored not or slowly growing tumors, which equates more than half of the control animals. Among those were four mice reinjected with tumor cells because on the first attempt no tumor growth was detected at all. The heterogeneity of the tumors was also seen when comparing the appearance of the tumors and the tumor onset. In contrast to the appearance, the tumor onset was not correlating with tumor growth.

Compared with the control group, tumor growth of the mice treated with BAY1238097 was less variable. It is not known why these animals with better tumor growth were pooled in the BAY1238097-treated group and were not equally distributed over both the BAY1238097 and the control group. In the BAY1238097-treated group only one tumor was not growing, whereas most of the mice harbored fast growing tumors. Comparing the growth curves, the exponential growth phase of the tumors started a few days earlier in the BAY1238097-treated mice.

Due to these results, it was questioned if the variable tumor growth might be linked with an inappropriate mouse strain chosen for the experiment. The CD-1 nude mice used for tumor growth have no thymus and therefore lack a T-cell response including cytotoxic T-cells. B-cells and innate immune system are present in this mouse strain [155]. Though the CD-1 nude mice are especially recommended for xenograft tumor models, it was questioned if the remaining immunological competence may be enough to prevent tumor growth in the animals to different extent.

5.3.3 Comparison of different mouse strains for their use in a subcutaneous neuroblastoma mouse model

Tumor growth of the IMR5/75 xenograft tumors in CD-1 nude mice was highly heterogeneous and slower as expected especially among the control mice. Due to these observations it was assumed, that the CD-1 nude mouse strain might not be suitable for a subcutaneous neuroblastoma mouse model. Therefore, two additional mouse strains of immunocompromized mice were tested for subcutaneous tumor growth of neuroblastoma tumor cells.

For the study, tumor growth of the neuroblastoma cell lines IMR5/75, LS, NBL-S and SH-SY5Y was tested in the mouse strains NSG and NMRI compared to CD-1 nude. $5x10^6$ tumor cells were subcutaneously injected in the flank and tumor size was measured twice per week. From each mouse strain, six animals were tested for each cell line. The experiment ended 50-56 days after tumor cell implantation, dependent on the growth behavior of the cell line used.

a) IMR5/75 xenografts

In CD-1 nude mice harboring IMR5/75 deriving tumors, again a high variability in tumor onset and growth was observed (Figure 47A). One tumor was fast growing; it was detectable at day 19 after implantation and reached the maximum tolerated tumor size at day 26. From the other five CD-1 nude mice, two harbored very small tumors with an average tumor weight of 260 mg (Figure 47B) and had a late tumor onset. In one mouse no tumor growth was detected at all, and in the remaining two animals a bulge was measured without a detectable tumor at dissection at the end of the experiment.

Using the mouse strain NMRI, tumors were growing in all six mice. Until day 19 after implantation, the tumors were growing in parallel with similar sizes. Later on, they divided into two groups: four tumors were growing continuously, and two tumors showed a growth arrest for approximately 2.5 weeks before growing again. The average tumor weight was 490 mg.

The most homogeneous growth of IMR5/75 tumors was observed in NSG mice. All mice harbored a tumor with similar growth curves and all six tumors reached the maximum tolerable tumor size before the endpoint of the experiment. The weight of the tumors showed a low deviation and the average tumor weight of 1.070 mg was the highest of all three mouse strains ($p<0.005$).

Altogether these results show that choosing a suitable mouse strain has high influence on tumor growth and tumor onset and thereby on the homogeneity of the group in total. A group of mice with a low deviation regarding the basic tumor growth increases the power of the complete data set of a mouse treatment study and facilitates finding of differences between control and drug-treated animals.

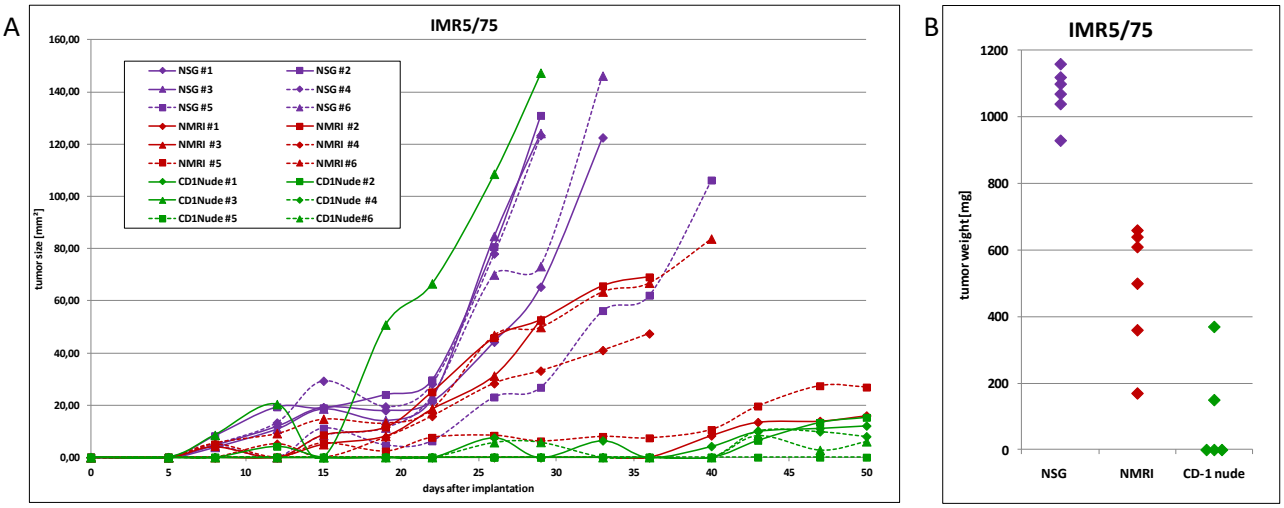

Figure 47: IMR5/75 tumor growth in three different mouse strains. NSG (purple), NMRI (red) and CD-1 nude mice (green) were subcutaneously injected with IMR5/75 cells. A) Tumor growth of six animals from each mouse strain. B) Tumor weight at the endpoint. The tumor weight of CD-1 nude#3 is unknown. P-value was <0.005 for NSG mice compared to both other mouse strains (student t-test).

b) other neuroblastoma cell lines: SH-SY5Y, LS, NBL-S

The comparison of different mouse strains with IMR5/75 deriving xenograft tumors revealed clear differences regarding tumor growth behavior. Comparable results have been observed for the other three neuroblastoma cell lines LS, NBL-S and SH-SY5Y, which were also planned to be included in the BAY1238097 treatment study.

With the cell line LS, tumor growth in the CD-1 nude mice showed the highest variability of all three mouse strains and the lowest growth rate (Figure 48A and B). In two CD-1 nude mice, no tumor was detected at all, two mice harbored a small and slowly growing tumor and two mice showed an intermediate tumor growth. In NMRI mice, five LS-derived tumors were growing in total. In NSG mice, tumors were growing in all six animals. The tumors were detected at day 18-21 after implantation and were growing quite homogeneously: four tumors showed a fast growth and two tumors were a bit delayed and growing in parallel with the tumors of the NMRI mice. Comparing size and weight of the LS-deriving tumors, the NSG mice had the largest tumors and the lowest variability in tumor size ($p<0.05$).

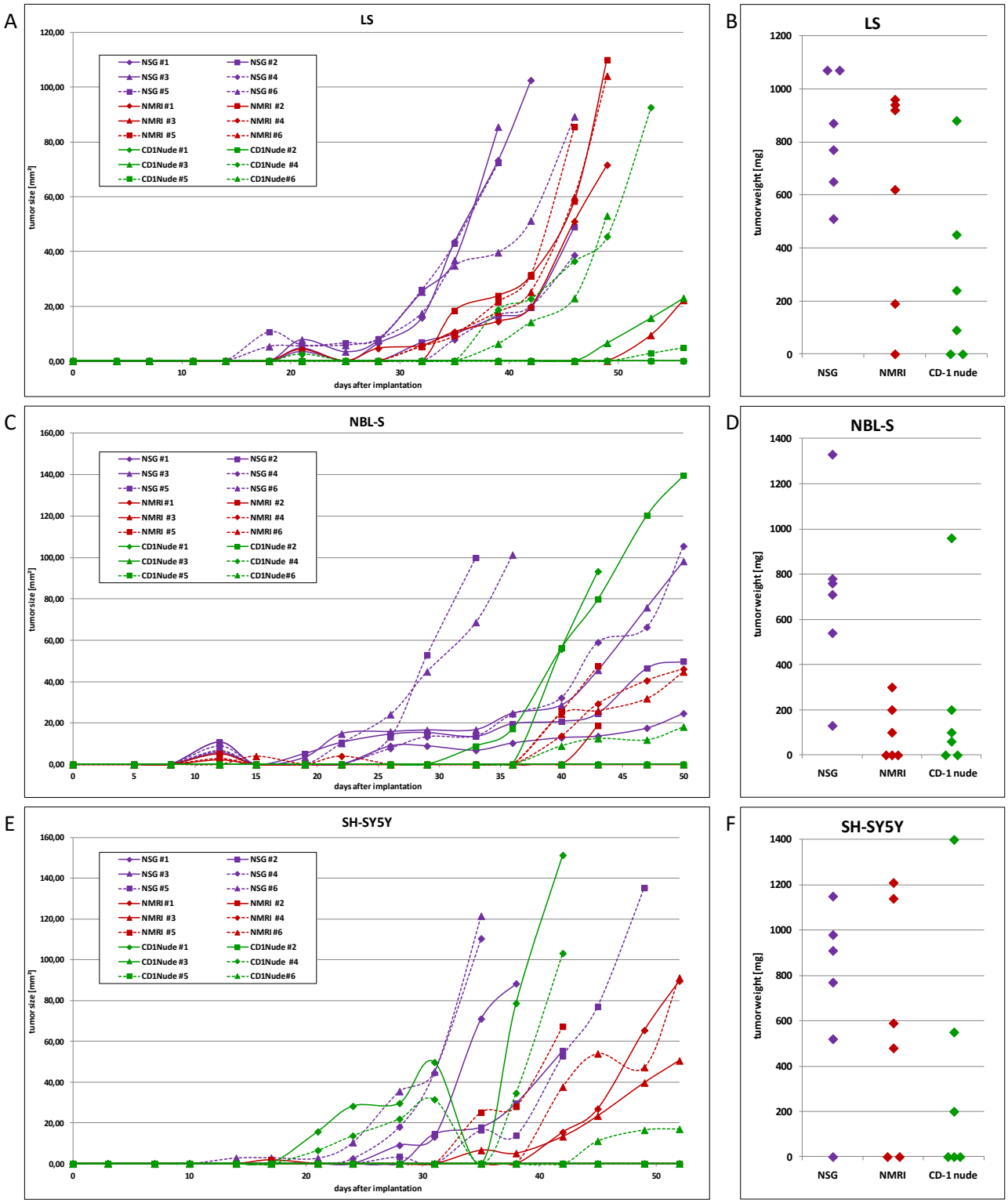

Figure 48: Neuroblastoma tumor growth in different mouse strains. NSG (purple), NMRI (red) and CD-1 Nude mice (green) were injected with different neuroblastoma cell lines subcutaneously. Significance was tested with student t-test. A) Tumor growth of mice injected with LS cells. B) Tumor weight of LS neuroblastoma tumors. C) Tumor growth of mice injected with NBL-S cells. D) Tumor weight of NBL-S neuroblastoma tumors. E) Tumor growth of mice injected with SH-SY5Y cells. F) Tumor weight of SH-SY5Y neuroblastoma tumors.

Among the tumors deriving from NBL-S cells, NSG mice showed the fastest tumor growth and the highest tumor weight (Figure 48C and D, $p<0.05$). Each NSG mouse harbored a tumor, whereas among the NMRI as well as the CD-1 nude mice 3 out of 6 animals were negative for a tumor or showed ambiguous results. Tumor growth in the NMRI mice started between day 36 and day 40 after implantation, in contrast to tumor onset in the NSG mice that took place between day 15 and day 22. In CD-1 nude mice the period until tumor growth was detectable was 28-36 days. In total, the variability within the NSG group was higher with NBL-S cells than for the cell lines LS and IMR5/75 discussed before. This is probably due to the clustering growth behavior of NBL-S cells, which is impeding equal implantation of the tumor cells. Still, tumor growth data in NSG mice showed better results regarding tumor growth, tumor onset and tumor size than in the other two mouse strains tested.

The SH-SY5Y cell line showed the worst tumor growth rate from all four cell lines included in the experiment (Figure 48E and F). In the NSG mice injected with SH-SY5Y, 5 out of 6 mice developed a tumor. Among the NMRI mice four animals harbored a tumor and three tumors were observed in CD-1 nude mice. The growth curves with each mouse strain were more variable with SH-SY5Y than with tumors deriving from other neuroblastoma cell lines. At first, SH-SY5Y tumors were detectable in the NSG mice 20-28 days after tumor cell implantation. From the time point on, when the tumors were measureable, the SH-SY5Y deriving tumors showed a fast growth and the maximum tolerable tumor size was reached after a short period in all three mouse strains. The mean tumor weight at the endpoint of the experiment was comparable in all three mouse strains with the highest variance in the CD-1 nude mice and the lowest variance in NSG mice ($p>0.05$).

The experiment with the other neuroblastoma cell lines LS, NBL-S and SH-SY5Y underlines that the NSG mice are the most suitable mouse strain for a subcutaneous neuroblastoma mouse model. NSG mice are a severely immunodeficient mouse strain with a non-functional T-, B- and NK-cell response [156]. In contrast, the CD-1 nude mice previously used for the subcutaneous mouse model are lacking a T-cell response, whereas the innate immune system is functional [157]. The differences between the mouse strains were most obvious with IMR5/75 cells but also the other three cell lines tested showed the best results in NSG mice.

5.3.4 Toxicity study with BAY1238097 in NSG mice

Before starting a complex treatment study with a large number of animals, it was tested if the aimed daily dose of BAY1238097 of 10 mg/kg body weight was tolerated by the NSG mice. For this experiment, NSG mice without tumors were treated with BAY1238097 in NaCl 0.9%/pH4 or control vehicle NaCl 0.9%/pH4 once daily for 30 days administered by oral gavage. Both the control and the BAY1238097 group comprised six animals each. The tolerance of the inhibitor was monitored by daily weighting of the mice. A weight loss of 10% or more would be the main sign that the administered dosage is too high. Aside weight loss other criteria, such as diarrhea or a poor general condition, were also monitored.

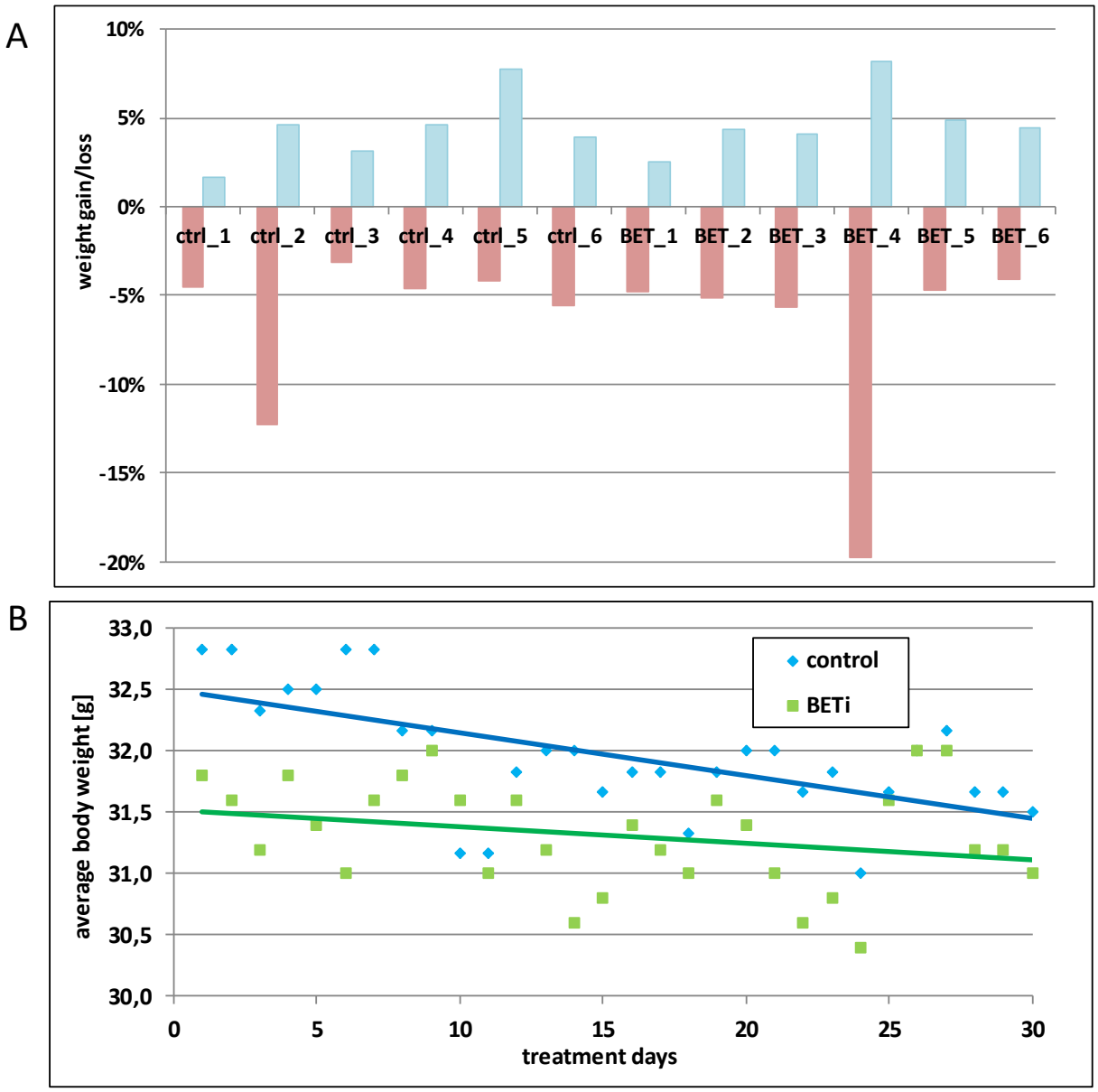

Figure 49: Weight variability of mice treated with BAY1238097. Six mice were treated daily with BAY1238097 or control for 30 days. Body weight of the mice was controlled daily. A) Highest and lowest weight of each mouse during the 30 days treatment compared to the average weight of this animal. B) Average body weight of all control and BAY1238097-treated mice for each treatment day. A trendline shows the change of body weight over time.

Figure 49A shows the variation in body weight for each of the control and BAY1238097-treated mice. The average body weight of each mouse was set to 100% and compared with the maximum and minimum body weight measured during the 30 days of the experiment. For most of the mice in both groups the maximum fluctuation ranged about 5% around the average body weight. In the control group, 1 out of 6 mice showed more than 10% weight loss, which was only temporary due to diarrhea. In general, BAY1238097 was well tolerated by the mice, no diarrhea or weight loss was observed in 5 out of 6 mice. One animal treated with BAY1238097 showed a weight loss >20% and was immediately euthanized.

Additional to the minimum and maximum body weight of each mouse it was interesting how the weight of the mice develops over the whole treatment period. Therefore, the mean body weight of all control and BAY1238097-treated mice was calculated for each treatment day (Figure 49B). A linear trendline gives an idea on the weight development over the whole 30 days of treatment. The BAY1238097-treated mouse euthanized due to weight loss was excluded from the analysis. The analysis shows that both the control and the BAY1238097-treated animals lost weight during the experiment.

As the weight loss occurs in both the BAY1238097-treated and control group and no signs of side effects such as diarrhea or apathy, it is likely that the substance itself is not the reason for the dropping weight. There are two other reasons that could be an explanation for the moderate weight loss in both groups. Supposably, the animals are stressed when they are taken out and gavaged daily. Second, a local irritation of the gullet due to the oral gavage might lead to a lower food uptake.

5.3.5 Full study: Treatment of NSG mice harboring heterotopic neuroblastoma xenograft tumors with BAY1238097

After the end of the preliminary experiments, the full study with BAY1238097 applied to NSG mice with neuroblastoma tumors deriving from four different cell lines was performed. For each cell line, 12 animals for control and 12 animals for the BAY1238097-treated group were subcutaneously injected with neuroblastoma tumor cells. The cell lines used for this experiment were IMR5/75, LS, NBL-S and SH-SY5Y. Tumor size was measured twice a week through the skin, using a caliper. When the tumors reached 3-4 mm in diameter, mice were randomized and the treatment was started. The mice were treated with BAY1238097 in NaCl 0.9%/pH4 or with the control vehicle NaCl 0.9%/pH4 once daily, administered by oral gavage for maximum 30 days. Criteria for a premature euthanasia of the mice were reaching of the maximum tolerated tumor size of 14 mm diameter in one direction, weight loss of more than 20%, injuries or poor health condition.

a) IMR5/75

The neuroblastoma cell line IMR5/75 is a *MYCN* amplified and highly proliferating cell line. In previous experiments under cell culture conditions, both BAY1238097 as well as JQ1 showed a high affectivity on IMR5/75 cells.

In vivo, the time from implantation of the tumor cells until tumor onset was varying among the tumors deriving from IMR5/75 cells. Resulting out of this, randomization and treatment start among the IMR5/75 control tumors were widely distributed between day 9 and day 21 after implantation. In the BAY1238097-treated group nearly all animals started treatment at day 18 after implantation, except two animals that were delayed until day 21 and 28.

The tumor growth curves from all IMR5/75 tumors are separately presented in Figure 50, giving an idea on the heterogeneity of the groups and the growth characteristics the tumors in the control or BAY1238097-treated group might have in common. In the control group, all tumors were growing continuously throughout the experiment (Figure 50A). They could be divided in a group of seven fast growing tumors and five tumors with a delayed growth compared to the others. Among the group treated with BAY1238097 10 out of 12 tumors were continuously growing, one tumor showed a growth arrest and one tumor was growing slowly (Figure 50B). Compared to the control group, the growth curves of the tumors in the BAY1238097-treated group were less precipitous, especially in the early treatment days. The entry of the tumors treated with BAY1238097 into the exponential growth phase was delayed.

Analysis of the tumor growth of IMR5/75 derving tumors was influenced by the differences in tumor onset, going along with varying growth characteristics of the tumors. Late onset tumors tended to present with fast tumor growth, reaching the maximum tolerated tumor size in relatively short time. As the mean tumor onset was five days earlier in the control group than in the BAY1238097-treated group, fast growing tumors could be overrepresented in BAY1238097-treated mice and disguise a potentially larger effect of drug treatment.

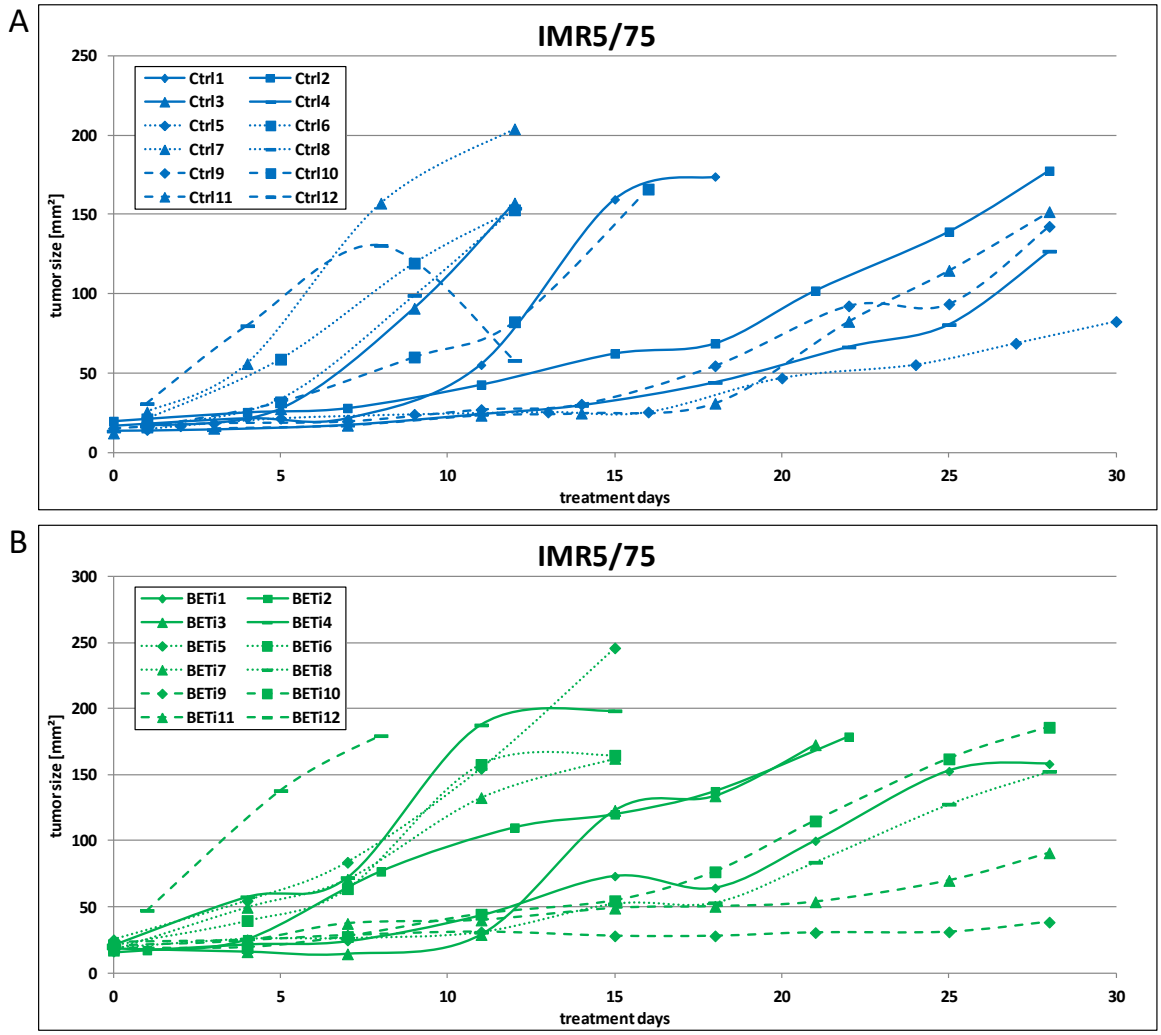

Figure 50: Tumor growth of IMR5/75 xenograft tumors. Treatment with BAY1238097 or control started at day one. The tumor size was measured through the skin twice a week. A) Tumor growth of control animals. B) Tumor growth of BAY1238097-treated animals.

The survival of the mice was visualized in a Kaplan-Meier plot (Figure 51A). The endpoint at day 31 was reached by one animal from the control group and by three of the BAY1238097-treated mice. All other mice reached the maximum tumor size before the experiment ended and therefore were euthanized earlier. Although the survival curves resemble each other, the median treatment duration was increased from 17.5 in the control group to 22.5 days in the BAY1238097-treated group. The increase of survival is not significant ($p>0.05$).

Figure 51B compares the tumor size at the last day of treatment of each mouse. For IMR5/75 the median tumor size of the control and the BAY1238097 group did not show significant differences ($p>0.05$). Most tumors had a weight between 150 mg and 200 mg, the variability was low.

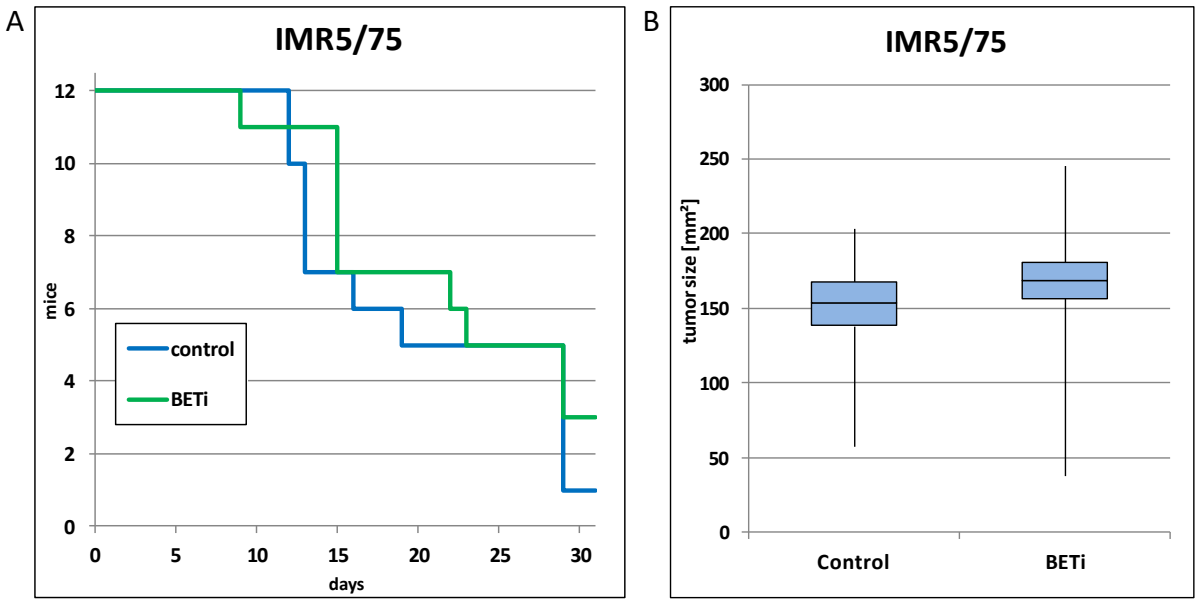

Figure 51: Effect of BAY1238097 treatment on IMR5/75 xenografts. The effectiveness of BAY1238097 on xenografts from IMR5/75 neuroblastoma cells in NSG mice is demonstrated. Significance was tested with student t-test. A) Kaplan Meier plot illustrates treatment duration for control and BAY1238097-treated mice. B) Tumor size at the end of the experiment. The tumor was measured through the skin with a caliper.

Altogether, no significant inhibitory effect was observed for IMR5/75 deriving tumors. This was unexpected regarding to the results with IMR5/75 under cell culture conditions, showing high sensitivity upon JQ1 treatment (section 5.2). The inhomogeneity of the tumor onset especially in the control treatment group, might have had an impact on the results.

b) LS

LS is a *MYCN* amplified cell line with additional proliferation promoting amplifications of *CCND1*, *MDM2* and *CDK4*. *In vitro* viability assays predicted an intermediate response to BAY1238097, whereas LS cells treated with the BRD4 inhibitor JQ1 showed high sensitivity to the substance.

Subcutaneous xenografts deriving from LS cells reached the size necessary for treatment start 20-25 days after tumor implantation. The mice in the control group showed a steady tumor growth with uniform tumor growth curves (Figure 52A). The maximum tumor size was reached by all 12 mice during treatment; no mice were treated for the complete 30 days. Compared to the control animals, the tumors in the BAY1238097-treated group were growing more slowly (Figure 52B). All tumors were getting larger continuously, but the growth curves were more plane than the tumor growth curves of the control animals. The tumor growth was homogeneous with most of the growth curves resembling each other. After 30 days of treatment with BAY1238097 two mice were alive, all other animals had to be euthanized due

to tumor burden. Tumor size of the BAY1238097-treated mice was significantly lower than tumor size of the control group at treatment day 24 ($p<0.001$) (Figure 52C).

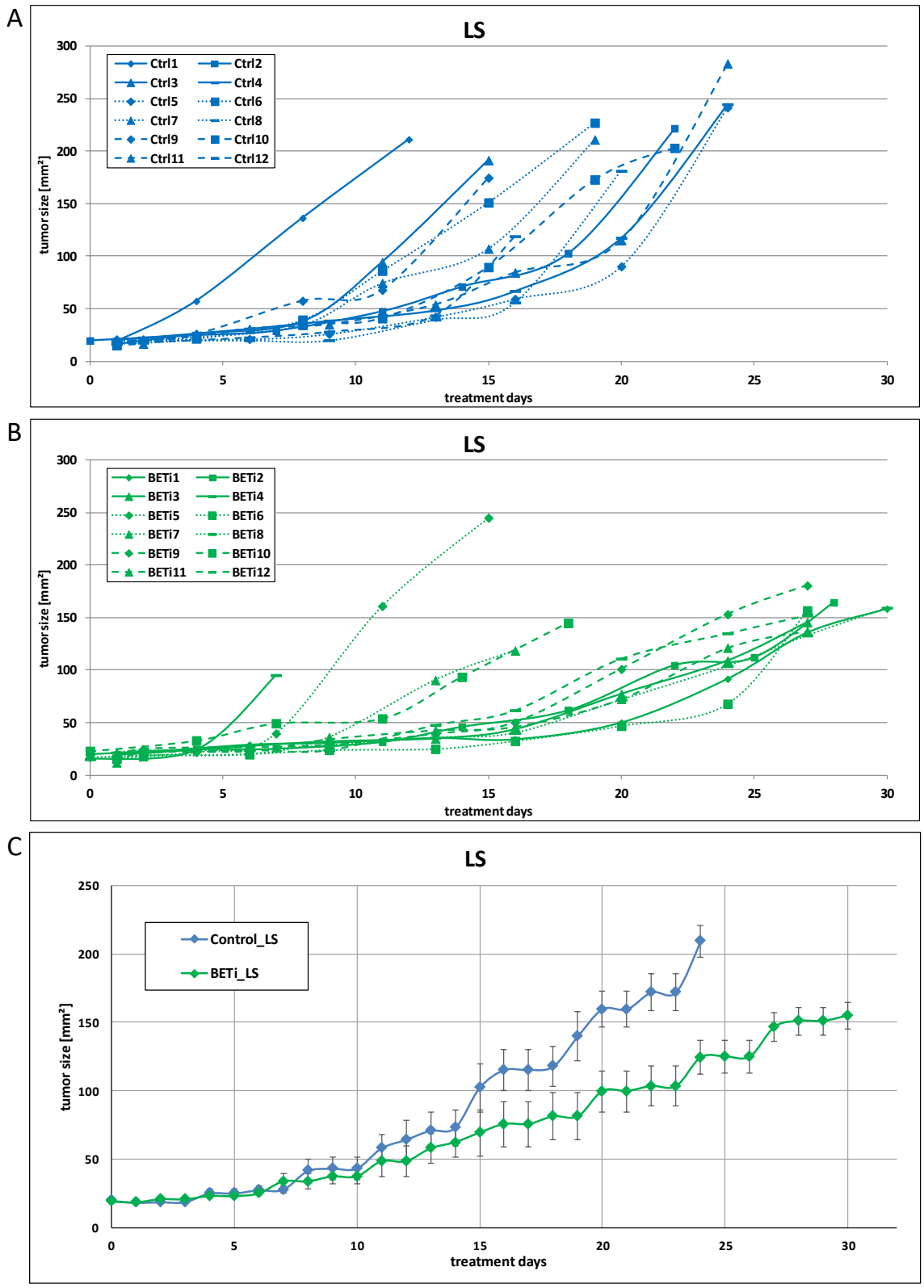

Figure 52: Tumor growth of LS xenograft tumors. Treatment with BAY1238097 or control started at day one. The tumor size was measured through the skin twice a week. A) Tumor growth of control animals. B) Tumor growth of BAY1238097-treated animals. C) LOCF analysis of tumor growth. Significance was tested with student t-test for day 24.

The Kaplan-Meier plot demonstrates that treatment with the inhibitor BAY1238097 effectively slowed down tumor growth and thereby prolonged the survival of mice with LS-derived tumors (Figure 53A). Until treatment day 18 the survival curves run parallel, then the remaining animals in the control group were dying fast with the last mice euthanized at day 24, whereas in the BAY1238097-treated group no further deaths occurred until treatment day 28. The median treatment duration was increased by therapy from 19.5 to 28 days, nevertheless this difference was not significant.

The tumor size at the last treatment day was about 50 mm² lower in the BAY1238097-treated animals compared to the control group, representing a significant decrease in tumor size ($p<0.01$) (Figure 53B). For both treatment groups, the variation of the tumor size within the group was low.

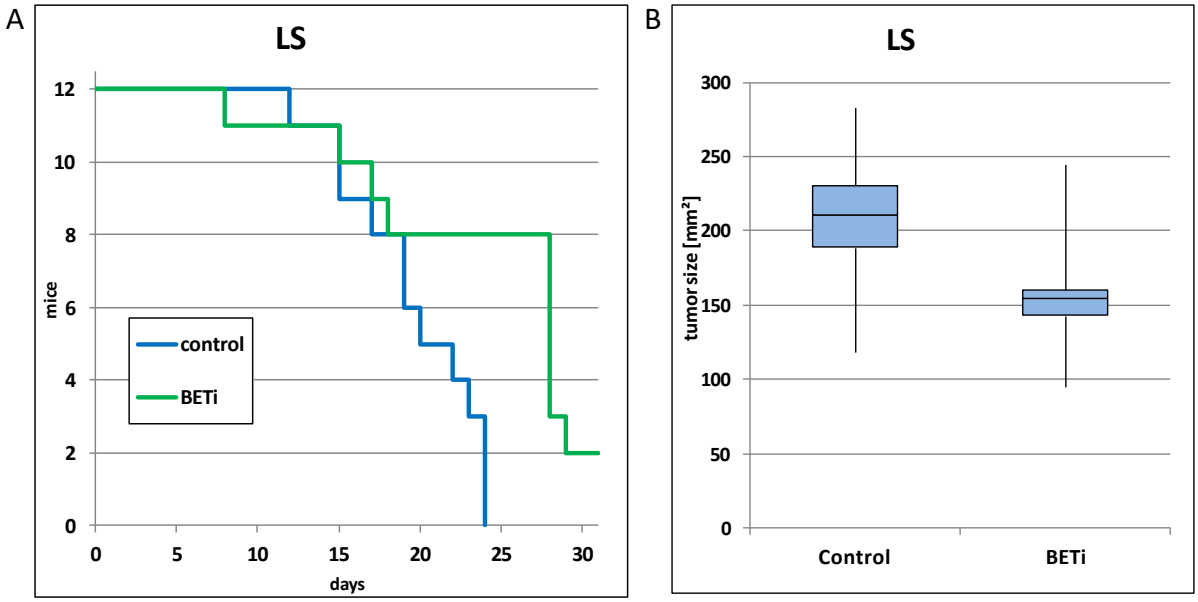

Figure 53: Effect of BAY1238097 treatment on LS xenografts. The effectiveness of BAY1238097 on xenografts from LS neuroblastoma cells in NSG mice is demonstrated. Significance was tested with student t-test. A) Kaplan Meier plot illustrates treatment duration for control and BAY1238097-treated mice. B) Tumor size at the end of the experiment. The tumor was measured through the skin with a caliper.

Taken together, the BRD4 inhibitor BAY1238097 is inhibiting tumor growth of subcutaneous neuroblastoma tumors deriving from LS cells. The treatment with the inhibitor leads to a prolonged survival of the mice and to a reduction in tumor size.

c) NBL-S

The neuroblastoma cell line NBL-S harbors a *MYCN* activating translocation leading to higher *MYCN* expression compared to *MYCN* non-amplified cell lines [158]. *In vitro,* NBL-S is classified as resistant to BAY1238097 and intermediate responding to JQ1.

Nearly all animals with tumors deriving from NBL-S cells reached the cutoff tumor size for the start of the therapy at day 20 or 23 after implantation. The tumors of control mice were in general all growing continuously (Figure 54A). In the BAY1238097-treated group four mice (BETi 1, 5, 9, 10) harbored tumors that were not growing larger than 100 mm² during the whole 30 days treatment period (Figure 54B). The remaining eight tumors were entering the exponential growth phase with a faster increase of tumor size after varying treatment periods.

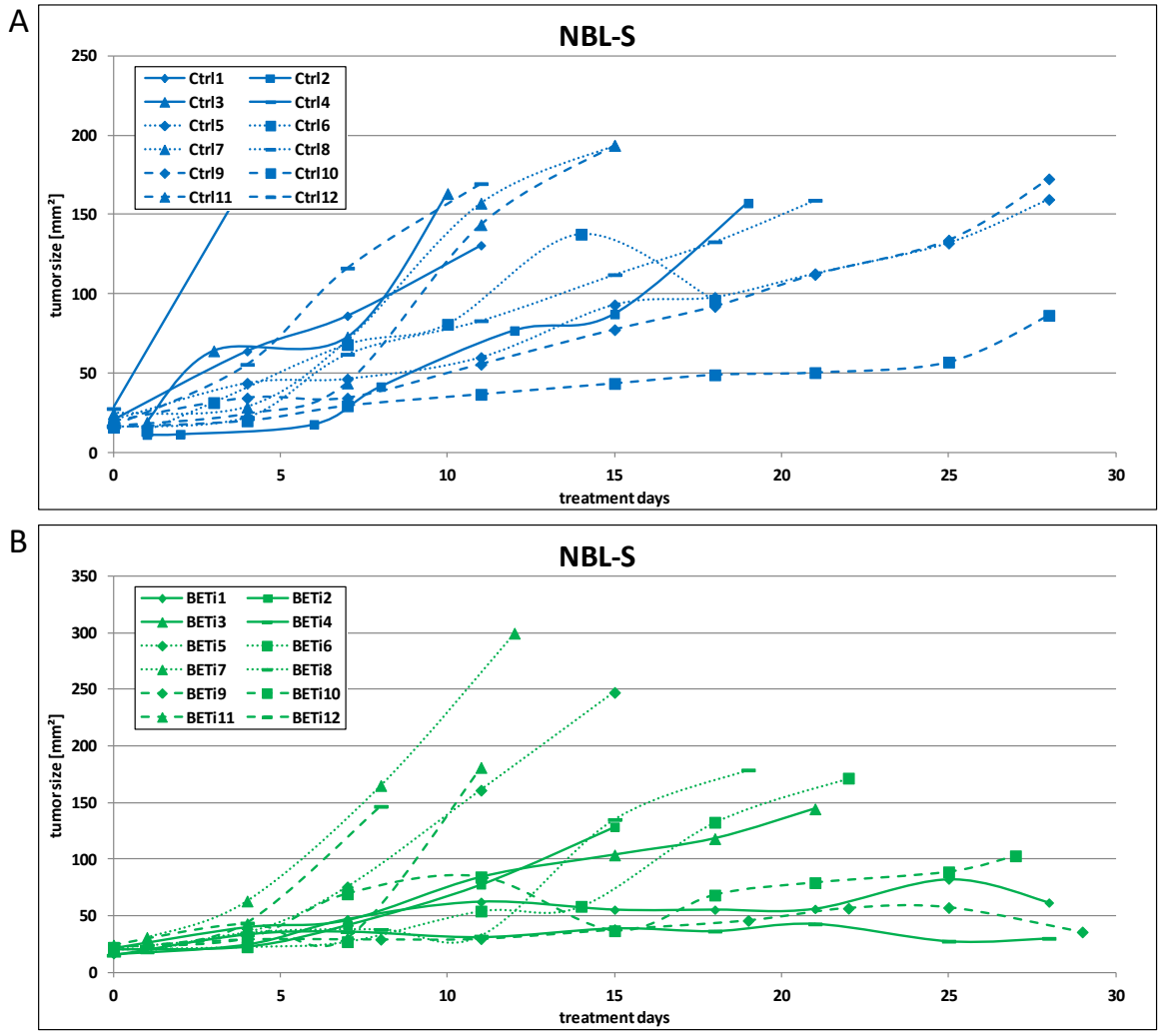

Figure 54: Tumor growth of NBL-S xenograft tumors. Treatment with BAY1238097 or control vehicle started at day one. The tumor size was measured through the skin twice a week with a caliper. A) Tumor growth of control animals. B) Tumor growth of BAY1238097-treated animals.

The Kaplan-Meier plot demonstrates that the mice from both the control and the BAY1238097-treated group died in a similar course and steadily throughout the experiment (Figure 55A). At

the last treatment day, one mouse from the control group and three mice from the BAY1238097-treated group were still alive, all others had to be euthanized earlier. The median treatment duration of the BAY1238097-treated group was 19.5 days, compared to 16.5 days in the control group. This difference is lower than for the two *MYCN* amplified neuroblastoma cell lines, IMR5/75 and LS, and was not significant ($p>0.05$).

No significant differences in tumor size were assessed comparing the control and BAY1238097-treated groups ($p>0.05$) (Figure 55B). Whereas the tumor size of the control group was uniform at the end of the experiment, the BAY1238097-treated group comprised eight larger and four smaller tumors.

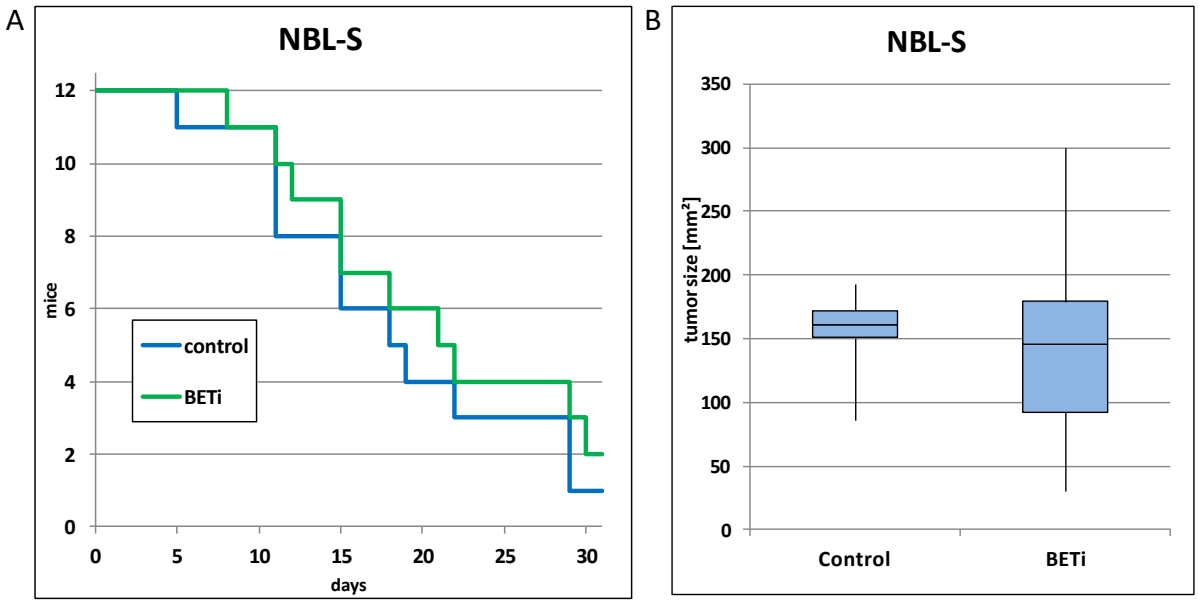

Figure 55: Effect of BAY1238097 treatment on NBL-S xenografts. The effectiveness of BAY1238097 on xenografts from NBL-S neuroblastoma cells in NSG mice is demonstrated. Significance was tested with student t-test. A) Kaplan Meier plot illustrates treatment duration for control and BAY1238097-treated mice. B) Tumor size at the end of the experiment. The tumor was measured through the skin with a caliper.

Altogether the effects of BRD4 inhibition with the substance BAY1238097 on NBL-S deriving subcutaneous xenografts were marginal. The main effect was a growth arrest for a fraction of tumors, whereas other tumors were growing continuously. The difference between fast and slow growing tumors impeded the analysis of the data from the NBL-S mouse collective.

d) SH-SY5Y

The neuroblastoma cell line SH-SY5Y does not have a *MYCN* amplification and is the only cell line used in the subcutaneous mouse model that is negative for *MYCN* expression. Instead, SH-SY5Y cells have high mRNA and protein levels of c-MYC due to an activating translocation,

and a mutation in the *ALK* gene. *In vitro*, SH-SY5Y was classified as an intermediate responder to JQ1 and BAY1238097.

For the SH-SY5Y tumors the tumor onset was inconsistent with a mean treatment start at day 15 for control and a mean tumor onset of 20 days for the BAY1238097 group. This difference regarding tumor onset could have influenced the results as described for IMR5/75. The tumor growth curves of the 12 control-treated mice injected with SH-SY5Y were uniform with all tumors growing continuously throughout the experiment (Figure 56A). Remarkable was the long period from onset of the tumor growth until the growth was entering the exponential growth phase for both control and BAY1238097-treated animals. Compared to the control group, the tumor growth of the BAY1238097-treated mice was more variable and included two mice (BETi 5, BETi 6) with no tumor growth at all, which was independent from early or late tumor onset (Figure 56B). Tumor growth of BAY1238097-treated animals was retarded late in the experiment.

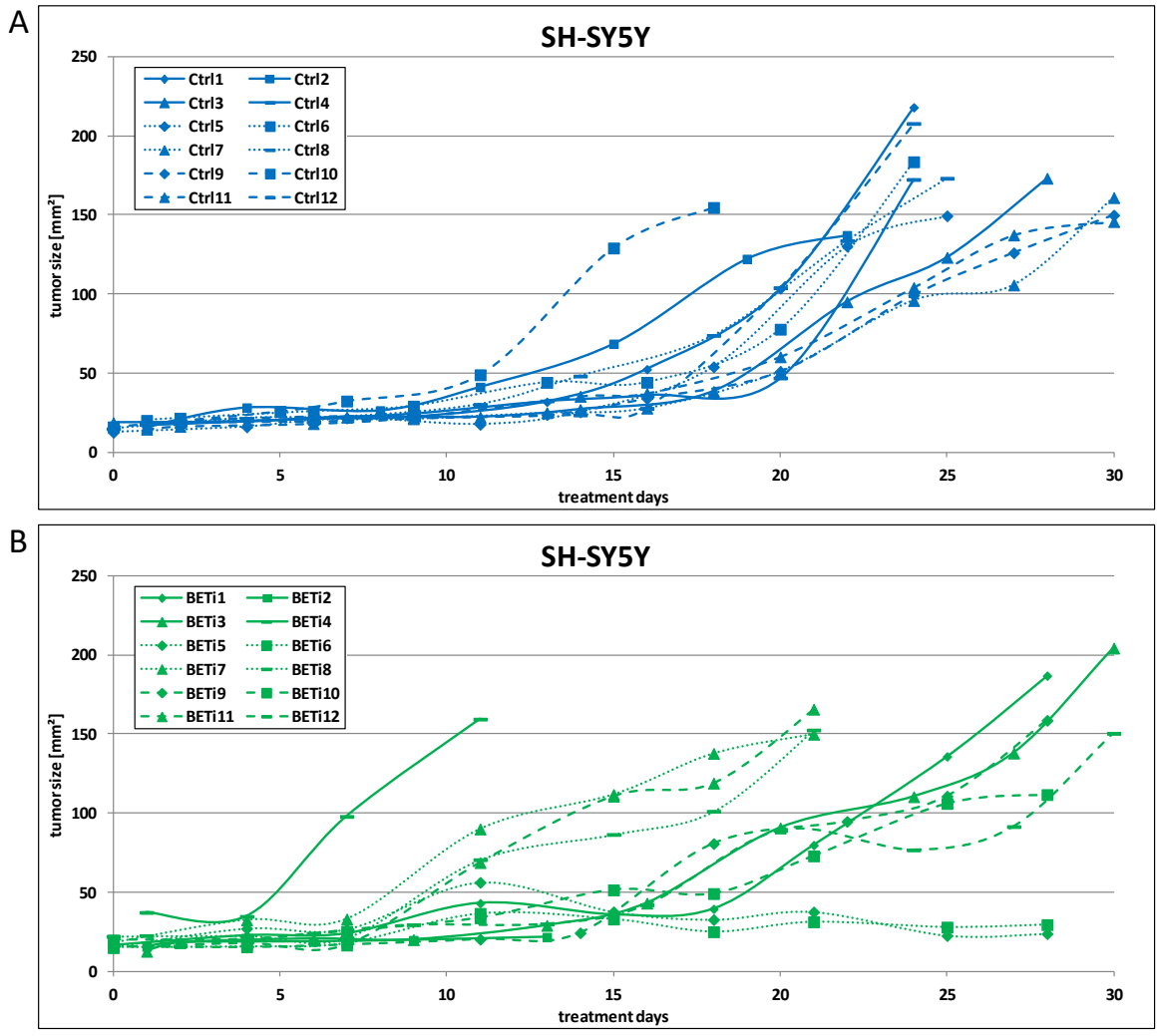

Figure 56: Tumor growth of SH-SY5Y xenograft tumors. Treatment with BAY1238097 or control started at day one. The tumor size was measured through the skin twice a week. A) Tumor growth of control animals. B) Tumor growth of BAY1238097-treated animals.

The Kaplan-Meier plot visualizes that up to treatment day 24 the control mice were surviving longer than the BAY1238097-treated mice due to two early deaths in the treatment group (Figure 57A). From day 24 on the tumors of the control group successively reached the maximum tumor size and had to be euthanized. In total, a prolonged median survival of 29 days was observed in the BAY1238097-treated group compared to 25 days in the control group (not significant). In contrast to the other cell lines used for the subcutaneous mouse model, a high number of animals injected with SH-SY5Y did not reach the maximum tumor size during the treatment period. At the last day of treatment, three mice from the control group and five BAY1238097-treated animals were still alive.

Although tumor growth within the BAY1238097-treated group was heterogeneous, a significant decrease in tumor size was observed for the BAY1238097-treated animals ($p<0.05$) (Figure 57B).

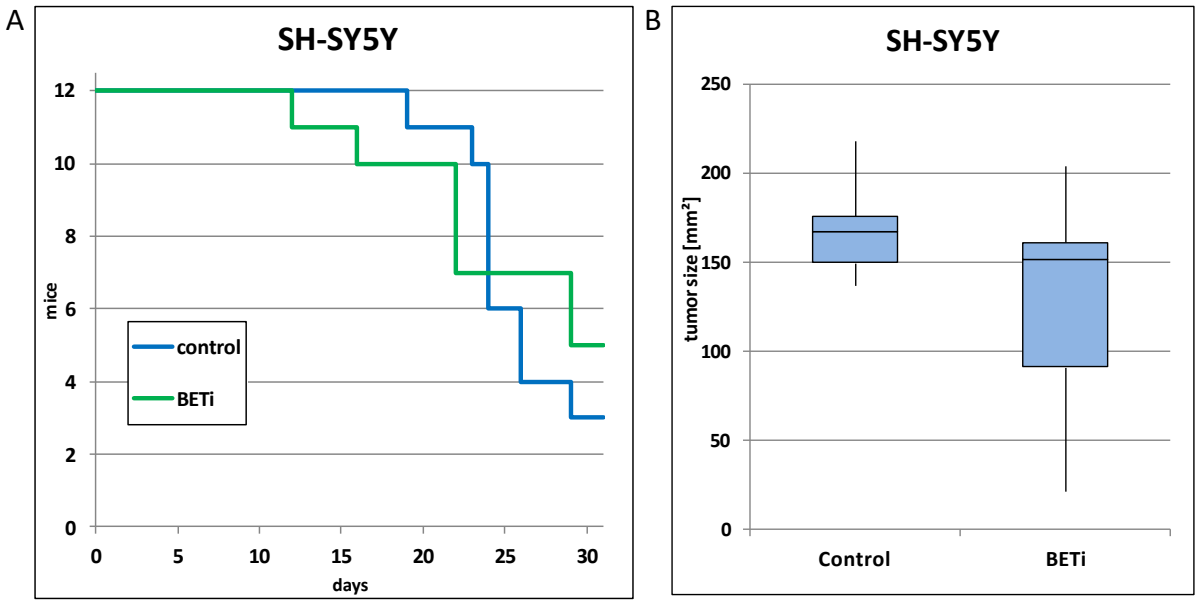

Figure 57: Effect of BAY1238097 treatment on SH-SY5Y xenografts. The effectiveness of BAY1238097 on xenografts from SH-SY5Y neuroblastoma cells in NSG mice is demonstrated. Significance was tested with student t-test. A) Kaplan Meier plot illustrates treatment duration for control and BAY1238097-treated mice. B) Tumor size at the end of the experiment. The tumor was measured through the skin with a caliper.

Taking together, BAY1238097 treatment significantly decreased tumor growth of SH-SY5Y deriving neuroblastoma xenograft tumors. As 25% of the control and 42% of the BAY1238097-treated animals were still alive at the end of the experiment, a longer period of treatment of approximately 40-50 days in total would have been adviceable to gain information on the final tumor growth of the remaining mice. This should be considered for further *in vivo* studies with SH-SY5Y cells.

The establishment of the subcutaneous neuroblastoma mouse model for different neuroblastoma cell lines including preliminary growth tests, the comparison of different mouse strains and the exclusion of drug toxicity were necessary to set up a preclinical *in vivo* study on BAY1238097 with reliable results. Especially the decision to analyze tumor growth in different mouse strains was indispensable to reduce variability of the data set and to increase the validity of the study. By repeating the BAY1238097 treatment study on IMR5/75 cells in NSG mice, the observed results with a tumor growth promoting effect of BAY1238097 in the CD-1 nude mice, could be relativized and explained as a result of the heterogeneity among the control animals in the CD-1 nude collective.

The experiment on NSG mice with the cell lines IMR5/75, LS, NBL-S and SH-SY5Y showed a significant inhibitory effect of BAY1238097 on LS-deriving tumors, but no or minimal effects for the tumors originating from the other three cell lines. However, the sensitivity of neuroblastoma cell lines to BAY1238097 does not in general predict for the responsiveness *in vivo*. In the case of LS, predicted as good to intermediate responding, the results from the cell culture experiments with BRD4 inhibitors were comparable. For IMR5/75, the expected high sensitivity to BAY1238097 failed to be observed *in vivo*, as well as an intermediate sensitivity of NBL-S and SH-SY5Y to treatment with BET inhibitors.

Especially for the IMR5/75 deriving tumors, the comparability of control and BAY1238097-treated animals is limited in NSG mice due to the high variability of tumor onset between the control and the BAY1238097 group. As observed for all cell lines, the tumor onset has an influence on the tumor growth speed, tumors with a late onset included late in the treatment reached the maximum tolerated tumor size in short time. Thereby a shift between tumor onset in control and treatment group could have a relevant influence and mask potential therapeutic effects. An increase of the total number of animals is adviceable to increase the number of animals with similar tumor onset and thereby to improve the power of the study.

5.4 Establishment of an orthotopic neuroblastoma mouse model

As described in the introduction, an orthotopic xenograft mouse model has many advantages compared to heterotopic tumors growing subcutaneously. One main part of this thesis was the establishment of an orthotopic neuroblastoma mouse model using the IMR5/75 *MYCN* high/low and IMR32 *MYCN* high/low cell systems described in the results part 5.1 in detail. Aim of this project was to establish a mouse model close to the situation in humans with low or high *MYCN* expression in the tumor cells, but besides this the same genetic background. For better visualization of even small tumors, *in vivo* bioluminescence imaging was planned to be used, detecting stable luciferase expression in the human tumor cells.

5.4.1 Luciferase is expressed by cells used for orthotopic implantation

First of all luciferase expressing cells were generated. IMR5/75 *MYCN* high/low and IMR32 *MYCN* high/low neuroblastoma cells were transfected with the commercially available pGL4.50 plasmid coding for a stable expressed firefly luciferase gene. Monoclonal subclones were tested for luciferase expression to identify clones with high levels of luciferase expression.

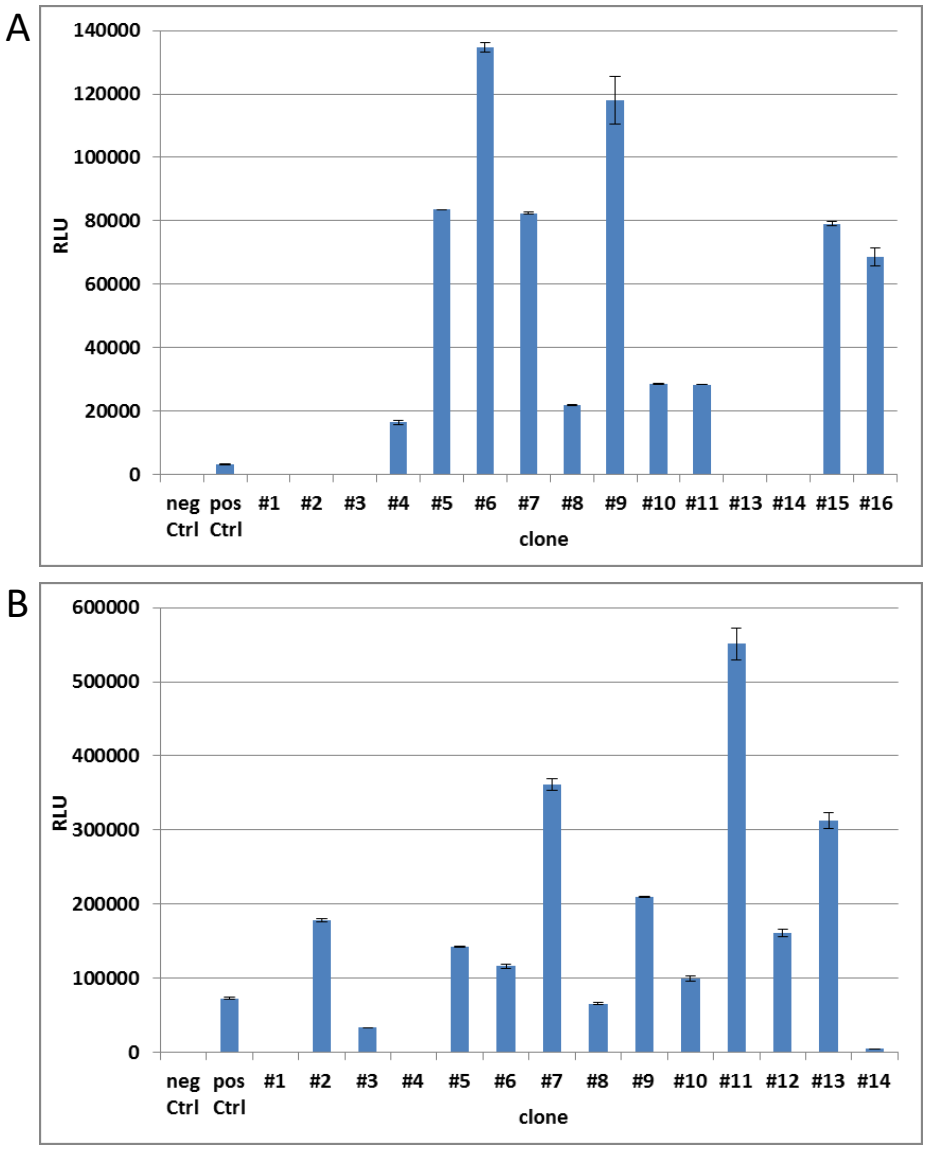

Figure 58: Luciferase expression of monoclonal cell lines. Monoclonal luciferase subclones were generated by a two-step selection process. Luminescence was measured over a period of 30 sec. Luciferase expression was normalized by using equal amounts of total protein. In the graphs the mean values are shown for each clone. A) Clones from IMR5/75 cell line. Untransfected IMR5/75 cells were used as a negative control. Luciferase expressing HeLa cells were used as positive control. Clones #6 and #9 had the highest luciferase expression. Those were frozen in liquid nitrogen and used for further experiments. B) Clones from IMR32 cell line. Untransfected IMR32 cells were used as a negative control. IMR5/75 clone #6 was used as a positive control. Clones #11 and #7 had the highest luciferase expression. Those were frozen in liquid nitrogen and used for further experiments.

From IMR5/75, 16 subclones could be generated by monoclonal selection (Figure 58A). Clone#12 stopped growing after a few weeks in culture and had to be excluded from luciferase measurement. Among the remaining 15 subclones, luciferase expression was detectable in 10 clones. The degree of the luciferase signals was quite varying between the different subclones. The highest levels of luciferase expression were measured in the subclones IMR5/75 luci#6 and IMR5/75 luci#9.

From IMR32, 14 subclones deriving from single cells were tested for luciferase expression (Figure 58B). 12 out of 14 subclones showed luciferase expression, with the highest expression levels in IMR32 luci#11, IMR32 luci#7 and IMR32 luci#13. IMR32 luci#13 showed divergent growth behavior; therefore this subclone was excluded from further culturing. The subclones IMR32 luci#11 and IMR32 luci#7 were chosen for further experiments.

Summarizing, from both the IMR5/75 *MYCN* high/low and IMR32 *MYCN* high/low cell line two stable subclones expressing high levels of luciferase in vitro were generated for use in mouse experiments.

5.4.2 Establishment of an orthotopic mouse model

During establishment of the orthotopic mouse model, many different aspects of the method had to be improved to achieve the aimed tumor growth rate of 80%. For method optimization, small mouse collectives, dead mice remaining from breeding in the animal core facility or isolated adrenal glands provided from other DKFZ groups were used. The main points to improve were needle size, injection volume and fixation of the adrenal gland as well as improvement of the implantation itself.

a) Needle size

The first challenge of surgery was to find the ideal needle size to inject the neuroblastoma cells into the adrenal gland. The needle had to completely fit with the cut into the adrenal gland to avoid leakage of the injected neuroblastoma cells. On the other hand, the inner diameter had to be large enough to make sure, that the cells were not mechanically harmed when passing the needle, which could have an influence on the tumor growth rate. Therefore, the aim was to find a needle size that accounts for both aspects.

For optimization of the needle size, 24 G (OD=0.55 mm), 27 G (OD=0.4 mm) and 30 G (OD=0.3 mm) were tested with IMR5/75 cells. The cells were assessed regarding fraction of dead cells, using trypanblue, and regrowth studies.

It was noticed that the fraction of dead cells increased proportional to the smaller diameter of the needle from 11.3% with the 24 G needle up to 27.8% dead cells with the smallest (30 G) needle tested (Table 16). Reseeding experiments, however, showed acceptable regrowth rates for all three needle sizes after 48h after reseeding.

For the following *in vivo* orthotopic studies the 30 G needle was used. The smaller diameter minimizes damage to the adrenal gland and the cut can be completely placed in the organ.

Table 16: Experimental scheme and results of the needle test.

Needle size	24 G	27 G	30 G
Outer diameter	0.55 mm	0.4 mm	0.3 mm
Viability cell counter	88,7%	85,4%	72,2%
Regrowth	Acceptable	Acceptable	Acceptable

b) Injection volume

A second issue for optimization was to define the maximum injection volume that fits into the adrenal gland, so that no cells are leaking out into the abdominal cavity. The adrenal gland of a mouse is about the size of a pinhead and has a dense structure. Literature research revealed that neuroblastoma research groups working with similar mouse models inject between 2 µl and 100 µl into the adrenal gland or the surrounding fat pad [126, 159, 160].

Different volumes of cell suspension, colored with bromophenol blue for optical control, were tested. The result was that maximum 10 µl can be injected without cells leaking out.

To avoid leakage of the tumor cell solution into the abdominal cavity, fibrin was used to seal the injection site directly after implantation of the cells, comparable to the method published by Cardoso et al. [161]. This failed because it was not possible to apply the fibrin fast enough and on the exact position of the puncture without spreading the fibrin along a larger area. Another attempt was to mix the cells with matrigel to make the cell suspension more viscous and to have the injection site sealed with matrigel, which hardens at body temperature. In this case, the total volumes working with were too small to mix cells and matrigel reproducible in defined proportions. Additionally, the small volumes of matrigel hardened before application, although usage of pre-chilled equipment and storage on ice.

In summary, it was decided to inject the cells resuspended in 10 µL cell culture medium. The usage of matrigel or fibrin was not further considered.

c) Fixation of the adrenal gland and automatically assisted injection

The fixation of the adrenal gland and optimization of the implantation procedure was the main part that had to be improved to generate comparable experimental conditions with the orthotopic neuroblastoma mouse model. The small size of the mouse adrenal gland requires precise work, which is hindered by the flexible position of the adrenal gland in the surrounding fat pad.

The adrenal gland was positioned in the field of view as seen in Figure 59B by holding skin and fat pad with a pair of forceps and using a spatula to clamp the kidney on the other side. The spatula as surgical instrument was chosen to make sure that the kidney was not harmed.

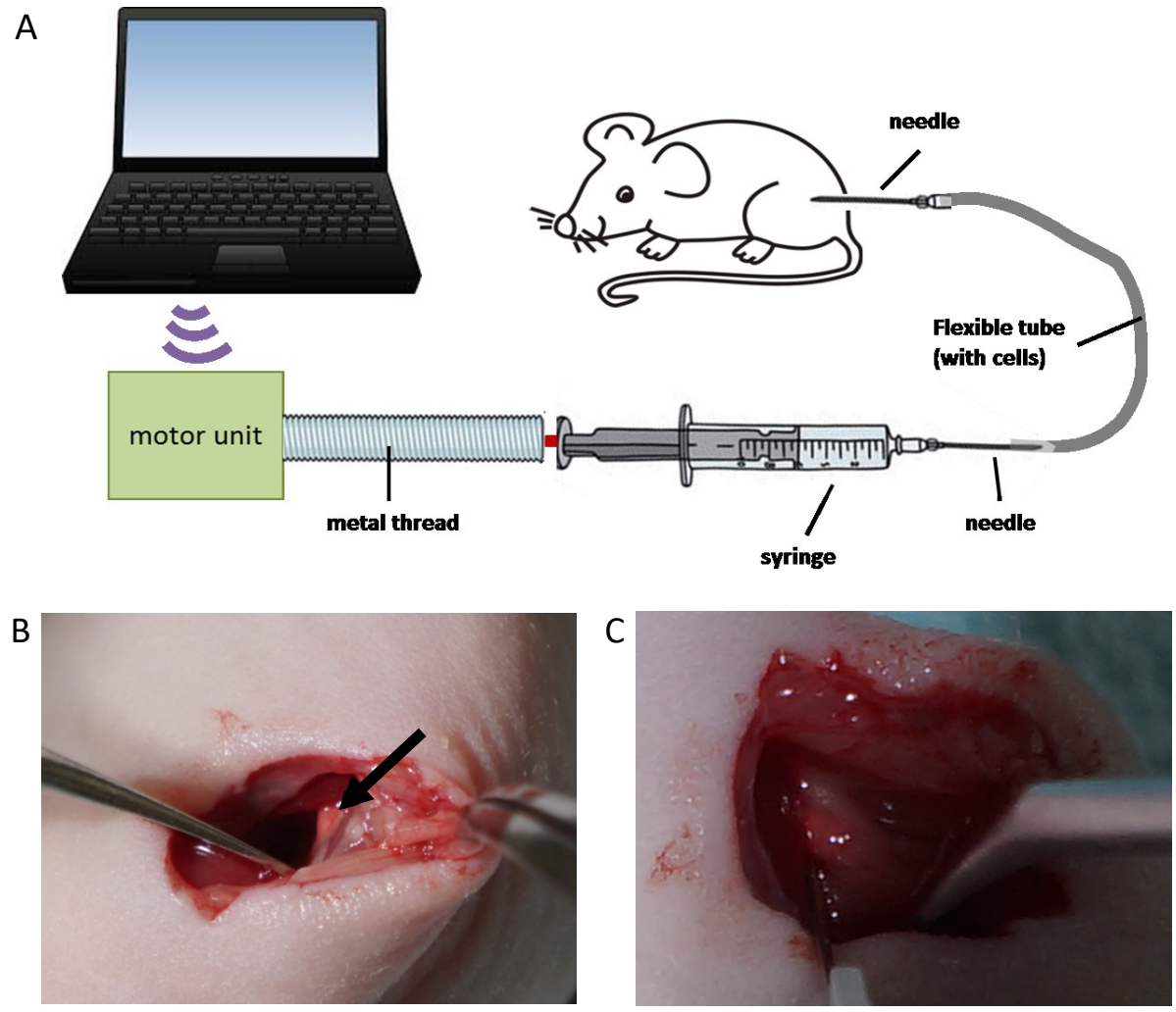

Figure 59: Implantation of tumor cells in the adrenal gland. A) Schematic representation of the injection assistant used for orthotopic implantation. B) Size and structure of the adrenal gland (black arrow). Skin and muscle are fixed with forceps, instrument on the right. The kidney is clamped with a spatula, instrument on the left. C) Size of the needle (bottom of the picture) used for implantation compared to the size of the adrenal gland during implantation.

During injection, the small size of the adrenal gland was challenging. The cut of the needle precisely fitted into the adrenal gland, as seen in Figure 59C showing the proportions of needle and adrenal gland. Small movements, however, as they usually happen when pressing the plunger of the syringe, generally resulted in perforating the adrenal gland completely or slipping out of the needle. Due to this problem, it was necessary to separate the implantation process from the insertion of the needle in the organ. An injection assistant was used, schematically shown in Figure 59A. Here, the plunger of the syringe was connected to a metal thread. A motor unit was turning the metal thread in small and defined steps, controlled by a computer. At the top end of the syringe, a flexible tube was installed with a 30 G needle on the end.

To inject cells into the adrenal gland, the needle was placed in a tube with cells in the right concentration and 10 µl were taken up two times by moving the plunger backwards assisted by the motor unit. After uptake, the needle was fixed in a needle holder and carefully inserted into the adrenal gland. At the right position, 10 µl of cell suspension were injected, controlled by the computer. The needle was kept in the adrenal gland for a few seconds after implantation and then taken out slowly. Between two injections, the tube was cleaned by ejection of 2x 10 µl.

The usage of the injection assistant had the big advantage, that insertion and implantation are completely separated. The surgeon can fully concentrate on correctly positioning the needle into the adrenal gland.

5.4.3 Pilot study: Orthotopic neuroblastoma mouse model

At the end of the method establishment process, a pilot study was started, implementing all results from the optimization experiments. A timeline visualizes the course of action of the experiment in Figure 60.

A group of ten CD-1 nude mice were orthotopically injected with $5x10^5$ human neuroblastoma cells from cell line IMR5/75 Luci#9 into the left adrenal gland. Swelling of the adrenal gland or the surrounding fat pad, indicative for a successful tumor cell implantation, was noticed for all mice except mouse #4 and #6.

All mice of this group survived surgery. Wound healing was fast and without swelling or other complications. Altogether, surgery and implantation of the neuroblastoma cells was satisfactory along the mice in the pilot study.

To compare tumor onset, tumor growth and metastasis of *MYCN* high and *MYCN* low conditions in the mouse model, *MYCN* knockdown started two weeks after implantation of the human neuroblastoma cells for half of the mice. The downregulation was based on the vector system consisting of tetracycline repressor and a *MYCN*-shRNA controlled by TetR-elements,

as described in results part 5.1. Mice #1-5 got doxycycline, which was orally administered in the drinking water. Doxycycline inactivates the tetracycline repressor, which enables transcription of the *MYCN*-shRNA and should selectively downregulate *MYCN* in the neuroblastoma cells. The results of *MYCN* downregulation in the mouse tumors are described in detail in results part 5.4.6. In the following sections, mice #1-5 will be referred to as *MYCN* low and mice #6-10 will be referred to as *MYCN* high describing the results of this experiment.

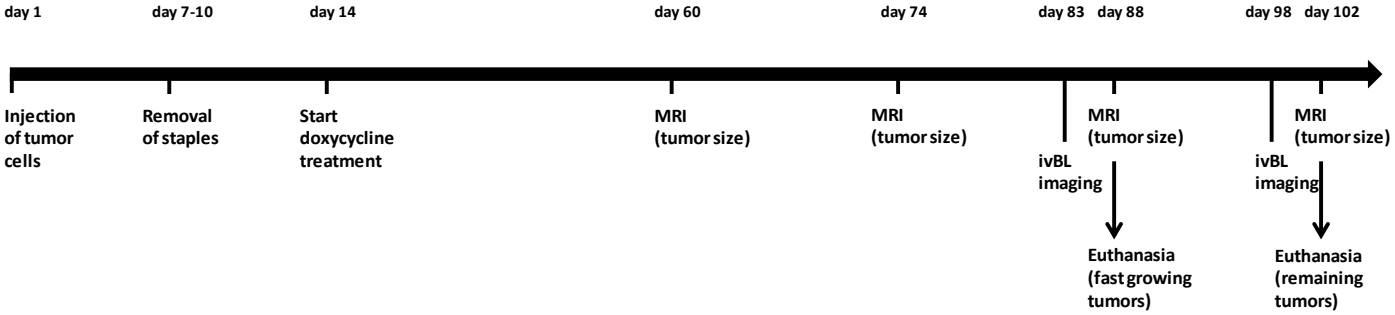

Figure 60: Timeline of orthotopic mouse experiment. Cells were implanted at day one. Doxycycline treatment started two weeks after surgery. Tumor growth was first monitored at day 60 by MRI, additional MRI scans were performed in two-week intervals. Bioluminescence was measured two times in total, scheduled a few days before the 3rd and 4th MRI scan. Depending on the size of the tumors, the mice were euthanatized at day 89 or at the end of the experiment at day 103.

Tumor growth was monitored by MR imaging fortnightly and by *in vivo* bioluminescence imaging at two additional sessions. In Figure 61 tumor growth is shown for each mouse. Table 17 contains the tumor size calculated by MR imaging.

With the first MR imaging at day 60 after tumor cell implantation, tumors at the adrenal gland could be identified in 7 out of 10 mice. In the *MYCN* low group, mice #1, #2 and #3 had a tumor, for mice #4 and #5 no tumor could be detected. Among the *MYCN* high group, mouse #6 was negative for tumor growth, for all other mice in this group MR imaging revealed tumor growth.

Both in the *MYCN* low and *MYCN* high group, tumor size was highly variable. At the first MR imaging, both in the *MYCN* low and in the *MYCN* high group, one large tumor was detected compared to the others. In the *MYCN* low group, mouse #2 had a tumor of 0.4 ml, the other tumors in this group had volumes of 0.09 ml and 0.11 ml. Among the *MYCN* high mice, mouse #10 had a large tumor of 0.34 ml, whereas the others were ranging between 0.05 ml and 0.07 ml.

The following MR imaging examinations at day 74 and 88 after implantation confirmed that there are slow and fast growing tumors, independent of *MYCN* low and *MYCN* high conditions. Mouse #6 from the *MYCN* high group still showed no detectable tumor until the third MR imaging at day 88, then the tumor was growing fast. At the fourth MR imaging the tumor of

mouse #6 was the largest among the remaining tumors with a volume of 1.31 ml, despite the late onset of tumor growth.

The fast growing tumors of mice #2, #7 and #10 exceeded the maximum tumor size before the endpoint of the experiment at day 89. All other mice were euthanized at the end of the experiment at day 103.

Altogether, a tumor gowth rate of 80% was achived in the pilot study. The *MYCN* low group had a tumor growth rate of 60%, including one fast growing tumor. No tumors were detected in mice #4 and #5. In the *MYCN* high group, tumors were growing in all five animals. From those, three tumors were fast growing, including one with late onset.

Table 17: Imaging results for each of the mice. Signal detectable (+ or ++), no signal/tumor (neg), no measurement (-).

		MRT [ml]				ivBL [+/neg]		end of experiment
day		60	74	88	102	83	98	
mouse 1	*MYCN* low	0.11	0.27	0,44	0.73	+	+	day 103
mouse 2		0.40	1.61	6,70	-	++	-	day 89
mouse 3		0.09	0.23	0,32	0.48	+	++	day 103
mouse 4		neg	neg	neg	neg	neg	-	day 103
mouse 5		neg	neg	neg	neg	-	-	day 103
mouse 6	*MYCN high*	neg	neg	0.17	1.31	-	+	day 103
mouse 7		0.07	1.07	5.55	-	++	-	day 89
mouse 8		0.05	0.10	0.19	0.49	neg	++	day 103
mouse 9		0.06	0.06	0.04	0.02	+	+	day 103
mouse 10		0.34	1.78	7.90	-	++	-	day 89

In both groups, the tumor growth was heterogeneous. As expected, in the *MYCN* high group more tumors were growing and the proportion of fast growing tumors was higher compared to the *MYCN* low group. As the total number of animals in the pilot study was low and as the experiment was not repeated for this thesis, the validity of the findings presented here is limited. The mouse model established here has been applied with a larger number of animals by the DKFZ group “Molecular Imaging” headed by Dorde Komljenovic. The tumor growth rate of 80% for the orthotopic neuroblastoma mouse model was verified by these experiments (data not shown).

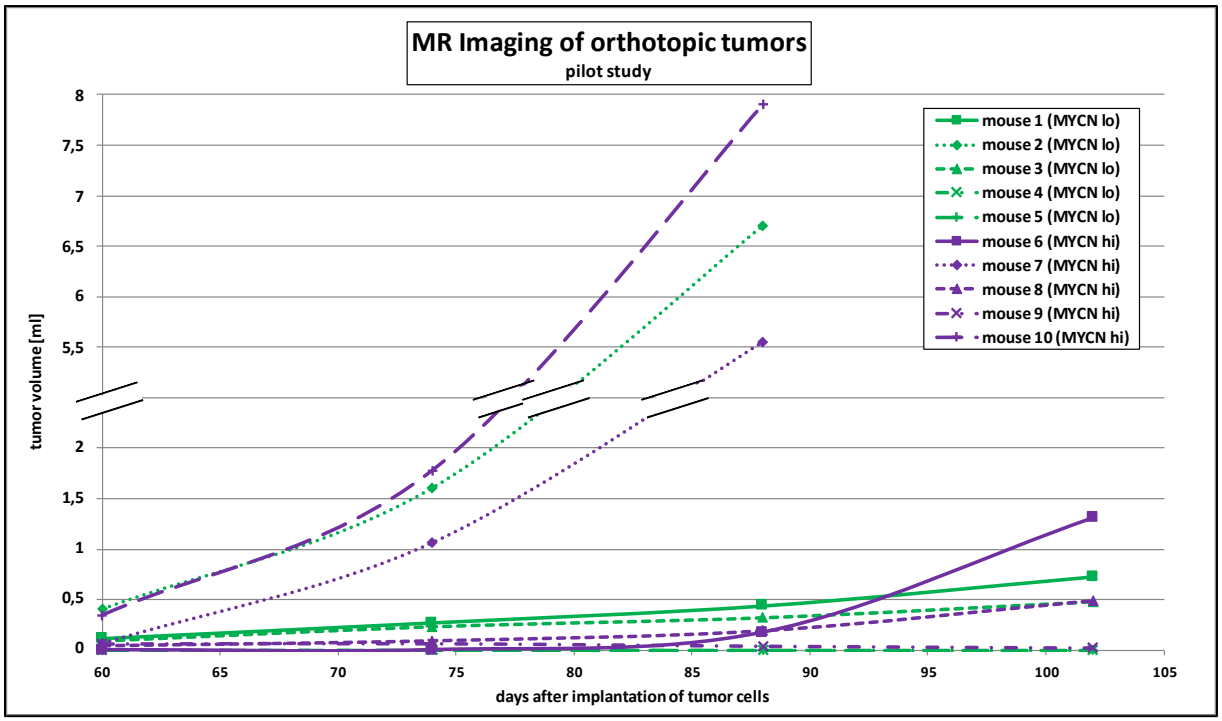

Figure 61: Tumor growth of orthotopic tumors. Tumor volume was calculated by MRI. *MYCN* low tumors are displayed in green, *MYCN high* tumors in purple. Both groups contain fast and slow growing tumors.

5.4.4 Imaging of orthotopic tumors

For imaging of the orthotopic tumors, two different imaging methods were used: magnet resonance imaging and *in vivo* bioluminescence.

MR imaging is a method widely used for imaging of organs and objects in medical and scientific applications. The patient is brought into a strong magnetic field, where protons, especially hydrogen in water molecules, are excited. These signals can be processed into an image [162]. In the used T2 measuring mode, water appears bright and solid tissues dark [163].

MR imaging was used to follow up tumor growth and to calculate the tumor volume. Measurements took place every two weeks starting at day 60 after tumor cell implantation and repeating the MR imaging at days 74, 88 and 102. Figure 62 shows exemplary images from the first and the third measurement at day 60 and day 88. The results and volume calculations of all MR images performed during this experiment are given in table 17.

MR imaging was suitable for the aimed application. Tumors and kidneys could be defined clearly. The calculation of tumor volume was accurate by tracing the tumor through the different slices (width 1.0 mm) generated during the measurement. The time points for measurement were well chosen, at the first time point 90% of the mice were correctly identified as positive or negative for tumor growth.

The fortnightly intervals between the measurements were sufficient for most of the tumors. Solely for the fast growing tumors of mice #2, #7 and #10, shorter intervals would have been necessary. In the two weeks between the second and the third measurement, the volume of these tumors became 4-5 times larger with the result, that the maximum tumor size was exceeded during these two weeks. For tumors that show fast growth in the previous measurements, an additional imaging after one week would be advisable.

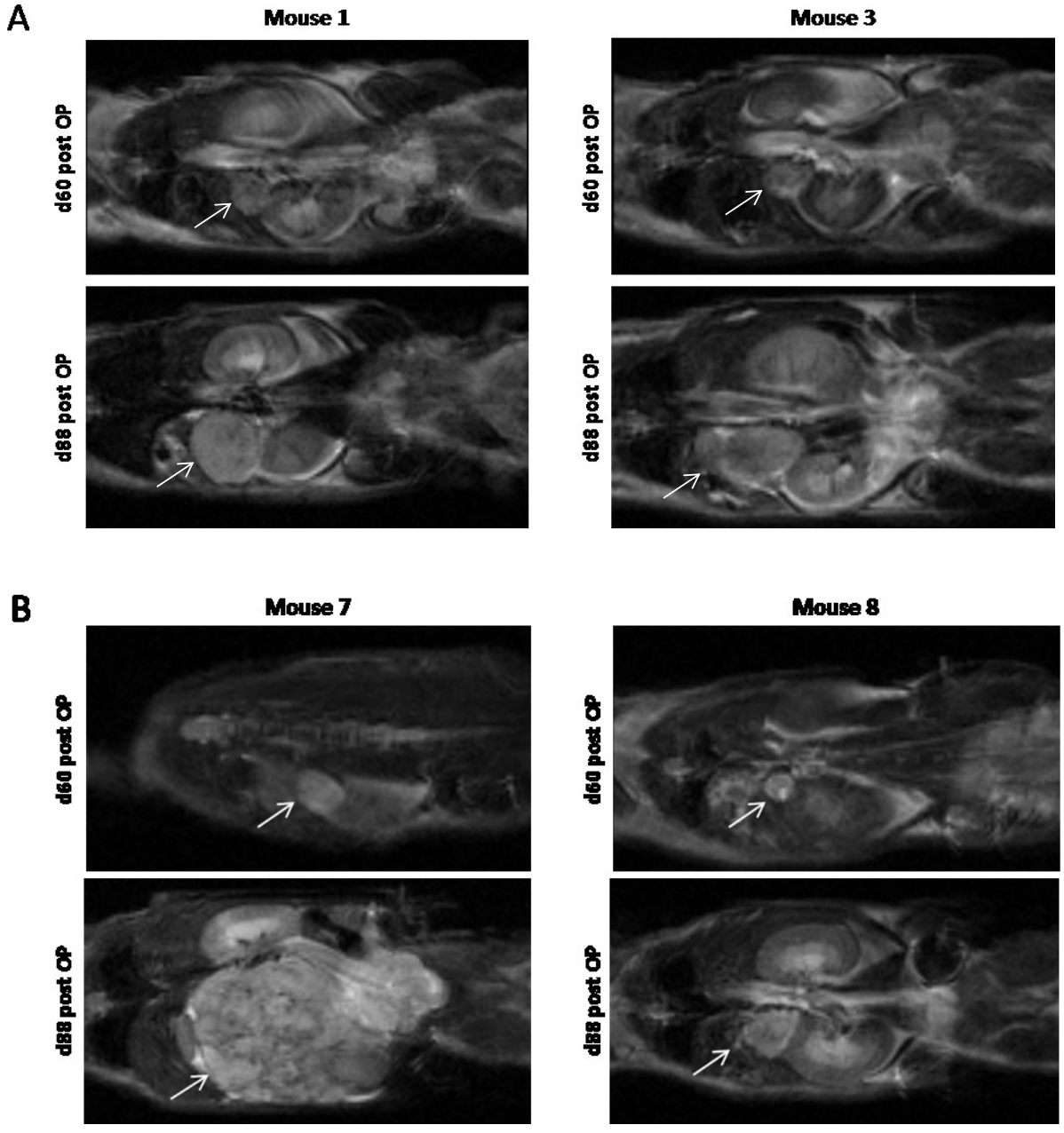

Figure 62: MRI images of orthotopic tumors. Exemplarily, coronal pictures are shown from two different time points. Arrows indicate the position of the tumors. A) Tumors from two mice of the *MYCN* low group. B) Tumors from two mice of the *MYCN* high group.

Additional to the MR imaging, *in vivo* bioluminescence imaging was performed twice during tumor follow-up. This imaging method specifically detects luciferase-expressing cells and is therefore very useful not only to visualize the primary tumor but also potential metastases.

For detection of the bioluminescence, the mice were intraperitoneally injected with a luciferin solution. The luciferase stable expressed by the human neuroblastoma cells converts the luciferin whereupon light is emitted and detected by a light sensitive camera.

The *in vivo* bioluminescence imaging was performed with two different imaging systems. An overview of all measurements and results is given in table 17. Pictures were taken from the back and from the side of the mice.

At day 83, a bioluminescence detector was used that was built at the DKFZ by the group “Functional and Molecular Emission Computed Tomography”. In this imaging study, 8 out of 10 mice were included. Exemplary images for mouse #1 from the MYCN low group and mouse #7 from the *MYCN* high group are shown in Figure 63A. The three fast growing tumors #2, #7 and #10 showed high luciferase activity. From the other five mice included in the bioluminescence imaging, moderate luciferase activity was detected in three animals. For mouse #4 no luciferase activity was expected, because MR imaging was negative for a tumor. Surprisingly, mouse #8 also showed no luciferase signal although a tumor was identified for this animal by MR imaging. Metastases were detected in none of the animals.

The second bioluminescence imaging session took place at day 98 of the experiment (Figure 63B). This time, a commercially available IVIS bioluminescence imager was used. From the remaining seven animals in the experiment at this timepoint (mice #2, #7 and #10 with fast growing tumors had been euthanized before due to tumor burden), five animals were included in the measurement. No imaging was performed with mice #4 and #5, which had been negative for tumor growth at all measurements up to this time point. All five mice showed luciferase activity in the area around the adrenal gland, which matches with the results of the MR imaging. Mouse #8, which was negative at the first bioluminescence imaging showed a strong luciferase signal this time. For each animal, there was a single location of the luciferase signal in the area of the adrenal gland and no hint for metastases.

In comparison, the results of the *in vivo* biolumenscence imaging showed similar results. However, the pictures look different in some aspects. The IVIS system uses a color code to display the intensity of the luciferase signal. These colors cover the incident light picture of the animal, which is recorded for localization of the luciferase signal. The DKFZ system in contrast displays the luciferase signal as dark spots. Integrating the luciferase image in the incident light image enables to see more details of the structure of the tumor due to more transparent images.

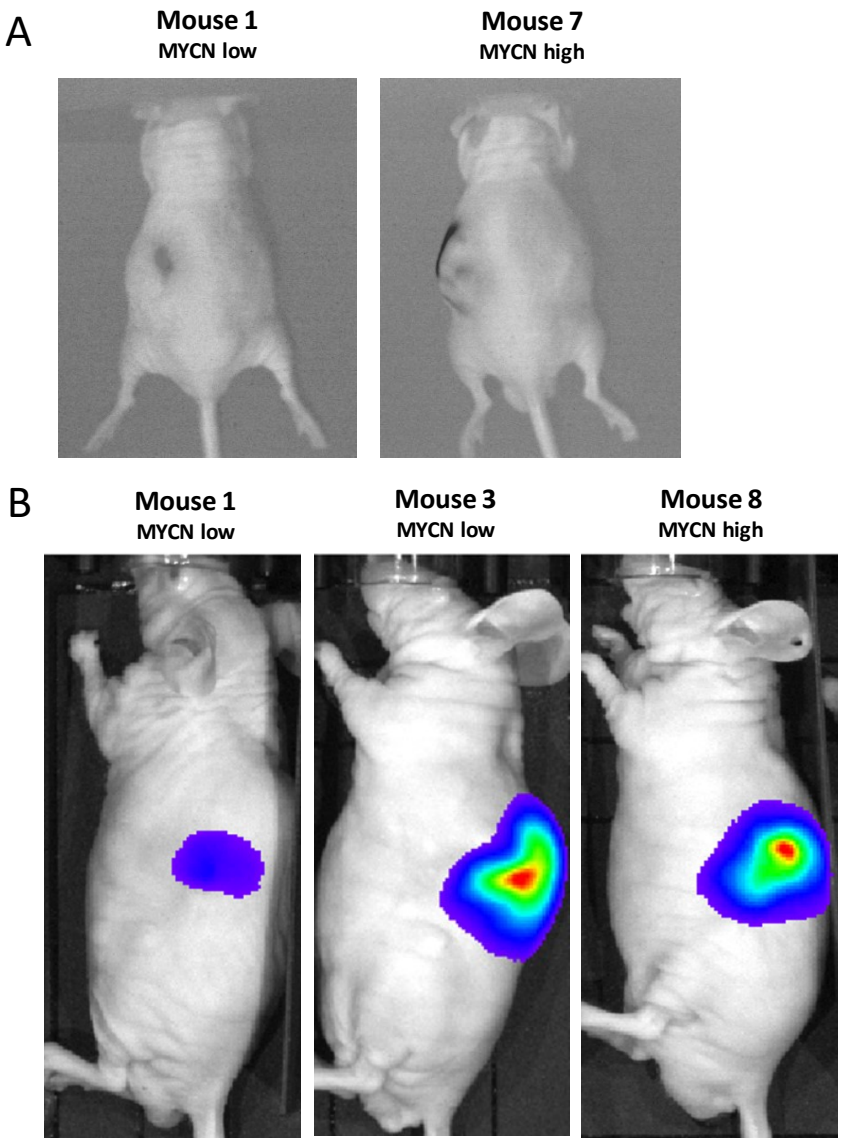

Figure 63: Bioluminescence images of orthotopic tumors. ivBL imaging was performed with two different systems. Luciferin solution was injected i.p. and after 5 min of incubation the luminescence was measured. Incident light pictures were taken to overlay the signal with the contures of the animal body. A) ivBL imaging at day 83. Exemplarily, one mouse of each group is shown. Exposure time was 3 min. Luminescence is shown in dark. B) ivBL imaging at day 98. Two mice from the *MYCN* low and one mouse from the *MYCN* high group are shown. Exposure time was 2 min. Luminescence signal is scaled using a color code.

5.4.5 Histologic analysis of orthotopic tumors

The tumor samples from the orthotopic xenograft mice described in section 5.4.3 were histologically viewed to confirm that the tumors grown in the mice were neuroblastomas. The preparation of cryoslices and staining with haematoxylin and eosin was done at the laboratory of the pathological institute Heidelberg. Appraisal of the tumor samples was done by Dr. med. vet. Tanja Poth. Exemplary images of the tumors are shown in Figure 64. Table 18 gives an overview of the results from the histological analysis.

All tumors included in the analysis were identified as neuroblastomas. In all tumor samples except tumor #8 necrotic areas were identified. From tumor #9 no histological analysis was prepared because there was not enough tumor material for both histology and other analyses.

Further analysis of the differentiation grade was not possible due to suboptimal quality of the tumor material. A preparation for paraffin embedding instead of cryo slides would allow further histological analysis.

Table 18: Results of the histological analysis.

No*	MYCN expression	Tumor size (endpoint)	diagnosis	Necrosis
Mouse 1	No	0.73 ml	Neuroblastoma	Yes
Mouse 2	No	6.70 ml	Neuroblastoma	Yes
Mouse 3	No	0.48 ml	Neuroblastoma	Yes
Mouse 6	Yes	1.31 ml	Neuroblastoma	Yes
Mouse 7	Yes	5.55 ml	Neuroblastoma	Yes
Mouse 8	Yes	0.49 ml	Neuroblastoma	No
Mouse 10	Yes	7.90 ml	Neuroblastoma	Yes

*Mouse 9: not enough material for histologic analysis

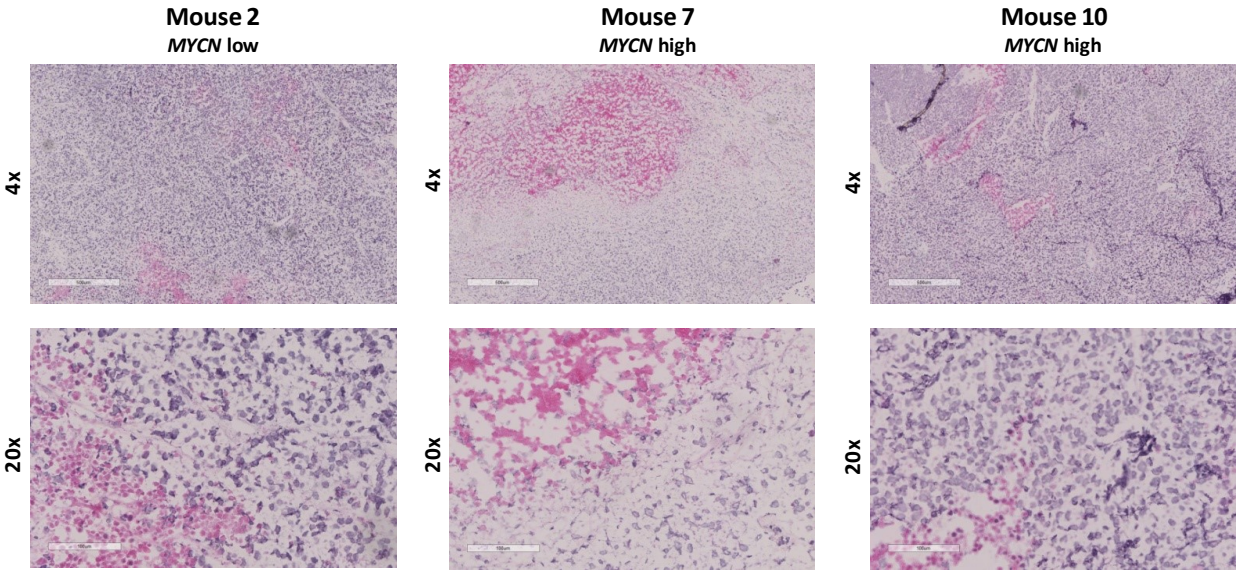

Figure 64: Histology pictures of orthotopic neuroblastomas. Cryoslides and HE staining were performed at the pathological institute. Tumors were identified as neuroblastoma with widespread necrosis (*T. Poth, pathological institute*).

Macroscopically, most of the tumors were of a dark red color and had a smooth or slightly nodose surface. The fast growing tumors did not look homogeneously but had darker and brighter areas. Tumors #3 and #9 were not dark red; instead they had a pale rose color.

5.4.6 MYCN expression and RNA-seq profiles of MYCN high/low tumors

In the previous sections, it was referred to the mice #1-#5 as *MYCN low* group and to mice #6-#10 as *MYCN* high group. The analysis of the *MYCN* expression in these two groups will be discussed in this section.

a) *MYCN* mRNA expression

To assess *MYCN* gene expression levels, the orthotopic tumor material was analyzed by quantitative real time PCR, relating the *MYCN* gene expression to the expression of the housekeeping genes *HPRT1* and *SDHA*.

Compared to the housekeeping genes, the relative *MYCN* expression of the tumors in the *MYCN* low group (mice #1-#3) ranged between 0.9 and 1.0 (Figure 65A). Among the *MYCN* high group (mice #6-#10) the relative *MYCN* expression was 0.97 to 1.12.

For the tumor sample of mouse #9 (*MYCN* high) no gene expression of *MYCN* and the housekeeping genes was measured by quantitative PCR. Analysis of the RNA sample on the bioanalyzer revealed that the RNA was degraded. Due to limited tumor material, the RNA isolation could not be repeated for this sample.

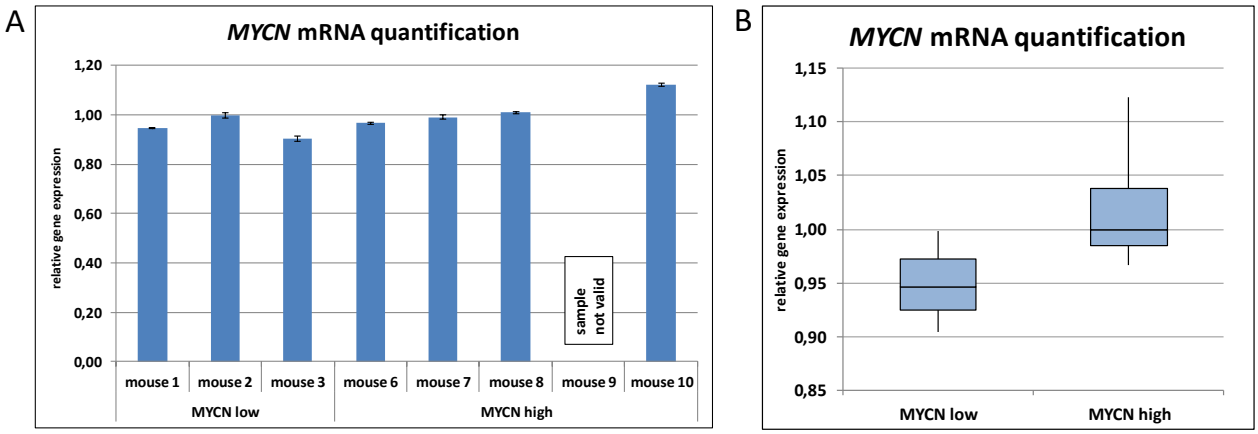

Figure 65: *MYCN* mRNA expression of orthotopic tumors. Quantitative PCR was performed with mRNA isolated from tumor material frozen in liquid nitrogen. *MYCN* expression was normalized to the housekeeping genes *HPRT1* and *SDHA*. A) *MYCN* mRNA expression of single orthotopic tumors. B) Comparison of *MYCN* mRNA expression of *MYCN* high and *MYCN* low orthotopic tumors. P-value was >0.05 (student t-test).

Apart from the single *MYCN* expression values of the tumors, the *MYCN* gene expression of the complete *MYCN* low and *MYCN* high group was analyzed (Figure 65B). The average relative *MYCN* expression of the *MYCN* low group, consisting of three tumors, was 0.95. The relative *MYCN* expression from the four tumors from the *MYCN* high group was 1.02 in

average. Although this difference is not significant, a tendency is seen, that the overall *MYCN* expression is slightly lower in the *MYCN* low group than in the *MYCN* high group.

b) MYCN protein expression

To validate the results from the *MYCN* mRNA expression analysis on protein level, western blot was performed with protein lysates generated from the xenograft tumors.

Unfortunately, there are no results available from this experiment due to methodic problems. The bands detected by western blot were weak or looked washy, therefore quantification of the MYCN protein levels was not possible. It is supposed that the measurement of the protein concentration was malfunctioning because of blood and other contaminations in the tumor samples. The varying concentrations of tumor material in the samples together with an overload of the polyacrylamide gel probably caused problems with detection of accurate MYCN and β-Actin bands in the western blot.

c) RNA-sequencing/ Comparison of expression profiles

The analysis of *MYCN* mRNA and protein expression by qPCR and western blot were an attempt to measure the effect on *MYCN* directly. As known from cell culture experiments, the impact of *MYCN* downregulation is not only seen in lower *MYCN* mRNA and protein levels, but results in widespread changes in the gene expression profiles of the cells [59]. Therefore, the RNA isolated from the tumor samples was prepared for RNA sequencing. Aim of this experiment was a comparison of the RNA sequencing data from the *MYCN* low and *MYCN* high tumors of the mice with RNA sequencing profiles from the IMR5/75 *MYCN* high/low cells generated by cell culture experiments [145].

2.313 genes upregulated by *MYCN* under cell culture conditions were compared with the 2.000 most upregulated genes in *MYCN* high tumors. Both gene expression profiles had 134 genes in common, which equates 1.8% of all genes analyzed in the Venn diagram. Similar results have been observed comparing 1.909 *MYCN* downregulated genes with the 2.000 most downregulated genes from the tumors. In this case, 145 genes were shared, which equates 2% of the genes in the analysis. Altogether, this leads to the conclusion that no similarity exists between the orthotopic tumors and *MYCN* dependent gene expression. Additionally, the genes shared by tumors and cell culture conditions were screened for known *MYCN* target genes. No genes typically up- or downregulated by *MYCN* expression have been identified among those genes.

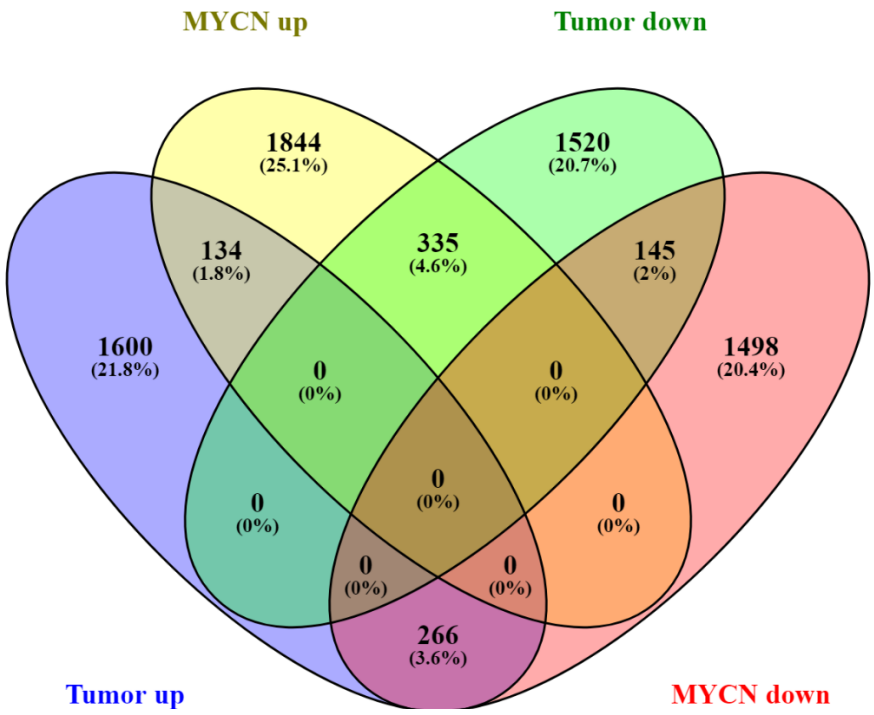

Figure 66: RNA-sequencing profiles of orthotopic tumors. RNA sequencing was performed with three *MYCN* low and five *MYCN* high tumors. All tumors from one category were analyzed together. A Venn diagram visualizes the overlap between genes up- and downregulated in *MYCN* high and *MYCN* low IMR5/75 cells in cell culture (*MYCN* up, *MYCN* down) and tumor material from the *MYCN* high and *MYCN* low-treated mice (tumor up, tumor down). *MYCN* knockdown was achieved by tetracycline treatment in cell culture or doxycycline administration to the mice.

Taking together the results from qRT-PCR, western blot and RNA-sequencing, no reduction of *MYCN* or *MYCN* dependent gene expression has been proven for the group of *MYCN* low mice, leading to the conclusion that no effective reduction of *MYCN* has been achieved in the orthotopic mouse model. One possible explanation is that the doxycycline applied by drinking water did not reach the human tumor cells at the adrenal gland in an appropriate concentration. Though it has been shown that the tumors were well connected to the blood vessels by distribution of the substrate for *in vivo* bioluminescence, the oral administration of the doxycycline might have been unsteady by inconsistent drinking behavior of the mice. Further, it must be considered that the human *MYCN* high/low cells have been treated with doxycycline for more than three months in the orthotopic mouse model. This is not comparable to the way the model was used for cell culture application with an induction of the *MYCN* knockdown for shorter time periods.

Altogether, the orthotopic neuroblastoma mouse model was successfully established in the DKFZ group “Neuroblastoma Genomics”. The methodic improvements installed increased the tumor growth rate to 80%. The tumor growth was monitored by MR imaging. *In vivo* bioluminescence revealed a constant expression of the luciferase cloned into the human tumor cells and thereby facilitated follow up of tumor growth and proved the absence of metastases.

Though, the heterogeneity of the tumor growth in both the *MYCN* high and the *MYCN* low group was complicating the analysis of the results. Among the group of ten mice, three mice showed a fast tumor growth, whereas the orthotopic tumors of the other mice were moderately or slowly growing. The possible impact of the mouse strain on this topic is discussed in section 6.3 in more detail.

On mRNA level, the *MYCN* knockdown of the xenograft tumor material was not convincing. Therefore, an indirect proof of the *MYCN* knockdown effects was aimed by RNA-sequencing of the orthotopic tumors and their comparison with a *MYCN* knockdown signature. Unfortunately, no similarity between the gene expression profiles was detected, leading to the conclusion that the *MYCN* knockdown was not effective in the orthotopic tumors, at least at the end of the experiment. Further work is necessary to ensure a long time stable *MYCN* knockdown in this mouse model.

6 Discussion

6.1 Categorization of neuroblastomas as sensitive/resistant upon BET inhibition *in vitro* and *in vivo*

For this thesis, several neuroblastoma cell lines were treated *in vitro* and *in vivo* with BET inhibitors. Thereby a large number of different experimental approaches were illuminating different biological aspects of BET inhibition in neuroblastomas. One central question of this work was to estimate how neuroblastoma cells with certain genetic features will respond to BET inhibitor treatment, aiming to be able to suggest a potential therapy with a BET inhibitor to the suitable patients based on the biology of their tumor. For comparison of *in vitro* and *in vivo* results the focus will be on the cell lines used in the animal experiments (IMR5/75, LS, NBL-S, SH-SY5Y) as well as NGP as example for a cell line not responding to BET inhibition.

Viability analysis of the neuroblastoma cell lines upon treatment with the BET inhibitors JQ1 and BAY1238097 revealed a higher effectivity of the inhibitor JQ1 for all cell lines. The cell lines LS and IMR5/75 were both classified as sensitive upon JQ1 treatment with similar EC50-values for JQ1 and BAY1238097. NGP cells presented as highly resistant with both inhibitors.

NBL-S cells were classified as intermediate responders to JQ1 treatment and an intermediate-resistant response upon BAY1238097 therapy. Despite the lower effectivity of BAY1238097, this inhibitor was chosen for the *in vivo* experiments due to its superior pharmacokinetic properties, whereas *in vitro* experiments were performed with JQ1.

Further insight into the functions of BET inhibition was gained by FACS-analyses used to estimate cell cycle and cell death of JQ1-treated neuroblastoma cells. An arrest in the G1 phase of the cell cycle was shown for IMR5/75, LS and NBL-S, which was strongest in IMR5/75 cells. This effect can be explained with the high proliferation rate of the IMR5/75 cells. IMR5/75 cells have a doubling time lower than 24h, in this case the cells are accumulating faster in G1 after completing the previous cell cycle than cells with a longer doubling time. An increase in cell death was observed in few *MYCN* amplified JQ1-treated cell lines only, most prominent in IMR5/75 cells. Despite the high levels of cell death, IMR5/75 were regrowing fast after washout of JQ1, showing that the long-term negative effects on cell proliferation of a shRNA induced *MYCN* knockdown were stronger than JQ1 treatment. These observations indicate that the effects induced by JQ1 treatment are temporary, especially for fast dividing IMR5/75 cells.

In two independent publications a direct regulation of *MYCN* by BRD4 in neuroblastoma was stated [121, 122], suggesting *MYCN* as a target gene of BET inhibition. To evaluate this, the MYCN protein expression was tested by two methods in a larger panel of *MYCN* amplified neuroblastoma cell lines, showing a reduction of MYCN in most of the cell lines. Especially for IMR5/75 and LS, the effects on the MYCN protein levels were minimal or ambiguous. For both cell lines, *MYCN* is also not listed among the differentially expressed genes identified by RNA-sequencing. For IMR5/75 and SK-N-BE(2)c treated with BRD4 siRNA the *MYCN* expression was not affected, leading to the conclusion that BRD4 is not absolutely required for *MYCN* expression in neuroblastoma.

Based on the data collected as part of this thesis it was not possible to finally clarify which factors are pivotal for sensitivity to BET inhibition. Though, some relations have been observed between the cell lines and their response to BET inhibitor treatment. One observation is that all three *MYCN* amplified cell lines with a doubling time of 24h and below (IMR5/75, SK-B-BE(2)c, IMR32) are BET inhibitor sensitive and show a prominent G1-arrest and high levels of cell death (Figure 67, left side). It is supposed that the fast cell cycle turnover causes a fast and strong accumulation of the cells in G1, presumably by the reduction of the transcription of cell cycle promoting genes, and an increase of cell death earlier than for cell lines dividing more slowly. On the other hand, the high proliferation rate goes in hand with a fast regrowth after the end of the therapy. Hence, this group of sensitive cells is characterized by early growth inhibitory effects that can be evaded immediately after removing the inhibitor and are thereby no permanent effects. For long term effects it is supposed that additional genetic aberrations

besides *MYCN* amplification are priming cells for BET inhibitor sensitivity (Figure 67, right side). This is the case for LS cells with amplifications of the cell cycle regulating genes *CDK4*, *MDM2* and *CCND1*. Amplifications of *CDK4* and *MDM2* are also detectable in BET inhibitor sensitive TR14 and in resistant NGP cells. In detail, a comparison of different cell lines for the definition of general rules is difficult as not enough neuroblastoma cell lines with comparable patterns of genetic aberrations could be analyzed.

For clinical settings, it is not only necessary to identify the most sensitive tumors, but also to define the group of tumors that will be highly resistant to avoid needless therapies. Among the group of *MYCN* amplified and JQ1 resistant cell lines are NGP and KELLY, both have an activation of *TERT* (Figure 67, bottom part). Besides the *TERT* activation, which was present solely in those two of the *MYCN* amplified cell lines, the genetic background of KELLY and NGP is quite different. In NGP, as described above, the cell cycle promoting genes *CDK4* and *MDM2* are amplified. KELLY harbor an inactivating mutation in the *TP53* gene and an activating mutation in the *ALK* gene. A *TERT* activation and an ALT phenotype are two ways how neuroblastoma cells enable a stabilization of telomere length and avoid cellular senescence [164]. Among the *MYCN* non-amplified neuroblastoma cell lines, two further cell lines with telomere stabilization and resistant to JQ1 treatment were identified: GIMEN cells have a *TERT* activation and SK-N-FI cells have an ALT phenotype. Those results hint that the presence of long telomeres might be involved in BET inhibitor resistance, independent from the *MYCN*-amplification status. However, a *TERT* activation or ALT phenotype are not consistent in predicting the resistance upon BET inhibitor therapy, as there are cell lines harboring those genetic aberrations that are JQ1 sensitive or intermediate responding, such as SK-N-AS with an activation of *TERT* or CHLA-90 with an ALT phenotype. It is supposed that the resistant cell lines harbor further genetic aberrations enabling those cells to grow upon BET inhibitor therapy. Also there are several *MYCN* amplified neuroblastoma cell lines resistant upon JQ1 treatment without *TERT* activation or an ALT phenotype

Altogether, clear definitions based on the genetic background of the cell lines could be formulated neither for BET inhibitor resistance nor for the identification of highly responsive cell lines. The panel of 23 neuroblastoma cell lines with diverging genetics was heterogeneous and too small to analyze universally valid hypotheses regarding BET inhibitor sensitivity statistically.

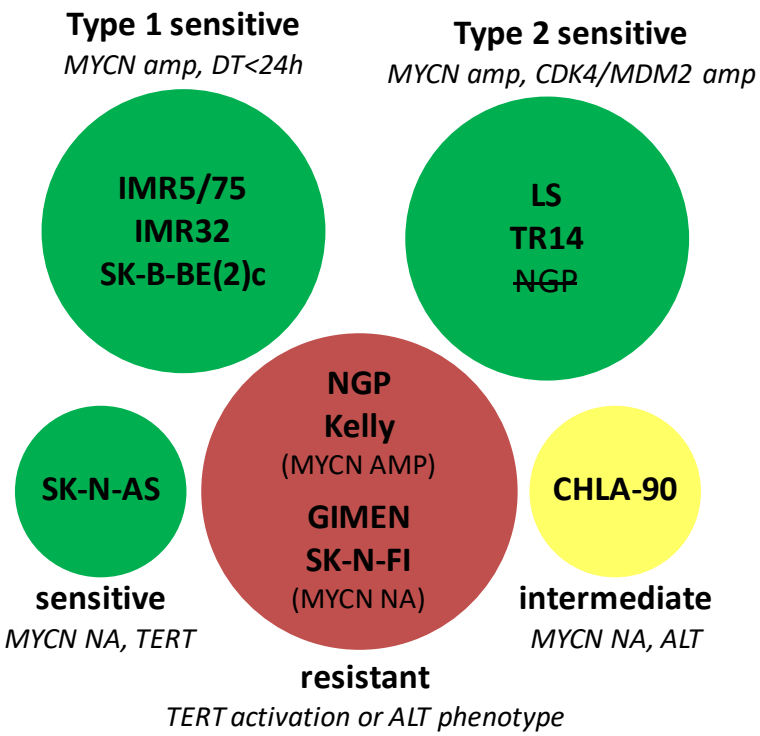

Figure 67: Resistance and sensitivity of neuroblastoma cells to BET inhibition. Genetic factors and growth characteristics supposed to be relevant factors for sensitivity or resistance of neuroblastoma cells upon JQ1 treatment. The categories sensitive, intermediate and resistant are based on the results of the viability screening (section 5.2.1). DT= doubling time; amp= amplification; NA= non-amplified. Crossed out cell lines show contrary behavior upon BET inhibition that other cells with similar genetic background.

In vivo, mice with LS deriving xenograft tumors showed a seven days prolonged survival upon treatment with BAY1238097, which is highly effective related to a total experimental duration of up to 30 days. No tumor growth inhibiting effects were detectable for tumors deriving from IMR5/75 cells although those cells had been highly sensitive to BET inhibitor treatment *in vitro*. The difference between both cell lines can be explained as those fulfill different criteria for JQ1 sensitivity (Figure 67), leading to a long-term effect of BET inhibition on LS cells and non-permanent effects on IMR5/75.

The experiments with IMR5/75 xenograft tumors were performed in two different mouse strains, however the validity of the results was limited due to variability of tumor onset and inhomogeneity of tumor growth especially among the control group. Besides the explanation for non-permanent growth inhibitiong effects in BET inhibitor-treated IMR5/75 cells and tumors, it cannot be excluded that a potential inhibitory effect for tumor growth was obscured by the inconsistent control group.

Summarizing the results for BET inhibitor treatment *in vitro* and *in vivo*, at present it is not possible to draw conclusions from a BET inhibitor sensitive cell culture setting to a successful therapy *in vivo*.

6.2 BRD4 target genes in the cellular context

The high-throughput analysis of mRNA and protein expression in various BET inhibitor-treated cell lines revealed high numbers of differentially expressed genes and proteins affected upon BET inhibitor treatment. Several proteins and genes belonged to pathways related to cell division, *wnt* signaling or *TP53* related pathways. In this section some chosen target genes will be integrated in the cellular context and discussed regarding their potential role in neuroblastoma.

A large number of publications dealing with BET proteins have shown an impact of BRD4 expression on cell cycle progression for several cancer entities. It has been revealed that BRD4 affects multiple steps of the cell cycle. On one hand, Dey et al. have shown that BRD4 has regulatory functions at the G2/M transition [111]. On the other hand, BRD4 is involved in the G1/S transition by interacting with replication factor C required for DNA replication [114]. In neuroblastoma cells, a growth arrest is observed for cells treated with the BET inhibitors JQ1 and I-BET726 [121, 122]. In line with these findings, the present work showed a significant cell cycle arrest in the G1 phase of the cell cycle for the JQ1 sensitive and intermediate responding neuroblastoma cell lines. Additionally, several genes belonging to pathways related to different phases of the cell cycle were identified as affected by JQ1 treatment. Besides the cell cycle effects in cancer cells, a G1 arrest is also induced in fibroblasts after BRD4 knockdown based on shRNA [113]. Mochizuki et al. showed that this G1 arrest was accompanied by a missing upregulation of G1 genes, which is induced by an increased binding of p-TEFb and RNA polymerase 2 to the promoters of these genes in untreated fibroblasts.

In neuroblastoma, high *CCND1* gene expression was detectable in a large proportion of cell lines, indicating a dependency of this cancer entity on Cyclin D1. Figure 68A compares the *CCND1* gene expression of 21 neuroblastoma cell lines, showing high *CCND1* levels especially in the *CCND1* amplified LS cells. In comparison to human normal tissue and other cancer entities, *CCND1* gene expression was elevated in neuroblastoma (Figure 68B). The DRIVE project realized a large-scale RNA-interference screening to identify potential synthetic lethal vulnerabilities in nearly 400 cancer cell lines, including nine neuroblastoma cell lines [165]. Compared to other entities, those neuroblastoma cell lines were highly dependent on *CCND1* gene expression, emphasizing the importance of Cyclin D1 function for cell cycle progression and survival in neuroblastoma.

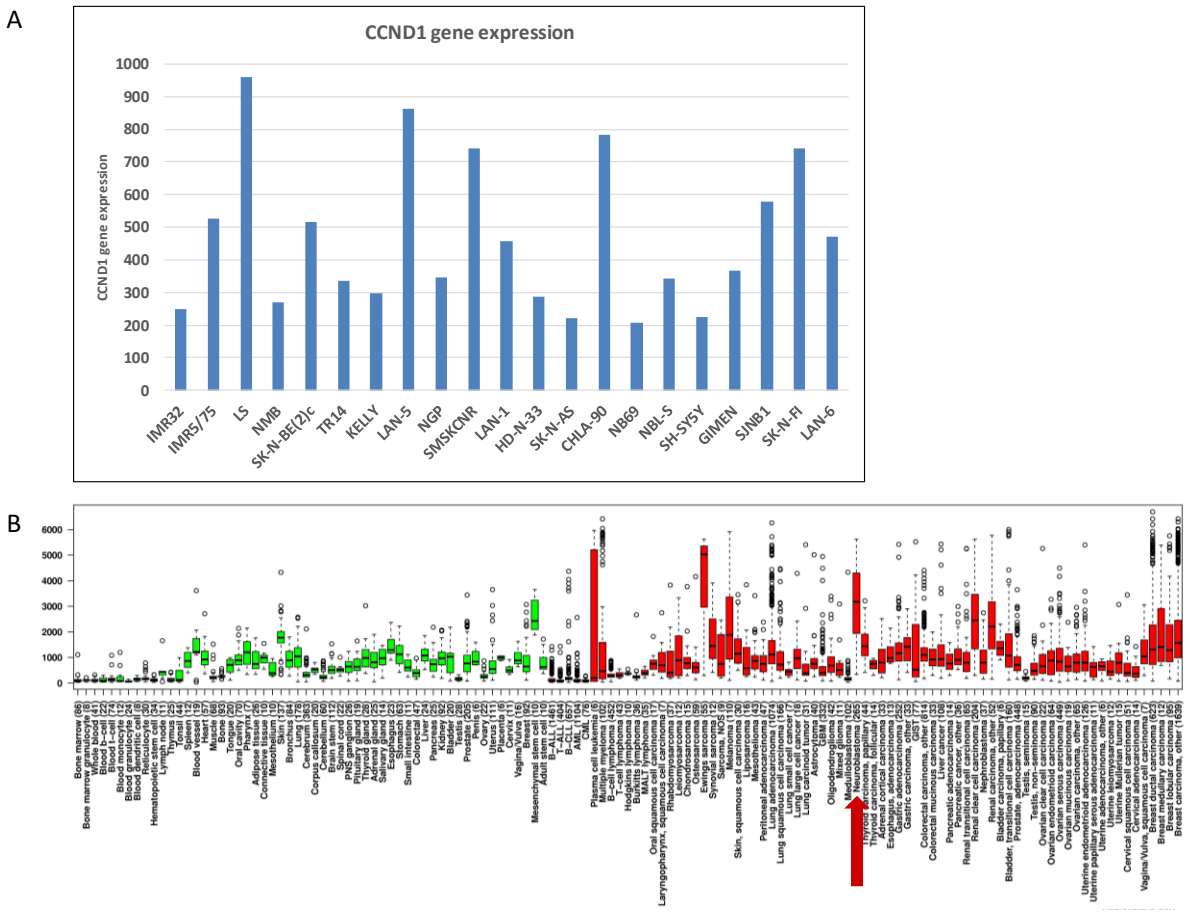

Figure 68: *CCND1* expression in neuroblastoma. A) *CCND1* gene expression in neuroblastoma cell lines. B) *CCND1* gene expression in normal tissue (green) and different cancer entities (red). Neuroblastoma tumors are indicated with a red arrow.

In this thesis, a decrease of cyclin D1 protein expression upon JQ1 treatment was observed in nearly all *MYCN* amplified neuroblastoma cell lines, verified by RPPA and western blot. As Cyclin D1 is important for G1/S transition and as neuroblastoma cell lines are highly dependent on Cyclin D1, it is supposed that the missing increase of Cyclin D1 levels in JQ1-treated cells abrogates cell cycle progression. This results in a G1 arrest as observed for JQ1 sensitive and intermediate responding cell lines.

Cyclin D1 has been identified as a target of BRD4 in various cancer entities. Henssen et al. treated high risk medulloblastoma cells with JQ1 and described a downregulation of Cyclin D1 in medulloblastoma with a siRNA mediated knockdown of BRD4 [166]. An influence of JQ1 on the Cyclin D1-CDK4-RB-axis going along with a reduction of the Cyclin D1 expression has also been observed in cell culture models of Merkel cell carcinoma and thyroid tumors [167, 168]. In NUT midline carcinoma, it was proven that an induction of Cyclin D1 expression was able to rescue carcinoma cells from a cell cycle arrest induced by JQ1 treatment [169]. Liao et al. additionally observed reduced Cyclin D1 protein expression upon JQ1 treatment and a synergistic effect of JQ1 and an inhibitor of CDK4/6 in the therapy of NUT midline carcinoma.

CDK4 and CDK6 are the corresponding CDKs of Cyclin D1 and essential for cell cycle progression at the G1/S transition, which explains the complete cell cycle arrest shown with this drug combination in NUT midline carcinoma.

It is known that BRD4 influences gene expression by inactivation of strong enhancers and superenhancers [95]. *CCND1* is regulated by a large superenhancer [146], which explains the sensitivity towards BET inhibitor treatment. In neuroblastomas, as this tumor entity is dependent on Cyclin D1, it is supposed that downregulation of the *CCND1* gene might be responsible for the growth inhibiting effects. This could also explain the sensitivity of the *CCND1* amplified LS cells towards BET inhibitor treatment *in vivo*, representing a neuroblastoma cell line highly dependent on elevated *CCND1* gene expression. Compared to *CCND1*, downregulation of *MYCN* observed in 70% of the *MYCN* amplified neuroblastoma cell lines analyzed by RPPA and western blot might not be the main pathway for the growth inhibiting effects of BET inhibition in neuroblastoma cell lines. As *CCND1* is a *c-MYC* target gene, it is possible that reduced *MYCN* expression upon JQ1 treatment additionally contributes to decreased Cyclin D1 expression in an indirect way.

Besides Cyclin D1, other proteins related to the G1/S transition are affected by BET inhibition. Those include CDK4 and CDK6 as the corresponding CDKs for D-type cyclins as well as members of the E2F-protein family, which are important effector proteins of CDK4/6 kinase activity. RNA-sequencing revealed that *CDK6* and *E2F2* belonged to the genes with the strongest downregulation upon JQ1 treatment in all four cell lines. *E2F1* did not belong to the most differentially expressed genes in RNA-sequencing but was downregulated on protein level in 4 out of 6 *MYCN* amplified neuroblastoma cell lines, as shown by western blot in this thesis. Lower *E2F2* and *E2F7* gene expression upon BRD4 knockdown is detected by Mochizuki et al., whereas *E2F1* is not affected in this study on fibroblasts [113]. Hong et al. identified *E2F2* as a direct target of BRD4 in hepatocellular carcinoma [170], showing that the results on gene and protein expression for neuroblastoma are applicable to other tissues and cancer entities.

Consistent with the downregulation of cell cycle promoting genes by JQ1 treatment, cell cycle inhibitors were identified among the genes upregulated upon BET inhibition. The genes *CDKN2D*, *CDKN2B* and *CDKN1A* encode for inhibitors of CDK4 and CDK6 and were overexpressed in IMR5/75, LS and NBL-S neuroblastoma cells treated with JQ1. Upregulation of these CDK4/6 inhibitors has also been shown for JQ1-treated primary pulmonary cells [171]. The CDK-inhibitors are enhancing the cell cycle arrest induced by JQ1 by abrogation of cell cycle promoting kinase activity at the G1-S transition. This prevents RB phosphorylation and S-phase entry of the cell cycle. Together the effects on Cyclin D1, CDKs, E2F proteins and

CDK inhibitors by BET inhibition resulted in a multifactorial impact on the G1-S transition and explain the G1 arrest observed for JQ1 sensitive and intermediate responding cell lines.

Besides the CDK4/Cyclin D-RB-E2F pathway, the *TP53* axis is another signaling pathway leading to cell cycle arrest or apoptosis. BRD4 directly binds to p53 and is involved in the transcription of p53 target genes [102]. JQ1 treatment of AML cells does not abrogate the association of BRD4 and p53 but has an impact on the interaction of the BRD4-p53 complex with p53 effector genes, resulting in cell cycle arrest and apoptosis [172]. In this thesis, lower p53 expression on mRNA and protein level was observed in neuroblastoma cell lines treated with JQ1. Related to this, a downregulation of pathways related to DNA damage and p53 was noted in IMR5/75 cells.

The stabilization of p53, resulting in its participation in cell cycle arrest and apoptosis, is induced by DNA damage, including double strand breaks [173]. In the recognition of double strand breaks, ATM plays a central role, phosphorylating p53 and histone H2AX, which is named γ-H2AX in its phosphorylated form and is an early marker for DNA damage in form of double strand breaks [174]. *H2AFX*, encoding for histone H2AX was upregulated in RNA-sequencing of all four neuroblastoma cell lines. Related to this, elevated protein levels of RAD17, a protein involved in the recognition of DNA damage, was detected by RPPA for all cell lines at the 48h time point.

The role of BRD4 in DNA damage response has been investigated by Floyd et al. [175]: In different human cancer cells treated with JQ1 a significantly higher increase of γ-H2AX was observed upon irradiation compared to DMSO-treated control. Isoform B of BRD4 acted as an inhibitor for DNA damage response signaling by interaction with condensin. JQ1 treatment inducing DNA damage response has also been observed for AML cells [172]. In general, JQ1 enhances the recognition and first-line response to DNA damage in several cancer types.

In contrast to this, effector pathways for DNA damage repair or cell cycle arrest induced by DNA damage seem to be not effective in neuroblastoma cell lines. By RNA-sequencing, downregulation of RAD50 was detected for 3 out of 4 cell lines. RAD50 is part of the MRN complex important for the repair of double strand breaks by homologous recombination and non-homologous end joining [176]. As discussed above, p53 is also downregulated in neuroblastoma cells. Taken together it can be supposed that JQ1 treatment is interrupting DNA damage signaling pathways, leading to an ineffective DNA damage response which on one hand sensitizes cells to DNA intercalating chemotherapeutics as shown by combined treatment of neuroblastoma cells with JQ1 and doxorubicin. On the other hand, it leads to an ineffective induction of cell death in cells treated with JQ1 alone due to lower p53 expression.

A variety of histone genes was strongly upregulated upon JQ1 treatment in all four neuroblastoma cell lines. This included genes for up to 42 different types of histones and was

observed for all time points. *HEXIM1* was identified as one of the genes most strongly and constantly overexpressed in JQ1-treated neuroblastoma cells. Upregulation of both *HEXIM1* and of histone genes upon JQ1 treatment was also observed by Zhu et al. in murine thyroid tumors, suggesting that the upregulation of histones might lead to an increase in chromatin remodeling and thereby has an impact on the transcription of further genes [168].

The broad upregulation of *HEXIM1* emphasizes its central role in the response to BET-inhibitor treatment. HEXIM1 is known to interact with Cyclin T, functioning as a negative regulator of pTEFb [177]. Further, HEXIM1 was identified to be a positive regulator of p53, inhibiting p53 ubiquitination and thereby enhancing its functions on cell cycle and cell death [178]. As HEXIM1 is a substrate of HDM2, the human homolog of MDM2 and responsible for p53 turnover, it is supposed that the regulation of p53 by HEXIM1 might result from competition of both HDM2-substrates [179].

In neuroblastoma cells, a broad downregulation of gene expression was observed upon JQ1 treatment. As negative regulator of p-TEFb based transcriptional regulation, elevated levels of HEXIM1 might contribute to deviant gene expression patterns in JQ1-treated neuroblastoma cells. In its second function as regulator of p53, high *HEXIM1* expression should enhance the stability of p53 and thereby cell cycle arrest, as observed in JQ1-treated neuroblastoma cells. Contrary to this, lower *TP53* gene expression and protein levels were detected in neuroblastoma cells upon JQ1 treatment. Possibly, the turnover of p53 was lower due to increased stability of p53, resulting in reduced *TP53* gene transcription.

GSK3-β was strongly upregulated upon JQ1 treatment both on mRNA and on protein level. The protein quantification by RPPA revealed a strong upregulation of GSK3-β both in *MYCN* amplified and *MYCN* non-amplified cell lines from the sensitive, intermediate or resistant group, especially at the late 48h time point. The inactive form of GSK3-β, phosphorylated at the Serine 9 residue [152], was not affected by JQ1 treatment in *MYCN* amplified neuroblastoma cells. In the RNA-sequencing analysis *GSK3-β* gene expression was upregulated for all cell lines. GSK3-β is a part of several signaling pathways including Wnt, Sonic hedgehog, PI3K/AKT or MAPK signaling and is thereby involved in fundamental cellular functions, such as cell proliferation, differentiation or apoptosis [149, 150].

The most prominent function of GSK3-β is its role in Wnt-signaling. In the absence of Wnt, GSK3-β initiates the degradation of β-Catenin by phosphorylation of two serine residues, whereas in the presence of Wnt β-Catenin is stabilized and functions as a cofactor for the TCF transcription factor in the nucleus [180]. β-Catenin is downregulated by treatment with JQ1 in colon cancer, equating a decrease in TCF/β-Catenin mediated gene transcription [181]. Pathway analysis of the differentially expressed genes identified by RNA-sequencing revealed an upregulation of genes assigned to the pathway “Formation of β-Catenin:TCF

transactivating complex" in LS and NBL-S cells at several time points. The upregulated genes mapping with the pathway among others included *CTNNB1*, coding for β-Catenin, *TLE4* and several histone genes. TLE4 is an inhibitor of the transcriptional activation by the β-Catenin/TCF complex and thereby reducing the transcription of Wnt target genes. The observed upregulation of both *GSK3-β* and *TLE4* may lead to a functional knockdown of the β-Catenin/TCF mediated gene transcription and potent downregulation of Wnt signaling in JQ1-treated neuroblastoma cells.

Besides the role in signaling, GSK3-β is a central factor for MYC protein turnover. GSK3-β phosphorylates MYC at the threonine 58 residue, which leads to ubiquitination of MYC by Fbw7 and to MYC proteolysis [50, 151]. Thereby high GSK3-β expression results in instability and a shorter half-life of MYC. Upregulation of GSK3-β observed upon JQ1 treatment could possibly contribute to the reduction of MYCN protein levels detected for a number of *MYCN* amplified neuroblastoma cell lines, independently from a direct targeting of *MYCN* by BRD4 inhibition. A study published by Duffy *et al.* showed reduced *MYCN* mRNA levels and an increase of apoptosis upon pharmacological GSK3-β inhibition in *MYCN* non-amplified but *MYCN* transgenic neuroblastoma cells [182]. Further research on the interaction of BET proteins and GSK3-β could illuminate the background of the observed upregulation of *GSK3-β* and, by suitable drug combinations, improve the therapeutic potential of a BET inhibition for neuroblastoma.

6.3 Impact of the mouse strain on the growth of neuroblastoma xenograft tumors

The experiments with the orthotopic neuroblastoma mouse model as well as the initial experiments using the subcutaneous neuroblastoma model were performed with CD-1 Nude mice, an immunodeficient mouse model broadly used for xenograft mouse models of several tumor entities. CD-1 Nude mice harbor an autosomal recessive mutation of the *nude* gene. Homozygous animals have a rudimentary, non-functional thymus resulting in absent T-cells and immunodeficiency, whereas animals heterozygous for the mutant *nude* allele are immunocompetent [157].

CD-1 Nude mice are largely used for xenograft applications at the subcutaneous and at the orthotopic setting with different human neuroblastoma cell lines. This includes IMR5, a cell line closely related to the IMR5/75 cell line used for both subcutaneous and orthotopic xenografts in this thesis and SH-SY5Y, which was included in the cell line panel for the subcutaneous animal experiments [126, 183]. Nevertheless, the results established as part of this thesis with the subcutaneous neuroblastoma model in CD-1 Nude mice clearly showed that tumor growth

and tumor heterogeneity are highly dependent on the mouse strain. As a delivery of heterozygous and thereby immunocompetent CD-1 Nude mice by mistake was excluded, the grade of immunodeficiency of the CD-1 Nude mouse strain was considered as a possible reason for the heterogeneous tumor growth.

Immunodeficient mouse strains can be categorized into three subgroups, according to their grade of immunodeficiency (Table 19). The mouse strains with the lowest grade of immunodeficiency (here defined as category 1) do not exhibit a T-cell response but possess mature B-cells as well as functional NK cells. The CD-1 Nude mice belong to this category. In contrast, mouse strains from category 3 neither have functional T-, B- or NK cells and thereby no remaining adaptive or innate immune response. Those highly immunodeficient animals include the NSG mouse strain successfully used as model for the subcutaneous xenografts in this thesis.

Table 19: Categorization of immunodeficient mouse strains. Categories are based on the level of immune defects. Adapted from Charles River Brochure [155].

	Category 1	**Category 2**	**Category 3**
Mature T-cells	No	No	No
Mature B-cells	Yes	No	No
NK cells	Yes	Yes	No
Mouse strains	CD-1 Nude NMRI Athymic Nude BALB/c	SCID hairless Fox Chase SCID	NSG NOD SCID CB17 SCID

The NSG (NOD SCID γ) mice have both a *scid* mutation resulting in an absent T- and B-cell response and lack the gamma chain of the IL2-receptor, leading to severe defects in the innate immune system including natural killer cells [156]. Due to the complete absence of any immune response, they are ideal for the engraftment of foreign tumor cells. Compared to the CD-1 Nude and the NMRI mouse strain, the subcutaneous neuroblastoma xenograft tumors of the NSG mice showed the lowest variability regarding tumor onset, growth behavior and final tumor size with the four cell lines used in the subcutaneous neuroblastoma model in this thesis.

According to current publications in the neuroblastoma research field, a variety of cell lines and mouse strains are used for subcutaneous and orthotopic neuroblastoma xenografts. For subcutaneous xenografts, both mouse strains from category 1 as athymic nude and from category 3 as NOD-SCID, CB17 SCID or NSG are common, mainly engrafting IMR32 or SH-SY5Y neuroblastoma cells. For orthotopic neuroblastoma mouse models, the neuroblastoma cell lines SH-SY5Y, IMR32, SK-N-AS and KELLY are most commonly used. The mouse strains used for orthotopic tumor establishment included BALB/c, CD-1 Nude or athymic Nude from category 1 as well as NOD SCID from the third category. Taken together, the mouse strains

and cell lines used for both kinds of xenograft neuroblastoma mouse models display a broad range of cellular genetics and different grades of immunodeficiency. Based on the results of this literature search it was not expected that CD-1 Nude mice might not be suitable for tumor hosting in a subcutaneous neuroblastoma mouse model.

Comparing the results from the subcutaneous neuroblastoma mouse model of IMR5/75 in CD-1 Nude mice with the corresponding orthotopic model, some analogies are noticeable regarding to the heterogeneity of tumor growth. Among the eight tumors from the orthotopic neuroblastoma model, three tumors grew fast, four tumors grew slow and one tumor was growth arrested. The growth characteristics were not dependent on *MYCN* high or *MYCN* low conditions. Similarly, fast growing, slow growing and growth arrested tumors occurred in the subcutaneous neuroblastoma mouse model in both the control and in the BAY1238097-treated group. Testing different mouse strains revealed that an implantation of the human tumor cells in highly immunodeficient NSG mice resulted in the lowest variability of subcutaneous tumor growth for all four cell lines. This emphasizes that the variable tumor growth in a CD-1 Nude host is not specific for IMR5/75, rather NSG mice should be preferred in general. Based on these findings, testing the orthotopic mouse model with the NSG mouse strain would be advisable, because CD-1 Nude mice might not be the best mouse strain for this application. Implanting the human neuroblastoma cells orthotopically in NSG mice might reduce the heterogeneity of tumor growth in this animal model.

6.4 Prognosis of the clinical relevance of BET inhibitors for neuroblastoma

Over the past years, BET inhibitors have been handled as important new strategy for the treatment of *c-MYC* and *MYCN* overexpressing malignancies. Nevertheless, the experimental work regarding BET inhibition in neuroblastoma cell lines and in a subcutaneous mouse model revealed mixed results. The BET inhibitor JQ1 was highly effectively reducing viability in 55% of the *MYCN* amplified and 30% of the *MYCN* non-amplified neuroblastoma cell lines, hinting that besides amplified *MYCN* further genetic factors may be required to prime neuroblastomas towards BET inhibitors. Although JQ1 treatment resulted in an arrest in the G1-phase of the cell cycle and in few cases in increased levels of cell death, these effects were not permanent, and the neuroblastoma cells started to regrow immediately after washout of the drug. An effect on the MYCN protein expression upon JQ1 treatment was noticeable for the majority of the *MYCN* amplified neuroblastoma cell lines, however it was shown that the decrease of the *MYCN* expression is not a direct effect of BRD4 inhibition. At this point, the findings of this

thesis differ from the results published by Puissant *et al.* and Wyce *et al.* showing by ChIP-sequencing that *MYCN* is a direct target of BRD4 in neuroblastoma [121, 122].

In vivo, the BET inhibitor BAY1238097 was well tolerated by the mice. However, the potency of BAY1238097 in animals was weak and the results from *in vitro* experiments regarding BET inhibitor sensitivity could not be transferred to *in vivo* applications using the same neuroblastoma cell lines. The cell line IMR5/75 highly sensitive *in vitro* did not show promising results *in vivo*, whereas IMR5 cells closely related to this cell line have been shown to respond well to therapy with the BET inhibitor OTX015 [123]. In this work, solely xenograft tumors deriving from the cell line LS were treated successfully with BAY1238097.

In preclinical research, BET inhibitors have been shown to be potent inhibitors for both BRD4 translocated and *MYC* overexpressing cancer cell lines, influencing cell proliferation, apoptosis and cellular differentiation [184]. Especially the option to target *MYC* genes on the transcriptional level and thereby having a potent drug for the therapy of *MYC* dependent cancers is promising. However, it should be kept in mind that only BET translocated or mutated cancers are treated with BET inhibitors as targeted small molecule therapy in the narrower sense. One example is the NUT midline carcinoma, where *BRD4-NUT* translocations are causative for the disease [115]. But also neuroblastomas harbor sporadic aberrations in the BRD4 gene. In the INFORM-study (Individual therapy for relapsed malignancies in childhood), tissue samples from relapsed childhood tumors are screened for mutations and genetic aberrations. In three cases of relapsed high-risk neuroblastoma, *BRD4* aberrations were detected including SNVs, insertions and outlier gene expression. Interestingly, none of the tumors with a *BRD4* aberration belongs to the group of *MYCN* amplified tumors, instead two of them have an ALT phenotype and one belongs to the *TERT* group of high-risk neuroblastomas. In a collective of newly diagnosed neuroblastoma tumors, no mutations of the *BRD4* gene have been identified.

Several clinical studies with BET inhibitors are currently ongoing, using BET inhibitors for different cancer types mainly aiming to treat *MYC* deregulated malignancies. This is striking insofar, that the knowledge of the biology of BET proteins and the mechanisms of its inhibition are relatively poorly understood. As epigenetic drugs, BET inhibitors have an impact on transcriptional initiation and elongation of various genes and are not specifically inhibiting *MYC* target genes. Beyond, all BET inhibitors available are not specific for BRD4, but are binding to all BET family members [116]. Thereby BET inhibition affects a broad range of biological processes, including insulin production, inflammation or adipogenesis [124]. It is unknown how those off-target-effects contribute to the cytotoxic effects of the therapy and if long-term effects will occur. The importance of BET proteins for cell biology can be estimated by the fact that mouse embryos homozygous for a BRD4 null allele are dying short after implantation, whereas

heterozygous mice still show severe abnormalities, such as head malformation or abnormal liver cells [185].

In all preclinical studies, as well as in this thesis, neuroblastoma xenograft mice well tolerated the therapy with BET inhibitors [121, 122]. Nevertheless, BET inhibition has an impact on the healthy mouse tissues as it was shown by Bolden *et al.*, who have generated an inducible BRD4 knockdown model in mice, based on shRNA knockdown [186]. Upon BRD4 knockdown the mice show skin abnormalities, such as hyperplasia and hyperkeratosis, a reduction of Paneth cells and crypt disruption in the intestine, as well as haematologic disorders.

An important side effect that needs to be considered when using BET inhibitors for cancer therapy is that an inhibition of BET proteins can lead to reactivation of HIV in T-cells latent infected and should therefore not be given to HIV positive patients [100]. Similar observations can be made for HPV and Herpesvirus [101, 187]. A study from Korb *et al.* shows that BRD4 activates transcription in neurons and that mice treated with JQ1 show deficits regarding their long-term memory [188]. It is unknown, if similar effects have to be expected in humans treated with the BET inhibitors used for clinical trials. At last, it is likely that BET inhibitors may lead to transient male sterility by coinhibition of the testis specific BET protein BRDT [189].

Due to the fast regrowth observed in neuroblastoma cells treated with JQ1 in this thesis, it is advisable to administer BET inhibitors in combination therapy in clinical settings. One possibility might be the combination of JQ1 and doxorubicin, a DNA intercalating drug commonly used for neuroblastoma chemotherapy, was tested for this thesis. The combination of both drugs was more effective than single therapy, especially when administered simultaneously or when doxorubicin was applied prior to JQ1 treatment. However, it was shown by Bolden *et al.* that a combination of those drugs *in vivo* results in a lower weight gain after therapy due to increased toxicity at the intestine [186]. A different approach to identify effective drug combinations for BET inhibitors was used by Liu *et al.*, who screened JQ1-treated neuroblastoma cells in combination with more than 2.500 drugs [190]. Among the 33 most effective drugs identified by the screen are several quinone containing compounds partly including DNA intercalating functions and anti-microtubule substances. Vincristine has the highest potency in this setting both *in vitro* and *in vivo*, whereas doxorubicin has not been found to belong to the potent synergistic substances.

Taken together the findings presented in this thesis and the state of knowledge regarding BET biology, it is debatable if clinical trials with BET inhibitors should be performed already. Relying on the JQ1 viability data in this thesis, no more than 55% of the *MYCN* amplified neuroblastoma cell lines show high sensitivity upon treatment with JQ1 and would therefore probably profit from a BET inhibitor therapy. Nevertheless, this means deciding for or against a treatment with a BET inhibitor based solely on the presence or absence of a *MYCN*

amplification would expose 45% of the neuroblastoma patients with a *MYCN* amplification to a highly unspecific, toxic and not approved therapy without clear benefit for the patients. Moreover, this thesis showed that the sensitivity of neuroblastoma cell lines *in vitro* does not necessarily predict the responsiveness of the same cell line *in vivo*. This indicates that the results from preclinical experiments with BET inhibitors cannot be transferred to patient therapy without questioning. Further research is indispensable to identify other genetic factors besides amplified or overexpressed *MYCN*, which may prime neuroblastoma tumors for a therapy with BET inhibitors. Including suitable patients in clinical trials for BET inhibitors based on the results of further research would enhance the significance and power of these studies.

7 Abbreviations

For chemical elements the common symbols were used for abbreviations. They are not listed here.

ALT	alternative lenghtening of telomeres
AML	acute myeloic leukemia
amp	amplified
APS	Ammonium persulfate
BAY	BAY1238097
BD	bromodomain
BET	bromodomain and extraterminal domain
BETi	BET inhibitor, abbreviation used for BAY1238097
BSA	bovine serum albumin
°C	degree Celcius
C (-terminus)	carboxyl (-terminus)
CDK	Cyclin dependent kinase
cDNA	complementary DNA
ChIP	Chromosome Immunoprecipitation
cm, cm²	Centimeter, square centimeter
CTD	C-terminal domain
Ctrl	control
DAPI	4',6-diamidino-2-phenylindole
DEG	Differentially expressed genes
DEPC	Diethyl pyrocarbonate
DKFZ	German cancer research center
DMSO	Dimethyl sulfoxide
DNA	deoxyribonucleic acid
dNTP	nucleoside triphosphate
doxy	doxycycline
DSM	needle code parameters: 3/8 circle, cutting, micro point
DT	doubling time
DTT	Dithiotreitol
EC50	Half maximal effective concentration
ECL	Enhanced chemiluminescence
EDTA	Ethylenediaminetetraacetic acid
EGF	epidermal growth factor
et al.	and others (lat)
FACS	fluorescence activated cell scanning
FCS	Fetal calf serum
FDR	False discovery rate
FGF	fibroblast growth factor
for	forward

g	gravitational constant
G	Gauge
g, mg, µg, kg	Grams, milligrams, micrograms, kilograms
G1/ G2 (phase)	Gap phase, cell cycle
h	hours
H_2O dest.	destilled water
hi	high
HIV	human immunodeficience virus
HPV	human papilloma virus
IC50	half maximal inhibitory concentration
IL2	Interleukin 2
INFORM	INdividual therapy FOr Relapsed Malignancies in childhood
INSS	international neuroblastoma staging system
IVC	isolated ventilated cages
kDa	Kilodalton
l, ml, µl	Liter, milliliter, microliter
LB	lysogeny broth
lo	low
LOCF	last observation carried forward
M (phase)	mitosis phase, cell cycle
M, mM, µM	molar, millimolar, micromolar
mA	Milliampere
(Opti-)MEM	minimum essential medium
min	minutes
mm, mm²	millimeter, square millimeter
mRNA	messenger RNA
MRI/MRT	magnetic resonance imaging/ tomography
N (-terminus)	Amino (-terminus)
NA	non-amplified
neg	negative
NK (cells)	natural killer (cells)
nm	Nanometer (wave lenght)
NSG	NOD SCID gamma
NV	not valid, viability category
OD	outer diameter
p, q (chromosomes)	short/ long chromosome arms
PAGE	polyacrylamide gel electrophoresis
PBS	Phosphate buffered saline
PCA	principal component analysis
PCR	polymerase chain reaction
PDX	patient derived xenograft
Pen/Strep	Penicillin/ streptomycin
PGA	polyglycolic acid (suture)
PI	propidium iodide
pmol	Picomol

POD	Peroxidase
pRB	retinoblastoma protein
qPCR	quantitative PCR
res	resistant, viability category
rev	reverse
RLU	relative light units
RNA	ribonucleic acid
rpm	rounds per minute
RPPA	Reverse Phase Protein Array
rRNA	ribosomal RNA
RT	room temperature
S (phase)	synthesis phase, cell cycle
SDS	Sodium dodecyl sulfate
sec	seconds
sens	sensitive, viability category
(RNA)-seq	(RNA)-sequencing
shRNA	small hairpin RNA
siRNA	silencer RNA
SNV	single nucleotide variation
TBS	Tris buffered saline
TEMED	Tetramethylethylenediamine
tet	tetracycline
TetO2	Tetracycline operator sequence
TetR	Tetracycline repressor
TH	tyrosine hydroxylase
tRNA	transfer RNA
V	Volt
WB	western blot
x	times

8 Figures and Tables

8.1 Figures

8.2 Tables

9 Literature

1. Kaatsch P, G.D., Spix C, *German Childhood Cancer Registry- Annual Report 2017 (1980-2016)*. 2018, Institute of Medical Biostatistics, Epidemiology and Informatics (IMBEI) at the University Medical Center of the Johannes Gutenberg University Mainz.
2. Schwab, M., et al., *Neuroblastoma: biology and molecular and chromosomal pathology.* Lancet Oncol, 2003. **4**(8): p. 472-80.
3. Maris, J.M., et al., *Neuroblastoma.* Lancet, 2007. **369**(9579): p. 2106-20.
4. DuBois, S.G., et al., *Metastatic sites in stage IV and IVS neuroblastoma correlate with age, tumor biology, and survival.* J Pediatr Hematol Oncol, 1999. **21**(3): p. 181-9.
5. D'Angio, G.J., A.E. Evans, and C.E. Koop, *Special pattern of widespread neuroblastoma with a favourable prognosis.* Lancet, 1971. **1**(7708): p. 1046-9.
6. Strother, D.R., et al., *Outcome after surgery alone or with restricted use of chemotherapy for patients with low-risk neuroblastoma: results of Children's Oncology Group study P9641.* J Clin Oncol, 2012. **30**(15): p. 1842-8.
7. Speleman, F., J.R. Park, and T.O. Henderson, *Neuroblastoma: A Tough Nut to Crack.* Am Soc Clin Oncol Educ Book, 2016. **35**: p. e548-57.
8. Baker, D.L., et al., *Outcome after reduced chemotherapy for intermediate-risk neuroblastoma.* N Engl J Med, 2010. **363**(14): p. 1313-23.
9. Levy, D., et al., *[Childhood cancer: progress but prognosis still very unequal. Example of Retinoblastoma and high-risk Neuroblastoma].* Bull Cancer, 2014. **101**(3): p. 250-7.
10. Schilling, F.H., et al., *Neuroblastoma screening at one year of age.* N Engl J Med, 2002. **346**(14): p. 1047-53.
11. Yamamoto, K., et al., *Marginal decrease in mortality and marked increase in incidence as a result of neuroblastoma screening at 6 months of age: cohort study in seven prefectures in Japan.* J Clin Oncol, 2002. **20**(5): p. 1209-14.
12. Schwab, M., et al., *Amplified DNA with limited homology to myc cellular oncogene is shared by human neuroblastoma cell lines and a neuroblastoma tumour.* Nature, 1983. **305**(5931): p. 245-8.
13. Valent, A., et al., *MYCN gene overrepresentation detected in primary neuroblastoma tumour cells without amplification.* J Pathol, 2002. **198**(4): p. 495-501.
14. Brodeur, G.M., *Neuroblastoma: biological insights into a clinical enigma.* Nat Rev Cancer, 2003. **3**(3): p. 203-16.
15. Attiyeh, E.F., et al., *Chromosome 1p and 11q deletions and outcome in neuroblastoma.* N Engl J Med, 2005. **353**(21): p. 2243-53.
16. Henrich, K.O., et al., *Reduced expression of CAMTA1 correlates with adverse outcome in neuroblastoma patients.* Clin Cancer Res, 2006. **12**(1): p. 131-8.
17. Spitz, R., et al., *Gain of distal chromosome arm 17q is not associated with poor prognosis in neuroblastoma.* Clin Cancer Res, 2003. **9**(13): p. 4835-40.
18. Oberthuer, A., et al., *Molecular characterization and classification of neuroblastoma.* Future Oncol, 2009. **5**(5): p. 625-39.
19. Look, A.T., et al., *Cellular DNA content as a predictor of response to chemotherapy in infants with unresectable neuroblastoma.* N Engl J Med, 1984. **311**(4): p. 231-5.
20. Chen, L., et al., *p53 is a direct transcriptional target of MYCN in neuroblastoma.* Cancer Res, 2010. **70**(4): p. 1377-88.
21. Osajima-Hakomori, Y., et al., *Biological role of anaplastic lymphoma kinase in neuroblastoma.* Am J Pathol, 2005. **167**(1): p. 213-22.
22. Cao, Y., et al., *Research progress of neuroblastoma related gene variations.* Oncotarget, 2017. **8**(11): p. 18444-18455.
23. Schonherr, C., et al., *Anaplastic Lymphoma Kinase (ALK) regulates initiation of transcription of MYCN in neuroblastoma cells.* Oncogene, 2012. **31**(50): p. 5193-200.
24. Otto, T., et al., *Stabilization of N-Myc is a critical function of Aurora A in human neuroblastoma.* Cancer Cell, 2009. **15**(1): p. 67-78.
25. Shang, X., et al., *Aurora A is a negative prognostic factor and a new therapeutic target in human neuroblastoma.* Mol Cancer Ther, 2009. **8**(8): p. 2461-9.

26. Carr-Wilkinson, J., et al., *High Frequency of p53/MDM2/p14ARF Pathway Abnormalities in Relapsed Neuroblastoma.* Clin Cancer Res, 2010. **16**(4): p. 1108-18.
27. Tweddle, D.A., et al., *The p53 pathway and its inactivation in neuroblastoma.* Cancer Lett, 2003. **197**(1-2): p. 93-8.
28. Mosse, Y.P., et al., *Germline PHOX2B mutation in hereditary neuroblastoma.* Am J Hum Genet, 2004. **75**(4): p. 727-30.
29. Peifer, M., et al., *Telomerase activation by genomic rearrangements in high-risk neuroblastoma.* Nature, 2015. **526**(7575): p. 700-4.
30. Duan, X.F. and Q. Zhao, *TERT-mediated and ATRX-mediated Telomere Maintenance and Neuroblastoma.* J Pediatr Hematol Oncol, 2018. **40**(1): p. 1-6.
31. Valentijn, L.J., et al., *TERT rearrangements are frequent in neuroblastoma and identify aggressive tumors.* Nat Genet, 2015. **47**(12): p. 1411-4.
32. Albihn, A., J.I. Johnsen, and M.A. Henriksson, *MYC in oncogenesis and as a target for cancer therapies.* Adv Cancer Res, 2010. **107**: p. 163-224.
33. Strieder, V. and W. Lutz, *Regulation of N-myc expression in development and disease.* Cancer Lett, 2002. **180**(2): p. 107-19.
34. Hatton, K.S., et al., *Expression and activity of L-Myc in normal mouse development.* Mol Cell Biol, 1996. **16**(4): p. 1794-804.
35. Davis, A.C., et al., *A null c-myc mutation causes lethality before 10.5 days of gestation in homozygotes and reduced fertility in heterozygous female mice.* Genes Dev, 1993. **7**(4): p. 671-82.
36. Stanton, B.R., et al., *Loss of N-myc function results in embryonic lethality and failure of the epithelial component of the embryo to develop.* Genes Dev, 1992. **6**(12A): p. 2235-47.
37. Bahram, F., et al., *c-Myc hot spot mutations in lymphomas result in inefficient ubiquitination and decreased proteasome-mediated turnover.* Blood, 2000. **95**(6): p. 2104-10.
38. Herbst, A., et al., *A conserved element in Myc that negatively regulates its proapoptotic activity.* EMBO Rep, 2005. **6**(2): p. 177-83.
39. Herbst, A., et al., *Multiple cell-type-specific elements regulate Myc protein stability.* Oncogene, 2004. **23**(21): p. 3863-71.
40. Stone, J., et al., *Definition of regions in human c-myc that are involved in transformation and nuclear localization.* Mol Cell Biol, 1987. **7**(5): p. 1697-709.
41. Blackwood, E.M. and R.N. Eisenman, *Max: a helix-loop-helix zipper protein that forms a sequence-specific DNA-binding complex with Myc.* Science, 1991. **251**(4998): p. 1211-7.
42. Eberhardy, S.R. and P.J. Farnham, *c-Myc mediates activation of the cad promoter via a post-RNA polymerase II recruitment mechanism.* J Biol Chem, 2001. **276**(51): p. 48562-71.
43. Eberhardy, S.R. and P.J. Farnham, *Myc recruits P-TEFb to mediate the final step in the transcriptional activation of the cad promoter.* J Biol Chem, 2002. **277**(42): p. 40156-62.
44. Ayer, D.E., L. Kretzner, and R.N. Eisenman, *Mad: a heterodimeric partner for Max that antagonizes Myc transcriptional activity.* Cell, 1993. **72**(2): p. 211-22.
45. Hurlin, P.J., C. Queva, and R.N. Eisenman, *Mnt, a novel Max-interacting protein is coexpressed with Myc in proliferating cells and mediates repression at Myc binding sites.* Genes Dev, 1997. **11**(1): p. 44-58.
46. Brenner, C., et al., *Myc represses transcription through recruitment of DNA methyltransferase corepressor.* EMBO J, 2005. **24**(2): p. 336-46.
47. Staller, P., et al., *Repression of p15INK4b expression by Myc through association with Miz-1.* Nat Cell Biol, 2001. **3**(4): p. 392-9.
48. Gregory, M.A. and S.R. Hann, *c-Myc proteolysis by the ubiquitin-proteasome pathway: stabilization of c-Myc in Burkitt's lymphoma cells.* Mol Cell Biol, 2000. **20**(7): p. 2423-35.
49. Sears, R., et al., *Multiple Ras-dependent phosphorylation pathways regulate Myc protein stability.* Genes Dev, 2000. **14**(19): p. 2501-14.

50. Welcker, M., et al., *The Fbw7 tumor suppressor regulates glycogen synthase kinase 3 phosphorylation-dependent c-Myc protein degradation.* Proc Natl Acad Sci U S A, 2004. **101**(24): p. 9085-90.
51. Cawley, S., et al., *Unbiased mapping of transcription factor binding sites along human chromosomes 21 and 22 points to widespread regulation of noncoding RNAs.* Cell, 2004. **116**(4): p. 499-509.
52. Fernandez, P.C., et al., *Genomic targets of the human c-Myc protein.* Genes Dev, 2003. **17**(9): p. 1115-29.
53. Nie, Z., et al., *c-Myc is a universal amplifier of expressed genes in lymphocytes and embryonic stem cells.* Cell, 2012. **151**(1): p. 68-79.
54. Gomez-Roman, N., et al., *Direct activation of RNA polymerase III transcription by c-Myc.* Nature, 2003. **421**(6920): p. 290-4.
55. Grandori, C., et al., *c-Myc binds to human ribosomal DNA and stimulates transcription of rRNA genes by RNA polymerase I.* Nat Cell Biol, 2005. **7**(3): p. 311-8.
56. Adhikary, S. and M. Eilers, *Transcriptional regulation and transformation by Myc proteins.* Nat Rev Mol Cell Biol, 2005. **6**(8): p. 635-45.
57. Mittnacht, S., *Control of pRB phosphorylation.* Curr Opin Genet Dev, 1998. **8**(1): p. 21-7.
58. Hermeking, H., et al., *Identification of CDK4 as a target of c-MYC.* Proc Natl Acad Sci U S A, 2000. **97**(5): p. 2229-34.
59. Westermann, F., et al., *Distinct transcriptional MYCN/c-MYC activities are associated with spontaneous regression or malignant progression in neuroblastomas.* Genome Biol, 2008. **9**(10): p. R150.
60. Philipp, A., et al., *Repression of cyclin D1: a novel function of MYC.* Mol Cell Biol, 1994. **14**(6): p. 4032-43.
61. Oliver, T.G., et al., *Transcriptional profiling of the Sonic hedgehog response: a critical role for N-myc in proliferation of neuronal precursors.* Proc Natl Acad Sci U S A, 2003. **100**(12): p. 7331-6.
62. Bouchard, C., et al., *Direct induction of cyclin D2 by Myc contributes to cell cycle progression and sequestration of p27.* EMBO J, 1999. **18**(19): p. 5321-33.
63. Ozaki, T. and A. Nakagawara, *p53: the attractive tumor suppressor in the cancer research field.* J Biomed Biotechnol, 2011. **2011**: p. 603925.
64. Eckerle, I., et al., *Regulation of BIRC5 and its isoform BIRC5-2B in neuroblastoma.* Cancer Lett, 2009. **285**(1): p. 99-107.
65. Seoane, J., H.V. Le, and J. Massague, *Myc suppression of the p21(Cip1) Cdk inhibitor influences the outcome of the p53 response to DNA damage.* Nature, 2002. **419**(6908): p. 729-34.
66. Chen, Y., et al., *Oncogenic mutations of ALK kinase in neuroblastoma.* Nature, 2008. **455**(7215): p. 971-4.
67. Zindy, F., et al., *Myc signaling via the ARF tumor suppressor regulates p53-dependent apoptosis and immortalization.* Genes Dev, 1998. **12**(15): p. 2424-33.
68. Egle, A., et al., *Bim is a suppressor of Myc-induced mouse B cell leukemia.* Proc Natl Acad Sci U S A, 2004. **101**(16): p. 6164-9.
69. Eischen, C.M., et al., *Bcl-2 is an apoptotic target suppressed by both c-Myc and E2F-1.* Oncogene, 2001. **20**(48): p. 6983-93.
70. Wanzel, M., et al., *Akt and 14-3-3eta regulate Miz1 to control cell-cycle arrest after DNA damage.* Nat Cell Biol, 2005. **7**(1): p. 30-41.
71. Bouchard, C., et al., *Myc-induced proliferation and transformation require Akt-mediated phosphorylation of FoxO proteins.* EMBO J, 2004. **23**(14): p. 2830-40.
72. Ruiz-Perez, M.V., A.B. Henley, and M. Arsenian-Henriksson, *The MYCN Protein in Health and Disease.* Genes (Basel), 2017. **8**(4).
73. Kang, J.H., et al., *MYCN silencing induces differentiation and apoptosis in human neuroblastoma cells.* Biochem Biophys Res Commun, 2006. **351**(1): p. 192-7.
74. Nara, K., et al., *Silencing of MYCN by RNA interference induces growth inhibition, apoptotic activity and cell differentiation in a neuroblastoma cell line with MYCN amplification.* Int J Oncol, 2007. **30**(5): p. 1189-96.

75. Prochownik, E.V. and P.K. Vogt, *Therapeutic Targeting of Myc.* Genes Cancer, 2010. **1**(6): p. 650-659.
76. Muller, I., et al., *Targeting of the MYCN protein with small molecule c-MYC inhibitors.* PLoS One, 2014. **9**(5): p. e97285.
77. Clausen, D.M., et al., *In vitro cytotoxicity and in vivo efficacy, pharmacokinetics, and metabolism of 10074-G5, a novel small-molecule inhibitor of c-Myc/Max dimerization.* J Pharmacol Exp Ther, 2010. **335**(3): p. 715-27.
78. Brockmann, M., et al., *Small molecule inhibitors of aurora-a induce proteasomal degradation of N-myc in childhood neuroblastoma.* Cancer Cell, 2013. **24**(1): p. 75-89.
79. Michaelis, M., et al., *Aurora kinases as targets in drug-resistant neuroblastoma cells.* PLoS One, 2014. **9**(9): p. e108758.
80. Segerstrom, L., et al., *Effects of small molecule inhibitors of PI3K/Akt/mTOR signaling on neuroblastoma growth in vitro and in vivo.* Int J Cancer, 2011. **129**(12): p. 2958-65.
81. Vaughan, L., et al., *Inhibition of mTOR-kinase destabilizes MYCN and is a potential therapy for MYCN-dependent tumors.* Oncotarget, 2016. **7**(36): p. 57525-57544.
82. Krytska, K., et al., *Crizotinib Synergizes with Chemotherapy in Preclinical Models of Neuroblastoma.* Clin Cancer Res, 2016. **22**(4): p. 948-60.
83. Gamble, L.D., et al., *MYCN sensitizes neuroblastoma to the MDM2-p53 antagonists Nutlin-3 and MI-63.* Oncogene, 2012. **31**(6): p. 752-63.
84. Shi, J. and C.R. Vakoc, *The mechanisms behind the therapeutic activity of BET bromodomain inhibition.* Mol Cell, 2014. **54**(5): p. 728-36.
85. Dhalluin, C., et al., *Structure and ligand of a histone acetyltransferase bromodomain.* Nature, 1999. **399**(6735): p. 491-6.
86. Belkina, A.C. and G.V. Denis, *BET domain co-regulators in obesity, inflammation and cancer.* Nat Rev Cancer, 2012. **12**(7): p. 465-77.
87. Filippakopoulos, P., et al., *Histone recognition and large-scale structural analysis of the human bromodomain family.* Cell, 2012. **149**(1): p. 214-31.
88. Jang, M.K., et al., *The bromodomain protein Brd4 is a positive regulatory component of P-TEFb and stimulates RNA polymerase II-dependent transcription.* Mol Cell, 2005. **19**(4): p. 523-34.
89. Yang, Z., N. He, and Q. Zhou, *Brd4 recruits P-TEFb to chromosomes at late mitosis to promote G1 gene expression and cell cycle progression.* Mol Cell Biol, 2008. **28**(3): p. 967-76.
90. Devaiah, B.N., et al., *BRD4 is a histone acetyltransferase that evicts nucleosomes from chromatin.* Nat Struct Mol Biol, 2016. **23**(6): p. 540-8.
91. Devaiah, B.N., et al., *BRD4 is an atypical kinase that phosphorylates serine2 of the RNA polymerase II carboxy-terminal domain.* Proc Natl Acad Sci U S A, 2012. **109**(18): p. 6927-32.
92. Kanno, T., et al., *BRD4 assists elongation of both coding and enhancer RNAs by interacting with acetylated histones.* Nat Struct Mol Biol, 2014. **21**(12): p. 1047-57.
93. Popovic, R. and J.D. Licht, *Emerging epigenetic targets and therapies in cancer medicine.* Cancer Discov, 2012. **2**(5): p. 405-13.
94. Jiang, Y.W., et al., *Mammalian mediator of transcriptional regulation and its possible role as an end-point of signal transduction pathways.* Proc Natl Acad Sci U S A, 1998. **95**(15): p. 8538-43.
95. Loven, J., et al., *Selective inhibition of tumor oncogenes by disruption of super-enhancers.* Cell, 2013. **153**(2): p. 320-34.
96. Wu, S.Y. and C.M. Chiang, *The double bromodomain-containing chromatin adaptor Brd4 and transcriptional regulation.* J Biol Chem, 2007. **282**(18): p. 13141-5.
97. Wang, F., et al., *Brd2 disruption in mice causes severe obesity without Type 2 diabetes.* Biochem J, 2009. **425**(1): p. 71-83.
98. Nicodeme, E., et al., *Suppression of inflammation by a synthetic histone mimic.* Nature, 2010. **468**(7327): p. 1119-23.
99. Spiltoir, J.I., et al., *BET acetyl-lysine binding proteins control pathological cardiac hypertrophy.* J Mol Cell Cardiol, 2013. **63**: p. 175-9.

100. Banerjee, C., et al., *BET bromodomain inhibition as a novel strategy for reactivation of HIV-1.* J Leukoc Biol, 2012. **92**(6): p. 1147-54.
101. Wu, S.Y., et al., *Brd4 links chromatin targeting to HPV transcriptional silencing.* Genes Dev, 2006. **20**(17): p. 2383-96.
102. Wu, S.Y., et al., *Phospho switch triggers Brd4 chromatin binding and activator recruitment for gene-specific targeting.* Mol Cell, 2013. **49**(5): p. 843-57.
103. Mertz, J.A., et al., *Targeting MYC dependence in cancer by inhibiting BET bromodomains.* Proc Natl Acad Sci U S A, 2011. **108**(40): p. 16669-74.
104. You, J., et al., *Regulation of aurora B expression by the bromodomain protein Brd4.* Mol Cell Biol, 2009. **29**(18): p. 5094-103.
105. Shi, J., et al., *Disrupting the interaction of BRD4 with diacetylated Twist suppresses tumorigenesis in basal-like breast cancer.* Cancer Cell, 2014. **25**(2): p. 210-25.
106. Denis, G.V., et al., *RING3 kinase transactivates promoters of cell cycle regulatory genes through E2F.* Cell Growth Differ, 2000. **11**(8): p. 417-24.
107. Zhang, L., et al., *microRNA-141 is involved in a nasopharyngeal carcinoma-related genes network.* Carcinogenesis, 2010. **31**(4): p. 559-66.
108. Delmore, J.E., et al., *BET bromodomain inhibition as a therapeutic strategy to target c-Myc.* Cell, 2011. **146**(6): p. 904-17.
109. Shi, J., et al., *Role of SWI/SNF in acute leukemia maintenance and enhancer-mediated Myc regulation.* Genes Dev, 2013. **27**(24): p. 2648-62.
110. Liu, W., et al., *Brd4 and JMJD6-associated anti-pause enhancers in regulation of transcriptional pause release.* Cell, 2013. **155**(7): p. 1581-1595.
111. Dey, A., et al., *A bromodomain protein, MCAP, associates with mitotic chromosomes and affects G(2)-to-M transition.* Mol Cell Biol, 2000. **20**(17): p. 6537-49.
112. Dey, A., et al., *The double bromodomain protein Brd4 binds to acetylated chromatin during interphase and mitosis.* Proc Natl Acad Sci U S A, 2003. **100**(15): p. 8758-63.
113. Mochizuki, K., et al., *The bromodomain protein Brd4 stimulates G1 gene transcription and promotes progression to S phase.* J Biol Chem, 2008. **283**(14): p. 9040-8.
114. Maruyama, T., et al., *A Mammalian bromodomain protein, brd4, interacts with replication factor C and inhibits progression to S phase.* Mol Cell Biol, 2002. **22**(18): p. 6509-20.
115. French, C.A., *Pathogenesis of NUT midline carcinoma.* Annu Rev Pathol, 2012. **7**: p. 247-65.
116. Filippakopoulos, P., et al., *Selective inhibition of BET bromodomains.* Nature, 2010. **468**(7327): p. 1067-73.
117. Prinjha, R.K., J. Witherington, and K. Lee, *Place your BETs: the therapeutic potential of bromodomains.* Trends Pharmacol Sci, 2012. **33**(3): p. 146-53.
118. Ferri, E., C. Petosa, and C.E. McKenna, *Bromodomains: Structure, function and pharmacology of inhibition.* Biochem Pharmacol, 2016. **106**: p. 1-18.
119. Gelato, K.A., et al., *Targeting epigenetic regulators for cancer therapy: modulation of bromodomain proteins, methyltransferases, demethylases, and microRNAs.* Expert Opin Ther Targets, 2016. **20**(7): p. 783-99.
120. Zuber, J., et al., *RNAi screen identifies Brd4 as a therapeutic target in acute myeloid leukaemia.* Nature, 2011. **478**(7370): p. 524-8.
121. Puissant, A., et al., *Targeting MYCN in neuroblastoma by BET bromodomain inhibition.* Cancer Discov, 2013. **3**(3): p. 308-23.
122. Wyce, A., et al., *BET inhibition silences expression of MYCN and BCL2 and induces cytotoxicity in neuroblastoma tumor models.* PLoS One, 2013. **8**(8): p. e72967.
123. Henssen, A., et al., *Targeting MYCN-Driven Transcription By BET-Bromodomain Inhibition.* Clin Cancer Res, 2016. **22**(10): p. 2470-81.
124. Andrieu, G., A.C. Belkina, and G.V. Denis, *Clinical trials for BET inhibitors run ahead of the science.* Drug Discov Today Technol, 2016. **19**: p. 45-50.
125. Iwakura, H.a.A., Takahashi, *Neuroblastoma*, in *Chapter Neuroblastoma Mouse Model*, M.A. Hayat, Editor. 2012, Springer Science+Business Media B.V. p. 31-38.
126. Teitz, T., et al., *Preclinical models for neuroblastoma: establishing a baseline for treatment.* PLoS One, 2011. **6**(4): p. e19133.

127. Weiss, W.A., et al., *Targeted expression of MYCN causes neuroblastoma in transgenic mice.* EMBO J, 1997. **16**(11): p. 2985-95.
128. Althoff, K., et al., *A Cre-conditional MYCN-driven neuroblastoma mouse model as an improved tool for preclinical studies.* Oncogene, 2015. **34**(26): p. 3357-68.
129. Houghton, P.J., et al., *The pediatric preclinical testing program: description of models and early testing results.* Pediatr Blood Cancer, 2007. **49**(7): p. 928-40.
130. Jamil, S., et al., *Tropism of the in situ growth from biopsies of childhood neuroectodermal tumors following transplantation into experimental teratoma.* Int J Cancer, 2014. **134**(7): p. 1630-7.
131. Braekeveldt, N., et al., *Neuroblastoma patient-derived orthotopic xenografts retain metastatic patterns and geno- and phenotypes of patient tumours.* Int J Cancer, 2015. **136**(5): p. E252-61.
132. Stewart, E., et al., *Development and characterization of a human orthotopic neuroblastoma xenograft.* Dev Biol, 2015. **407**(2): p. 344-55.
133. Khanna, C., et al., *Biologically relevant orthotopic neuroblastoma xenograft models: primary adrenal tumor growth and spontaneous distant metastasis.* In Vivo, 2002. **16**(2): p. 77-85.
134. Braekeveldt, N. and D. Bexell, *Patient-derived xenografts as preclinical neuroblastoma models.* Cell Tissue Res, 2018. **372**(2): p. 233-243.
135. Corallo, D., et al., *The zebrafish as a model for studying neuroblastoma.* Cancer Cell Int, 2016. **16**: p. 82.
136. He, S., et al., *Synergy between loss of NF1 and overexpression of MYCN in neuroblastoma is mediated by the GAP-related domain.* Elife, 2016. **5**.
137. Pei, D., et al., *Distinct neuroblastoma-associated alterations of PHOX2B impair sympathetic neuronal differentiation in zebrafish models.* PLoS Genet, 2013. **9**(6): p. e1003533.
138. Zhu, S., et al., *Activated ALK collaborates with MYCN in neuroblastoma pathogenesis.* Cancer Cell, 2012. **21**(3): p. 362-73.
139. Oliveros, J.C. *Venny. An interactive tool for comparing lists with Venn's diagrams*. 2007-2015; Available from: http://bioinfogp.cnb.csic.es/tools/venny/index.html.
140. Fabregat, A., et al., *The Reactome Pathway Knowledgebase.* Nucleic Acids Res, 2018. **46**(D1): p. D649-D655.
141. Apweiler, R., et al., *UniProt: the Universal Protein knowledgebase.* Nucleic Acids Res, 2004. **32**(Database issue): p. D115-9.
142. Čermák, V. *Molbiotools- Molecular Biology Online Apps*. 2014-2018; Available from: http://www.molbiotools.com/.
143. Ryan, J.A., *Cell Cloning by serial Dilution in 96 Well Plates*. 2008, In, C. Incorporated, ed.
144. Invitrogen, *T-REx System*, in *A Tetracycline-Regulated Expression System for Mammalian Cells*. 2006.
145. Ryl, T., et al., *Cell-Cycle Position of Single MYC-Driven Cancer Cells Dictates Their Susceptibility to a Chemotherapeutic Drug.* Cell Syst, 2017. **5**(3): p. 237-250 e8.
146. Kennedy, A.L., et al., *Functional, chemical genomic, and super-enhancer screening identify sensitivity to cyclin D1/CDK4 pathway inhibition in Ewing sarcoma.* Oncotarget, 2015. **6**(30): p. 30178-93.
147. Baker, S.J. and E.P. Reddy, *CDK4: A Key Player in the Cell Cycle, Development, and Cancer.* Genes Cancer, 2012. **3**(11-12): p. 658-69.
148. Moll, U.M. and O. Petrenko, *The MDM2-p53 interaction.* Mol Cancer Res, 2003. **1**(14): p. 1001-8.
149. Cohen, P. and S. Frame, *The renaissance of GSK3.* Nat Rev Mol Cell Biol, 2001. **2**(10): p. 769-76.
150. Medina, M. and F. Wandosell, *Deconstructing GSK-3: The Fine Regulation of Its Activity.* Int J Alzheimers Dis, 2011. **2011**: p. 479249.
151. Gregory, M.A., Y. Qi, and S.R. Hann, *Phosphorylation by glycogen synthase kinase-3 controls c-myc proteolysis and subnuclear localization.* J Biol Chem, 2003. **278**(51): p. 51606-12.

152. Rayasam, G.V., et al., *Glycogen synthase kinase 3: more than a namesake.* Br J Pharmacol, 2009. **156**(6): p. 885-98.
153. Nortmeyer, M., *Genetische und pharmakologische Hemmung des MYCN Onkogens in Zellkultur*. 2012, Albert-Ludwigs-Universität Freiburg i. Br. p. 102.
154. Picaud, S., et al., *Generation of a Selective Small Molecule Inhibitor of the CBP/p300 Bromodomain for Leukemia Therapy.* Cancer Res, 2015. **75**(23): p. 5106-5119.
155. Charles River Laboratories International, I. *Immunodeficient Models-North America*. 2017; Available from: https://www.criver.com/sites/default/files/Technical%20Resources/Immunodeficient%20Mice%20and%20Rats.pdf.
156. Shultz, L.D., et al., *Human lymphoid and myeloid cell development in NOD/LtSz-scid IL2R gamma null mice engrafted with mobilized human hemopoietic stem cells.* J Immunol, 2005. **174**(10): p. 6477-89.
157. Pantelouris, E.M., *Absence of thymus in a mouse mutant.* Nature, 1968. **217**(5126): p. 370-1.
158. Van Roy, N., et al., *Chromosome 2 short arm translocations revealed by M-FISH analysis of neuroblastoma cell lines.* Med Pediatr Oncol, 2000. **35**(6): p. 538-40.
159. Sun, W., et al., *EWS-FLI1 and RNA helicase A interaction inhibitor YK-4-279 inhibits growth of neuroblastoma.* Oncotarget, 2017. **8**(55): p. 94780-94792.
160. Chiu, B., et al., *Surgery combined with controlled-release doxorubicin silk films as a treatment strategy in an orthotopic neuroblastoma mouse model.* Br J Cancer, 2014. **111**(4): p. 708-15.
161. Cardoso, C.C., S.R. Bornstein, and P.J. Hornsby, *Optimizing orthotopic cell transplantation in the mouse adrenal gland.* Cell Transplant, 2010. **19**(5): p. 565-72.
162. Wikipedia. *Magnetic resonance imaging*. 2018; Available from: https://en.wikipedia.org/wiki/Magnetic_resonance_imaging.
163. Jacobs, M.A., T.S. Ibrahim, and R. Ouwerkerk, *AAPM/RSNA physics tutorials for residents: MR imaging: brief overview and emerging applications.* Radiographics, 2007. **27**(4): p. 1213-29.
164. Hertwig, F., M. Peifer, and M. Fischer, *Telomere maintenance is pivotal for high-risk neuroblastoma.* Cell Cycle, 2016. **15**(3): p. 311-2.
165. McDonald, E.R., 3rd, et al., *Project DRIVE: A Compendium of Cancer Dependencies and Synthetic Lethal Relationships Uncovered by Large-Scale, Deep RNAi Screening.* Cell, 2017. **170**(3): p. 577-592 e10.
166. Henssen, A., et al., *BET bromodomain protein inhibition is a therapeutic option for medulloblastoma.* Oncotarget, 2013. **4**(11): p. 2080-95.
167. Shao, Q., et al., *BET protein inhibitor JQ1 attenuates Myc-amplified MCC tumor growth in vivo.* Cancer Res, 2014. **74**(23): p. 7090-102.
168. Zhu, X., et al., *Bromodomain and Extraterminal Protein Inhibitor JQ1 Suppresses Thyroid Tumor Growth in a Mouse Model.* Clin Cancer Res, 2017. **23**(2): p. 430-440.
169. Liao, S., et al., *Genetic modifiers of the BRD4-NUT dependency of NUT midline carcinoma uncovers a synergism between BETis and CDK4/6is.* Genes Dev, 2018. **32**(17-18): p. 1188-1200.
170. Hong, S.H., et al., *Epigenetic reader BRD4 inhibition as a therapeutic strategy to suppress E2F2-cell cycle regulation circuit in liver cancer.* Oncotarget, 2016. **7**(22): p. 32628-40.
171. Mumby, S., et al., *Bromodomain and extra-terminal protein mimic JQ1 decreases inflammation in human vascular endothelial cells: Implications for pulmonary arterial hypertension.* Respirology, 2017. **22**(1): p. 157-164.
172. Stewart, H.J., et al., *BRD4 associates with p53 in DNMT3A-mutated leukemia cells and is implicated in apoptosis by the bromodomain inhibitor JQ1.* Cancer Med, 2013. **2**(6): p. 826-35.
173. Menon, V. and L. Povirk, *Involvement of p53 in the repair of DNA double strand breaks: multifaceted Roles of p53 in homologous recombination repair (HRR) and non-homologous end joining (NHEJ).* Subcell Biochem, 2014. **85**: p. 321-36.

174. Scully, R. and A. Xie, *Double strand break repair functions of histone H2AX.* Mutat Res, 2013. **750**(1-2): p. 5-14.
175. Floyd, S.R., et al., *The bromodomain protein Brd4 insulates chromatin from DNA damage signalling.* Nature, 2013. **498**(7453): p. 246-50.
176. Lamarche, B.J., N.I. Orazio, and M.D. Weitzman, *The MRN complex in double-strand break repair and telomere maintenance.* FEBS Lett, 2010. **584**(17): p. 3682-95.
177. Yik, J.H., et al., *Inhibition of P-TEFb (CDK9/Cyclin T) kinase and RNA polymerase II transcription by the coordinated actions of HEXIM1 and 7SK snRNA.* Mol Cell, 2003. **12**(4): p. 971-82.
178. Lew, Q.J., et al., *Identification of HEXIM1 as a positive regulator of p53.* J Biol Chem, 2012. **287**(43): p. 36443-54.
179. Lau, J., et al., *Ubiquitination of HEXIM1 by HDM2.* Cell Cycle, 2009. **8**(14): p. 2247-54.
180. Lustig, B. and J. Behrens, *The Wnt signaling pathway and its role in tumor development.* J Cancer Res Clin Oncol, 2003. **129**(4): p. 199-221.
181. Zhang, Y., et al., *JQ-1 Inhibits Colon Cancer Proliferation via Suppressing Wnt/beta-Catenin Signaling and miR-21.* Chem Res Toxicol, 2018. **31**(5): p. 302-307.
182. Duffy, D.J., et al., *GSK3 inhibitors regulate MYCN mRNA levels and reduce neuroblastoma cell viability through multiple mechanisms, including p53 and Wnt signaling.* Mol Cancer Ther, 2014. **13**(2): p. 454-67.
183. Morscher, R.J., et al., *Inhibition of Neuroblastoma Tumor Growth by Ketogenic Diet and/or Calorie Restriction in a CD1-Nu Mouse Model.* PLoS One, 2015. **10**(6): p. e0129802.
184. Schnepp, R.W. and J.M. Maris, *Targeting MYCN: a good BET for improving neuroblastoma therapy?* Cancer Discov, 2013. **3**(3): p. 255-7.
185. Houzelstein, D., et al., *Growth and early postimplantation defects in mice deficient for the bromodomain-containing protein Brd4.* Mol Cell Biol, 2002. **22**(11): p. 3794-802.
186. Bolden, J.E., et al., *Inducible in vivo silencing of Brd4 identifies potential toxicities of sustained BET protein inhibition.* Cell Rep, 2014. **8**(6): p. 1919-1929.
187. You, J., et al., *Kaposi's sarcoma-associated herpesvirus latency-associated nuclear antigen interacts with bromodomain protein Brd4 on host mitotic chromosomes.* J Virol, 2006. **80**(18): p. 8909-19.
188. Korb, E., et al., *BET protein Brd4 activates transcription in neurons and BET inhibitor Jq1 blocks memory in mice.* Nat Neurosci, 2015. **18**(10): p. 1464-73.
189. Matzuk, M.M., et al., *Small-molecule inhibition of BRDT for male contraception.* Cell, 2012. **150**(4): p. 673-84.
190. Liu, P.Y., et al., *The BET bromodomain inhibitor exerts the most potent synergistic anticancer effects with quinone-containing compounds and anti-microtubule drugs.* Oncotarget, 2016. **7**(48): p. 79217-79232.

10 Danksagung

Eine Doktorarbeit zu erstellen ist ein zeitaufwändiges und komplexes Unterfangen, das für einen erfolgreichen Abschluss die Unterstützung einer Reihe von Personen benötigt. Aus diesem Grund möchte ich die Möglichkeit nutzen, mich hier bei den wichtigsten zu bedanken.

Zunächst einmal danke ich Frank Westermann, der es mir ermöglicht hat, meine Doktorarbeit am DKFZ in der Arbeitsgruppe Neuroblastomgenomik anzufertigen und auf dessen Ideen das Thema meiner Arbeit aufbaut.

Kooperationen mit anderen Wissenschaftlern sind ein unverzichtbarer Vorteil bei der Arbeit an einem Wissenschaftsstandort wie Heidelberg. Ich bedanke mich daher bei Chunxuan Shao, Carl Herrmann und Umut Toprak für die Unterstützung bei der Auswertung der RNA-seq Daten, bei Eileen Reinz für die gemeinsame Arbeit an den RPPA-Daten, bei Xiaoqi Jiang für die Berechnung der IC50 und EC50 Werte, sowie bei Volker Ehemann für die FACS-Messungen. Bei der Arbeit mit den Mäusen hat Karin Müller-Decker von der Core facility Tumormodelle mit ihrem Team mitgewirkt, Tanja Poth beurteilte die Tumorproben histologisch und Jörg Peter stellte mir den Biolumineszenz-Imager seiner Arbeitsgruppe zur Verfügung.

Mit der Arbeit an den Mausmodellen hatte ich die Aufgabe zu bewältigen, erstmals seit vielen Jahren wieder ein Projekt mit Mäusen in der Arbeitsgruppe zu realisieren. Ein ganz besonderer Dank geht daher an Sina Gogolin und Lisa Seyler, die mich bei diesem Teil der Arbeit wahnsinnig unterstützt haben. Ohne ihren Input bei der gemeinsamen Suche nach Lösungen wäre ich mit dem Projekt vermutlich nicht zu so einem guten Ergebnis gekommen. Sina möchte ich darüber hinaus für unzählige wertvolle Hinweise und Kommentare zu dieser Arbeit danken, die mir bei der Anfertigung der Doktorarbeit abseits des DKFZ sehr geholfen haben.

Bei der Arbeit verbringt man einen nicht unerheblichen Teil seines Tages mit Menschen, die man sich nicht aussuchen kann. Aus diesem Grund bin ich sehr dankbar dafür, dass ich im Labor der Neuroblastomgenomik so viele unglaublich nette Menschen kennen lernen durfte. Einen herzlichen Dank an meine Kollegen und Kolleginnen für die tolle Arbeitsatmosphäre, die vielen Kuchenbäcker und Kartenschreiber, die Mädels-Eisrunden wenn am Nachmittag das Gehirn zu überhitzen drohte und die gemeinsamen Ausflüge und Konferenzen. Allen voran meine Sitznachbarin Sabine Hartlieb: Danke fürs immer wieder Motivieren und Aufbauen, fürs gemeinsame Lachen und die guten Gespräche in den letzten Jahren.

Die akademische Laufbahn beginnt bereits weit vor der Promotion. Daher möchte ich mich auf diesem Wege auch bei den Menschen bedanken, die mich schon länger auf meinem Weg begleiten. Allen voran meine Eltern Christine und Hans-Detlef Nortmeyer, die nicht nur mein Studium finanziert haben, sondern mich auch bereits als Kind mit voller Kraft dabei unterstützt

haben, allen meinen Interessen nachzugehen. Ich danke meiner Schwester Astrid Nortmeyer, die es geschafft hat mir einfach nur zuzuhören wenn ich mal wieder frustriert war, weil mein Projekt in einer Sackgasse zu hängen schien. Und natürlich meinem Freund Paul Adametz, der mich wie kein anderer dazu motiviert hat, mich durchzuboxen und die Promotion auch in der Elternzeit und parallel zum neuen Job durchzuziehen, ohne ihn hätte es dieser Text niemals in den Druck geschafft. Danken möchte ich auch meiner Tochter Ronja für ihre Geduld, wenn die Mama mal wieder keine Zeit hatte, weil sie am Schreibtisch saß.